Design and Synthesis of Novel Self-Assembled Supramolecular Coordination Cages

Thesis for Receiving the Degree of

"Doctor rerum naturalium"

TU Dortmund

Fakultät für Chemie und Chemische Biologie

technische universität dortmund

Name: Bo Zhang
from Urumchi, Xinjiang, China
Dortmund, 2019

To ordain conscience for Heaven and Earth.

To settle the livehood for populations.

To trace the lost learnings for past sages.

To establish peace for all future generations.

by Zai Zhang

Principal advisor:	Prof. Dr. Guido Clever
Secondary surveyor:	JProf. Dr. Sebastian Henke
Filed on:	January 1, 2020

Eidesstattliche Versicherung (Affidavit)

Name, Vorname
(Surname, first name)

Matrikel-Nr.
(Enrolment number)

Belehrung:
Wer vorsätzlich gegen eine die Täuschung über Prü- fungsleistungen betreffende Reg(Surname, first name)(Enrolment number)elung einer Hochschul- prüfungsordnung verstößt, handelt ordnungswidrig. Die Ordnungswidrigkeit kann mit einer Geldbuße von bis zu 50.000,00 € geahndet werden. Zuständige Verwaltungs- behörde für die Verfolgung und Ahndung von Ordnungs- widrigkeiten ist der Kanzler/die Kanzlerin der Techni- schen Universität Dortmund. Im Falle eines mehrfachen oder sonstigen schwerwiegenden Täuschungsversu- ches kann der Prüfling zudem exmatrikuliert werden, § 63 Abs. 5 Hochschulgesetz NRW.
Die Abgabe einer falschen Versicherung an Eides statt ist strafbar.
Wer vorsätzlich eine falsche Versicherung an Eides statt abgibt, kann mit einer Freiheitsstrafe bis zu drei Jahren oder mit Geldstrafe bestraft werden, § 156 StGB. Die fahrlässige Abgabe einer falschen Versicherung an Eides statt kann mit einer Freiheitsstrafe bis zu einem Jahr oder Geldstrafe bestraft werden, § 161 StGB.
Die oben stehende Belehrung habe ich zur Kenntnis genommen:

Official notification:
Any person who intentionally breaches any regulation of university examination regulations relating to deception in examination performance is acting improperly. This offence can be punished with a fine of up to EUR 50,000.00. The competent administrative authority for the pursuit and prosecution of offences of this type is the chancellor of the TU Dortmund University. In the case of multiple or other serious attempts at deception, the candidate can also be unenrolled, Section 63, paragraph 5 of the Universities Act of North Rhine-Westphalia.

The submission of a false affidavit is punishable.
Any person who intentionally submits a false affidavit can be punished with a prison sentence of up to three years or a fine, Section 156 of the Criminal Code. The negligent submission of a false affidavit can be punished with a prison sentence of up to one year or a fine, Section 161 of the Criminal Code.

I have taken note of the above official notification.

Ort, Datum
(Place, date)

Unterschrift
(Signature)

Titel der Dissertation:
(Title of the thesis):

Ich versichere hiermit an Eides statt, dass ich die vorliegende Dissertation mit dem Titel selbstständig und ohne unzulässige fremde Hilfe angefertigt habe. Ich habe keine anderen als die angegebenen Quellen und Hilfsmittel benutzt sowie wörtliche und sinngemäße Zitate kenntlich gemacht.
Die Arbeit hat in gegenwärtiger oder in einer anderen Fassung weder der TU Dortmund noch einer anderen Hochschule im Zusammenhang mit einer staatlichen oder akademischen Prüfung vorgelegen.

I hereby swear that I have completed the present dissertation independently and without inadmissible external support. I have not used any sources or tools other than those indicated and have identified literal and analogous quotations.
The thesis in its current version or another version has not been presented to the TU Dortmund University or another university in connection with a state or academic examination.*

*Please be aware that solely the German version of the affidavit ("Eidesstattliche Versicherung") for the PhD thesis is the official and legally binding version.

Ort, Datum
(Place, date)

Unterschrift
(Signature)

List of Publications and Conference Contributions

Publications

1. **B. Zhang**, H. Lee, J. J. Holstein, G. H. Clever, *Non-statistical Multicomponent Assembly of Coordination Cages* (in preparation).
2. **B. Zhang**, J. J. Holstein, R. A. Mata, G. H. Clever, *Control of London Dispersion Interactions in Self-Assembled Host-Guest System* (in preparation).
3. S. Löffler, A. Wuttke, **B. Zhang**, J. J. Holstein, R. A. Mata, G. H. Clever, *Chem. Commun*. **2017**, *53*, 11933.
4. X. Shen, H. Huo, C. Wang, **B. Zhang**, K. Harms, E. Meggers, *Chem. Eur. J.* **2015**, *21*, 9720.

Conference Contributions

2017

- **poster contribution** on 10th Day of Chemistry of TU Dortmund.
- **poster contribution** on Fachsymposium SupraChem 2017.

2018

- **poster contribution** on 14th Koordinationschemie-Treffen (KCT2018).
- **poster contribution** on 9th Münster Symposium on Cooperative Effects in Chemistry (MSCEC2018).

2019

- **oral presentation** on 12th Day of Chemistry of TU Dortmund.
- **poster contribution** on 10th Münster Symposium on Cooperative Effects in Chemistry (MSCEC2019).
- **poster contribution** accepted for 14th International Symposium on Macrocyclic and Supramolecular Chemistry (ISMSC2019).
- **oral presentation** on 4th Summer school of the SPP 1807 “Control of London dispersion” interactions in molecular chemistry”.
- **poster contribution** International Symposium 2019 on "Confinement-Controlled Chemist

Abstract

The research emphases of the Ph.D. projects focus on two topics: construction of heteroleptic self-assembled cage structures based on coordination chemistry and control of London dispersion interactions in self-assembled supramolecular host-guest systems.

Metal-mediated self-assembly has been heavily employed for constructing nanosized structures. For instance, supramolecular cages, formed by coordination of organic ligands and metal cations, have drawn broad interests and been intensively studied in the last decades. The hollow structures have been applied in fields such as molecular recognition, drug delivery and catalysis. However, to date, most functionalized self-assemblies contain only one type of modification. In order to expand functions by introducing various chemical moieties into one single self-assembled architecture, a novel strategy has been developed. In chapter 2, a series of heteroleptic coordination cages comprising up to four different organic ligands in a non-statistical distribution can be produced by combining concepts of shape complementarity, coordination site tuning and template effects. The novel heteroleptic cages are formed by bridging Co(III)-salphen complex-based binuclear macrocycles with carefully designed banana-shaped ligands to obtain hollow structures with unique anisotropic shapes. Altogether five different organic ligands were synthesized. Depending on the combination, these ligands can selectively form five self-assembled cages with Pd(II) or Co(III) cations, four of which are heteroleptic. All the cage structures were fully characterized by NMR, HRMS and single crystal structure analysis.

London dispersion interactions are weak non-covalent interactions, but these attractive interactions can also play important roles in structural stability with a large number of interacting atoms. On the other hand, increasing the number of interaction atoms bears also the risk for enhancement of the steric repulsion. To have a better idea on how to adjust the balance between London dispersion and steric repulsion, a series of endohedrally functionalized $[Pd_2L_4]^{4+}$-type coordination cages have been designed and synthesized, which will be described in in chapter 4. One of these cages was equipped with methyl groups (cage $[Pd_2\mathbf{L}^{\mathbf{Me}}{}_4]^{4+}$) as the reference, the other two with sterically bulky *n*-butyl (cage $[Pd_2\mathbf{L}^{\mathbf{Bu}}{}_4]^{4+}$) or phenyl ($[Pd_2\mathbf{L}^{\mathbf{Ph}}{}_4]^{4+}$) groups as dispersion energy donors. All the cage structures were characterized by NMR, HRMS and partly by X-ray analysis. Investigation of their guest binding behaviors was performed through NMR analysis and ITC experiments. By comparison of binding constants and thermodynamic fingerprints of host-guest complex formation, the sterically less crowed cage $[Pd_2\mathbf{L}^{\mathbf{Me}}{}_4]^{4+}$ revealed the highest binding affinity; whereas similar energy changes for guest binding were observed for cage $[Pd_2\mathbf{L}^{\mathbf{Bu}}{}_4]^{4+}$ and cage $[Pd_2\mathbf{L}^{\mathbf{Ph}}{}_4]^{4+}$. However, in case of $[Pd_2\mathbf{L}^{\mathbf{Ph}}{}_4]^{4+}$, the

guest encapsulation was mainly driven by entropy, while by contrast, enthalpic effects, which might relate to the dispersion contributions donated by *n*-butyl groups, also play an important role in case of $[Pd_2\mathbf{L}^{\mathbf{Bu}}{}_4]^{4+}$.

Zusammenfassung

Die Forschungsschwerpunkte der Promotionsarbeit befassen sich mit zwei Themen: Den Aufbau von heteroleptischen selbstassemblierten Koordinationskäfigen und die Kontrolle von London'schen Dispersionswechselwirkungen in selbstassemblierten supramolekularen Wirt-Gast-Systemen. Metallvermittelte Selbstassemblierung ist im großen Umfang zum Aufbau von nanoskaligen Strukturen eingesetzt worden. Durch die Koordination von Metallkationen mit organischen Liganden konnten supramolekulare Käfige gebildet werden, welche ein breites Interesse geweckt haben und in den letzten Jahrzehnten intensiv untersucht wurden.

Diese Hohlstrukturen finden in vielen Gebieten, wie beispielsweise Molekülerkennung, Wirkstoffabgabe, Katalyse, etc. Anwendung. Jedoch besitzen die meisten dieser funktionalisierten Strukturen nur eine Art von Modifikation. Um die Funktionalität durch die Einführung verschiedener funktioneller Gruppen in einer einzigen Architektur zu erweitern, wurde in Kapitel 2 eine neue Strategie entwickelt. Durch Kombination von Konzepten der Formkomplementarität, chemische Modifikation der Koordinationstellen und Templateffekten wurde eine Reihe heteroleptischer Koordinationskäfige mit bis zu vier verschiedenen organischen Liganden in rationalen Positionen hergestellt. Diese neuen heteroleptischen Käfige werden durch die Verbrückung von zweikernigen Co(III)-Salphen-Makrozyklen mit exakt konfigurierten bananenförmigen Liganden gebildet, sodass hohle Strukturen mit einzigartigen anisotropen Formen erhalten werden können. Insgesamt sind fünf verschiedene organische Liganden synthetisiert worden. Abhängig von der Kombination, können diese Liganden selektiv fünf verschiedene selbstassemblierte Käfige mit Pd(II) oder Co(III) bilden, wovon vier heteroleptisch sind. Alle Käfigstrukturen wurden vollständig durch NMR, HRMS und Kristallstrukturanalyse charakterisiert.

London'sche Dispersionswechselwirkungen sind schwache nichtkovalente Wechselwirkungen, jedoch können diese anziehenden Wechselwirkungen eine wichtige Rolle bei der Strukturstabilität bei einer großen Anzahl wechselwirkender Atome spielen. Die Erhöhung der Anzahl dieser Wechselwirkungen birgt jedoch auch das Risiko einer Verstärkung von sterischen Abstoßungen. Um ein besseres Verständnis zu erlangen wie das Gleichgewicht zwischen der London-Dispersion und der sterischen Abstoßung ausgeglichen werden kann, wird eine Reihe von endohedral funktionalisierten $[Pd_2L_4]^{4+}$ Koordinationskäfigen entworfen und synthetisiert (Kapitel 4). Einer dieser Käfige war mit Methylgruppen (Käfig $[Pd_2L^{Me}{}_4]^{4+}$) als Referenz ausgestattet, bei zwei weiteren Käfigen wurden sterisch anspruchsvolle Butylgruppen (Käfig $[Pd_2L^{Bu}{}_4]^{4+}$) und Phenylgruppen ($[Pd_2L^{Ph}{}_4]^{4+}$) als Dispersionsenergiedonoren verwendet. Alle Käfigstrukturen wurden durch NMR, HRMS und zwei davon auch durch Röntgenstrukturanalyse charakterisiert. Die Wirt-Gast Chemie wurde mit

verschiedenen Methoden wie der NMR-Analyse und der isothermen Titrationskalorimetrie (ITC) untersucht. Durch den Vergleich der Bindungskonstanten und der thermodynamischen Fingerabdrücke der Wirt-Gast-Komplexbildung ergab der Käfig $[Pd_2L^{Me}{}_4]^{4+}$ mit geringerer sterischer Abstoßung die höchste Bindungsaffinität. Ähnliche Energieänderungen wurden für die Gastbindungen der Käfige $[Pd_2L^{Bu}{}_4]^{4+}$ und $[Pd_2L^{Ph}{}_4]^{4+}$ beobachtet. Im Falle des Käfigs $[Pd_2L^{Ph}{}_4]^{4+}$ wurde die Gastbindung von der Entropie vorangetrieben. Im Gegensatz dazu spielen enthalpische Effekte, welche sich auf die von den *n*-Butylgruppen gegebenen Dispersionsbeiträge beziehen könnten, eine wichtige Rolle beim $[Pd_2L^{Bu}{}_4]^{4+}$ Käfig.

Contents

1. Introduction

"Supramolecular chemistry may be defined as 'chemistry beyond the molecule'".

by Jean-Marie Lehn, in 1987 Nobel lecture. [1]

The objects studied in supramolecular chemistry are the chemical species that construct or aggregate from intermolecular non-covalent interactions, such as van der Waals forces, hydrogen bonding, π-π stacking, electrostatic interactions, hydrophobic effect, etc. Sometimes, these interactions do not work alone, but collaborate with one or more other effects to form supramolecular complexes with highly sophisticated structures and functionalities.

1.1. The history of supramolecular chemistry

The history of supramolecular chemistry started in the late 19th century. The first landmark was the "Lock and Key" model proposed by Emil Fischer[2] describing binding mechanism of enzymes: only the substrate which has the specific shape to fit the enzyme cavity, can be encapsulated and react. Since then, this elegant model has often been used to explain the principle of molecular recognition and has been refined in the following decades by Koshland ("induced fit" model)[3] and Paul Ehrlich (developed the concept of "receptor").[4] However, limited by technical reasons, supramolecular chemistry developed slowly for a long time until the 1960s.

In 1967, a breakthrough was reported by Pederson.[5] By synthesizing a bisphenol derivative, a by-product of the reaction draw his attention, which resulted from impurities (Figure 1.1).[6] This accidentally produced compound was determined to have a cyclic structure and to be able to increase the solubility of potassium permanganate in nonpolar solvents, as well as its own solubility in methanol by addition of sodium salts. Because the shape of the compound resembles a crown after binding a metal ion, it was named as crown ether by Pederson.

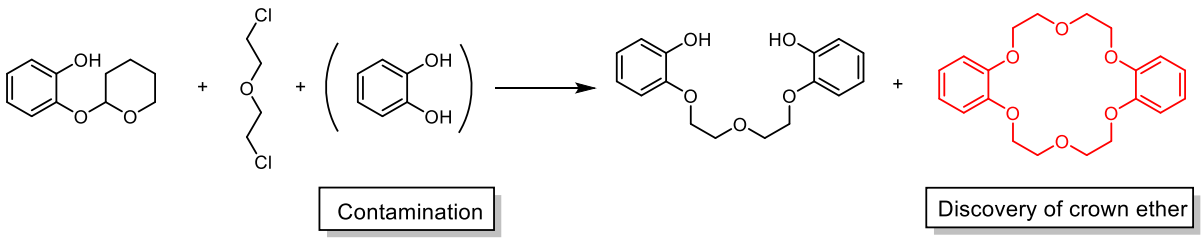

Figure 1.1. Discovery of the first crown ether.[6]

After two years in 1969, Lehn reported 3-dimensional hosts that can bind metal cations with even higher affinity, named as cryptands (Figure 1.2a).[7] Later, in 1979, Cram published the first paper

about spherands (Figure 1.2b).[8] The relatively rigid macrocyclic host is composed of six meta-phenylene units functionalized with methoxy groups pointing to the centre of the cycle with oxygen atoms. Benefiting by the pre-organization of the binding-sites, the host molecule revealed much stronger binding affinity to alkali metal ion in comparison to crown ethers or cryptands.

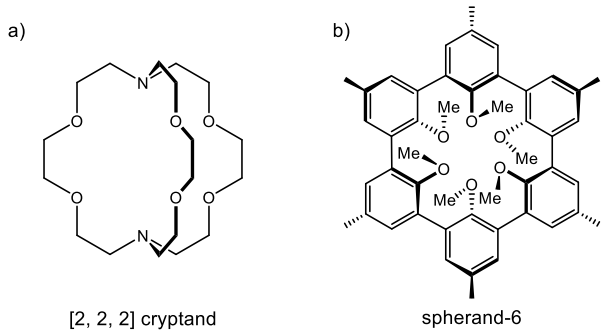

Figure 1.2. a) The cryptand reported by Lehn in 1969, [7] b) the spherand reported by Cram in 1979.[8]

1987 was a remarkable year in the history of supramolecular chemistry. In this year the Noble prize was awarded to three supramolecular chemists: Jean-Marie Lehn, Charles J. Pederson and Donald J. Cram, "for their development and use of molecules with structure-specific interactions of high selectivity."

Beside host-guest chemistry, achievements in other fields of supramolecular chemistry is also remarkable.

A fledgling area of supramolecular chemistry, namely molecular machinery, appeared and rapidly developed in the last 30 years. In 1983, Sauvage invented the first catenane (Figure 1.3a),[9] in which two rings were mechanically interlocked with each other. This work has developed a new approach to connect molecules together and laid the foundation for molecular machines. In 1991, Stoddart reported the first molecular shuttle[10] based on another mechanically bonded structure, the rotaxane, composed of a linear molecule that goes through a cyclic one and equipped at both ends with sterically bulky groups as stopper to keep the ring from slipping away. By varying the temperature, the ring could move back and forth along the thread. In accordance with this work, Stoddart invented more precise molecular machines in the following years such as molecular elevator (Figure 1.3c),[11] molecular pump[12] and molecular muscle.[13]

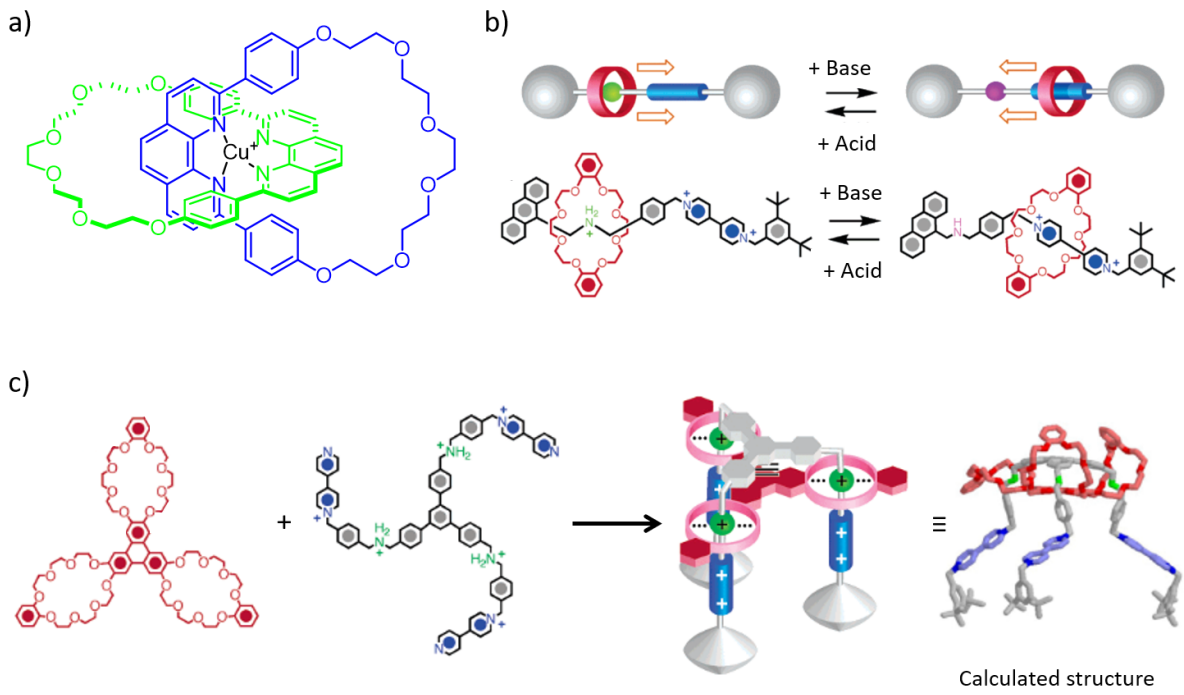

Figure 1.3. a) Formation of a catenane using template effect, adapted from Ref[[9] b) molecular shuttle: the crown ether (red) is able to switch between two different recognition sites controlled by base/acid addition, c) molecular elevator. b) and c) adapted from Ref[11], © American Chemical Society.

The other type of molecular machine, which draw many attentions, is molecular motor. Starting from 1999, Feringa's group has reported over 50 molecular motors.[14] These motors are single chiral molecules consisting of two "paddles" connected by C-C double bonds and able to rotate unidirectionally. In one of the representative works, Feringa and co-workers synthesized a nano car equipped with four molecular motors (Figure 1.4).[15] Due to the steric hindrance caused by the blue part (Figure 1.4b), the motor existed in helical conformations with different stabilities. Upon electronic excitation, the double bond was broken and the rotation of the paddles around the axle was enabled (red part Figure 1.4b) to finish a *trans-to-cis* isomerization, thus, the bulky group moved to the energetically unfavourable position, which could interconvert to more stable conformation using vibrational excitation. Two times electronic excitations and two times vibrational excitations were necessary to complete a 360° rotation. The stereo centre was necessary to decide the direction of the rotation and the stability of each conformer. Monitored by STM, the car was able to move linearly on a Cu(111) surface.

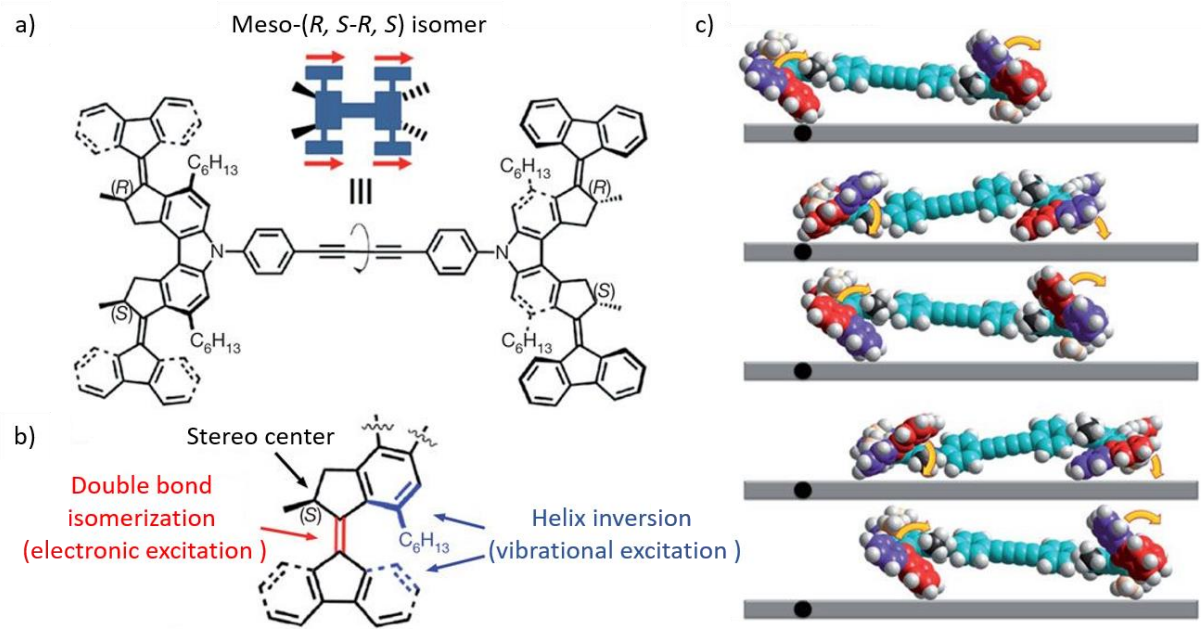

Figure 1.4. a) chemical structure of the molecular car, b) structure detail of molecular motor, c) the nano car is moving on the surface with the four motor units rotate in a single direction. Adapted from Ref[15] ©Springer Nature.

In the year of 2016, Jean-Pierre Sauvage, J. Fraser Stoddart and Bernard L. Feringa shared the Noble prize for chemistry "for the design and synthesis of molecular machines", indicating the significance and potential of molecular machines has been already recognized, even though its development is still at early stage.

Achievements of the other branches of supramolecular chemistry are also undeniable. Coordination-driven self-assembly is one of them and have developed into a mature field. Using metal-mediate self-assembly, a large number of nano-sized structures have been produced and used for different aims. For example, the Nitschke group reported a tetrahedral capsule form by subcomponent self-assembly, which can be utilized for encapsulation and stabilization of white phosphor.[16] Raymond have synthesized an anionic coordination cage for catalysis of cyclization reaction.[17] In 2016, Fujita and co-workers reported a self-assembled tetravalent Goldberg polyhedral composed of 144 small components (48 palladium ions and 96 organic ligands), which was the first time Goldberg polyhedral being reported at molecular level.[18] The Clever group has recently published a work about helicene based chiral [Pd_2L_4] cage, which shows different binding affinity to optical isomer of anionic guest and was able to be used for distinguishing non-chiral guests of different lengths.[19]

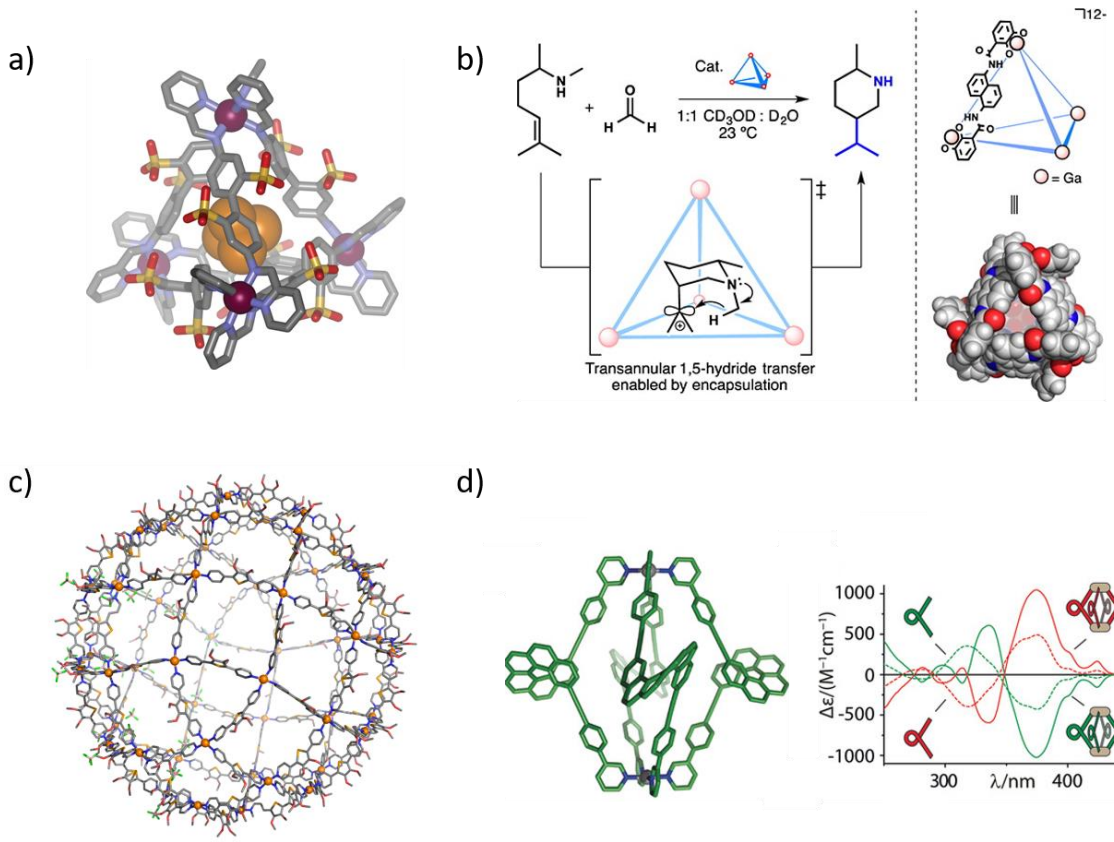

Figure 1.5 a) Tetrahedral capsule reported by the Nitschke group, which can encapsulate and stabilize white phosphorus, adapted from Ref[16]. © The American Association for the Advancement of Science. b) Tetrahedral anionic coordination cage from the Raymond group, able to encapsulate cationic reaction intermediate, adapted from Ref[17]. © American Chemical Society. c) X-ray structure of the tetravalent Goldberg polyhedral [$Pd_{48}L_{96}$] complex reported by Fujita group, adapted from Ref[18]. ©Springer Nature. d) DFT calculated structure of helicene based chiral [Pd_2L_4] cage and CD spectra for optical isomers of helicene ligands (dash line) and corresponding cages (solid line), reported by Clever group, adapted from Ref[19]. © Wiley-VCH Verlag GmbH & Co. KGaA, Weinheim.

At last, to summarize the achievements and developments of supramolecular chemistry, I would like to cite following words:

"It (supramolecular chemistry) has over the last half a century grown into a major field and has fuelled numerous developments at the interfaces with biology and physics; from basic knowledge to applications, from noncovalent interactions to drug design, and from materials and polymers to solid state engineering."

by Jean-Marie Lehn, in 2017.[20]

1.2. Motivation

Despite the field of supramolecular chemistry has grown rapidly in the last decades, there are still large potentials for development.

Self-assembly is a progress in which the disordered components of a system organized into ordered structure or patterns driving by the local interactions among the components themselves, without any external direction.[21] Coordination-driven self-assembly have attracted many attentions and has been proved as highly efficient for generating nanosized supramolecular structures. The outcome of self-assembly is the result of collaboration or competition of entropic and enthalpic effects. While the reports to date are dominated by highly symmetric self-assembled structures, only a handful of approaches have been developed to against the entropic effect, which leading to the formation of heteroleptic self-assemblies (Figure 1.5a). On the other side, interactions like hydrogen bonding or hydrophobic effect have been well studied and applied as driving forces for guest encapsulation in host-guest chemistry (Figure 1.6b), in comparison, London dispersion interactions, which provide enthalpic contribution and could offer extra stability, have been only limited studied. Therefore, the investigation of the Ph.D. projects has focused on heteroleptic self-assembly and control of London dispersion effect.

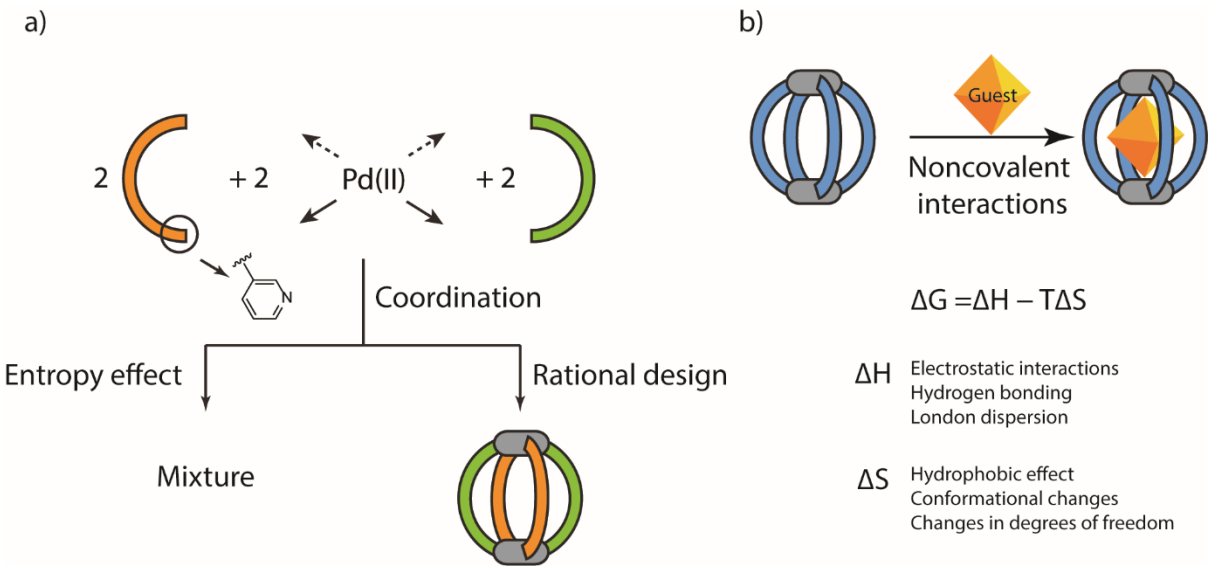

Figure 1.6 a) A rational design is demand for making heteroleptic coordination self-assembled cage, otherwise a mixture would be formed due to entropy effect, b) guest encapsulation using noncovalent interactions and examples of enthalpy and entropy related effects.

To minimize the chaos that could be caused by entropy, most of time, self-assembled structures are formed by coordination of one type of organic ligand and metal ion. However, self-assembly in Nature is much more complicated, which can happen in an environment, where various molecules coexist.

Also, biological molecules are rarely composed by only one type of moiety but consist of different functional parts on determined positions. On the other hand, as mentioned before, the development of molecular machinery is still at a quite early stage, referring to the molecular machine in nature (e.g. ATP synthase), the current artificial molecular machines (e.g. motors, switches, shuttles) are more like mechanical components. It can be predicted that the development of multicomponent molecular machines, which carry various functional components and are able to finish more complicated tasks, would be one of the emphases for future research in the area. However, due to entropy effect, by mixing various organic ligands together with coordinating metals, a statistical mixture would be the most probable outcome. Despite serval approaches have been reported for construction of integrative self-sorted coordination cages with two different organic ligands (refer to introduction in chapter 2), the possibility to make more complicated multifunctional artificial hosts or multicomponent molecular machines via coordination-driven self-assembly remained an open question. Therefore, the first project in this thesis is focused on developing a novel approach for heteroleptic self-assembly using coordination chemistry, which will be discussed in detail in chapter 2.

For a long time, London dispersion interactions, which belong to the attractive part of van der Waals interactions, have not drawn enough attention of chemists for they are the weakest noncovalent interactions. However, this is true only when there is a very limited amount of interacting atom pairs, but when there is a cumulative effect, their role becomes non-neglectable. Evidence show that dispersive interactions play very important role in biosystem. For instance, a significant contribution of dispersion has been found for the ligand binding of proteins[22] and the interactions between nucleic acid and proteins are considered highly related to dispersion effects.[23] Although in recently years, there are also successful examples of utilizing dispersion forces in supramolecular system (refer to introduction in chapter 4), control of London dispersion forces is still challenging. In chapter 4, the effects of dispersion were studied in a host-guest system by introducing sterically bulky dispersion energy donor into self-assembled supramolecular cages, through which, we expect to have a better understanding about adjustment of the balance between London dispersion effects and steric hindrance and provide new aspect for structure design of supramolecular architectures.

1.3. Reference

[1] J.-M. Lehn, *Angew. Chem. Int. Ed.* **1988**, *27*, 89-112.

[2] E. Fischer, *Eur. J. Inorg. Chem*. **1894**, *27*, 2985-2993.

[3] D. E. Koshland, *Proc. Natl. Acad. Sci. U.S.A.* **1958**, *44*, 98-104.

[4] P. Ehrlich, *Studies on Immunity,* Wiley*,* New York, **1906**.

[5] C. J. Pedersen, *J. Am. Chem. Soc.* **1967**, *89*, 7017-7036.

[6] K. Ariga, T. Kunitake, *Suprmolecular chemistry- fundamentals and applications. Advanced textbook*, Springer*,* Berlin*,* Heidelberg, **2006**.

[7] B. Dietrich, J. M. Lehn, J. P. Sauvage, *Tetrahedron Lett.* **1969**, *10*, 2889-2892.

[8] D. J. Cram, T. Kaneda, R. C. Helgeson, G. M. Lein, *J. Am. Chem. Soc.* **1979**, *101*, 6752-6754.

[9] C. O. Dietrich-Buchecker, J. P. Sauvage, J. P. Kintzinger, *Tetrahedron Lett.* **1983**, *24*, 5095-5098.

[10] P. L. Anelli, N. Spencer, J. F. Stoddart, *J. Am. Chem. Soc.* **1991**, *113*, 5131-5133.

[11] J. D. Badjic, C. M. Ronconi, J. F. Stoddart, V. Balzani, S. Silvi, A. Credi, *J. Am. Chem. Soc.* **2006**, *128*, 1489-1499.

[12] C. Cheng, P. R. McGonigal, S. T. Schneebeli, H. Li, N. A. Vermeulen, C. Ke, J. F. Stoddart, *Nat. Nanotechnol.* **2015**, *10*. 547-553

[13] Y. Liu, A. H. Flood, P. A. Bonvallet, S. A. Vignon, B. H. Northrop, H.-R. Tseng, J. O. Jeppesen, T. J. Huang, B. Brough, M. Baller, S. Magonov, S. D. Solares, W. A. Goddard, C.-M. Ho, J. F. Stoddart, *J. Am. Chem. Soc.* **2005**, *127*, 9745-9759.

[14] M. Peplow, *Nature* **2015**, *525*, 18-21.

[15] T. Kudernac, N. Ruangsupapichat, M. Parschau, B. Maciá, N. Katsonis, S. R. Harutyunyan, K.-H. Ernst, B. L. Feringa, *Nature* **2011**, *479*, 208-211.

[16] P. Mal, B. Breiner, K. Rissanen, J. R. Nitschke, *Science* **2009**,*324*, 1697-1699.

[17] D. M. Kaphan, F. D. Toste, R. G. Bergman, K. N. Raymond, *J. Am. Chem. Soc.* **2015**, *137*, 9202-9205.

[18] D. Fujita, Y. Ueda, S. Sato, N. Mizuno, T. Kumasaka, M. Fujita, *Nature* **2016**, *540*, 563-566.

[19] T. R. Schulte, J. J. Holstein, G. H. Clever, *Angew. Chem. Int. Ed.* **2019**, *58*, 5562-5566.

[20] J.-M. Lehn, *Chem. Soc. Rev.* **2017**, *46*, 2378-2379.

[21] M. Varga, in *Fabrication and Self-Assembly of Nanobiomaterials* (Ed.: A. M. Grumezescu), William Andrew Publishing, **2016**, pp. 57-90.

[22] R. Malham, S. Johnstone, R. J. Bingham, E. Barratt, S. E. V. Phillips, C. A. Laughton, S. W. Homans, *J. Am. Chem. Soc.* **2005,** *127*, 17061-17067.

[23] S. Jones, D. T. A. Daley, N. M. Luscombe, H. M. Berman, J. M. Thornton, *Nucleic Acids Res.* **2001,** *29*, 943-954.

2. Non-statistical Multicomponent Assembly of Coordination Cages

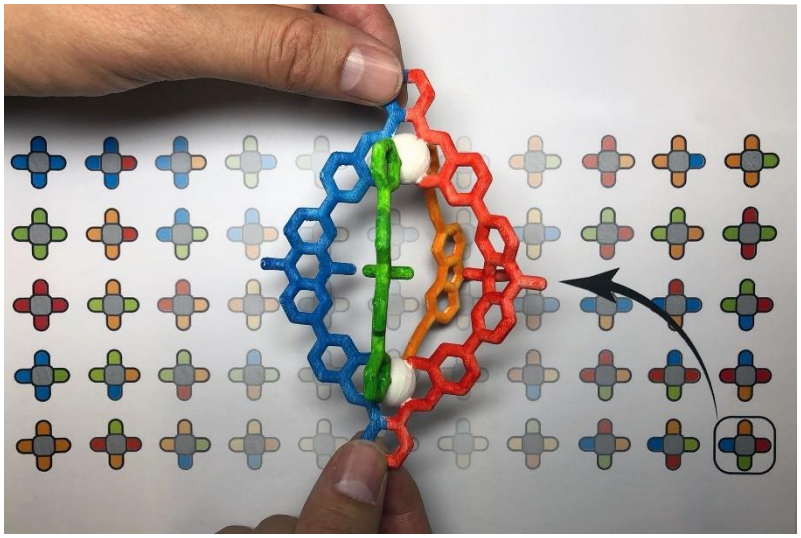

2.1. Introduction

Coordination-driven self-assembly is one of the most powerful tools for generating 2D or 3D structures, such as lantern-shaped cages,[1][2][3] rings,[4][5] and polyhedra.[6][7][8][9][10][11] Usually, these structures are highly symmetric and composed of only one specific type of ligand. Despite being applied for catalysis,[12][13][14] molecular recognition[15][16], drug delivery[17][18][19] and others[20][21][22], the single composition in terms of building blocks strongly restricts the expansion of functionalities of the supramolecular self-assemblies. In nature, most of the biological reactions are catalyzed by enzymes. These natural macromolecules can bind specific substrates precisely, being able to catalyze reactions efficiently under mild conditions and yielding products with high enatio- and regioselectivity. A look into their cavities reveals that they are often of low symmetry and equipped with various functional moieties. Inspired by this, supramolecular chemists start to focus on constructing structures with low symmetry and multiple functionalities. One of the options to fulfil the task is using organic covalent methods, which usually demands multiple-step syntheses and purifications. Rarely, there are reports about solving the problem using multicomponent reactions[23] or dynamic covalent self-assembly.[24][25][26] On the other hand, although metal-mediated self-assembly could produce a convoluted library of complexes in presences of more than one kind of organic ligand due to entropic effects, it is employed more frequently for building heteroleptic constrictions. In recent year, various approaches have been reported (Figure 2.1),[27][28] which will be discussed in detail in the following.

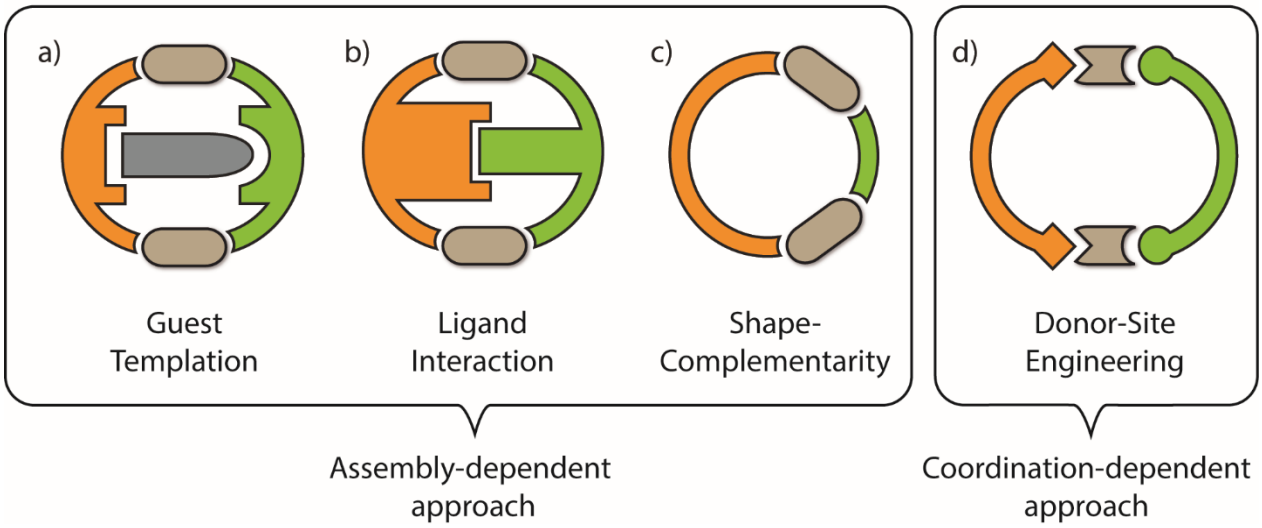

Figure 2.1. A succinct summary of approaches that have been developed for rationally constructing coordination-driven heteroleptic self-assemblies, a)-c) utilizing functional or geometrical complementary between organic ligands, d) by engineering coordination environments around the metal centers. Adapted from Ref[27]

2.1.1. Heteroleptic self-assembly mediated by the template effect

Integrative self-sorting can be achieved by utilizing a guest as template. In the year 2011, the group of Yoshizawa reported an artificial fullerene binder consisting of anthracene-based ligand **2.1** and square planar Pd(II) cations.[29] In the following work,[30] the elongated version, ligand **2.2**, was synthesized, which can also form a $[Pd_2L_4]$-type cage with a larger cavity. The cage $[Pd_2\mathbf{L^{2.2}}_4]^{4+}$can encapsulate not only C_{60}, but also C_{70} and derivates of C_{60}. Due to the very similar architectural and chemical features, a library of coordination cages of the general formula $[Pd_2\mathbf{L^{2.1}}_n\mathbf{L^{2.2}}_{(4-n)}]^{4+}$ (n= 0, 1, 2, 3, 4) was obtained by mixing of cage $[Pd_2\mathbf{L^{2.1}}_4]^{4+}$ with cage $[Pd_2\mathbf{L^{2.2}}_4]^{4+}$ in a ratio of 1:1. However, after addition of C_{60} as the guest, the statistical mixture converted into a single species of $[C_{60}@Pd_2\mathbf{L^{2.1}}_2\mathbf{L^{2.2}}_{2)}]^{4+}$, which points to the fact that the C_{60} helped to stabilize the heteroleptic structure. Evidence of $[C_{60}@Pd_2\mathbf{L^{2.1}}_2\mathbf{L^{2.2}}_{2)}]^{4+}$ formation and absence of other species were provided by 2D NMR and ESI-MS. On the basis of theoretical calculations, the heteroleptic complex should be present in *cis* conformation (Figure 2.2).

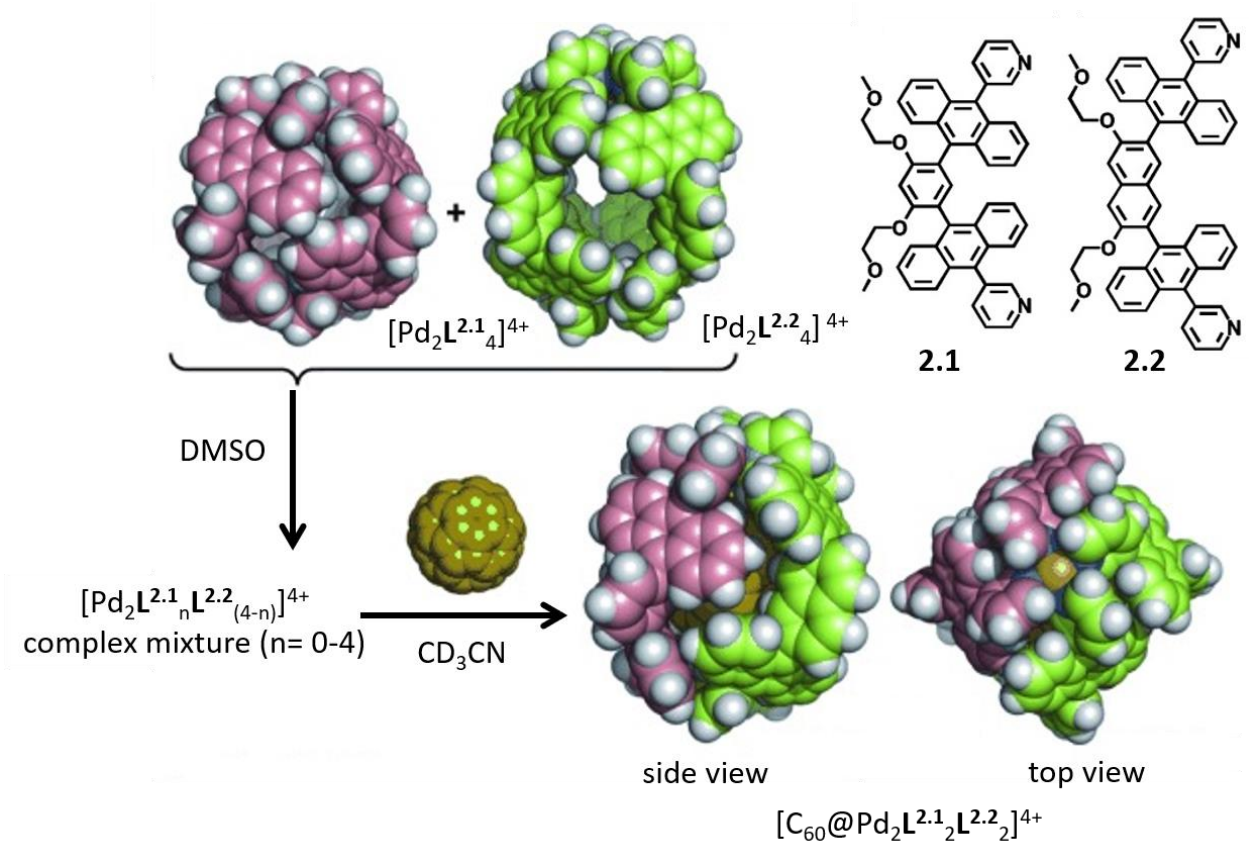

Figure 2.2. Homoleptic cage $[Pd_2\mathbf{L^{2.1}}_4]^{4+}$ (red) and $[Pd_2\mathbf{L^{2.2}}_4]^{4+}$ (green) were mixed in a 1 : 1 ratio and resulted in a statistical mixture in DMSO. Subsequently addition of C_{60} in acetonitrile lead to a reorganization and produce a heteroleptic integrative self-sorting product $[C_{60}@Pd_2\mathbf{L^{2.1}}_2\mathbf{L^{2.2}}_{2)}]^{4+}$. Adapt from Ref[30]. © Wiley-VCH Verlag GmbH & Co. KGaA, Weinheim

2.1.2. Heteroleptic self-assembly dominated by ligand interactions

Making good use of the interactions like π-π stacking, or steric hindrance is not only important for the design of a host-guest system, but also allows the production of rationally constructed multicomponent complexes. For example, a series of bis-monodentate ligands endohedrally modified with substituents in different sizes was synthesized by Hooley and co-workers (Figure 2.3)[31] While sterically less demanding, ligands **2.3** and **2.4** afforded lantern-shaped $[Pd_2L_4]$ type cages, owing to the over crowed steric hindrance, coordination of ligands **2.5** or **2.6** with $Pd(NO_3)_2$, formed complex mixtures. In the self-sorting experiments, a combination of the small-size substituents-modified ligands **2.3** and **2.4** in a ratio of 3 : 1 assembled with $Pd(NO_3)_2$ in DMSO generating a mixture of $[Pd_2\mathbf{L^{2.3}}_n\mathbf{L^{2.4}}_{(4-n)}]$ with a preference for $[Pd_2\mathbf{L^{2.3}}_3\mathbf{L^{2.4}}]^{4+}$. However, when 3.0 eq. of medium size substituent functionalized ligand **2.5** mixed with 1.0 eq. sterically small **2.3**, NMR and ESI-MS studies revealed only two complexes existed in solution, namely $[Pd_2\mathbf{L^{2.3}}_3\mathbf{L^{2.5}}]^{4+}$ and $[Pd_2\mathbf{L^{2.3}}_4]^{4+}$, indicating heteroleptic assembly directed by a steric complement. Ligand **2.6** was synthesized as reference. For the reason of the over-sized substituent group, this ligand can hardly cooperate with other ligands to form any kind of lantern-shaped cages.

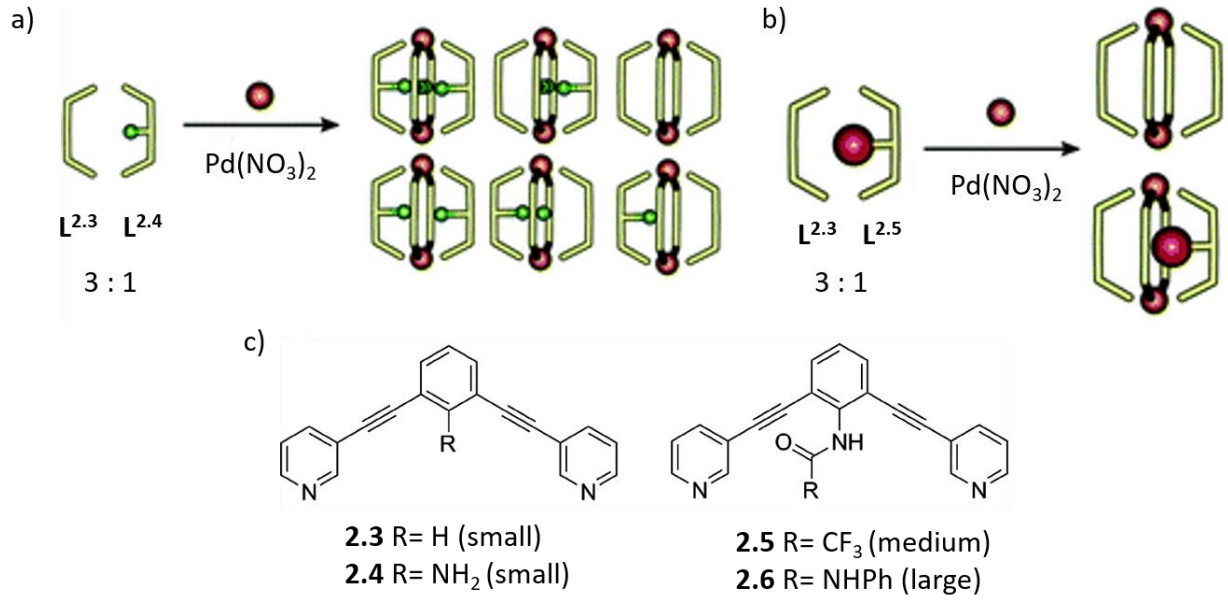

Figure 2.3. a) Statistical self-sorting of **2.3** and **2.4**; b) two component mixture generated by self-assembly of **2.3** and sterically medium demanding **2.5** in a ratio of 3 : 1, c) bis-monodentate ligands modified with substituents of different sizes. Adapt from Ref[31]. © American Chemical Society.

Later, in the year 2015, the Nitschke group published an approach for heteroleptic self-assembly using π-π stacking interactions.[32] The electron-poor NDI-based ligand precursor **2.7** was able to form tetrahedral cage complex $[M_4\mathbf{L^{2.7}}_6]^{8+}$ via subcomponent self-assembly with 2-formylpyridine and metal cations M (M= Fe^{II}, Co^{II}, Zn^{II}). Based on the different reaction stoichiometries, electron-rich precursor

2.8 can either form C_3-symmetric pseudo-tetrahedron $[M_4\mathbf{L^{2.8}}_6]^{8+}$ (M= Fe^{II}, Co^{II}, Zn^{II}) or box-like complex $[M_2\mathbf{L^{2.8}}_2]^{4+}$ (M= Co^{II}, Zn^{II}). While the X-ray structure of $[M_4\mathbf{L^{2.8}}_6]^{8+}$ shows face-to-face stacking of pyrene units on the adjacent ligands, the box $[M_2\mathbf{L^{2.8}}_2]^{4+}$ is suitable for encapsulation of electron-poor aromatic guests into the cavity. Thus, it has been proposed that a combination of electron-deficient NDI **2.7** and electron-rich **2.8** could yield an integrative self-sorting product. Indeed, a heteroleptic complex $[M_4\mathbf{L^{2.7}}_2\mathbf{L^{2.8}}_4]^{8+}$ (M= Fe^{II}, Co^{II}, Zn^{II}) can be prepared by: 1) heteroleptic subcomponent self-assembly using a 1 : 2 mixture of **2.7** and **2.8** reacting with formylpyridine and divalent metal cations; 2) cage-to-cage transformation of homoleptic cages $[M_4\mathbf{L^{2.7}}_6]^{8+}$ and $[M_4\mathbf{L^{2.8}}_6]^{8+}$ in a ratio of 1 : 2; 3) box like complex $[M_2\mathbf{L^{2.8}}_2]^{4+}$ reacts with 1.0 eq. ligand **2.7** in present of formylpyridine. The solid-state analysis of $[M_4\mathbf{L^{2.7}}_2\mathbf{L^{2.8}}_4]^{8+}$ revealed a unique sandwich structure formed by pyrene-pyrene-NDI stacking (Figure 2.4d), demonstrating the prediction that the heteroleptic self-assembly is dominated by π-π interactions.

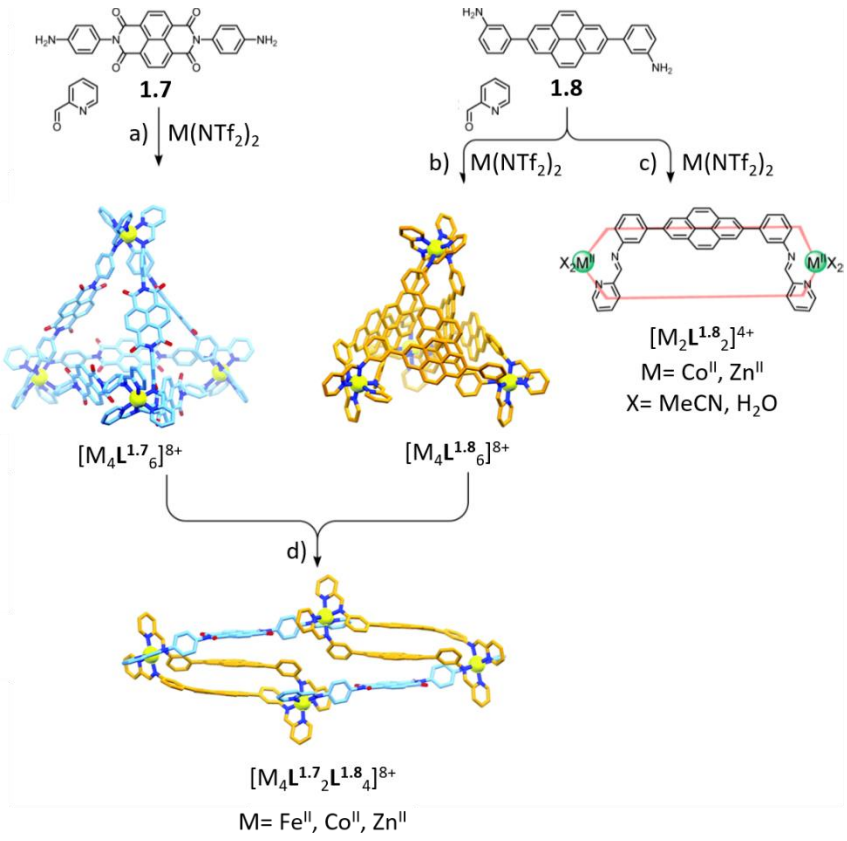

Figure 2.4. a-c) Sub-component self-assembled homoleptic cages $[M_4\mathbf{L^{2.7}}_6]^{8+}$, $[M_4\mathbf{L^{2.8}}_6]^{8+}$ and $[M_2\mathbf{L^{2.8}}_2]^{4+}$ and the corresponding ligand precursors **2.7** and **2.8**, d) heteroleptic structure $[M_4\ \mathbf{L^{2.7}}_2\mathbf{L^{2.8}}_4]^{8+}$ formed by cage-to-cage transformation. Adapt from Ref[32]. © The Royal Society of Chemistry, American Chemical Society.

2.1.3. Heteroleptic self-assembly using shape complementarity of ligands

Fujita and co-workers explored heteroleptic self-assembly in a cuboctahedral system formed by Pd(II) and two bis-monodentate pyridyl ligands **2.8** and **2.9**, which have similar bend angles of around 120°, but different lengths.[33] Both ligands are able to construct homoleptic $[Pd_{12}L_{24}]$ cuboctahedral complexes. When ligands **2.8** and **2.9** were mixed with Pd(II) in the ratio of 1 : 1 : 1, a clean NMR spectrum that similarly with the overlapping of the signals of homoleptic complexes $[Pd_{12}\mathbf{L^{2.8}}_{24}]^{24+}$ and $[Pd_{12}\mathbf{L^{2.9}}_{24}]^{24+}$ was obtained. Surprisingly, the results of CSI-TOF-MS measurement confirmed forming of a new species containing both **2.8** and **2.9,** without any evidence of homoleptic complex formation. In addition, a DOSY experiment revealed only one species existing in the solution, indicating a clean integrative self-sorting. In accordance with the analytical data, a T_d symmetric cantellated tetrahedral complex $[Pd_{12}\mathbf{L^{2.8}}_{12}\mathbf{L^{2.9}}_{12}]^{24+}$ was supposed to be obtained. However, X-ray analysis provided a C_3 symmetric isomeric structure, which is slightly energetically unfavorable compared to the T_d symmetric structure based on theoretical calculations. According to the interpretation of the author, both of the geometrical isomers of the heteroleptic architecture an coexisting in the solution.

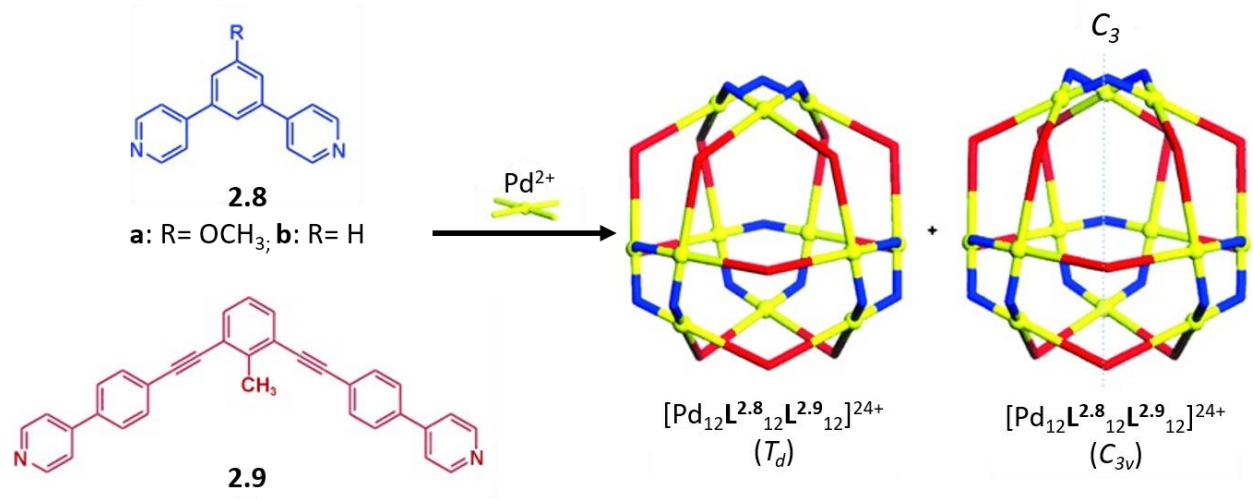

Figure 2.5. Integrative self-sorting between ligand **2.8** and **2.9** resulting two geometrical isomers of the heteroleptic architecture $[Pd_{12}\mathbf{L^{2.8}}_{12}\mathbf{L^{2.9}}_{12}]^{24+}$. Adapt from Ref[33]. © Wiley-VCH Verlag GmbH & Co. KGaA, Weinheim.

The emphasis on study of heteroleptic self-assembly in Clever group focused on control of geometric parameters. Banana-shaped ligands with various bend angles were designed and synthesized. In 2016, Clever and co-workers have reported an example for integrative self-assembly, where multicomponent *cis*-$[Pd_2\mathbf{L^{1.9}}_2\mathbf{L^{1.11}}_2]^{4+}$ cage was successfully obtained by combing ligand **1.9** and **1.11**, which have bend angles of 60° and 120° respectively, with Pd(II) in a ratio of 1 : 1 : 1.[34]

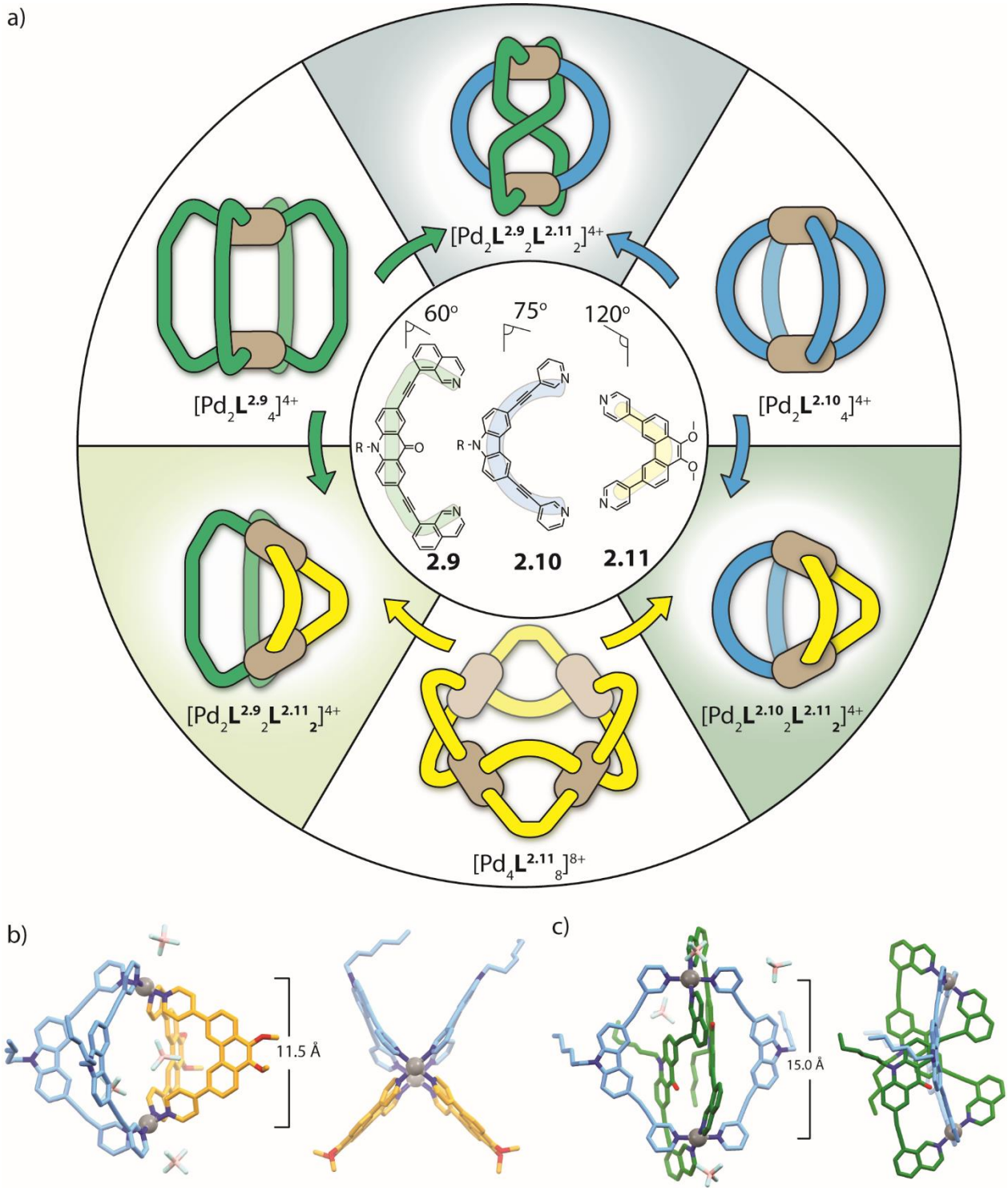

Figure 2.6. a) Geometrically complemental bis-monodentate banana-shaped ligand and corresponding homoleptic and heteroleptic self-assembled cages. b) crystal structure of $[Pd_2\mathbf{L}^{2.9}{}_2\mathbf{L}^{2.10}{}_2]^4$, c) crystal structure of $[Pd_2\mathbf{L}^{2.10}{}_2\mathbf{L}^{2.11}{}_2]^{4+}$. © Wiley-VCH Verlag GmbH & Co. KGaA, Weinheim.

Following this work, Clever and co-workers continued the investigation of geometric complementarity more systematically.[35] Besides **2.9** and **2.11**, carbazole-based ligand **2.10** with a bend angle of 75° was introduced for the study. All the three ligands readily form homoleptic self-assemblies by

interacting with Pd(II) cations. Nevertheless, mixing each two of them led to formation of clean heteroleptic species (Figure 2.6a). Despite bearing different bend angle compare to **2.9**, the Pd-mediated self-sorting of ligand **2.10** with ligand **2.11** generate heteroleptic cage $[Pd_2\mathbf{L^{2.10}}_2\mathbf{L^{2.11}_2}]^{4+}$ in *cis*-conformation. The structure was characterized by NMR, ESI-MS and X-ray analysis (Figure 2.6b). On the other hand, by mixing **2.9**, **2.10** and Pd(II) in a 1 : 1 : 1 ratio in CD_3CN, ^1H NMR study revealed an unusual spectrum with each half of every ligand showing independent signals. However, DOSY experiment revealed a single species in the solution and ESI-MS indicates the formation of heteroleptic complex $[Pd_2\mathbf{L^{2.9}}_2\mathbf{L^{2.10}}_2]^{4+}$. Thus, the complex formed by self-sorting of **2.9** with **2.10** supposedly provided a novel topology. Indeed, an unexpected structure confirmed by single crystal analysis: the two carbazole based ligands **2.10** arranged on the opposite coordination positions of Pd(II) resulting a macrocycle, the two **2.11** penetrated the ring and bound to palladium center with an *anti*-conformation generating a integrative self-sorted *trans*-$[Pd_2\mathbf{L^{2.9}}_2\mathbf{L^{2.10}}_2]^{4+}$ cage (Figure 2.6c). What's more, heteroleptic cage transformations are enabled by ligand substitution reactions. Either addition of free ligand **2.9** into the solution of $[Pd_2\mathbf{L^{2.10}}_2\mathbf{L^{2.11}_2}]^{4+}$, or addition of **2.11** into the solution of $[Pd_2\mathbf{L^{2.9}}_2\mathbf{L^{2.10}_2}]^{4+}$ led to reassembly of the heteroleptic complexes to $[Pd_2\mathbf{L^{2.9}}_2\mathbf{L^{2.11}_2}]^{4+}$, indicating a higher shape complementarity match between **2.9** and **2.11**.

In addition, similar approach also employed by Mukherjee[36], Chand[37] and Zhou[38] to construct heteroleptic self-assembled structures.

2.1.4. Heteroleptic self-assembly controlled by donor site engineering.

Rationally constructed heteroleptic complexes can be further obtained by decorating coordination donor sites with functional moieties offering secondary interactions like hydrogen bonding or steric effect. According to the study reported by Crowley in 2016, amino groups equipped on the donor pyridine of banana-shaped ligands help to steer the outcome of self-assembly.[39] The tripyridyl ligand **2.12** formed homoleptic cage $[Pd_2\mathbf{L^{2.12}}_4]^{4+}$ and was fully transferred to cage $[Pd_2\mathbf{L^{2.13}}_4]^{4+}$ after addition of *ortho*-substituted ligand **2.13** thanks to the stronger coordination ability enhanced by the amino group. NMR and ESI-MS experiments showed that the *meta*-substituted ligand **2.14** is capable to partly displace the ligands of cage $[Pd_2\mathbf{L^{2.12}}_4]^{4+}$ providing a multicomponent complex $[Pd_2\mathbf{L^{2.12}_2L^{2.13}}_2]^{4+}$. Hydrogen bonds formed between the *ortho*-amino group on ligand **2.13** and acidic *α*-proton on the neighboring ligand **2.12** was supposed to be responsible for maintaining the heteroleptic structure. However, formation of $[Pd_2\mathbf{L^{2.12}_2L^{2.13}}_2]^{4+}$can only be achieved by the ligand exchange reaction, neither cage-to-cage transformation, nor coordination by mixing ligand **2.12**, **2.13** and Pd(II) in a 1 : 1 :1 ratio could produce the same structure. Furthermore, DFT calculation suggested the heteroleptic cage

should be the *cis* isomer and a metastable kinetic product, which is also confirmed by competition experiments.

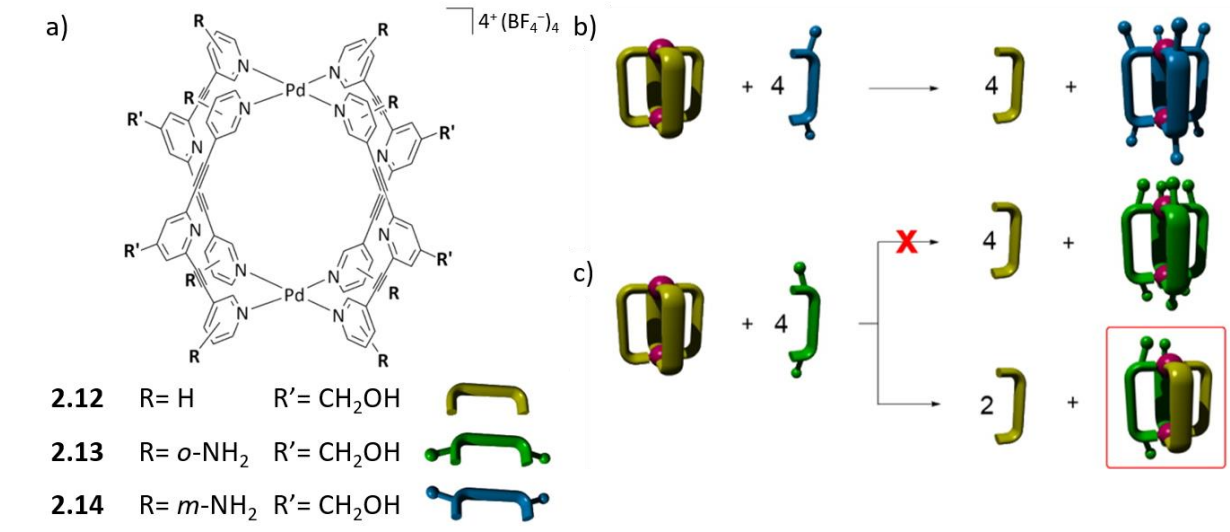

Figure 2.7. a) Cartoon representations of tripyridyl ligands (**2.12**, **2.13** and **2.14**) and corresponding homoleptic self-assembled cages, b) cage transformation from $[Pd_2\mathbf{L}^{\mathbf{2.12}}{}_4]^{4+}$ to $[Pd_2\mathbf{L}^{\mathbf{2.14}}{}_4]^{4+}$ via ligand exchange reaction, c) addition of ligand **2.13** into the solution of cage $[Pd_2\mathbf{L}^{\mathbf{2.12}}{}_4]^{4+}$ do not result to $[Pd_2\mathbf{L}^{\mathbf{2.13}}{}_4]^{4+}$ but the heteroleptic cage $[Pd_2\mathbf{L}^{\mathbf{2.12}}{}_2\mathbf{L}^{\mathbf{2.13}}{}_2]^{4+}$. Adapt from Ref[39]. © American Chemical Society.

The Clever group attempted to direct rational assembly of heteroleptic complexes using a steric effect.[40] Instead the commonly used pyridyl donor group, picoline was installed onto organic ligands with the methyl group pointing either inward or outward the cage cavity (Figure 2.8). The authors first examined the homoleptic assembly. Influenced by the steric effect, efficient formation of $[Pd_2\mathbf{L}_4]$ type cages by the picolyl ligands can hardly be observed. For instance, in accordance with the observation from ^{1}H NMR and ESI-MS analysis, the methyl-inward pointing ligands **2.15** preferred to generate a bowl-shaped $[Pd_2\mathbf{L}^{\mathbf{2.15}}{}_3(CD_3CN)_2]^{4+}$ complex at ambient temperature, while the outward pointing ligand **2.16** produced a mixture containing $[Pd_2\mathbf{L}^{\mathbf{2.16}}{}_3(CD_3CN)_2]^{4+}$ and $[Pd_2\mathbf{L}^{\mathbf{2.16}}{}_2(CD_3CN)_4]^{4+}$. Nevertheless, combining **2.15** and **2.16** in a ratio of 1 : 1 offered a relatively clean NMR spectrum revealing two set of signals which can be assigned to **2.15** and **2.16** respectively. DOSY analysis confirmed the signals corresponding to **2.15** and **2.16** belong to a same species. In addition, prominent peaks relevant to the formula $[Pd_2\mathbf{L}^{\mathbf{2.15}}{}_2\mathbf{L}^{\mathbf{2.16}}{}_2 + nBF_4]^{(4-n)+}$ (n= 0, 1) in ESI-MS showed the formation of a heteroleptic cage. Based on the results of DFT calculation, the *cis* conformation is more energetically favorable compared to the *trans* isomer. Furthermore, the approach was tested between geometrically similar but chemically different ligands. Interestingly, whilst heating **2.15** and **2.18** with a stoichiometry of 1 : 1 at 70 °C for 8 h allows generation of $[Pd_2\mathbf{L}^{\mathbf{2.15}}{}_2\mathbf{L}^{\mathbf{2.18}}{}_2]^{4+}$, mixing of Pd(II), **2.16** and **2.17** in a 1 : 1 : 1 ratio

using same reaction condition gave mixture of $[Pd_2\mathbf{L^{2.16}}_3(CD_3CN)_2]^{4+}$ and unidentifiable complexes formed by **2.18**. However, the heteroleptic cage $[Pd_2\mathbf{L^{2.16}}_2\mathbf{L^{2.17}}_2]^{4+}$ could be obtained by microwave-irradiation followed by overnight heating at 70 °C with a same reaction stoichiometry. The distinct backbone structures were supposed to be the reason for causing the different coordination behavior.

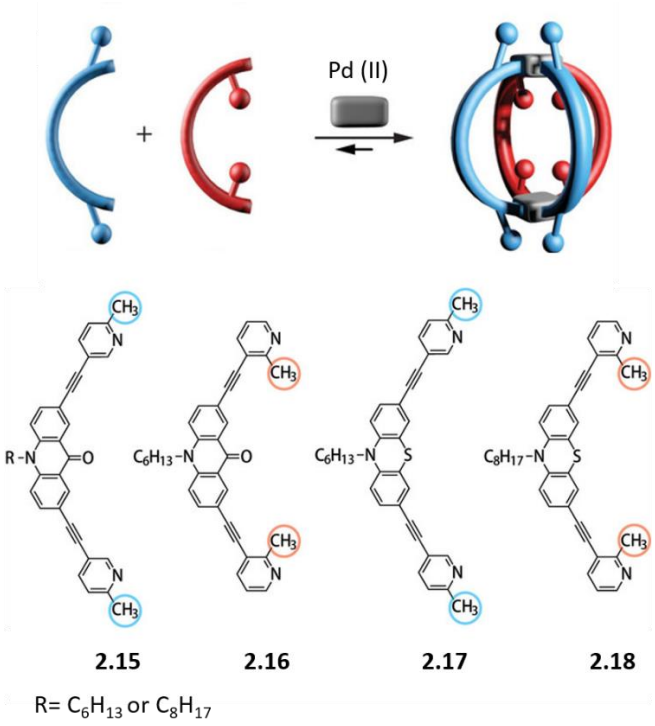

Figure 2.8. Steric effect direct heteroleptic self-assembly using picoline functionalized banana-shaped ligands. Adapt from Ref[40]. © Wiley-VCH Verlag GmbH & Co. KGaA, Weinheim.

Cis-protected metal ions were employed extensively as building block for constructing heteroleptic self-assembled structures.[41] [42] On one hand, blocking of coordination sites on the metal ions using protection groups helps to minimize the degree of self-sorting, on the other hand, however, it also restricts the number of bridging ligands. In 2005, Fujita and co-workers reported construction of a series multicomponent 2D and 3D structures utilizing *cis*-protected Pd(II) in combination with steric complementary pyridyl ligands (Figure 2.9a). [43] [44] Similarly, with the help of steric repulsion, Kobayashi and co-workers successfully connected two distinct cavitand-ligands to $Pd/Pt(dppp)(OTf)_2$ forming hetero-cavitand cages. Zhang, Stang et al developed a unique approach utilizing charge separation (Figure 2.9b). [45] Heteroleptic prisms formed from the reaction of *cis*-$Pt(PEt_3)_2(OTf)_2$ with organic moieties equipped with pyridine and carboxylate donors, respectively. Furthermore, Mukherjee,[46][36] Chand[37] also published related work of making use of *cis*-protected metal ions for heteroleptic self-assembly.

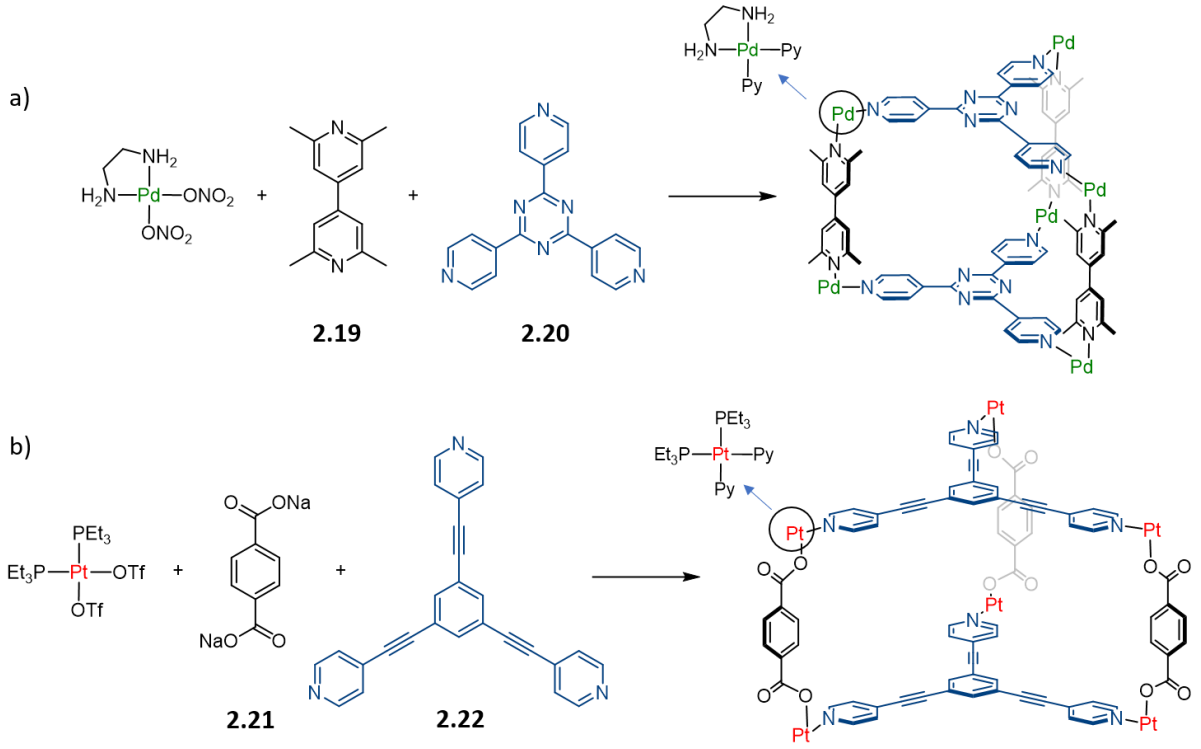

Figure 2.9. Multicomponent self-assemblies using *cis*-protected metal ions as coordination nodes; a) side chain-direct formation of heteroleptic trigonal prism,[43] b) construction of heteroleptic trigonal prism utilizing charge separation.[45] (Protection groups were omitted in cage structures for clarity)

Another approach was developed by Ribas and co-workers, in which hexa-aza macrocycles, saturated by metal ions yield multicomponent structures with installation of another component equipped with carboxylic donors.[47][48][49] For instance, in figure 2.10, the macrocycle **2.23** was chelated to Pd (II) forming binuclear Pd (II) complexes $[Pd_2\mathbf{L}^{\mathbf{2.23}}]^{4+}$ leaving one of the coordination sites free for coordination of tetra-carboxylate Zn(II) porphyrin $[Zn\mathbf{L}^{\mathbf{2.24}}]^{2+}$ for formation of a prim framework $[(Pd_2\mathbf{L}^{\mathbf{2.23}})_4(Zn\mathbf{L}^{\mathbf{2.24}})_2]^{12+}$. Again, the selective construction of a heteroleptic hierarchical assembly benefited from charge separation. The prismatic structure was utilized for fullerenes purification or asymmetric catalysis by functionalization of chiral Ru-catalysis in the cavity via coordination. [50] [51]

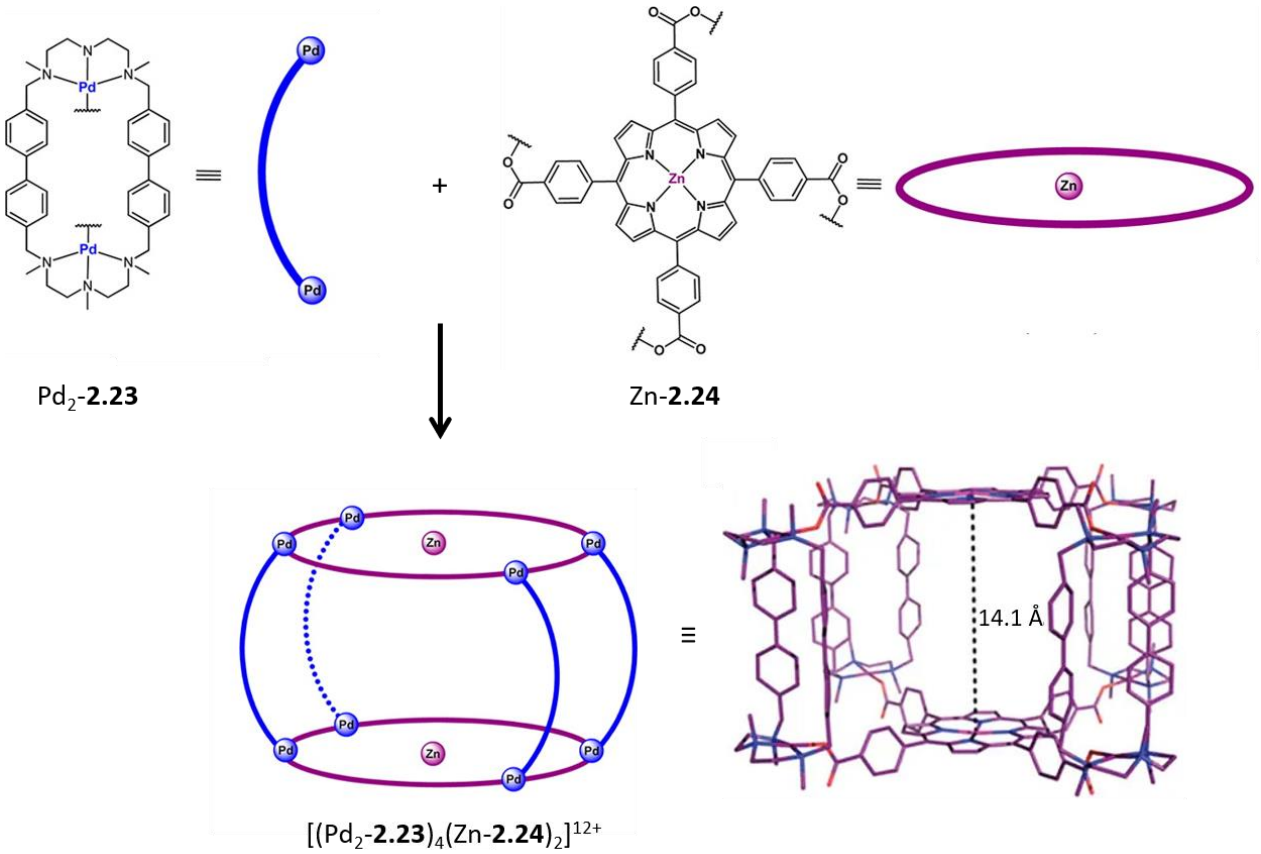

Figure 2.10. Heteroleptic hierarchical assembly by saturating metallo-macrocycles with bridging ligands. Adapt from Ref[50-51]. © Springer Nature, American Chemistry Society.

Despite all the approaches mentioned above, that have been developed for controlling the formation of heteroleptic self-assemblies, rarely there are examples about constructing coordination-driven multicomponent complexes with more than two different organic ligands. Noteworthy, by using the combination of various coordination motifs, Schmittel and co-workers pushed the complexity of coordination complexes to a higher level. In their recent work, a trigonal prism has been reported, which consists of three different organic ligands and two kind of metal cations.[52] The authors first showed the selective binding in a equimolar mixture of engineered coordination moieties (**a**-**f**) with Cu^{+} or Zn^{2+} in the solution and provide three complexes as outcomes (Figure 2.11a): moiety **a** together with **d** coordinate to free zinc ions forming complex [Zn**ad**]$^{2+}$, the dipole interaction between methoxy group and Zn^{2+} was confirmed helping to enhance the selectivity and this approach was named by the author as HETTAP (HETeroleptic Terpyridine And Phenanthroline) algorithm; due to steric repulsion, pyridine moiety **f** is preferred by Zn-porphyrin **c** over lutidine **e**; surprisingly, evidenced by UV-vis titration, the formation of the sterically more crowded complex [Cu**be**]$^{+}$ is energetically more favorable compared to the combination [Cu**bf**]$^{+}$. In accordance with the results of the self-sorting experiment, panel ligand **2.25** installed with moieties **c**, **d**, **e**; braces **2.26** and **2.27,** equipped with

moieties **a**, **b** and **f** respectively, were synthesized. The heteroleptic coordination prism was produced via a one-pot reaction and characterized by NMR and ESI-MS spectroscopy.

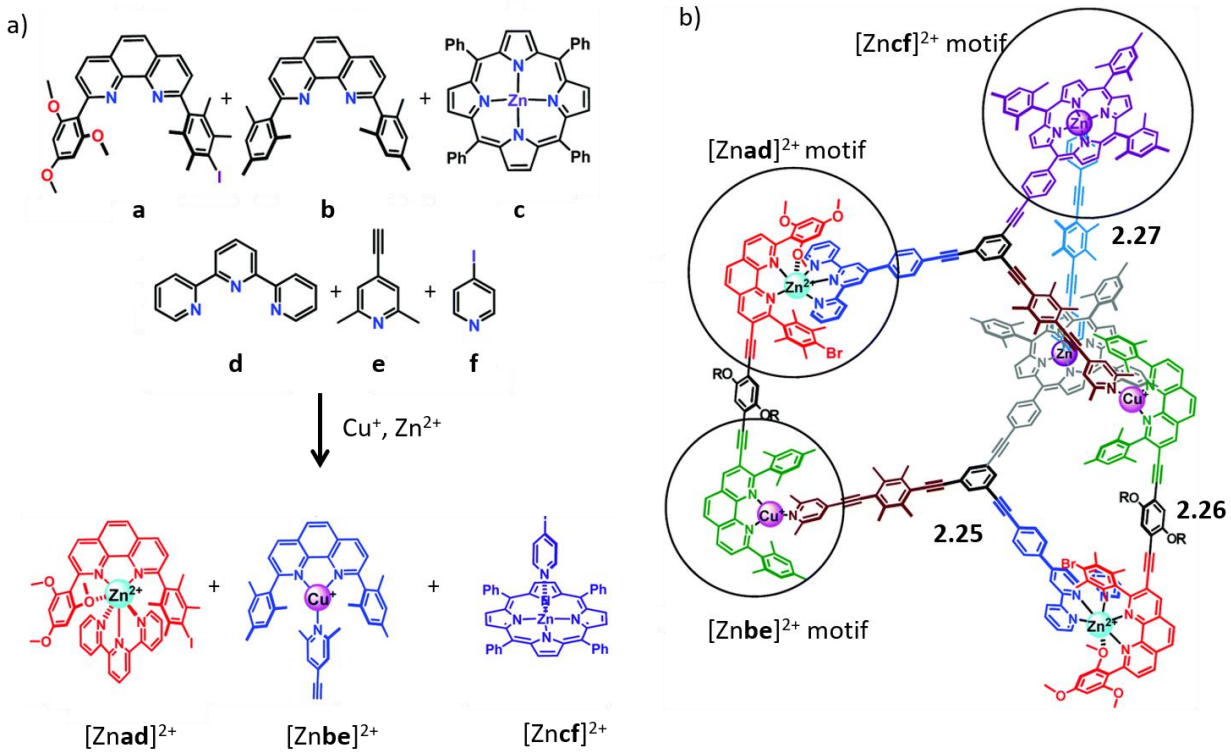

Figure 2.11. a) Self-sorting experiment of six coordination moieties with Cu^{+} and Zn^{2+}; b) multicomponent coordination prism consists of three different organic ligands and two kind of metal ions. Adapt from Ref [52]. © Royal Society of Chemistry.

2.1.5. Bridged salphen complexes

Salen ligand is a kind of Schiff-base ligands, which able to coordinate with various metal cations. Metal-salen complexes and its derivate, such as salphen complex, have not only been widely used for homogeneous and heterogeneous catalysis,[53][54] but also for building up supramolecular structures. For example, various multinuclear macrocycles based on salphen complex has been synthesized and reported by the groups of MacLachlan,[55] Akine[56] and Yashima[57] for different applications. Vives and co-workers installed metal-salphen complex on switchable molecular tweezers for magnetic and photochemistry studies.[58][59] Cui and co-workers produced chiral supramolecular self-assemblies consist of salen complex.[60]

In the year 2017, a novel cryptand-like tricobalt cage was reported by Akine and co-workers.[61] Interestingly, the cationic cage was able to encapsulate metal cations such as Na^{+}, K^{+}. Rb^{+} and Cs^{+} into its cavity Furthermore, by bridging the cobalt(III) salphen units using bifunctional diamine ligand via coordination reaction, the apertures of the cage can be closed (Figure 2.12a). In comparison with the open cage, in which the axial coordination sites of cobalt complexes were occupied by monodentate ligands, the kinetic of guest encapsulation in case of closed cage was way slower. While the guest

binding achieved to equilibrium in 5 mins for the open formed cage, it took about one week for the closed cage to finish the guest encapsulation.

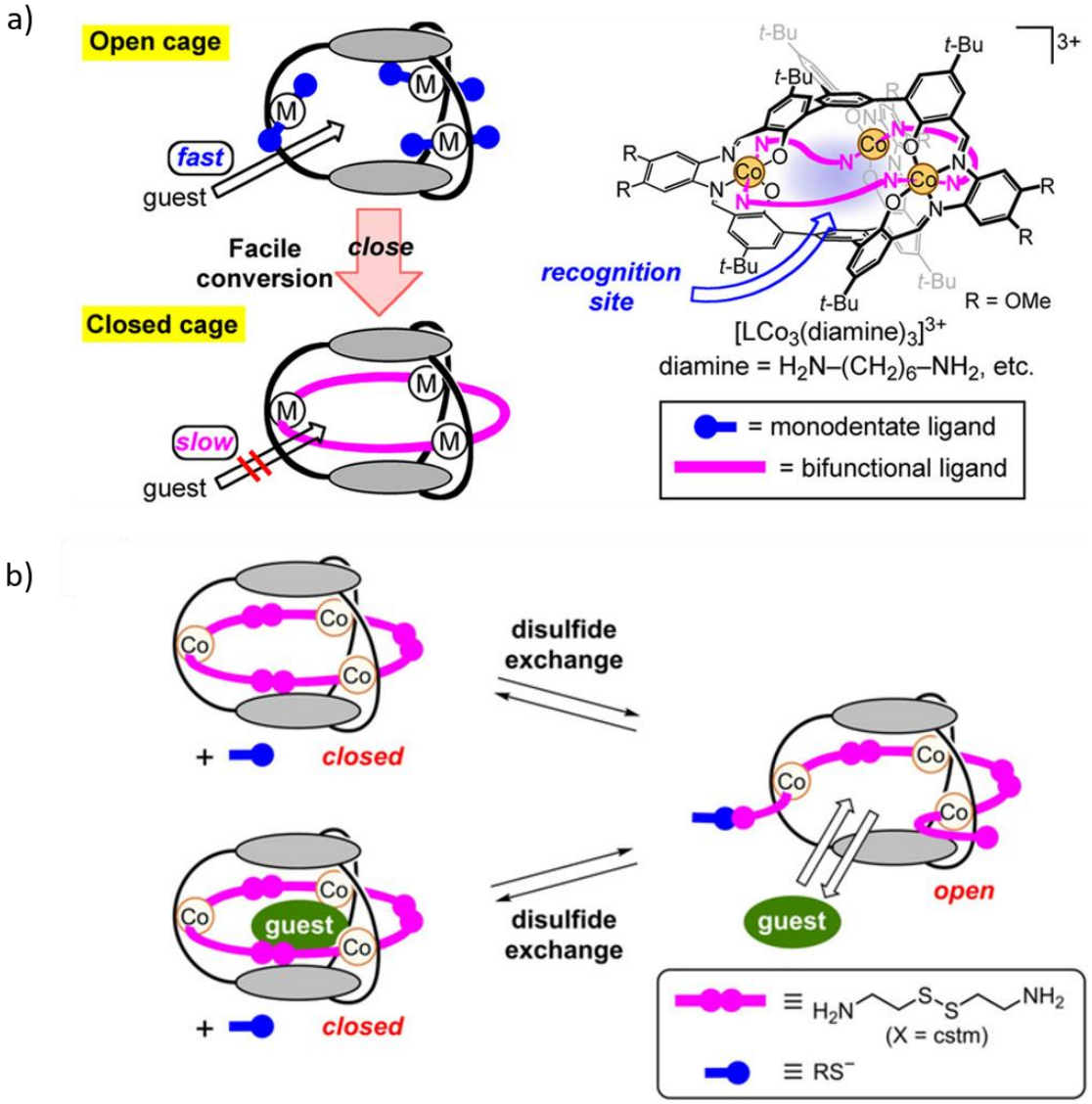

Figure 2.12. a) Cryptand-like tricobalt cage, the cavity of which could be closed by installation of bridging ligands; b) cystamine ligands were utilized to close the aperture, the guest binding behavior could be accelerated by disulfiide exchange reaction via addition of thiolate anion. © American Chemistry Society, Wiley-VCH Verlag GmbH & Co. KGaA, Weinheim.

Later in 2018, this system was updated by the same group.[62] Instead of using 1,6-hexanediamine, the salphen moieties were connected using cystamine ligands. Thus, the aperture could not only be closed by the bridging ligand but can also be open by disulphide exchange reaction (Figure 2.12b). The authors could show that the cystamine ligands worked similarly compared to the hexanediamine ligand, guest encapsulation was heavily inhibited for the closed cage. In contrast, in present of thiolate anion, which was produced in suit by reaction of 1-dodecanethiol and triethylamine, the bridging ligand was cleaved and allowed guest encapsulation more unhindered. The evidence came from NMR

study, which revealed the guest binding after thiolate anion addition was 14 times faster than closed cage.

The similar approach has also been employed in for the Ph.D. project. By bridging cobalt-salphen units with bismonodentate ligands, a series heteroleptic cage with much larger cavities and higher structure complexity have been generated, which will be discussed in detail in the rest part of this chapter.

2.2. Aims and objectives

To lay the foundation of preparing multifunctional artificial enzyme-like hosts and multicomponent molecular machinery, in our previous works, several strategies for heteroleptic self-assembly of $[Pd_2L_2L'_2]$-type cages have been reported, including shape complementarity between ligands or donor site engineering.[35][34][40] However, by increasing the variety of ligands, the challenges are enormous for obtaining integrative self-sorted products with three or more ligands. In principle, if four different monodentate ligands **A**, **B**, **C** and **D** are mixed to bind with square-planar metals, a library of complexes will be formed containing up to 55 distinct cage-like species (Figure 2.13).

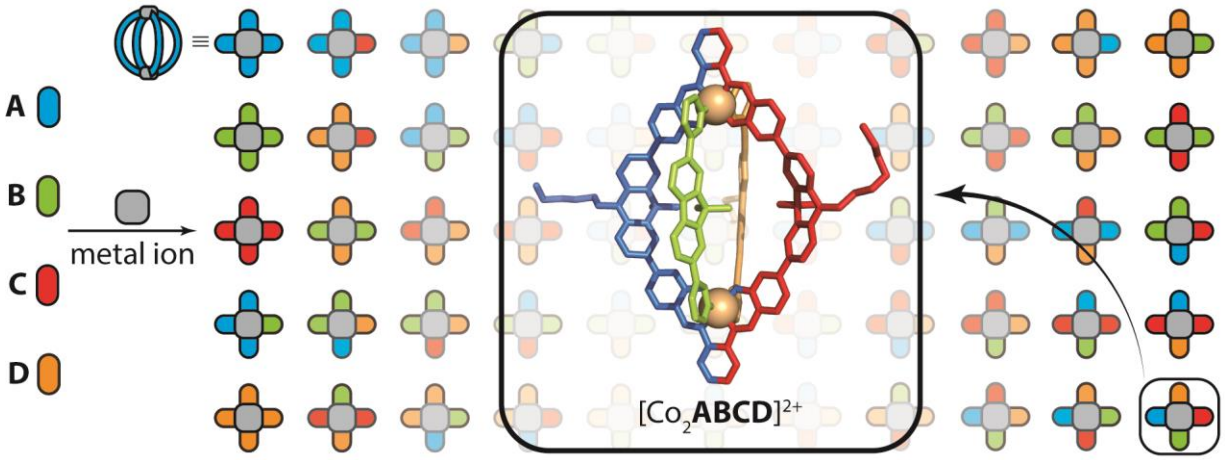

Figure 2.13. Heteroleptic self-assembly of $[M_2L_4]$ lantern-shaped cages (one in schematic side view, all in top-view) from four different bis-monodentate ligands **A**, **B**, **C** and **D** and two metal cations leading to a maximum of 55 possible products. In this work, the selective assembly of cage $[Co_2$**ABCD**$]$ is described.

Therefore, to reach the final goal of producing a lantern-shaped $[M_2$**ABCD**$]$ structure with four different organic ligands on the rational position via self-assembly, a novel synthetic strategy has been developed in this work by combining three approaches: 1) metal dominated template effect helps the formation of salphen macrocycle, 2) 3D cavity formed by installation of two bridges to saturate free coordination sites on metallo-macrocycles and 3) shape-complementarity controlled self-sorting. In the following, it will be reported in detail and systematically, how these three approaches were utilized to gradually increase the structural complexity. Five different organic ligands can be combined selectively with each other through coordination with Pd(II) or Co(II) cations to provide 5 novel cages structures, four of which are heteroleptic (Figure 2.14). All the cage structures are fully characterized by NMR spectra, high resolution mass spectrum and single crystal X-ray analysis.

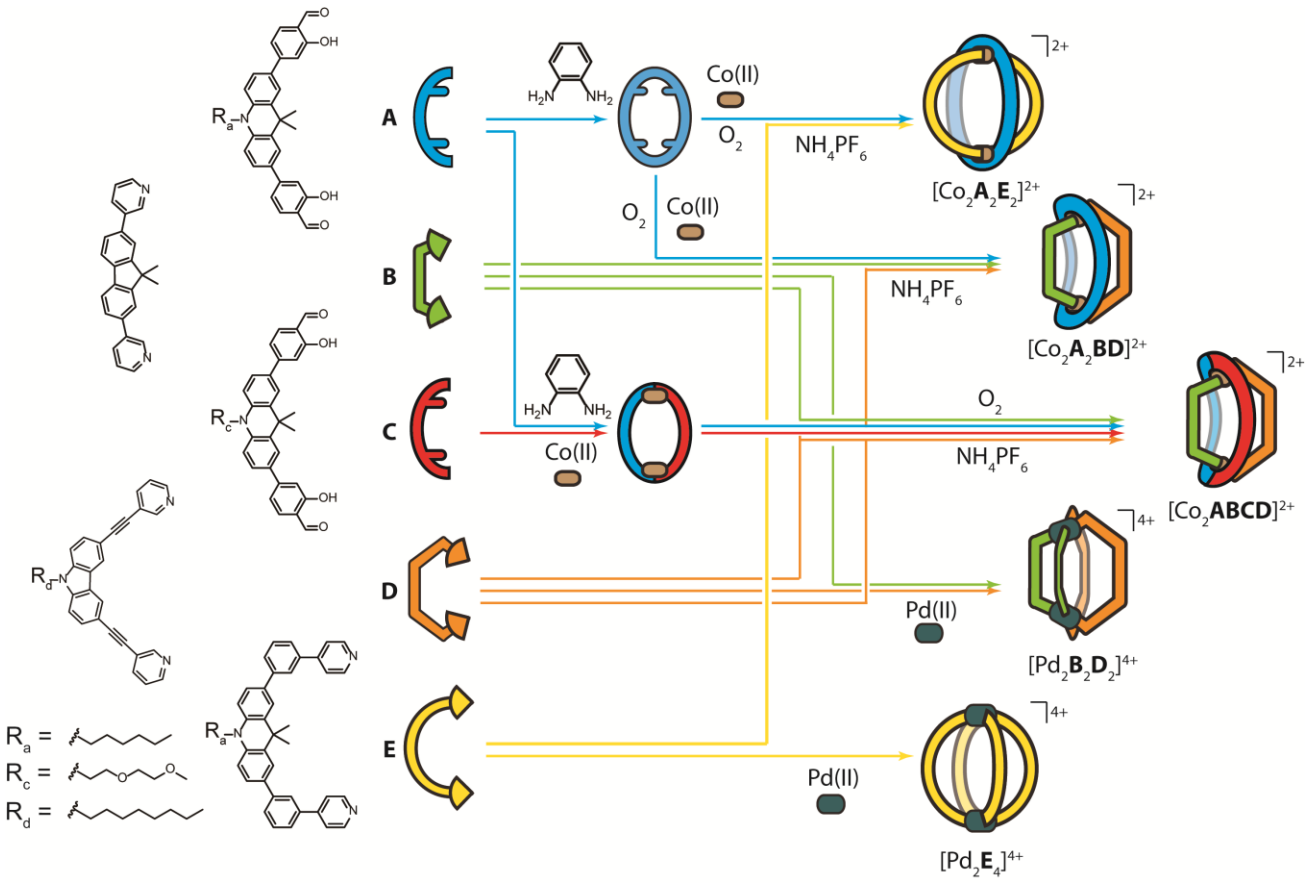

Figure 2.14. Construction of homo- and heteroleptic [M_2L_4] cages. The structural complexity was gradually increased by using a combination of *dynamic-covalent* salphen macrocyclization, *saturation* with two bridges and bridge-differentiation via *shape-complementarity*.

2.3. Heteroleptic cage $[Co_2A_2E_2]^{2+}$

The first attempt focuses on making a heteroleptic coordination cage contains two different ligands. **A** salphen macrocycle ($\mathbf{A}_2$) was formed by dynamic covalent bonding by bridging aldehyde functionalized ligand **A** with *o*-phenylenediamine via a condensation reaction. Co(acetate)$_2$ was used as the metal source to provide kinetically labile Co(II), which can be easily oxidized to diamagnetic Co(III) by oxygen in the air for a diminished ligand exchange rate after self-assembly.[63] The four equatorial coordination sites of the octahedral Co(III) cation were occupied by the salphen moieties and left the coordination sites on the axial positions free for the installation of ligand **E** with an appropriate length to build the 3D cavity.

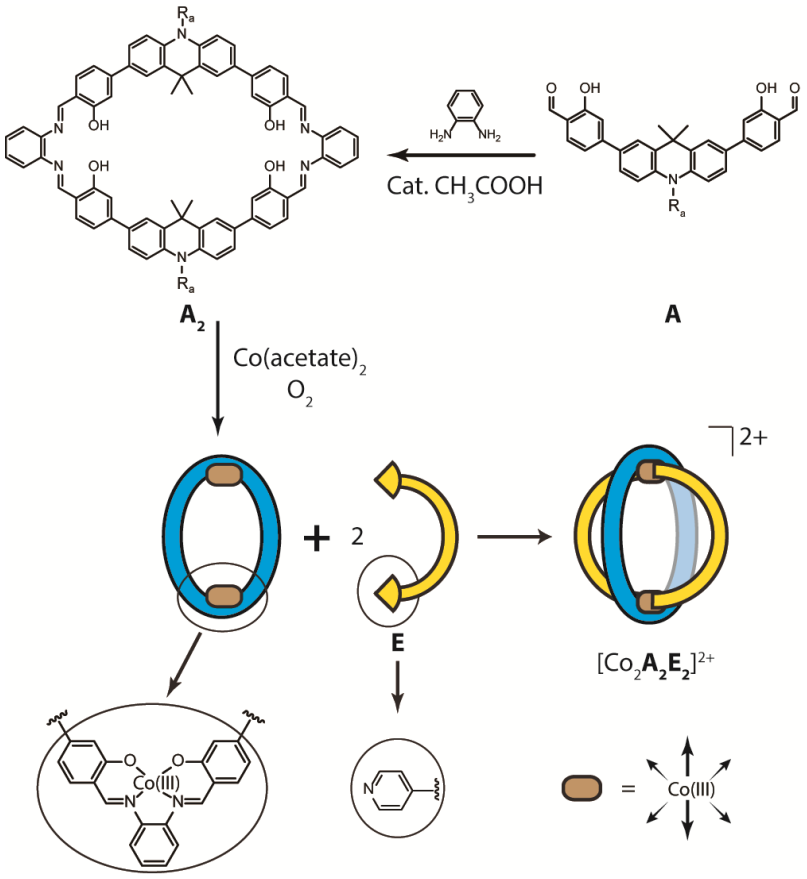

Figure 2.15. Synthesis of salphen-based macrocycle $\mathbf{A}_2$ and self-assembly of heteroleptic cage $[Co_2\mathbf{A}_2\mathbf{E}_2]^{2+}$.

Ligand **A** was synthesized by Suzuki cross-coupling of 2,7-dibromo-10-hexyl-9,9-dimethyl-9,10-dihydroacridine and 4-formyl-3-hydroxyphenylboronic acid pinacol ester. To obtain macrocycle $\mathbf{A}_2$, an acid catalyzed condensation of **A** with *o*-phenylenediamine was performed in a solvent mixture of DCM : MeOH = 1 : 1, which offers a quantitative yield (for synthetic details see the experimental section).

For the self-assembly of cage $[Co_2\mathbf{A}_2\mathbf{E}_2]^{2+}$, $Co(OAc)_2$ and $\mathbf{A}_2$ were stirred vigorously in an $CH_3CN/CHCl_3$ mixture (*v/v* = 1 : 1) under aerobic conditions for 15 mins. Afterwards, ligand **E** was added and the reaction mixture was heated at 60 °C overnight. Subsequently, with the addition of NH_4PF_6 the reaction was stirred for one more hour. The crude product was purified by precipitation to offer pure cage $[Co_2\mathbf{A}_2\mathbf{E}_2]^{2+}$ as a dark red powder in 90% isolated yield (Figure 2.15). A prominent signal corresponding to the formula $[Co_2\mathbf{A}_2\mathbf{E}_2]^{2+}$ was observed in the ESI-TOF mass spectrum at *m/z* = 1262.0 for a 2+ species, which is in excellent agreement with the calculated mass.

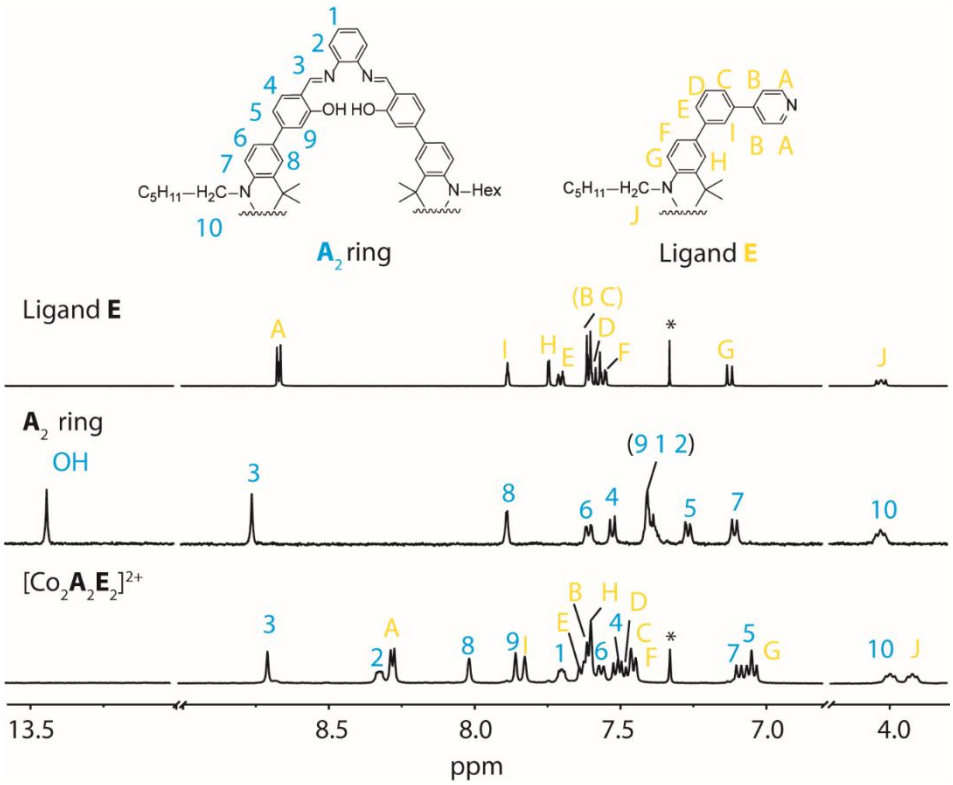

Figure 2.16. Partial ^{1}H NMR spectrum (500 MHz/CD_2Cl_2, 298K) of cage $[Co_2\mathbf{A}_2\mathbf{E}_2]^{2+}$ compared with spectra of free ligand **E** and macrocycle $\mathbf{A}_2$.

^{1}H NMR analysis indicate a single species consisted of **A** and **E** in a 1 : 1 ratio (Figure 2.16). In addition, a clear cross signal has been observed between proton *9* of the macrocycle $\mathbf{A}_2$ and proton *A* of banana-shaped ligand **E** in the ^{1}H-^{1}H NOESY NMR (Figure S2.5, experimental section), confirming a close contact between $\mathbf{A}_2$ and **E**. The dark red plate-shaped crystals, suitable for X-ray analysis were obtained by slow evaporation of ethyl acetate into a solution of $[Co_2\mathbf{A}_2\mathbf{E}_2]^{2+}$ in DMSO. As expected, the heteroleptic cage $[Co_2\mathbf{A}_2\mathbf{E}_2]^{2+}$ is a C_2-symmetric structure. The macrocycle $\mathbf{A}_2$ presents a slightly twisted conformation with the geminal methyl groups pointing to the opposite directions (Figure 2.17c). The two salphen (Co(III)N_2O_2) moieties are nearly coplanar with a Co-Co distance of 14.2 Å and bridged by ligand **E** in axial positions on the both faces.

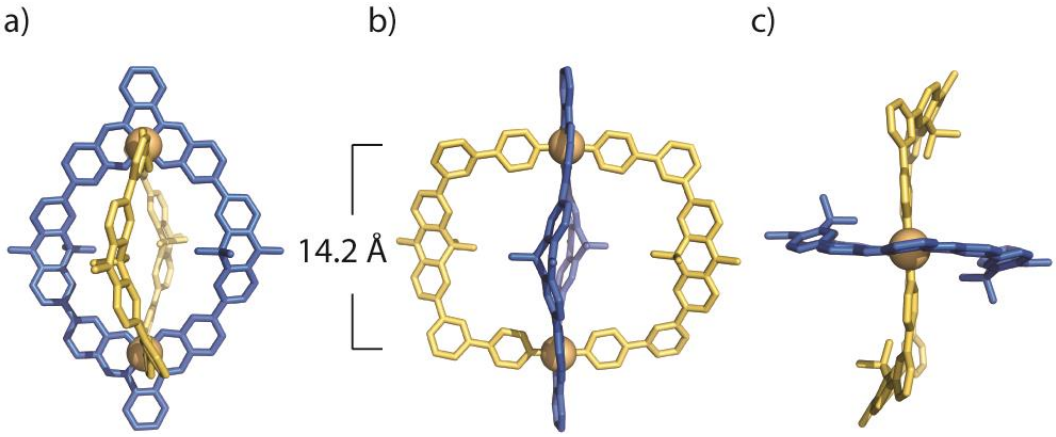

Figure 2.17. a)-c) Front, side, and top views of the single crystal X-ray structures of heteroleptic cage $[Co_2\mathbf{A}_2\mathbf{E}_2]^{2+}$ (hydrogen atoms, counterions, and side chains were omitted for clarity).

2.4. Heteroleptic cage $[Co_2A_2BD]^{2+}$

When the structure of the macrocyclic fragment $[Co_2\mathbf{A}_2(dmso)_4]^{2+}$ was simulated using molecular modeling, two energetically favorable conformations have been found. In one case, as already described for the crystal structure of cage $[Co_2\mathbf{A}_2\mathbf{E}_2]^{2+}$, the ring $\mathbf{A_2}$ is slightly twisted with two salphen moieties coplanar providing the coordination sites on axial position parallel. In the other case, the ring is bent like a crescent moon. As thus, the two faces of the macrocycle are no longer identical, the angle formed between the axial coordination sites indicating a possibility for installation of two bridging ligands with different binding angle and lengths (Figure 2.21c), which remind us of our former work on heteroleptic self-assembly of *cis*-configured $[Pd_2\mathbf{L}_2\mathbf{L'}_2]$ cages using shape complementarity approach. Indeed, a novel heteroleptic cage $[Co\mathbf{A}_2\mathbf{BD}]^{2+}$ with three different kinds of organic ligands was successfully synthesized. To fulfil the demand of the shape complementarity of the bent conformation, fluorene-based ligand **B** and carbazole-based ligand **D** were synthesized. Macrocycle $\mathbf{A}_2$ combined with cobalt acetate formed a dark red complex in a mixture of CH_3Cl and CH_3CN (1:1 v/v). After ligand **B** and ligand **D** were added, the mixture was then stirred overnight at 60 °C. With addition of NH_4PF_6 the reaction was stirred for one more hour to provide a dark red solid with a isolate yield of 79% (for synthetic details see the experimental section).

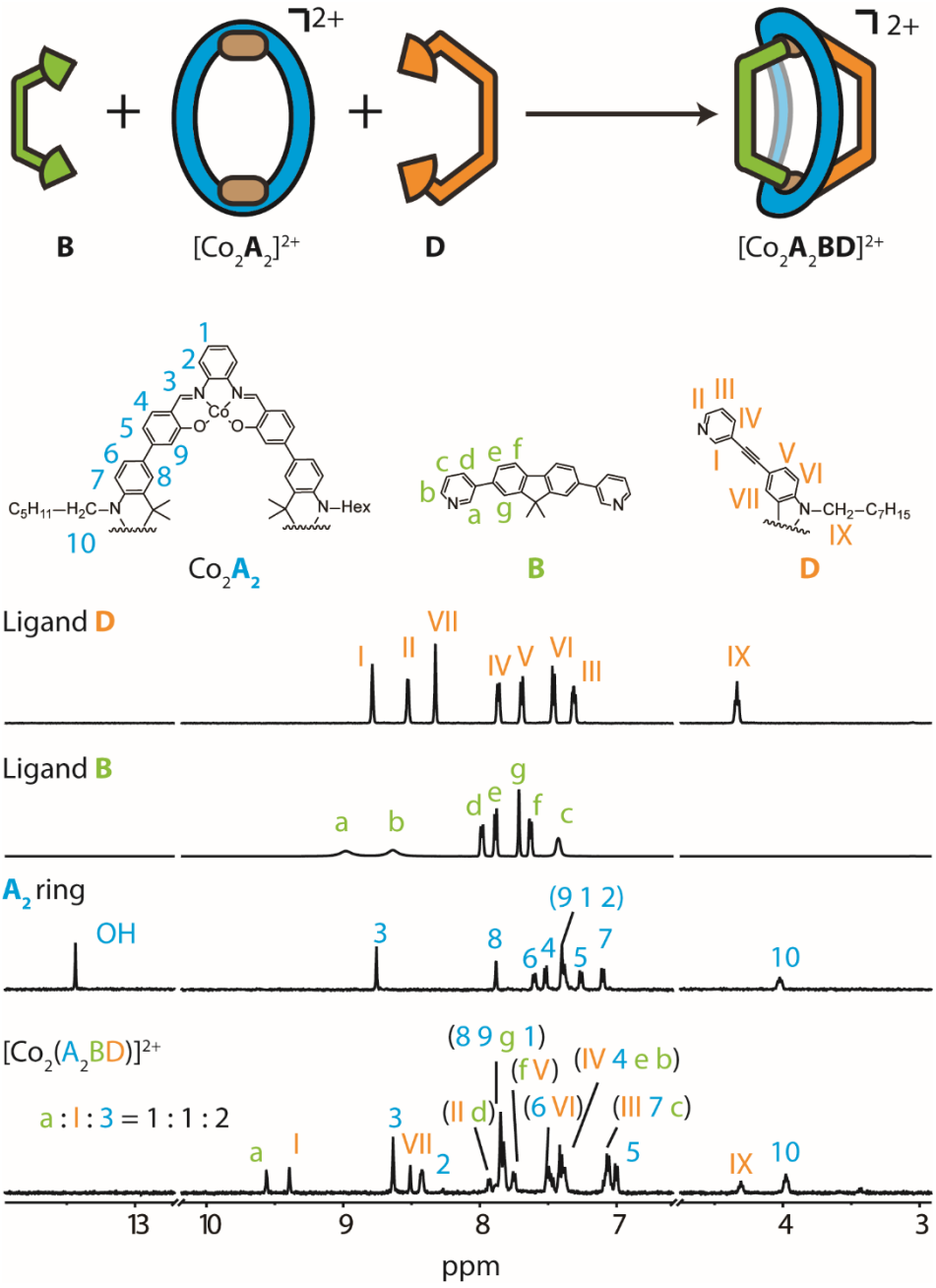

Figure 2.18. Partial ^{1}H NMR spectrum (700 MHz/CD_2Cl_2, 298K) of cage $[Co_2\mathbf{A_2BD}]^{2+}$ compared with free ligand **B**, **D** and macrocycle $\mathbf{A_2}$ (500 MHz/CD_2Cl_2, 298K).

^{1}H NMR characterization shows a 2 : 1 : 1 ration of the integrations of protons belonging to **A**, **B** and **D**, which fit to the expected stoichiometry of $[Co_2\mathbf{A_2BD}]^{2+}$. Because of the coordination effect, significant downfield shift on pyridyl protons H_a of ligand **B** and H_I of ligand **D** has been observed. On the contrary, pyridyl protons H_b of ligand **B** and H_{II} of ligand **D** revealed upfield shifting, which could be explained by shielding effects since both of them point directly to the salphen phenylene moieties (Figure 2.18). In the ^{1}H-^{1}H NOESY experiment, clear cross-peaks between the macrocycle $\mathbf{A_2}$ and both ligand **B** and ligand **D**, respectively, confirmed all three ligands being integral components of the same

supramolecular assembly (Figure S2.11). ESI-TOF mass measurement gave a prominent peak at *m/z* = 1077.4 which is consistent with the calculated isotopic pattern for $[Co_2\mathbf{A}_2\mathbf{BD}]^{2+}$ (Figure 2.19).

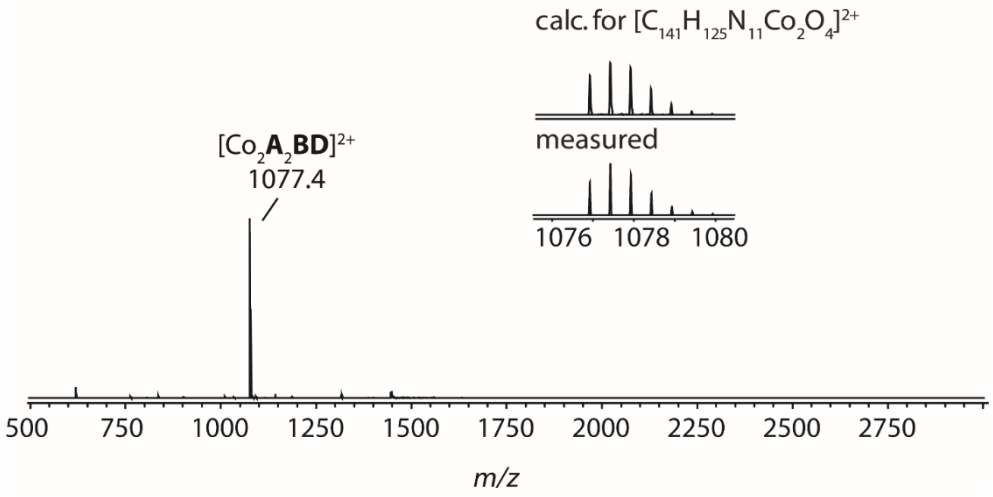

Figure 2.19. High resolution ESI mass spectrum of cage $[Co_2\mathbf{A}_2\mathbf{BD}]^{2+}$ with calculated and observed isotope patterns.

Suitable crystals for X-ray diffraction generated by means of layering of ethyl acetate with a solution of cage $[Co_2\mathbf{A}_2\mathbf{BD}]^{2+}$ in DCM (Figure 2.20). Different from the observation in the case of $[Co_2\mathbf{A}_2\mathbf{E}_2]^{2+}$, in cage $[Co_2\mathbf{A}_2\mathbf{BD}]^{2+}$, the geminal methyl groups on the macrocycle $\mathbf{A}_2$ are pointing in the same direction (Figure 2.20c), which leads to a slightly bent conformation of the entire ring. As designed, ligand **B** and ligand **D** show great shape complementarity with the bent conformation of $\mathbf{A}_2$: the concave face connects with the shorter ligand **B** with diverging set of donors, while the convex side binds with longer ligand **D** with converging donor sites.

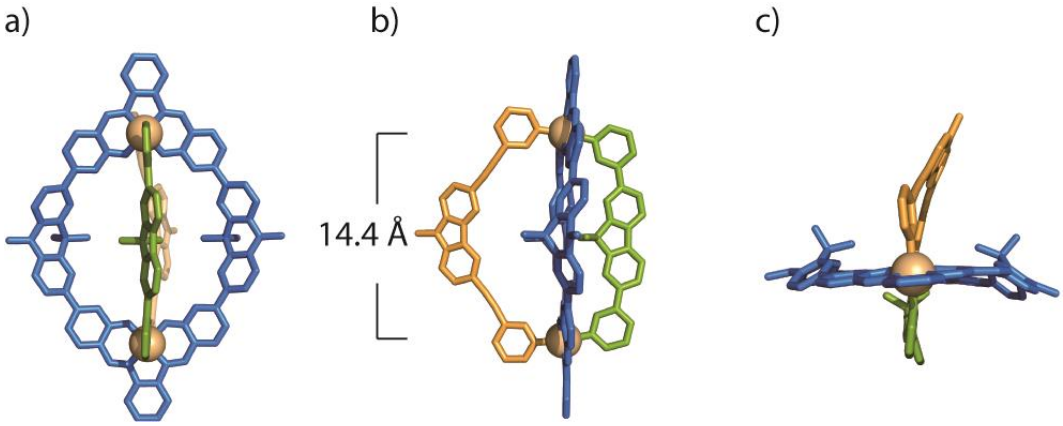

Figure 2.20. a)-c) Front, side, and top views of the single crystal X-ray structures of heteroleptic cage $[Co_2\mathbf{A}_2\mathbf{BD}]^{2+}$ (hydrogen atoms, counterions, and side chains were omitted for clarity).

2.5. Geometric complementarity, self-sorting experiment and computational studies

Next, a series of further experiments was performed for getting a more comprehensive understanding of the factors governing the heteroleptic self-assembly. Firstly, the behavior of the bis-pyridyl banana-shaped ligands **B**, **D** and **E** reacting with the square planar Pd(II) cations was investigated. Without any surprise, ligands **E** forms a monomeric cage $[Pd_2\mathbf{E}_4]^{4+}$ by coordination with Pd(II) in a ratio of 2 : 1 in acetonitrile, the structure was characterized by NMR, HRMS (See experimental section) and X-ray structure is shown in Figure 2.21a. Interestingly, a new heteroleptic cage *cis*-$[Pd_2\mathbf{B}_2\mathbf{D}_2]^{4+}$ was obtained by mixing ligand **B** and **D** with $[Pd(CH_3CN)_4](BF_4)_2$ in 1 : 1 : 1 ratio in CD_3CN (characterization by NMR and HRMS in experimental section). By comparing the X-ray structures of $[Pd_2\mathbf{B}_2\mathbf{D}_2]^{4+}$ (Figure 2.21b) and $[Co_2\mathbf{A}_2\mathbf{BD}]^{2+}$, the remarkable geometrical consistency between ligand **B**, ligand **D** and macrocycle $\mathbf{A}_2$ can be explained. The angle between two palladium coordination surfaces was determined to be 21 °(β, Figure 2.21b), which has a great agreement with the angle α (19 °) of cage $[Co_2\mathbf{A}_2\mathbf{BD}]^{2+}$ (Figure 2.21c). In addition, the Pd-Pd distance (13.6 Å) is also quite close to the Co-Co distance (14.4 Å) (Table S2.4).

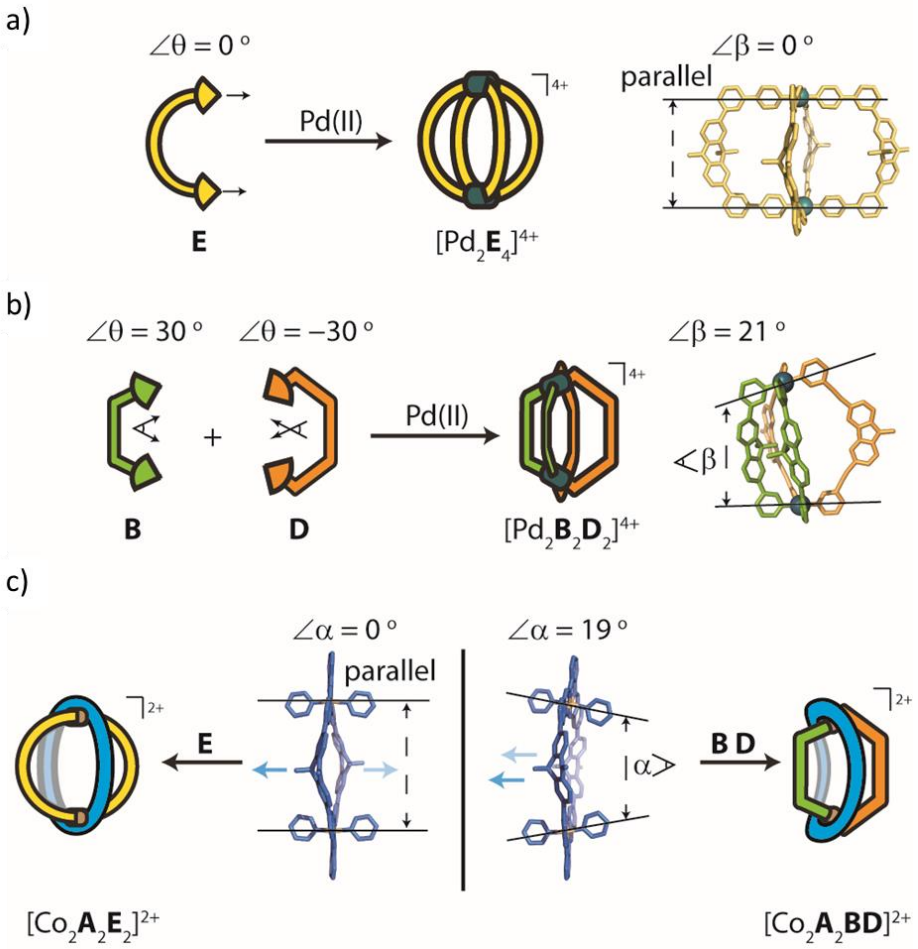

Figure 2.21. Structural features of cages a) $[Pd_2\mathbf{E}_4]^{4+}$, b) $[Pd_2\mathbf{B}_2\mathbf{D}_2]^{4+}$, c) $[Co_2\mathbf{A}_2\mathbf{E}_2]^{2+}$ and $[Co_2\mathbf{A}_2\mathbf{BD}]^{2+}$.

Owing to the excellent shape complementarity between the bent conformation of $\mathbf{A}_2$ and ligands **B** and **D**, the heteroleptic self-assembles $[Co_2\mathbf{A}_2\mathbf{BD}]^{2+}$ have been obtained as the major thermodynamic product. This was confirmed by a self-sorting experiment (Figure 2.22): Two independent flasks were charged with the same amount of macrocycle $\mathbf{A}_2$ (1.0 eq.) and Co(acetate)$_2$ (2.0 eq.) in DMSO. After addition of 2.0 eq. of **B** or **D** into the flasks, respectively, the mixture was heated in air to 70 °C for 12 h. The results were examined with high-resolution mass spectrometry. In the flask where ligand **D** was added**,** a statistical mixture with up to four carbazole-based ligands **D** on the binuclear cobalt complex $[Co_2\mathbf{A}_2]^{2+}$ has been observed, indicating ligand **D** alone has a poor geometric complementarity with the macrocycle to form a cage like structure $[Co_2\mathbf{A}_2\mathbf{D}_2]^{2+}$. In the flask where ligand **B** was charged, only the complexes with up to three ligands **B** were observed, which hints **B** is favorable on one face of the bent conformation of macrocycle to form bridged fragment $[Co_2\mathbf{A}_2\mathbf{B}]^{2+}$, but matching poorly on the other face. Next, the two samples were mixed with a ratio of 1:1 and heating at 70 ˚C for 24 h. As the result, a strong new signal at *m/z* = 1077.4 raised up correspond to the cage compound $[Co_2\mathbf{A}_2\mathbf{BD}]^{2+}$, indicating the formation is thermodynamically driven.

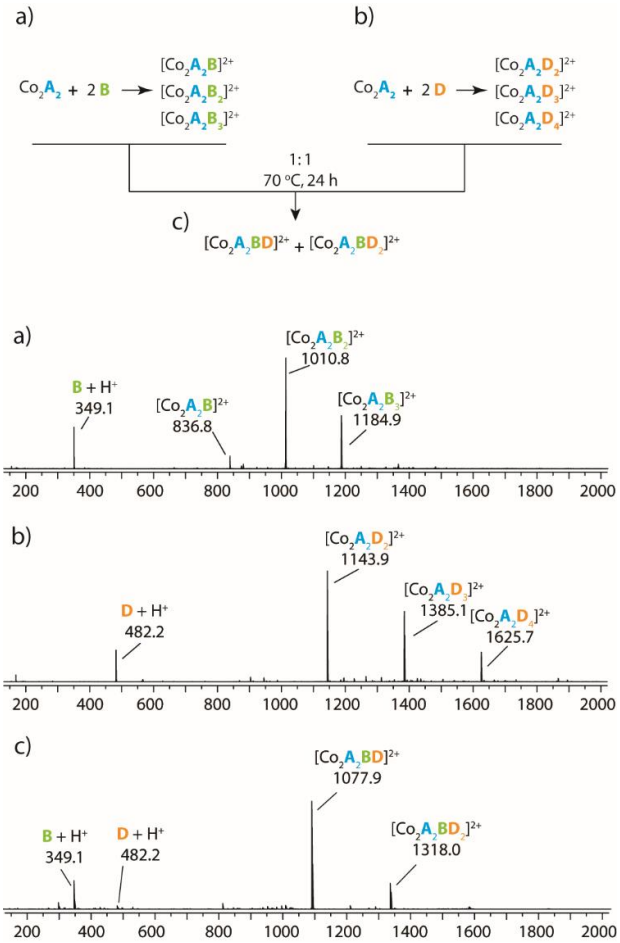

Figure 2.22. Self-sorting experiment monitored by ESI mass spectrometry: a) binuclear cobalt complex $[Co_2\mathbf{A}_2]^{2+}$ reacted with 2.0 equiv. of ligand **B**; b) binuclear Cobalt complex $[Co_2\mathbf{A}_2]^{2+}$ reacted with 2.0 equiv. of ligand **D**; c) samples from a) and b) mixed in a ratio of 1:1 and heated at 70 °C for 24 h.

The heteroleptic cage assembly was further investigated by DFT geometry optimizations. The relative energy for cage formation was calculated by the simplified reaction equation: $[Co_2\mathbf{A}_2(DMSO)_4]^{2+}$ + 2 **L** → $[Co\mathbf{A}_2\mathbf{L}_2]^{2+}$ + 4 DMSO (**L** = **B**, **D** or **E**; neglecting solvent and counter cation effects, Table S2.1, experimental section). As the result, the energy demand for forming cage $[Co_2\mathbf{A}_2\mathbf{BD}]^{2+}$ is much smaller compared to the tentative cage complexes $[Co_2\mathbf{A}_2\mathbf{B}_2]^{2+}$ (about 50 kJ/mol) and $[Co_2\mathbf{A}_2\mathbf{D}_2]^{2+}$ (about 30 kJ/mol). What's more, formation of cage $[Co_2\mathbf{A}_2\mathbf{E}_2]^{2+}$, which is composed of macrocycle $\mathbf{A}_2$ and two identical bi-pyridyl ligands **E**, is even more energetically favorable, due to the well-designed geometric complementarity.

2.6. Heteroleptic cage $[Co_2ABCD]^{2+}$

By taking advantage of the literature-known method for preparation of non-symmetric salen/salphen,[64] [65] we successfully produced an unsymmetrical binuclear salphen macrocycle $[Co_2\mathbf{AC}]^{2+}$ in which **A** has a *n*-hexyl chain attached, while **C** carries with a 3,6-dioxaheptyl group for the convenience of NMR analysis. By combining the approaches, we have reported above, the self-assembly of lantern-shaped $[Co_2\mathbf{ABCD}]$ cage is possible.

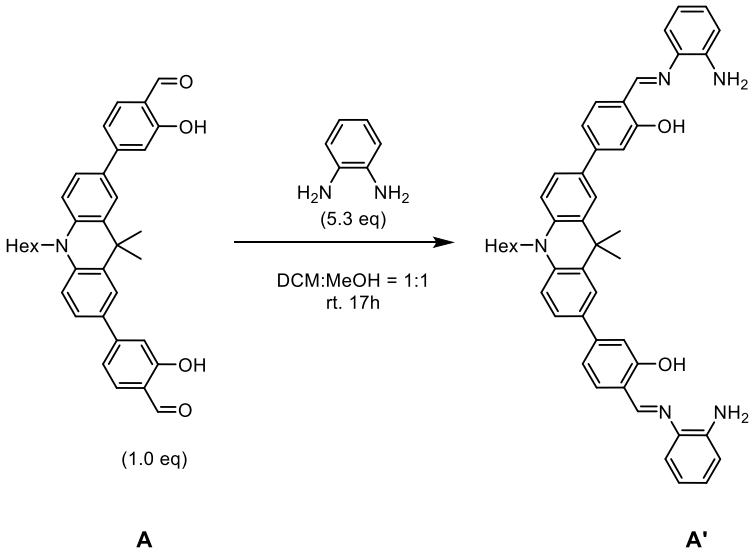

Figure 2.23. Synthesis of the precursor half macrocycle **A'**.

For making fragment $[Co_2\mathbf{AC}]^{2+}$, the precursor half macrocycle **A'** was synthesized using a condensation reaction under controlled conditions without acid catalysis offering quantitative yield (Figure 2.23). Here it is important to notice that **A'** is a kinetic product; heating, prolonged reaction or addition of acetic acid as catalyst can all lead to the formation of the full macrocycle $\mathbf{A_2}$.

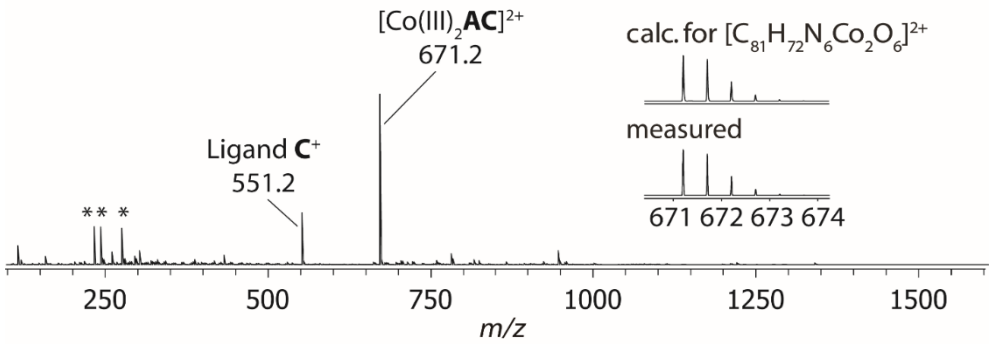

Figure 2.24. High resolution ESI mass spectrum of cobalt complex $[Co_2\mathbf{AC}]^{2+}$ measured without any purification. According to the mass spectrum, $[Co_2\mathbf{AC}]^{2+}$ was the only Cobalt complex formed, no signals corresponding to $[Co_2\mathbf{A}_2]^{2+}$ and $[Co_2\mathbf{C}_2]^{2+}$ species were found.

Cage $[Co_2\mathbf{ABCD}]^{2+}$ is can be prepared by a one-pot stepwise reaction. Unlike macrocycle $\mathbf{A}_2$, pure **AC** ring can hardly be produced. By simply mixing the precursors **A'** and **C**, the outcome of the reaction is a mixture of $\mathbf{A}_2$, $\mathbf{C}_2$ and **AC**. However, if $Co(acetate)_2$ was added together with ligand **A'** and **C** in a ratio of 2:1:1 in DMSO under N_2 protection, the complex $[Co_2\mathbf{AC}]$ is the only the intermediate (Figure 2.24), which is supposed to benefit from the template effect of cobalt cation. A decent yield of cage $[Co_2\mathbf{ABCD}]^{2+}$ was then obtained by addition of ligand **B**, **D** and NH_4PF_6 into the reaction mixture followed by purification.

More efficiently, cage $[Co_2\mathbf{ABCD}]^{2+}$ was produced by a five-component self-assembly: ligands **A'**, **B**, **C** and **D** together with $Co(acetate)_2$ were mixed in DMSO under N_2 atmosphere and stirred at 60 °C overnight. After adding NH_4PF_6, the mixture was exposed to air for one further hour to finish the reaction. The crude product was purified by the described precipitation method to provide cage $[Co_2\mathbf{ABCD}]^{2+}$ 57% isolated yield.

NMR analysis confirmed the successful formation of complex $[Co_2\mathbf{ABCD}]^{2+}$. ^{1}H NMR revealed clear peaks of 3,6-dioxaheptyl group (proton *C1-C5*) and hexyl chain (proton *10*) from the two different halves of ring **AC**. In the case of $[Co_2\mathbf{A}_2\mathbf{BD}]^{2+}$ a singlet belonging to proton *3* was found at 8.63 ppm, while two overlapped singlets have been observed for $[Co_2\mathbf{ABCD}]^{2+}$, because of the reduced symmetry on the macrocycle (Figure 2.25d). In addition, proton H_h which is assigned to the two methyl groups on ligand **B**, showed up as two singlets in the ^{1}H NMR spectrum, indicating a desymmetrized chemical environment inside of the cavity (Figure S2.16). The clear cross signals revealed by a NOESY experiment indicated again the close contact between macrocycle **AC** and ligand **B** and **D** (Figure 2.25b). Only one single peak in the ESI-TOF mass spectrum has been found at *m/z* = 1086.4, which is in excellent agreement with the calculated mass to the formula of $[Co_2\mathbf{ABCD}]^{2+}$ (Figure 2.25c). In addition, cage $[Co_2\mathbf{ABCD}]^{2+}$ and $[Co_2\mathbf{A}_2\mathbf{BD}]^{2+}$ can also be distinguished by trapped ion mobility ESI-TOF

mass spectrometry by a co-injection experiment providing collisional cross section (CCS) value of 557.8 Å^2 and 562.8 Å^2, respectively (Figure S2.20).

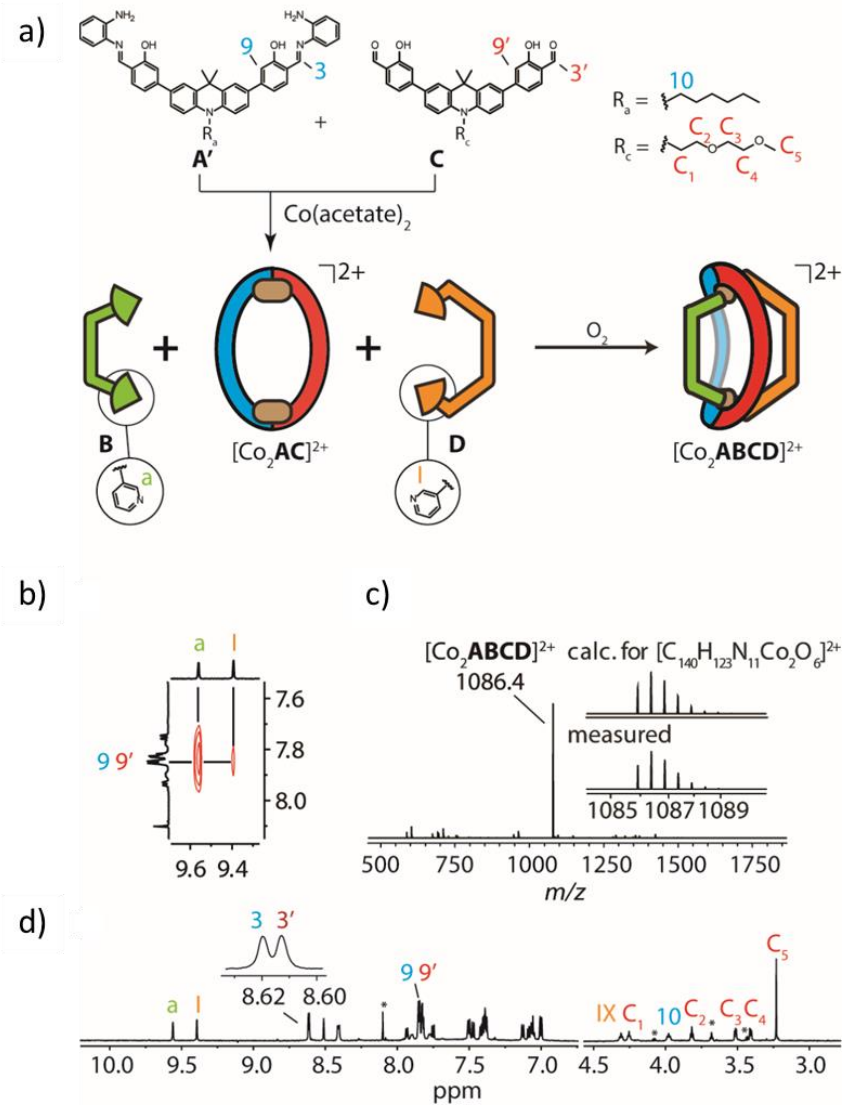

Figure 2.25. a) Self-assembly of heteroleptic cage [Co$_2$**ABCD**]$^{2+}$. b) Partial ^{1}H-^{1}H NOESY NMR shows cross signals between macrocycle **AC** and ligands **B** and **D**; c) high-resolution mass spectrum with calculated and observed isotope patterns; d) ^{1}H NMR spectrum (700 MHz) measured in CD_2Cl_2 at 298K.

The structure was further characterized by X-ray analysis. Red plate-shaped crystals were produced by layering ethyl acetate to a solution of [Co$_2$**ABCD**]$^{2+}$ in DCM. Unsurprisingly, complex [Co$_2$**ABCD**]$^{2+}$ has a similar structure compare to [Co$_2$**A**$_2$**BD**]$^{2+}$ (Figure 2.26). The broken symmetry of the fragment [Co$_2$**AC**]$^{2+}$ is confirmed by matching the observed electron densities of the side chains attaches to ligands **A** and **C** in the X-ray diffraction results.

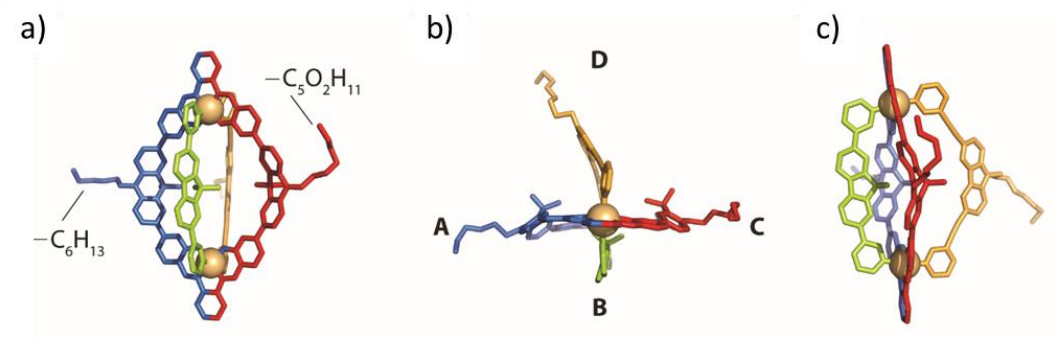

Figure 2.26. a)-c) Front, top and side views of the single crystal X-ray structures of hetroleptic cage $[Co_2\mathbf{ABCD}]^{2+}$ (hydrogen atoms, counterions, and side chains were omitted for clarity).

2.7. Conclusions

To prepare a nano-sized hollowed structure, usually there are two major strategies. The first is by means of purely organic synthesis, which allows to bring various parts into the artificial host compounds, however, normally also demands multifarious syntheses and purifications. The second way is utilizing self-assembly that is driven by non-covalent interactions or dynamic covalent formation. Obviously, this strategy is more efficient and elegant for generating high symmetric 2D or 3D structures. Nevertheless, most self-assemblies consist of only one type of the building blocks, thus strongly limited the variety of the induced functionalities. Due to entropic reasons, making an integrative self-sorted complex with multiple different components is very challenging, often the outcome is rather a statistical mixture.

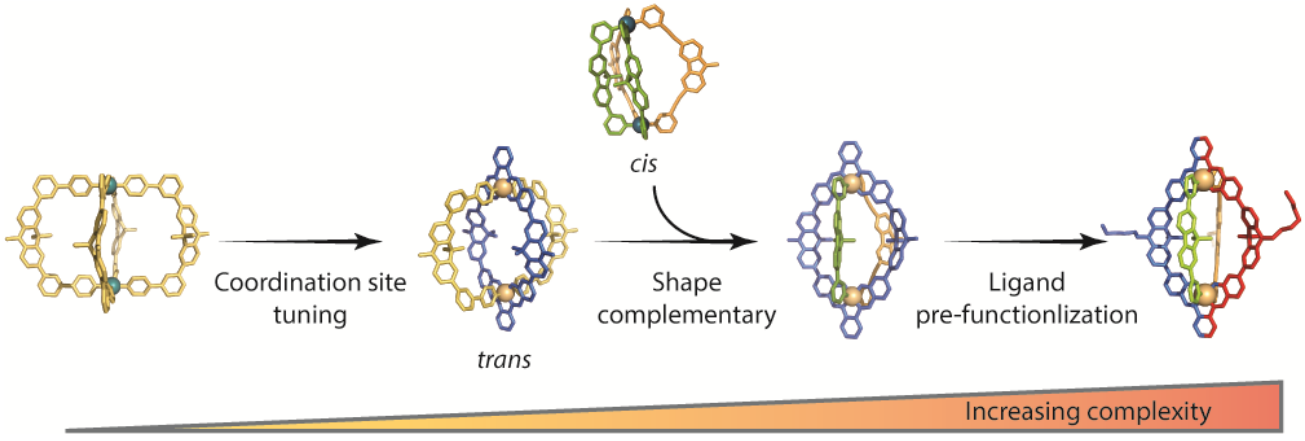

Figure 2.27. Evolution of coordination cages by gradually increasing structural complexity.

In this project, by combining a dynamic-covalently connected macrocycle which is equipped by two identical cobalt-salphen units, with two shape-complementary bridges installed to the axial positions of the octahedral coordination centre, we have developed a new approach able to produce heteroleptic self-assembled cages with up to 5 different components (including four different organic ligands and one metal coordination node)via a one-pot reaction. This lays the foundation of building

anisotropic supramolecular constructions with potential to be decorated with multiple functionalities. Meanwhile, research focused on converting form “multi-component” to “multi-functional” is currently undergoing.

2.8. Experimental section

2.8.1. Materials and methods

Unless otherwise stated, all chemicals were obtained from commercial sources and used as received. Compound **1**, [66] boronic acid pinacol esters **4** [67] and **7** [68] as well as ligand **D** [69] were prepared according to literature procedures. Dry solvents were purchased or purified and dried over absorbent-filled columns on a GS-Systems solvent purification system (SPS). Reactions were monitored with thin layer chromatography (TLC) using silica coated aluminium plates (Merck, silica 60, fluorescence indicator F254, thickness 0.25 mm). For column chromatography, silica (Merck, silica 60, 0.02 – 0.063 mesh ASTM) was used as the stationary phase, if not mentioned otherwise. Flash chromatography was performed on a Biotage Isolera One fraction collector with Biotage SNAP Ultra columns. Recycling gel permeation chromatography (GPC) was performed on Japan Analytical Industry NEXT and LaboACE instruments using JAIGEL 1-HH and 2-HH 20 mm x 600 mm columns with a flowrate of 7 mL/min.

The NMR spectroscopic data was measured on Bruker AV 500 Avance NEO, Bruker AV 700 Avance III HD and Agilent Technologies DD2 spectrometers. For ^{1}H NMR spectra, the chemical shifts were calibrated on the lock signals of the solvents ($CDCl_3$: 7.26 ppm, CD_3CN: 1.94 ppm, CD_2Cl_2: 5.32 ppm). For ^{13}C NMR spectra, solvent signals were used as internal standards (CD3CN: 1.32, 118.26 ppm, CD_2Cl_2: 54.00 ppm, $CDCl_3$: 77.00 ppm). Chemical shifts δ are given in ppm, coupling constants *J* in Hz. All spectra were recorded in standard 5 mm NMR tubes at 25 °C.

Mass spectrometry data were measured on Bruker timsTOF, Bruker Compact, Bruker Apex IV FTICR or Waters Synapt G2 ESI-MS instruments (positive mode). Trapped ion mobility data were measured on Bruker ESI-timsTOF. For calibration of the TIMS and TOF devices, Agilent ESI Tuning Mix was used. Signals in the NMR spectra and HRMS spectrum assigned to minor impurities are marked with an asterisk (*).

Single crystal X-ray diffraction data was collected at macromolecular beamline P11, Petra III, DESY, Germany, or on our in-house diffractometer Bruker D8 venture equipped with an INCOATEC microfocus sealed tube (Iμs 3.0) using CuK_α radiation at 100 K. For further details, see experimental section on X-ray crystallography in each chapter.

2.8.2. Synthesis of ligands A and C

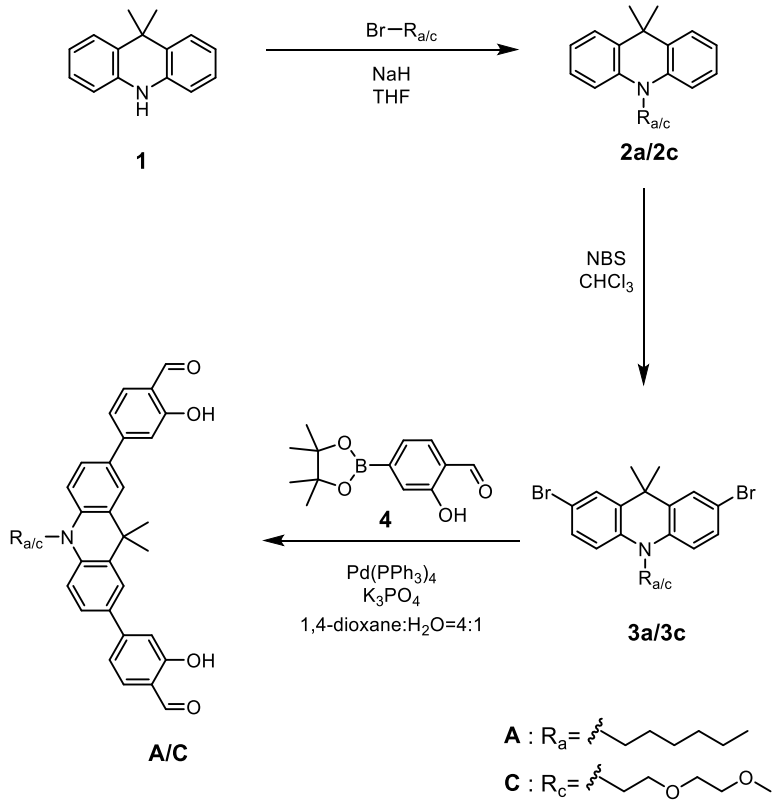

Scheme S2.1. Synthetic route to ligands **A** and **C**

*2.8.2.1 Synthesis of 10-hexyl-9,9-dimethyl-9,10-dihydroacridine (**2a**)*

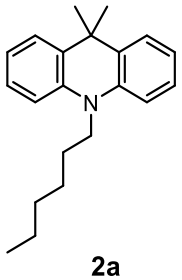

2a

A flame-dried Schlenk flask was charged with compound **1** (1.0 g, 4.78 mmol, 1.0 equiv.) and anhydrous THF (28 ml) under nitrogen atmosphere. Then NaH (344 mg, 14.34 mmol, 3.0 equiv. 60% dispersion in mineral oil) was added slowly. After stirring for 1 hour at room temperature, 1-bromohexane was added. The reaction was finished after heating at 65 °C for 48 h. The excess of NaH was quenched by addition of NH_4Cl (aq.) and the reaction mixture was extracted with dichloromethane (3 × 50 ml). Organic phases were combined and dried over Na_2SO_4. After evaporating the solvent under reduced pressure, the crude product was purified by column chromatography with DCM: Pentane = 1: 20 to provide 1.2 g of the product as a colorless solid (83% yield).

^{1}H NMR (500 MHz, CD_3CN) δ 7.42 (dd, *J* = 7.7, 1.6 Hz, 2H), 7.23 – 7.16 (m, 2H), 7.03 (dd, *J* = 7.9, 1.1 Hz, 2H), 6.97 – 6.91 (m, 2H), 3.93 (t, *J* = 7.5 Hz, 2H), 1.84 – 1.74 (m, 2H), 1.54 – 1.42 (m, 8H), 1.40 – 1.31 (m, 4H), 0.91 (t, *J* = 7.1 Hz, 3H).

^{13}C NMR (125 MHz, CH_3CN) δ 141.57, 133.00, 127.67, 125.35, 121.28, 113.69, 46.41, 36.90, 32.29, 29.13, 27.46, 26.67, 23.40, 14.3.

ESI-HRMS ($C_{21}H_{28}N+ H^+$): measured: 349.1681, calculated: 349.1699.

*2.8.2.2. Synthesis of 10-(2-(2-methoxyethoxy)ethyl)-9,9-dimethyl-9,10-dihydroacridine (**2c**)*

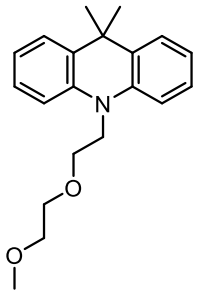

2c

Compound **2c** was synthesized following the same procedure as described for **2a**. Compound **1** (150 mg, 0.72 mmol) was used for the reaction. The crude product was purified by column chromatography with DCM: pentane = 1:1 to yield the product as a brown oil (176 mg, 79%).

^{1}H NMR (500 MHz, CD_3CN) δ 7.43 (dd, *J* = 7.8, 1.6 Hz, 2H), 7.24 – 7.16 (m, 2H), 7.09 (dd, *J* = 8.1, 1.1 Hz, 2H), 6.99 – 6.92 (m, 2H), 4.17 (t, *J* = 6.0 Hz, 2H), 3.82 (t, *J* = 6.1 Hz, 2H), 3.60 – 3.53 (m, 2H), 3.49 – 3.40 (m, 2H), 3.26 (s, 3H), 1.49 (s, 6H).

^{13}C NMR (125 MHz, CD_3CN) δ 141.87, 133.60, 127.63, 125.23, 121.61, 114.04, 72.60, 71.05, 68.35, 46.43, 37.03, 28.67.

ESI-HRMS ($C_{20}H_{25}NO_2+ H^+$): measured: 312.1956, calculated: 312.158.

*2.8.2.3. Synthesis of 2,7-dibromo-10-hexyl-9,9-dimethyl-9,10-dihydroacridine (**3a**)*

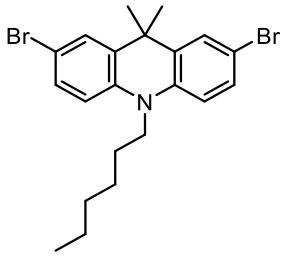

3a

Compound **2a** (500 mg, 1.70 mmol, 1.0 equiv.) and NBS (606.5 mg, 3.40 mmol. 2.0 equiv.) were dissolved in $CHCl_3$ (14 ml) and stirred for 3 h. Afterwards, the solvent was removed under reduced pressure and the residues were purified by column chromatography with pentane to yield the product as a colorless solid (667.3 mg, 87%).

^{1}H NMR (500 MHz, CD_3CN) δ 7.51 (d, *J* = 2.3 Hz, 2H), 7.33 (dd, *J* = 8.7, 2.3 Hz, 2H), 6.96 (d, *J* = 8.8 Hz, 2H), 3.87 (t, *J* = 7.9 Hz, 2H), 1.78 – 1.70 (m, 2H), 1.50 – 1.41 (m, 8H), 1.41 – 1.31 (m, 4H), 0.90 (t, *J* = 6.6 Hz, 3H).

^{13}C NMR (125 MHz, CD_3CN) δ 140.49, 134.98, 130.49, 128.28, 115.90, 113.51, 46.71, 37.30, 32.21, 28.86, 27.32, 26.36, 23.37, 14.30.

ESI-HRMS ($C_{21}H_{25}NBr_2 + H^+$): measured: 452.0370, calculated: 452.0407.

*2.8.2.4. Synthesis of 2,7-dibromo-10-(2-(2-methoxyethoxy)ethyl)-9,9-dimethyl-9,10-dihydroacridine (**3c**)*

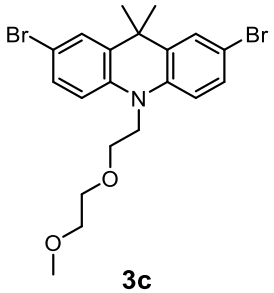

3c

Compound **3c** was synthesized following the same procedure as described for **3a**. Compound **2c** (176 mg, 0.57 mmol) was used for the reaction. The crude product was purified by column chromatography with DCM to yield the product as a brown oil (245 mg, 92%).

^{1}H NMR (500 MHz, CD_3CN) δ 7.53 (d, *J* = 2.4 Hz, 2H), 7.35 (dd, *J* = 8.7, 2.4 Hz, 2H), 7.04 (d, *J* = 8.7 Hz, 2H), 4.13 (t, *J* = 5.7 Hz, 2H), 3.79 (t, *J* = 5.7 Hz, 2H), 3.59 – 3.50 (m, 2H), 3.46 – 3.39 (m, 2H), 1.48 (s, 6H).

^{13}C NMR (125 MHz, CD_3CN) δ 140.72, 135.45, 130.30, 128.02, 116.26, 113.74, 72.42, 70.91, 67.96, 58.80, 46.63, 37.35, 28.18.%).

ESI-HRMS ($C_{20}H_{23}NO_2Br_2$ + Na^+): measured: 491.9964, calculated: 491.9968.

*2.8.2.5. Synthesis of 4,4'-(10-hexyl-9,9-dimethyl-9,10-dihydroacridine-2,7-diyl)bis(2-hydroxy-benzaldehyde) (ligand **A**)*

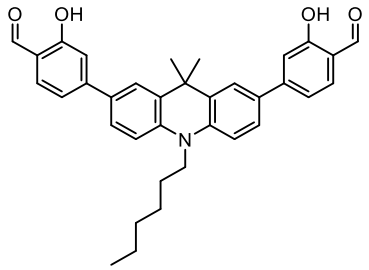

A

Compound **3a** (355 mg, 0.79 mmol, 1.0 equiv.), pinacol ester **4** (586 mg, 2.37 mmol, 3.0 equiv.), $Pd(PPh_3)_4$ (91 mg, 0.079 mmol, 10 mol%) and K_3PO_4 (663.4 mg, 2.84 mmol, 3.6 equiv.) were mixed in 32 ml of a 1,4-dioxane:H_2O = 4:1 mixture. The mixture was degassed (via freeze-thaw cycles) and then heated to 95 °C under N_2 atmosphere for 48 h. After cooling to room temperature, the solvent was removed under vacuum. Aqueous HCl (2M, 50 ml) was added and the mixture extracted with $CHCl_3$ (3 × 30ml), organic phases combined and dried over Na_2SO_4. The solvent was removed under reduced pressure. The crude product was purified by column chromatography ($CHCl_3$: Pentane = 2:1) to provide the product as a bright yellow solid (227 mg, 54 % yield).

^{1}H NMR (500 MHz, CD_2Cl_2) δ 11.15 (s, 2H), 9.90 (s, 2H), 7.77 (d, *J* = 2.4 Hz, 2H), 7.63 (d, *J* = 8.1 Hz, 2H), 7.58 (dd, *J* = 8.6, 2.3 Hz, 2H), 7.32 (dd, *J* = 8.2, 1.8 Hz, 2H), 7.24 (d, *J* = 1.8 Hz, 2H), 7.11 (d, *J* = 8.6 Hz, 2H), 4.01 (t, *J* = 8.0 Hz, 2H), 1.95 – 1.82 (m, 2H), 1.65 (s, 6H), 1.46 1.35 (m, 4H), 0.94 (t, *J* = 7.0 Hz, 3H).

^{13}C NMR (126 MHz, CD_2Cl_2) δ 196.48, 162.57, 150.09, 141.37, 134.72, 133.02, 131.65, 126.43, 124.36, 119.67, 118.59, 114.80, 113.86, 46.87, 37.05, 32.14, 29.96, 27.36, 26.53, 23.28, 14.37.

ESI-HRMS ([$C_{35}H_{36}NO_4$+ H^+): measured: 534.2631, calculated: 534.2639.

*2.8.2.6. Synthesis of 4,4'-(10-(2-(2-methoxyethoxy)ethyl)-9,9-dimethyl-9,10-dihydroacridine-2,7-diyl)bis(2-hydroxybenzaldehyde) (ligand **C**)*

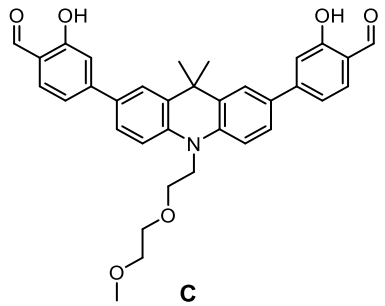

C

Ligand **C** was synthesized following the same procedure as described for Ligand **A**. Compound **3c** (102 mg, 0.57 mmol) was used for the reaction. The crude product was purified by column chromatography with $CHCl_3$: EtOAc= 40:1 to yield the product as a yellow solid (37.9 mg, 32 %).

^{1}H NMR (500 MHz, CD_2Cl_2) δ 11.15 (s, 1H), 9.90 (s, 1H), 7.76 (d, *J* = 2.3 Hz, 1H), 7.64 (d, *J* = 8.1 Hz, 1H), 7.57 (dd, *J* = 8.5, 2.3 Hz, 1H), 7.32 (dd, *J* = 8.0, 1.7 Hz, 1H), 7.24 (d, *J* = 1.7 Hz, 1H), 7.19 (d, *J* = 8.6 Hz, 1H), 4.29 (t, *J* = 6.3 Hz, 1H), 3.92 (t, *J* = 6.3 Hz, 1H), 3.68 – 3.62 (m, 1H), 3.57 – 3.48 (m, 1H), 3.34 (s, 2H), 1.66 (s, 3H).

^{13}C NMR (126 MHz, CD_2Cl_2) δ 196.51, 162.57, 150.06, 141.57, 134.73, 133.39, 132.05, 126.45, 124.32, 119.72, 118.65, 114.90, 114.21, 72.53, 71.21, 68.07, 59.27, 46.65, 37.13, 29.71.

ESI-HRMS ([$C_{34}H_{34}NO_6$+ H^+): measured: 552.2370, calculated: 552.2381.

2.8.3 Synthesis of banana-shaped ligands B and E

*2.8.3.1. Synthesis of 3,3'-(9,9-dimethyl-9H-fluorene-2,7-diyl)dipyridine (ligand **B**)*

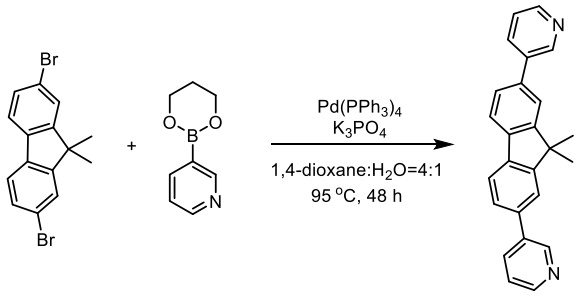

5 **6** **B**

Compound **5** (200 mg, 0.57 mmol, 1.0 equiv.), compound **6** (277 mg, 1.71 mmol, 3.0 equiv.), $Pd(PPh_3)_4$ (39 mg, 0.034 mmol, 6 mol%) and K_3PO_4 (436 mg, 2.05 mmol, 3.6 equiv.) were mixed in 15 ml of a 1,4-

dioxane : H_2O = 4 : 1 mixture. The mixture was degassed (via freeze-thaw cycles) and then heated to 95 °C under N_2 atmosphere for 48 h. After cooling to room temperature, the solvent was removed under vacuum. Water (30 ml) was added and the mixture was extracted with EtOAc (3 × 20 ml), organic phases combined and dried over Na_2SO_4. The solvent was removed under reduced pressure. The crude product was purified by column chromatography (EtOAc) and then further purified by GPC to provide the product as a light brown solid (104 mg, 52 % yield).

^{1}H NMR (500 MHz, CH_3CN) δ 8.95 (dd, *J* = 2.5, 0.9 Hz, 2H), 8.57 (dd, *J* = 4.8, 1.6 Hz, 2H), 8.11 – 8.04 (m, 2H), 7.94 (dd, *J* = 7.9, 0.7 Hz, 2H), 7.87 (dd, *J* = 1.7, 0.6 Hz, 2H), 7.70 (dd, *J* = 7.9, 1.7 Hz, 2H), 7.48 – 7.41 (m, 2H), 1.59 (s, 6H)

^{13}C NMR (126 MHz, CD_3CN) δ 156.09, 149.48, 149.13, 139.45, 138.21, 137.45, 135.17, 127.36, 124.69, 122.64, 121.97, 48.16, 27.25.

ESI-HRMS ($C_{25}H_{20}N_2$+ H^+): measured: 349.1681, calculated: 349.1699.

*2.8.3.2. Synthesis of 10-hexyl-9,9-dimethyl-2,7-bis(3-(pyridin-4-yl)phenyl)-9,10-dihydroacridine (ligand **E**)*

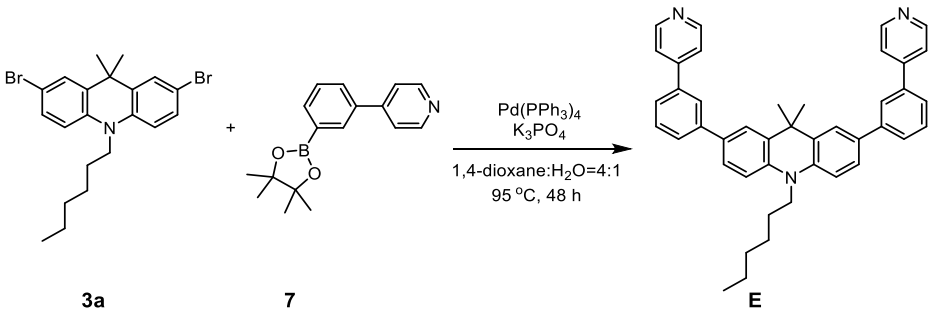

3a **7** **E**

Compound **3a** (100 mg, 0.22 mmol, 1.0 equiv.), compound **7** (149 mg, 0.53 mmol, 2.4 equiv.), $Pd(PPh_3)_4$ (15.25 mg, 13.2 µmmol, 6 mol%) and K_3PO_4 (168 mg. 0.79 mmol, 3.6 equiv.) were placed in a flame-dried Schlenk flask, which was charged with 12.5 ml of a 1,4-dioxane : H_2O = 4 : 1 mixture. After degassing (via freeze-thaw cycles), the mixture was heated to 95 °C for 48 h. Then the solvent was removed under vacuum. Afterwards, water (30 ml) was added and the mixture was extracted with DCM (3 × 30 ml). The organic phases were combined and dried over Na_2SO_4. The solvent was removed under reduced pressure. The crude product was purified by column chromatography (MeOH : $CHCl_3$ = 1 : 40) and then further purified by GPC to provide the product as a light-yellow solid (74 mg, 56 % yield).

^{1}H NMR (500 MHz, CD_3CN) δ 8.65 (br, 4H), 7.99 (s, 2H), 7.82 (d, *J* = 2.0 Hz, 2H), 7.75 (d, *J* = 7.1 Hz, 2H), 7.71 (d, *J* = 5.8 Hz, 4H), 7.67 (d, *J* = 8.2 Hz, 2H), 7.63 – 7.54 (m, 4H), 7.18 (d, *J* = 8.6 Hz, 2H), 4.03 (t, 2H), 1.91 – 1.81 (m, 2H), 1.67 (s, 6H), 1.58 – 1.48 (m, 2H), 1.47 – 1.32 (m, 4H), 0.93 (t, *J* = 6.9 Hz, 3H).

^{13}C NMR (125 MHz, CD_3CN) δ 151.27, 148.93, 142.91, 140.98, 139.59, 133.44, 133.37, 130.65, 128.17, 126.56, 126.16,125.98, 124.54, 122.71, 114.37, 46.64, 37.40, 32.33, 29.74, 27.43, 26.75, 23.43, 14.35.

ESI-HRMS ($C_{43}H41N_3$+ H^+): measured: 600.3392, calculated: 600.3373.

2.8.4 Synthesis of macrocycle A_2 and ligand A'

2.8.4.1. Synthesis of macrocycle ***A***$_2$

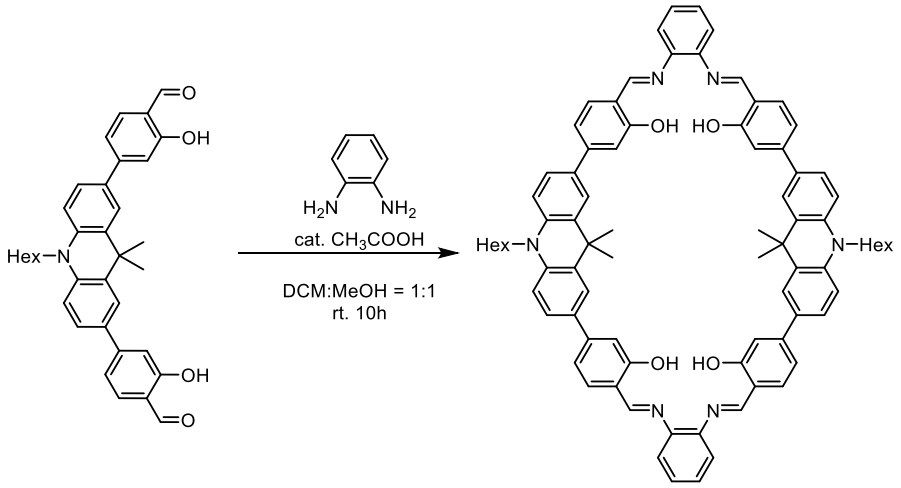

A **A_2**

Ligand **A** (10 mg**,** 0.019 mmol**,** 1.0 equiv.) and 1,2-benzenediamine (2.4 mg. 0.038 mmol, 1.2 equiv.) were dissolved in 2ml DCM : MeOH = 1 : 1. After addition of CH_3COOH (40 µl), the reaction was stirred at room temperature for 10 h. Then, the solvent was removed under reduced pressure. The residue was washed with anhydrous methanol (3 × 1 ml) and dried in high vacuum to provide the product as an orange powder in quantitative yield.

^{1}H NMR (500 MHz, CD_2Cl_2) δ 13.36 (s, 2H), 8.68 (s, 2H), 7.80 (d, *J* = 2.4 Hz, 2H), 7.52 (d, *J* = 8.9 Hz, 2H), 7.44 (d, *J* = 7.9 Hz, 2H), 7.35 – 7.24 (m, 6H), 7.18 (d, *J* = 8.2 Hz, 2H), 7.02 (d, *J* = 8.5 Hz, 2H), 3.94 (t, *J* = 7.0 Hz, 2H), 1.87 – 1.78 (m, 2H), 1.64 (s, 6H), 1.38 – 1.27 (m, 4H), 0.87 (t, *J* = 7.0 Hz, 3H).

^{13}C NMR (125 MHz, CD_2Cl_2) δ 163.29, 162.34, 146.65, 143.29, 140.91, 133.35, 133.14, 132.29, 128.32, 125.84, 124.68, 119.64, 118.37, 117.69, 114.91, 113.51, 46.79, 37.14, 32.18, 30.24, 27.40, 26.51, 23.31, 14.39.

ESI-HRMS ($C_{82}H_{78}N_6O_4$ + Na^+): measured: 1233.5960, calculated: 1233.5977.

*2.8.4.2. Synthesis of half-macrocycle **A'***

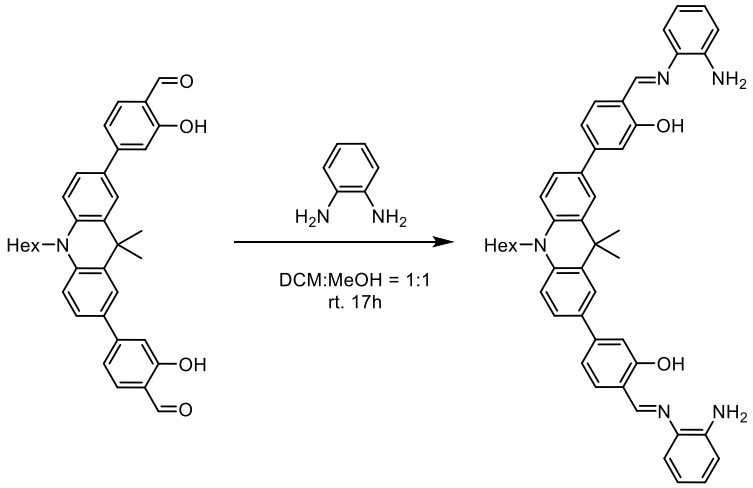

A **A'**

Ligand **A** (2.0 mg, 3.7 µmol**,** 1.0 equiv.) and 1,2-benzenediamine (2.2 mg. 0.020 mmol, 5.3 equiv.) were dissolved in 1 ml DCM : MeOH = 1 : 1. After stirring at room temperature for 17 h, the solvent was removed under reduced pressure. The residue was washed with anhydrous methanol (3 × 1 ml) and dried in high vacuum to provide the product as a light orange powder in quantitative yield.

^{1}H NMR (500 MHz, CD_2Cl_2) δ 13.10 (s, 2H), 8.68 (s, 2H), 7.79 (d, *J* = 2.4 Hz, 2H), 7.58 (dd, *J* = 9.0, 2.4 Hz, 2H), 7.50 (d, *J* = 7.9 Hz, 2H), 7.31 – 7.24 (m, 4H), 7.14 – 7.06 (m, 6H), 6.86 – 6.74 (m, 4H), 4.05 (d, *J* = 18.5 Hz, 4H), 4.01 (d, *J* = 7.9 Hz, 2H), 1.96 – 1.86 (m, 2H), 1.67 (s, 6H), 1.48 – 1.37 (m, 4H), 0.95 (t, *J* = 6.9 Hz, 3H).

^{13}C NMR (126 MHz, CD_2Cl_2) δ 162.17, 161.73, 146.25, 141.69, 140.94, 135.97, 133.24, 132.96, 132.27, 128.51, 126.10, 124.12, 119.21, 118.79, 118.62, 117.95, 116.19, 114.58, 113.69, 46.81, 37.07, 32.17, 29.99, 27.40, 26.55, 23.30, 14.39.

ESI-HRMS ($C_{47}H_{48}N_5O_2$+ H^+): measured: 714.3808, calculated: 714.3803.

2.8.5. Self-assembly of multicomponent cages

2.8.5.1. Self-assembly of cage $[Co_2\boldsymbol{A}_2\boldsymbol{E}_2]^{2+}$

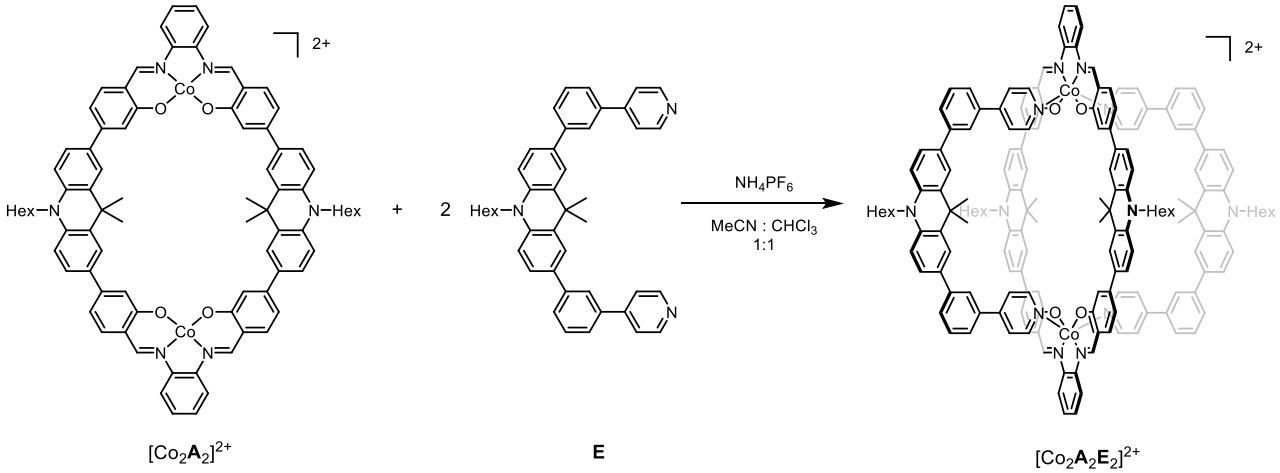

Macrocycle $\boldsymbol{A}_2$ (4.00 mg 3.30 µmol, 1.0 equiv.), combined with Co(acetate)$_2$ (1.17 mg, 6.60 µmol, 2.0 equiv.), was dissolved in a mixture of $CHCl_3$: CH_3CN = 1 : 1 (4 ml) under air atmosphere. After reacting for 15 min at room temperature, banana-shaped ligand **E** (3.96 mg, 6.60 µmol, 2.0 equiv.) was added and the mixture was stirred at 60 °C overnight. Subsequently, after addition of NH_4PF_6 (0.64 mg, 3.90 µmol, 2.0 equiv.), the mixture was heated at 60 °C for one more hour. Afterwards, the reaction was cooled to room temperature and the solvent was removed under reduced pressure. The crude product was dissolved in a minimal amount of DCM and precipitated with Et_2O to give 9.3 mg (90% yield) of the product as a dark red solid.

^{1}H NMR (500 MHz, CD_2Cl_2) δ 8.69 (s, 4H, H_3), 8.31 (dd, *J* = 6.3, 3.5 Hz, 4H, H_2), 8.27 (d, *J* = 6.3 Hz, 8H, H_A), 8.01 (d, *J* = 2.1 Hz, 4H, H_8), 7.85 (s, 4H, H_9), 7.82 (s, 4H, H_I), 7.69 (dd, *J* = 6.2, 3.5 Hz, 4H, H_1), 7.66 – 7.59 (m, 16H, H_E, H_B, H_H), 7.55 (d, *J* = 8.1 Hz, 4H, H_6), 7.53 – 7.43 (m, 16H, H_4, H_D, H_C, H_F), 7.12 – 7.01 (m, 12H, H_7, H_5, H_G), 3.99 (t, *J* = 7.8 Hz, 4H, H_{10}), 3.92 (t, *J* = 8.1 Hz, 4H, H_J), 1.85 – 1.79 (m, 8H, CH_2), 1.69 (s, 12H, methyl groups from $\boldsymbol{A}_2$ ring), 1.61 (s, 12H, methyl groups from ligand **E**), 1.46 (br, 16H CH_2), 1.36 – 1.29 (m, 8H, CH_2), 0.88 (m, 12H, CH_3).

ESI-HRMS $[C_{168}H_{156}N_{12}O_4Co_2]^{2+}$: measured: 1262.0557, calculated: 1262.0529.

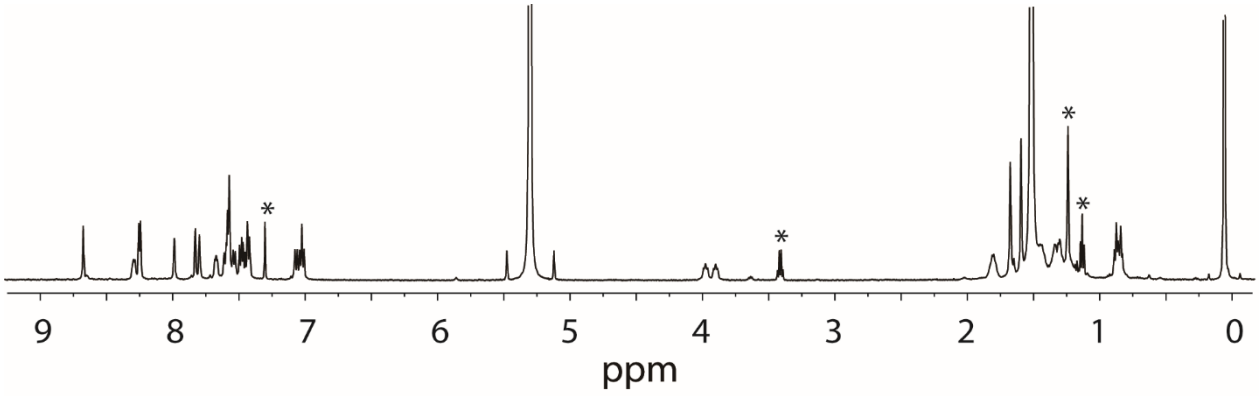

Figure S2.2. ^{1}H NMR spectrum (500 MHz/CD_2Cl_2) of cage $[Co_2\mathbf{A}_2\mathbf{E}_2]^{2+}$.

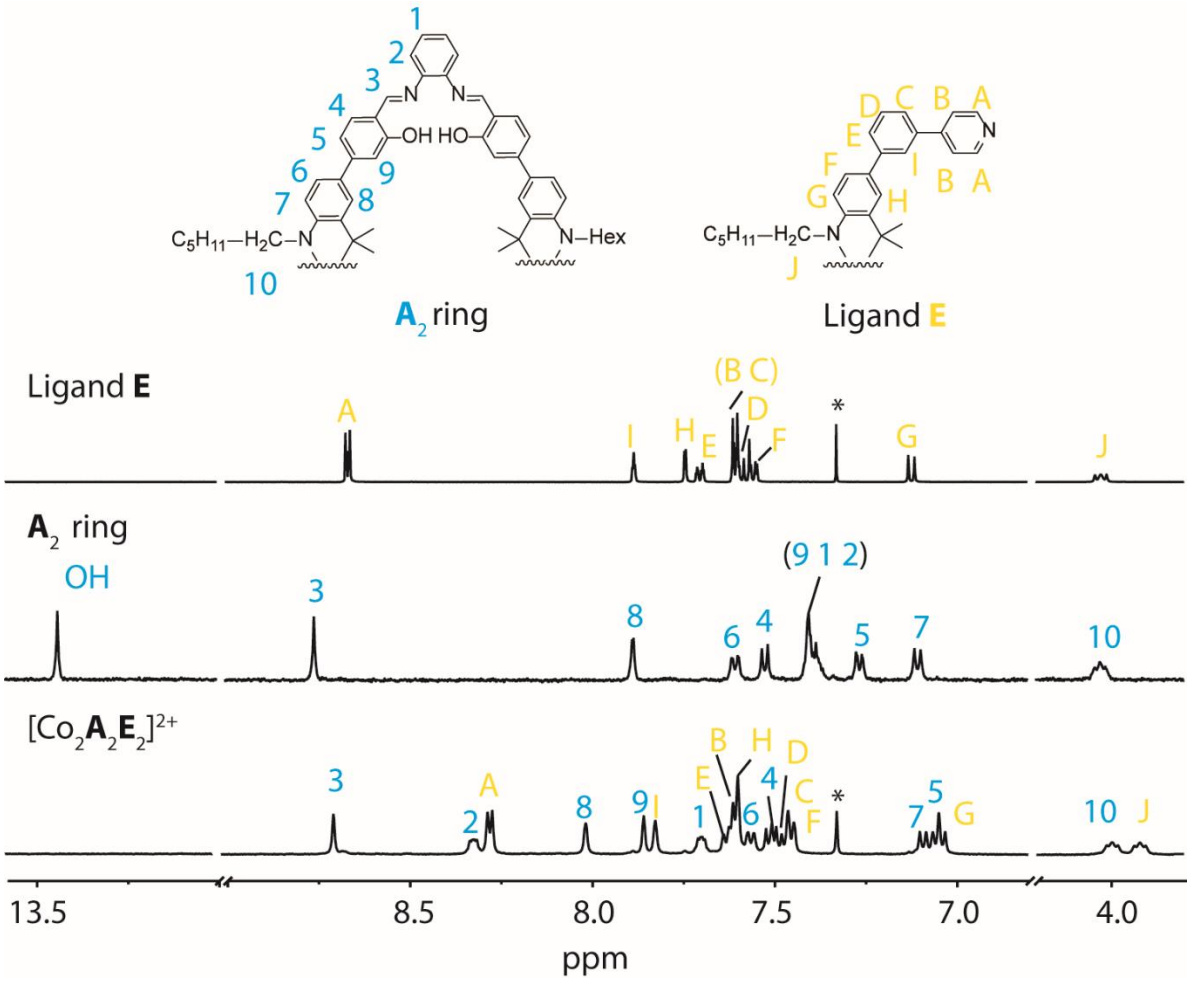

Figure S2.3. Partial ^{1}H NMR spectrum (500 MHz/CD_2Cl_2) of cage $[Co_2\mathbf{A}_2\mathbf{E}_2]^{2+}$ compared with spectra of free ligand **E** and macrocycle $\mathbf{A}_2$.

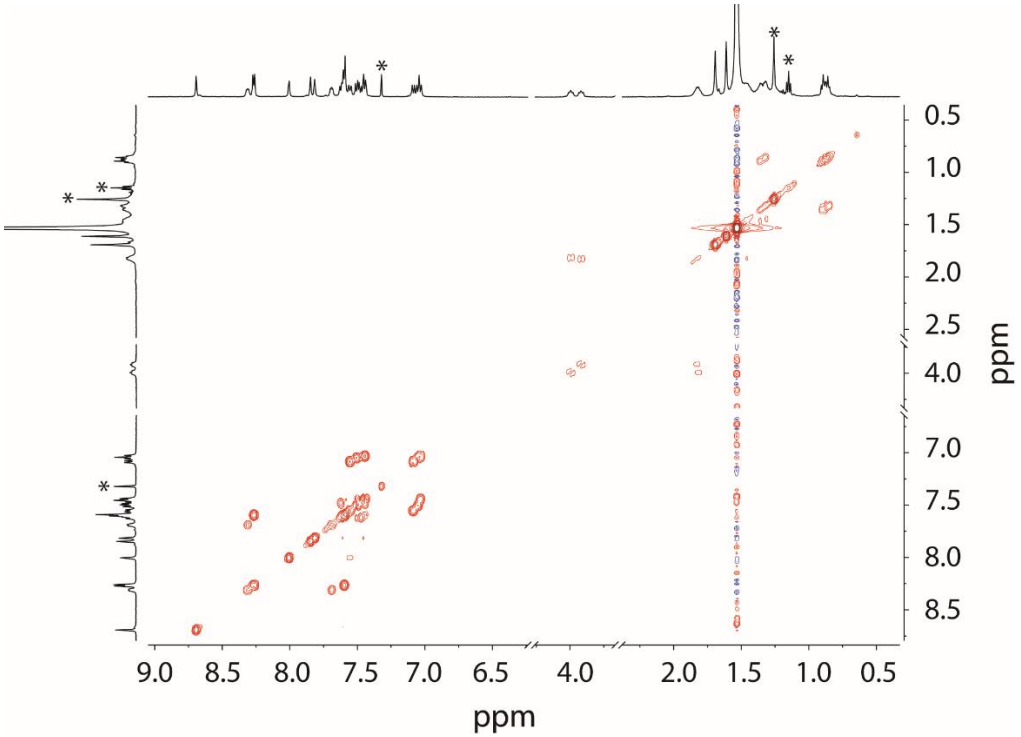

Figure S2.4. ^{1}H-^{1}H COSY spectrum (500 MHz/CD_2Cl_2) of cage $[Co_2\mathbf{A}_2\mathbf{E}_2]^{2+}$.

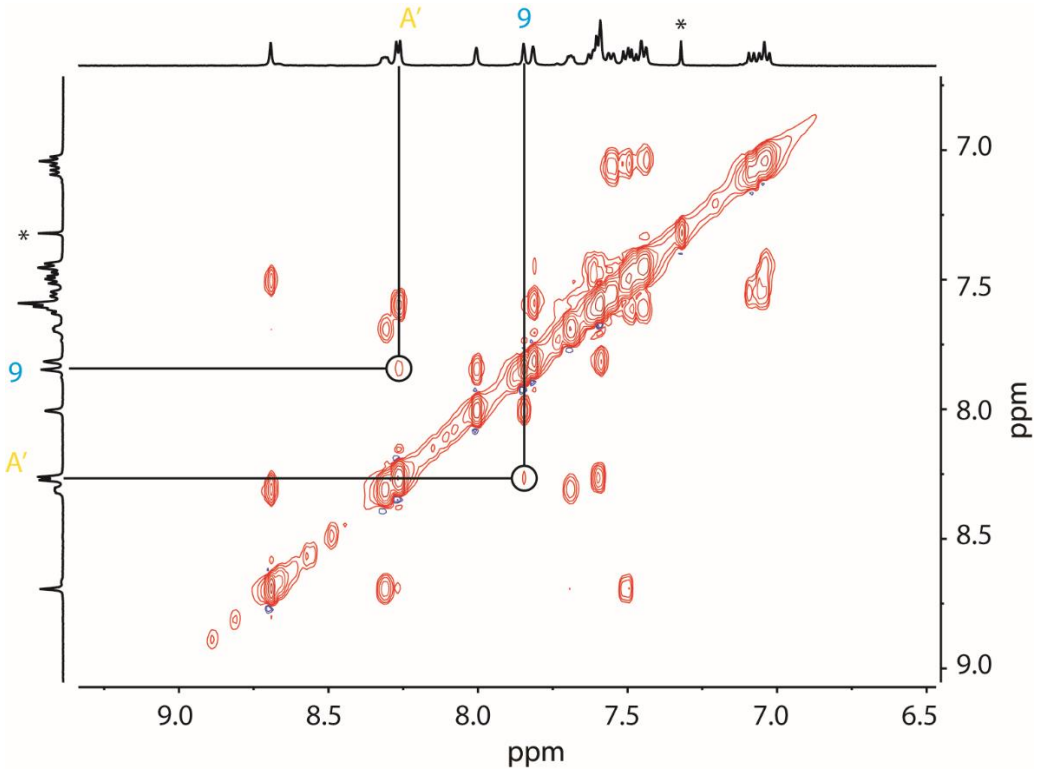

Figure S2.5. Partial ^{1}H-^{1}H NOESY spectrum (500 MHz/CD_2Cl_2) of cage $[Co_2\mathbf{A}_2\mathbf{E}_2]^{2+}$.

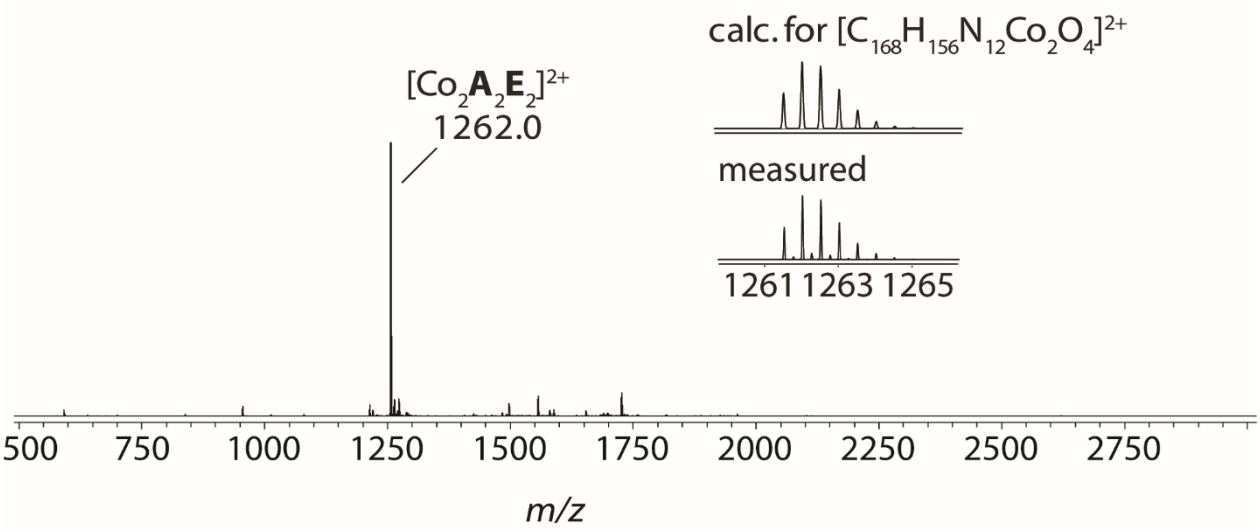

Figure S2.6. ESI mass spectrum of cage $[Co_2\mathbf{A}_2\mathbf{E}_2]^{2+}$.

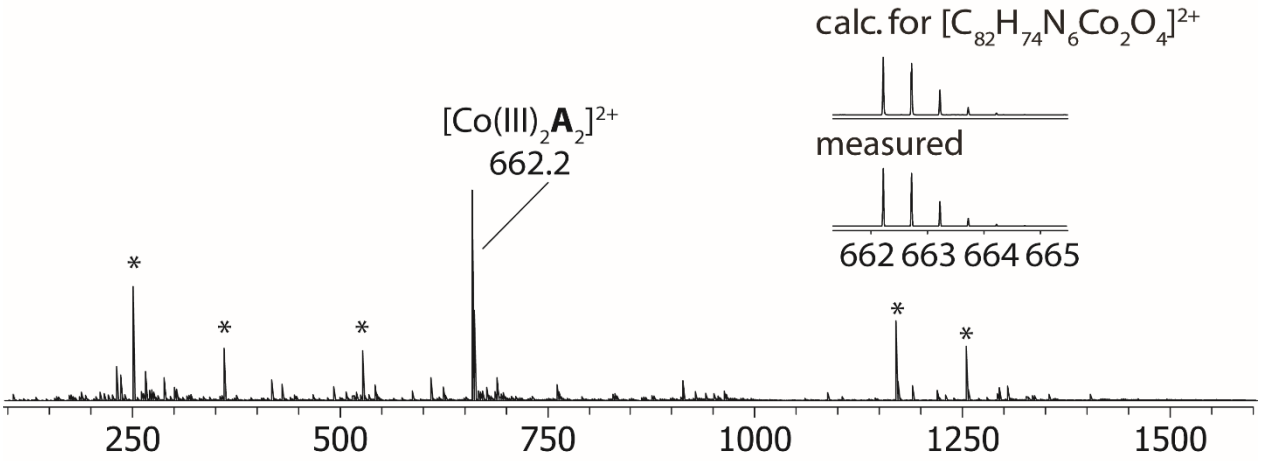

Figure S2.7. ESI mass spectrum measured before addition of ligand **E**. A prominent signal assigned to $[Co(III)_2\mathbf{A}_2]^{2+}$ is observed.

2.8.5.2 Self-assembly of cage $[Co_2\mathbf{A}_2\mathbf{BD}]^{2+}$

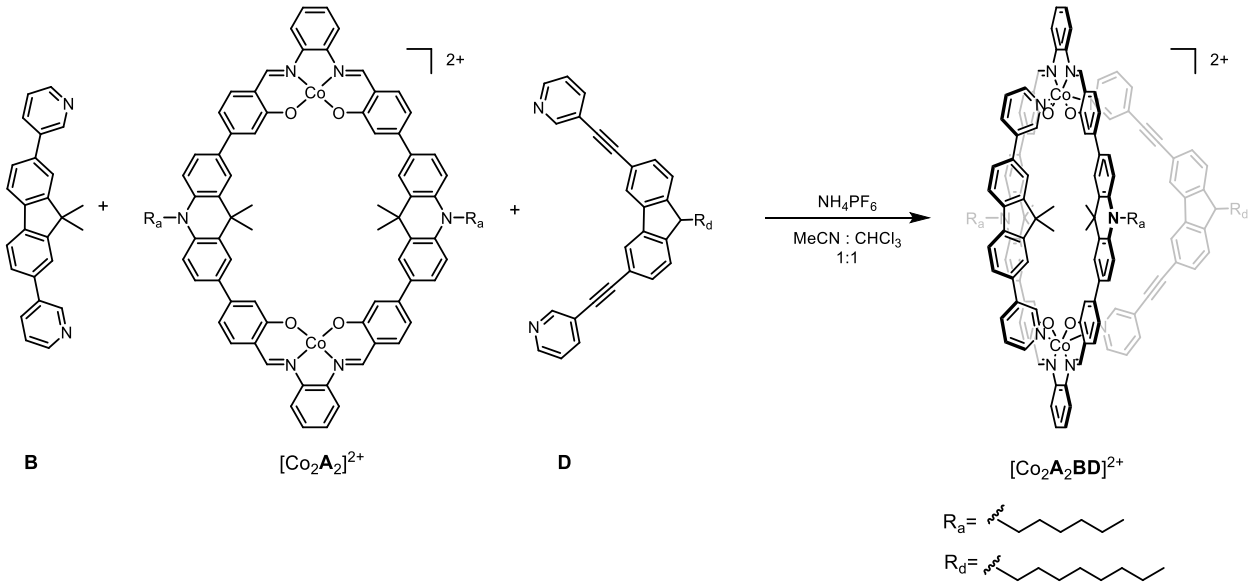

Macrocycle $\mathbf{A}_2$ (2.36 mg, 1.95 µmol, 1.0 equiv.), combine with $Co(acetate)_2$ (0.69 mg, 3.90 µmol, 2.0 equiv.), was dissolved in a mixture of $CHCl_3$: CH_3CN = 1 : 1 (2 ml) under air atmosphere. After reacting for 15 min at room temperature, banana-shaped ligands **B** (0.82 mg, 2.30 µmol, 1.2 equiv.) and **D** (1.42 mg, 2.93 µmol, 1.5 equiv.) were added and the mixture stirred at 60 °C for 24 h. After addition of NH_4PF_6 (0.64 mg, 3.90 µmol, 2.0 equiv.), the mixture was heated at 60 °C for one more hour. Afterwards, the reaction was cooled to room temperature and the solvent was removed under reduced pressure. The crude product was dissolved in DCM and filtrated to remove the undissolved residues. The solvent was evaporated under vacuum. Subsequently, the dark red solid was then again dissolved in a minimal amount of DCM and precipitated with Et_2O, this step was repeated for three to four times to provide 3.77 mg (79% yield) of the product as dark red powder.

^{1}H NMR (500 MHz, CD_2Cl_2) δ 9.56 (s, 2H, H_a), 9.39 (s, 2H, H_I), 8.64 (s, 4H, H_3), 8.51 (s, 2H, H_{VII}), 8.42 (d, *J* = 5.0 Hz, 4H, H_2), 7.93 (d, *J* = 7.7 Hz, 2H, H_{IV}), 7.84 – 7.81 (m, 16H, H_d, H_8, H_9, H_1, H_g), 7.75 – 7.74 (m, 4H, H_f, H_V), 7.49 – 7.46 (m, 6H, H_6, H_{VI}), 7.44 – 7.35 (m, 10H, H_{II}, H_4, H_e, H_b), 7.09 – 7.03 (m, 8H, H_{III}, H_7, H_c), 7.00 (d, *J* = 8.1 Hz, 4H, H_5), 4.31 (t, *J* = 8.7 Hz, 2H, H_{IX}), 3.98 (t, *J* = 8.3 Hz, 4H, H_{10}), 1.86 (s, 6H, methyl groups from $\mathbf{A}_2$ ring), 1.84 – 1.77 (m, 6H, CH_2), 1.75 (s, 6H, methyl groups from ligand **B**), 1.44 – 1.42 (m, 4H, CH_2), 1.33 – 1.26 (m, 16H, CH_2), 1.21 (s, 6H, methyl groups from $\mathbf{A}_2$ ring), 1.20 – 1.18 (m, 2H, CH_2), 0.86 (t, *J* = 7.1 Hz, 6H, CH_3), 0.82 (t, *J* = 7.1 Hz, 3H, CH_3).

ESI-HRMS $[C_{141}H_{125}N_{11}O_4Co_2]^{2+}$: measured: 1077.4304, calculated: 1077.4301.

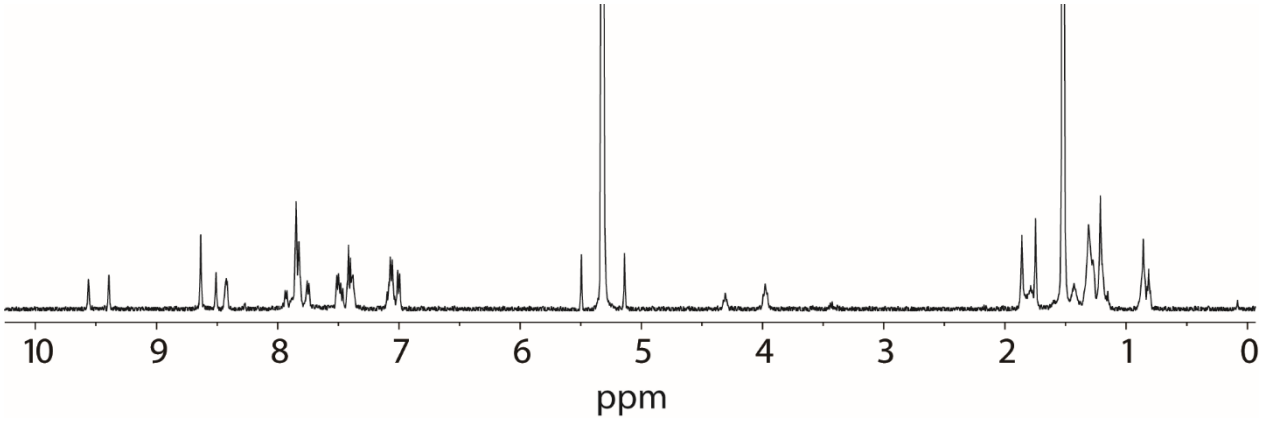

Figure S2.8. ^{1}H NMR spectrum (500 MHz/CD_2Cl_2) of cage $[Co_2\mathbf{A}_2\mathbf{BD}]^{2+}$.

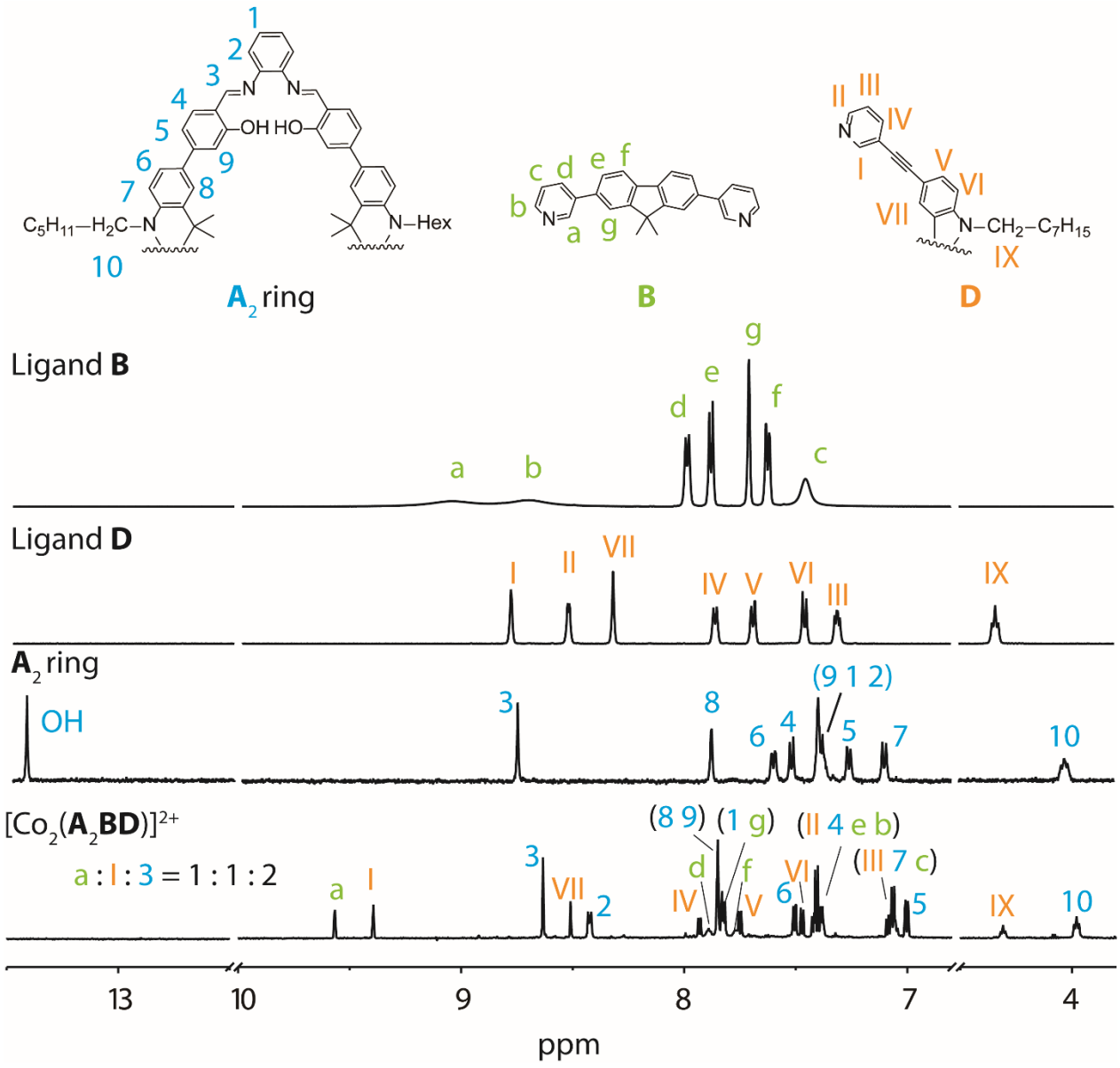

Figure S2.9. Partial ^{1}H NMR spectrum (700 MHz/CD_2Cl_2) of cage $[Co_2\mathbf{A}_2\mathbf{BD}]^{2+}$ compared with free ligand **B**, **D** and macrocycle $\mathbf{A}_2$ (500 MHz/CD_2Cl_2).

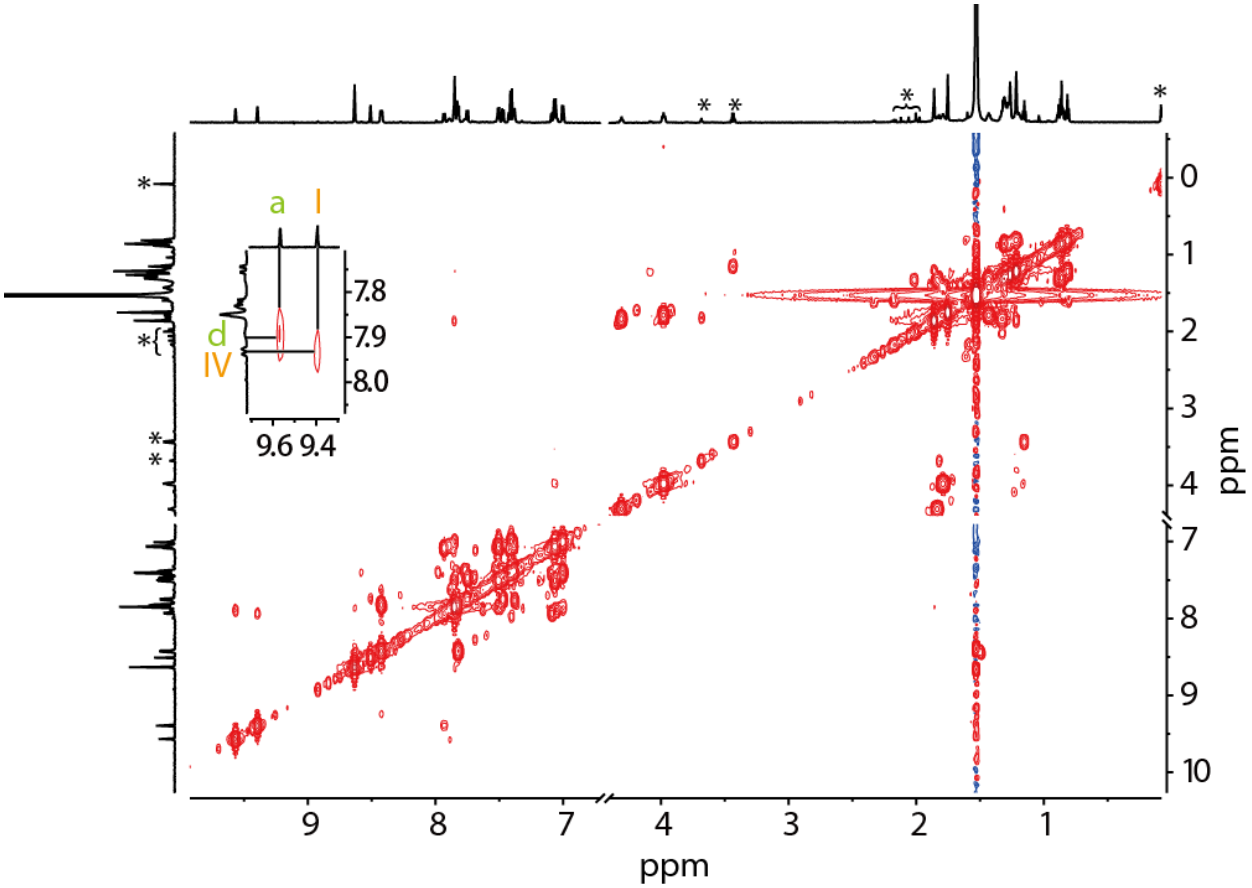

Figure S2.10. ^{1}H-^{1}H COSY spectrum (700 MHz/CD_2Cl_2) of cage $[Co_2\mathbf{A}_2\mathbf{BD}]^{2+}$.

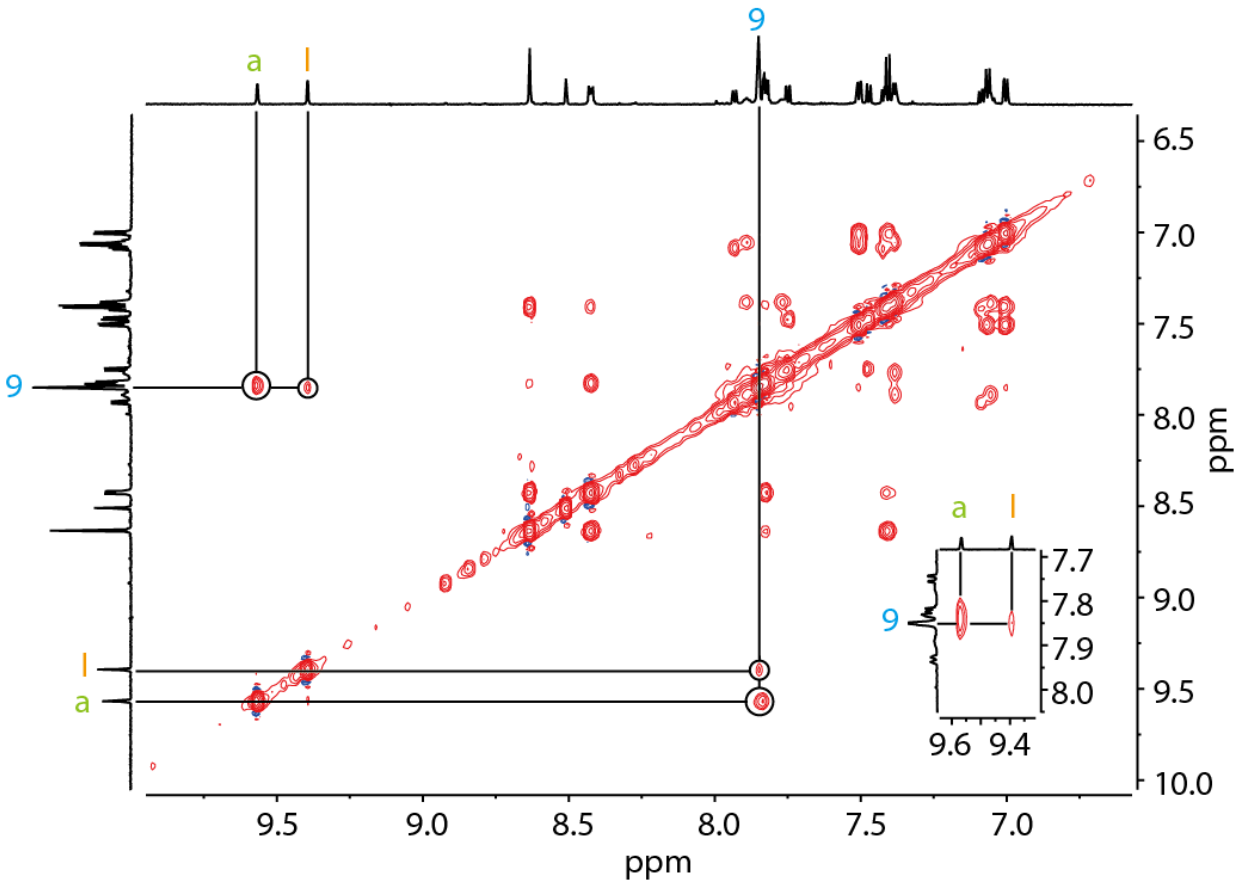

Figure S2.11. Partial ^{1}H-^{1}H NOESY spectrum (700 MHz/CD_2Cl_2) of cage $[Co_2\mathbf{A}_2\mathbf{BD}]^{2+}$.

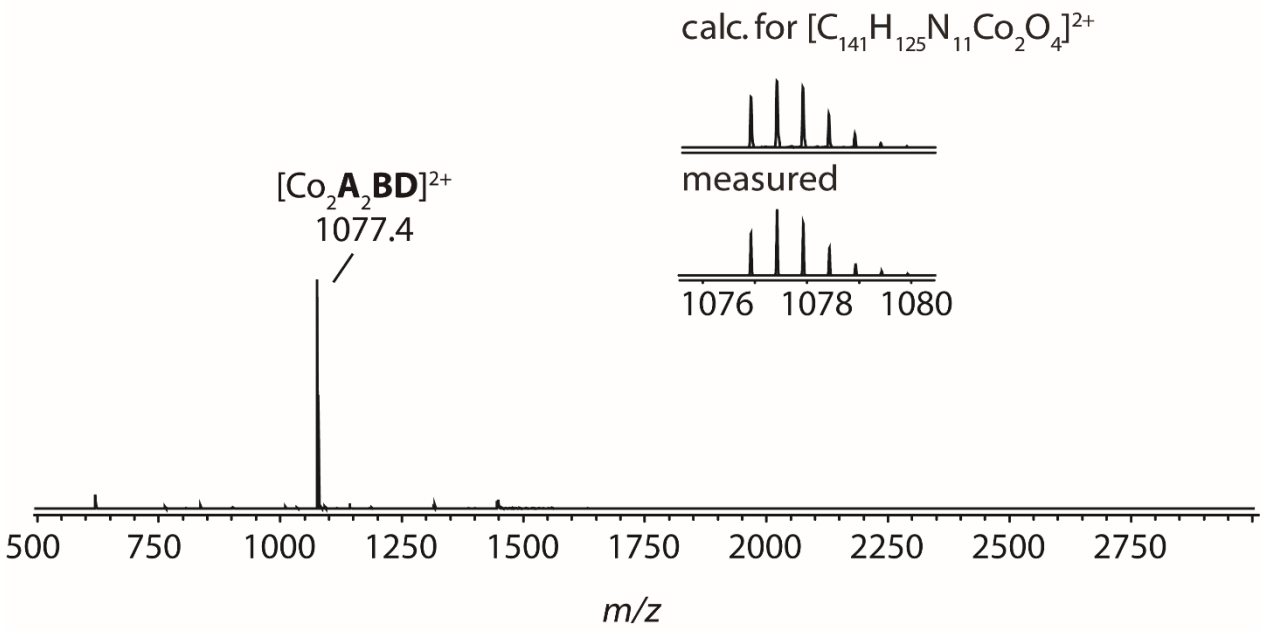

Figure S2.12. ESI mass spectrum of cage $[Co_2\mathbf{A}_2\mathbf{BD}]^{2+}$.

*2.8.5.3. Self-assembly of cage [Co_2**ABCD**]$^{2+}$*

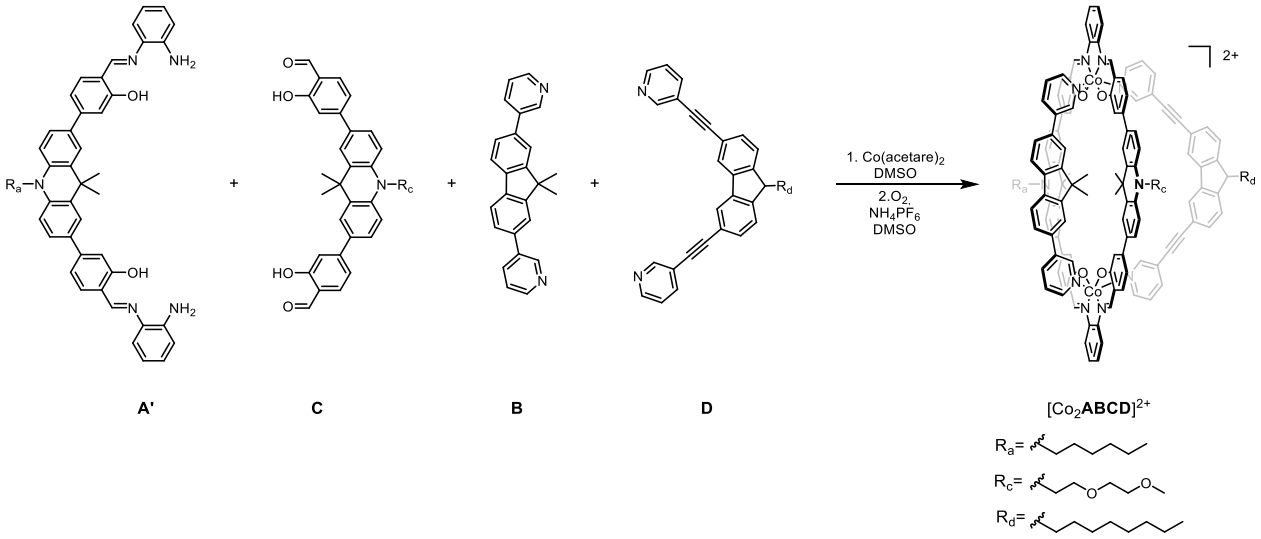

Method 1.

Ligand fragments **A'** (4.19 mg, 5.87 µmol, 1.0 equiv.) and **C** (3.24m mg, 5.87 µmol, 1.0 equiv.) as well as Co(II)(acetate)$_2$ (2.09 mg, 11.75 µmol, 2.0 equiv.) were dissolved in DMSO (2 ml). After stirring at 60 °C overnight, banana-shaped ligands **B** (2.47 mg, 7.04 µmol, 1.2 equiv.) and **D** (4.26 mg, 8.81 µmol, 1.5 equiv.) were added and the mixture stirred under air atmosphere at 90 °C for 24 h. Then, NH_4PF_6 (1.91 mg, 11.75 µmol, 2.0 equiv.) was added and the mixture was heated to 90 °C for one more hour until the color of the solution turned from brown to dark red. After cooling to room temperature, DCM (2 ml) was added and the crude product was collected by precipitation with pentane (10 ml). The solid was then dissolved in DCM and undissolved residues were removed by filtration. The solvent was evaporated under reduced pressure. Afterwards, the dark red solid was then again dissolved in a minimal amount of DCM and precipitated with pentane, this step was repeated for three to four times. The precipitate was collected and dried in high vacuum to provide 7.38 mg (52% yield) of the product as a dark red powder.

Method 2.

Ligand fragments **A'** (2 mg, 2.80 µmol, 1.0 equiv.), **C** (1.55 mg, 2.80 µmol, 1.0 equiv.), **B** (1.18 mg, 3.36 µmol, 1.2 equiv.), and **D** (2.03 mg, 4.20 µmol, 1.5 equiv.) were mixed in 2 ml DMSO. After addition of Co(acetate)$_2$ (1.00 mg, 5.60 µmol, 2.0 equiv.), the mixture was stirred under Argon atmosphere for 12 h at 60 °C. Subsequently, NH_4PF_6 (0.91 mg, 5.60 µmol, 2.0 equiv.) was added and the reaction was stirred in air for one more hour. After cooling to room temperature, a saturated aqueous KPF_6 solution was given to the reaction mixture. The precipitate was collected by centrifugation and redissolved in DCM. Undissolved residues were removed by filtration. The solvent was evaporated under reduced

pressure. The dark red solid was then again dissolved in a minimal amount of DCM and precipitated with pentane. This step was repeated three times to provide 3.93 mg (57%) dark red powder as the target product.

^{1}H NMR (700 MHz, CD_2Cl_2) δ 9.56 (d, *J* = 2.1 Hz, 2H, H_a), 9.39 (d, *J* = 1.9 Hz, 2H, H_I), 8.62 (d, *J* = 4.8 Hz, 4H, $H_{3+3'}$), 8.51 (s, 2H, H_{VII}), 8.41 (dd, *J* = 5.8, 3.8 Hz, 4H, $H_{2+2'}$), 7.95 – 7.92 (m, 2H, H_{IV}), 7.90 (d, *J* = 7.5 Hz, 2H, H_d), 7.86 – 7.84 (m, 8H, $H_{8+8'}$, $H_{9+9'}$), 7.83 – 7.81 (m, 6H, $H_{1+1'}$, H_g), 7.79 – 7.74 (m, 4H, H_f, H_V), 7.50 (d, *J* = 8.2 Hz, 4H, $H_{6+6'}$), 7.47 (d, *J* = 8.6 Hz, 2H, H_{VI}), 7.43 – 7.38 (m, 10H, H_{II}, $H_{4+4'}$, H_e, H_b), 7.13 (d, *J* = 8.4 Hz, 2H, $H_{7'}$), 7.10 – 7.05 (m, 6H,H_{III}, H_7, H_c), 7.00 (dd, *J* = 7.1, 2.0 Hz, 4H, $H_{5+5'}$), 4.31 (t, *J* = 6.9 Hz, 2H, H_{IX}), 4.25 (t, *J* = 6.1 Hz, 2H, H_{C1}), 3.98 (t, *J* = 7.7 Hz, 2H, H_{10}), 3.82 (t, *J* = 6.0 Hz, 2H, H_{C2}), 3.51 (t, *J* = 7.7 Hz, 2H, H_{C3}), 3.41 (t, *J* = 7.7 Hz, 2H, H_{C4}), 3.23 (s, 3H, H_{C5}), 1.87 (d, *J* = 21.5 Hz, 6H, methyl groups from **AC** ring), 1.84 – 1.77 (m, 4H, CH_2), 1.75 (d, *J* = 16.3 Hz, 6H, methyl groups from ligand **B**), 1.45 – 1.41 (m, 2H, CH_2), 1.37 – 1.25 (m, 12H, CH_2), 1.23 – 1.18 (m, 8H, CH_2, methyl groups from **AC** ring), 0.87 (t, *J* = 7.0 Hz, 3H, CH_3), 0.82 (t, *J* = 7.1 Hz, 3H, CH_3).

ESI-HRMS $[C_{140}H_{123}N_{11}O_6Co_2]^{2+}$: measured: 1086.4167, calculated: 1086.4171.

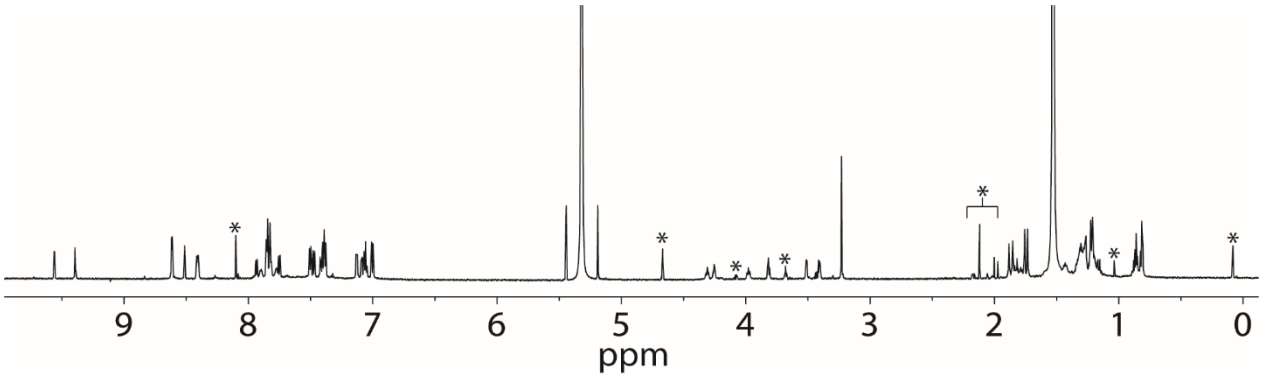

Figure S2.13. ^{1}H NMR spectrum (700 MHz/CD_2Cl_2) of cage $[Co_2$**ABCD**$]^{2+}$.

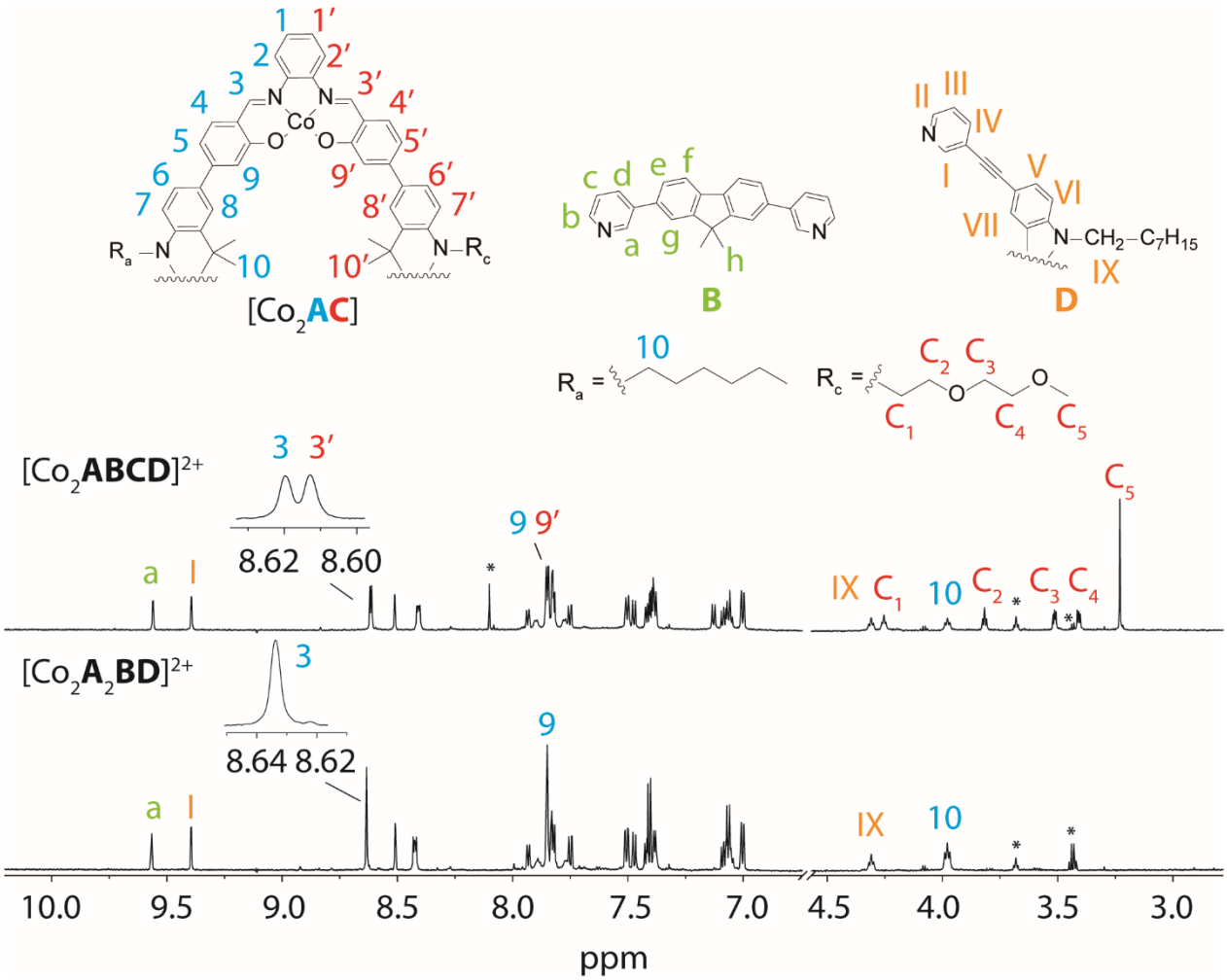

Figure S2.14. Partial ^{1}H NMR spectra (700 MHz/CD_2Cl_2) of cage $[Co_2\mathbf{ABCD}]^{2+}$ compared with cage $[Co_2\mathbf{A}_2\mathbf{BD}]^{2+}$.

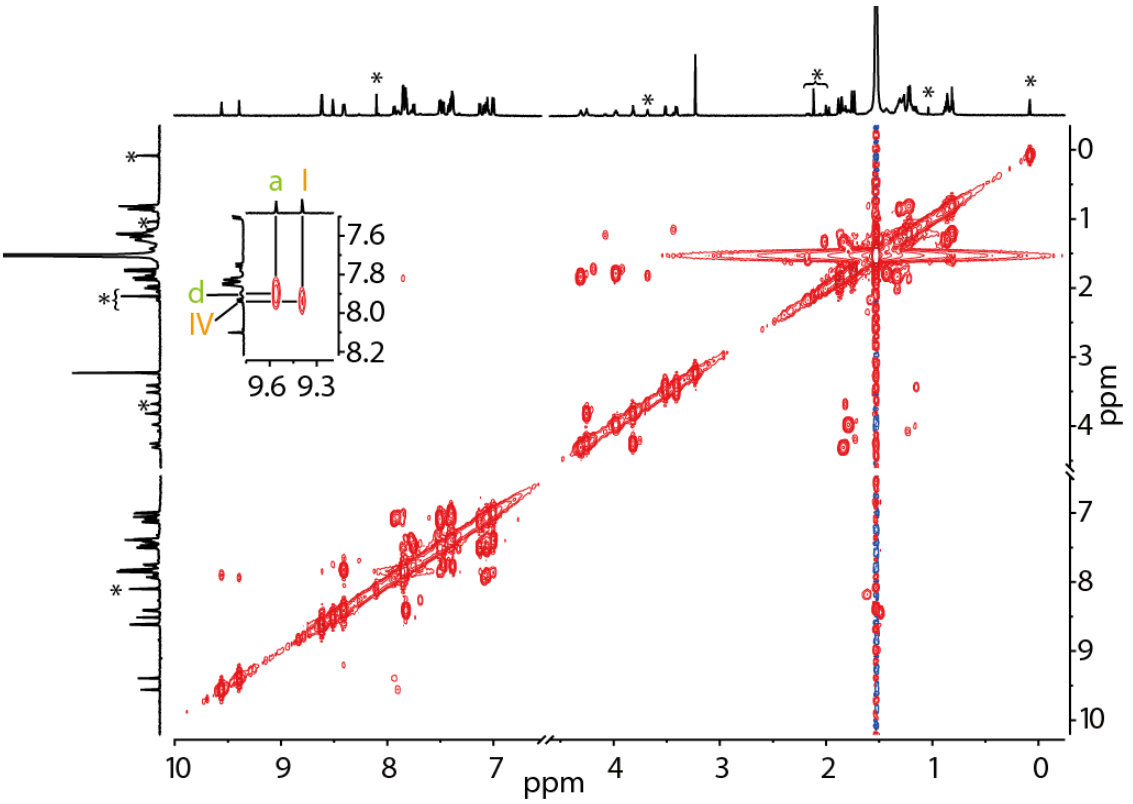

Figure S2.15. ^{1}H-^{1}H COSY spectrum (700 MHz/CD_2Cl_2) of cage [Co_2**ABCD**]$^{2+}$.

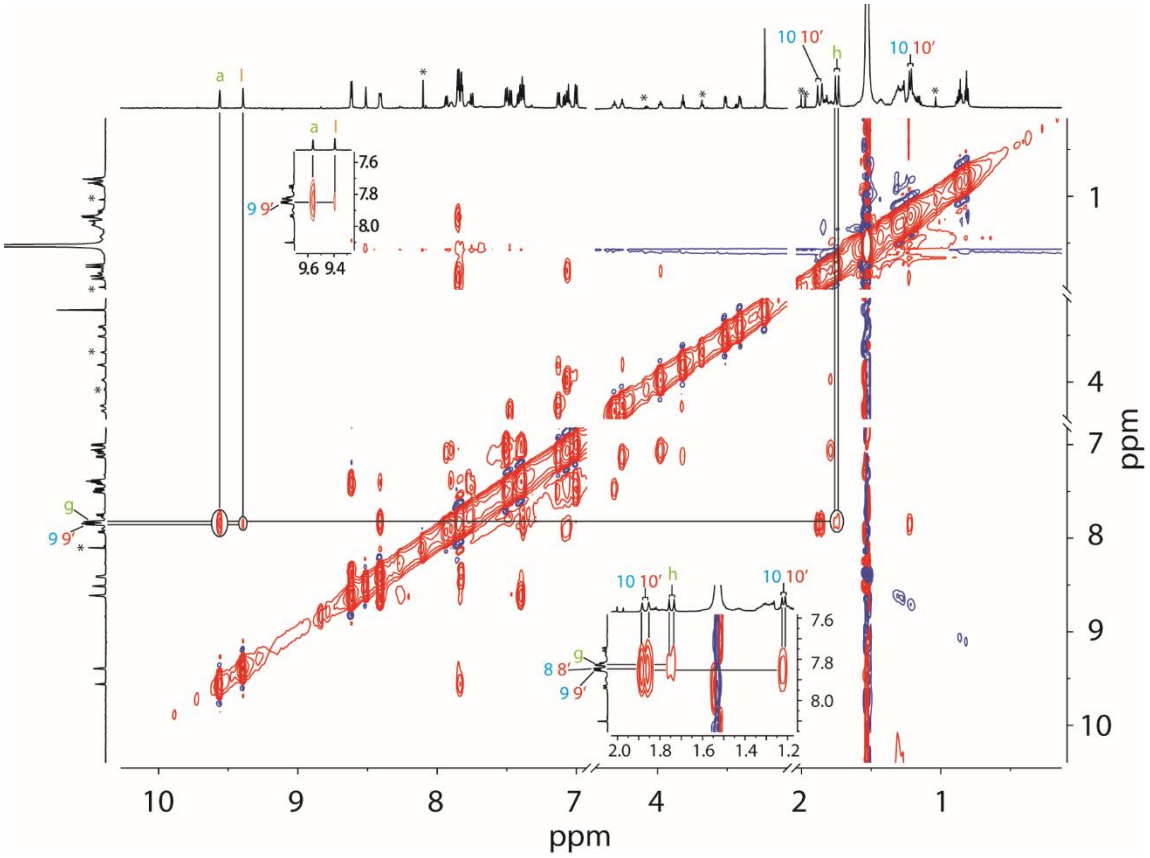

Figure S2.16. ^{1}H-^{1}H NOESY spectrum (700 MHz/CD_2Cl_2) of cage [Co_2**ABCD**]$^{2+}$.

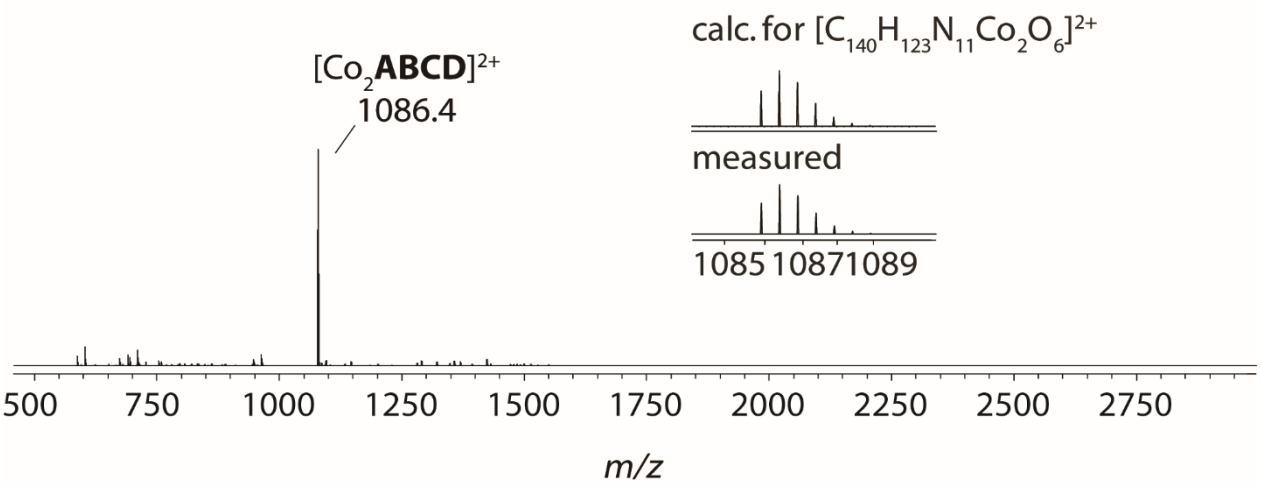

Figure S2.17. ESI mass spectrum of cage $[Co_2\mathbf{ABCD}]^{2+}$.

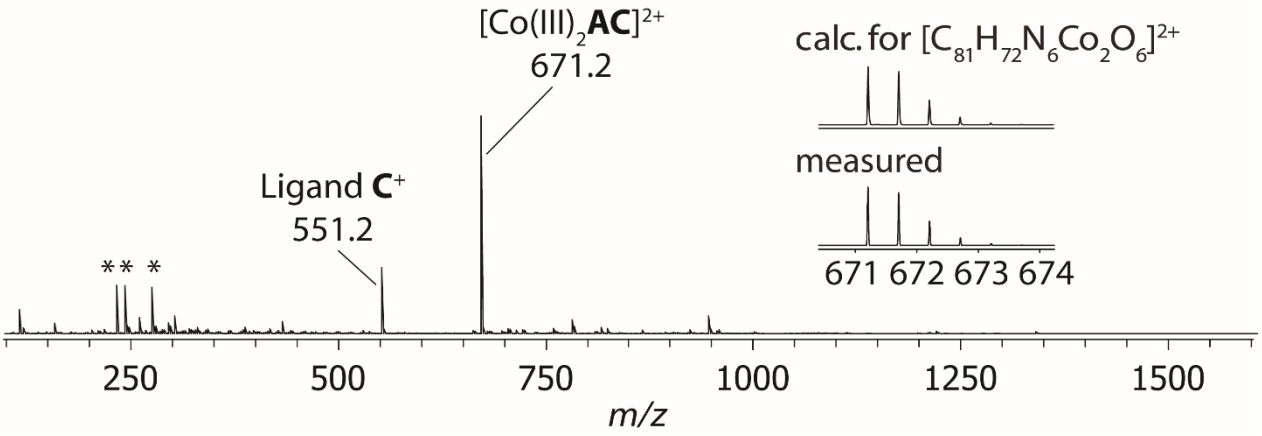

Figure S2.18. ESI mass spectrum of cobalt complex $[Co_2\mathbf{AC}]^{2+}$. Ligands **A'**, **C** and Co(acetate)$_2$ were mixed in a ratio of 1 : 1.1 : 2 in DMSO and heated overnight. Afterwards, the mixture was stirred at room temperature under air atmosphere for 8 h, then directly subjected to HRMS analysis without any purification. According to the mass spectrum, $[Co_2\mathbf{AC}]^{2+}$ was the only Cobalt complex formed, no signals corresponding to $[Co_2\mathbf{A}_2]^{2+}$ and $[Co_2\mathbf{C}_2]^{2+}$ species were found.

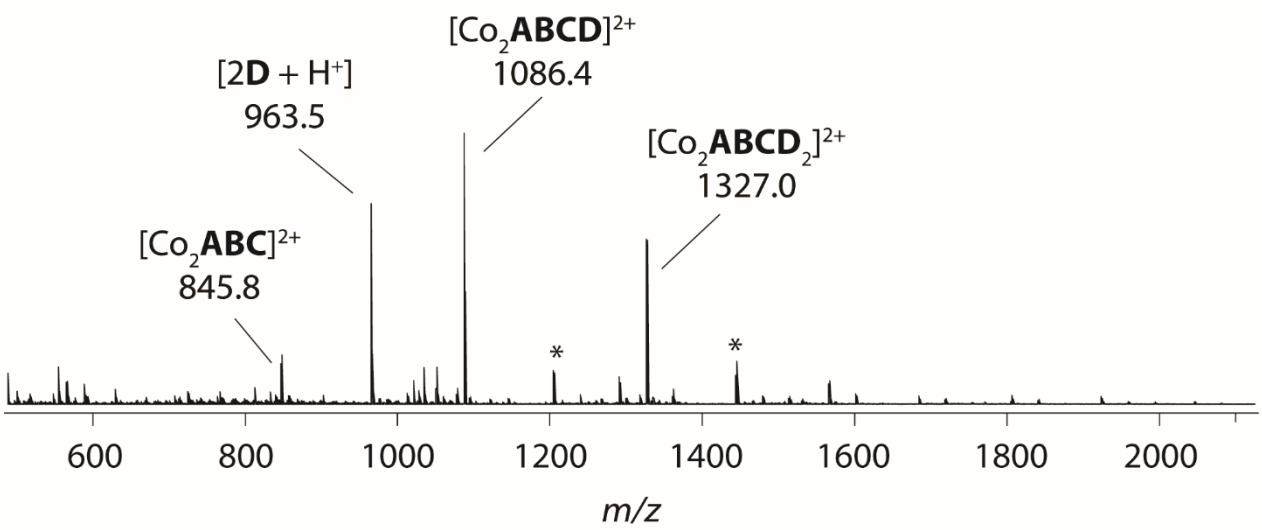

Figure S2.19. ESI mass spectrum of the $[Co_2\mathbf{ABCD}]^{2+}$ crude product produced by method 2.

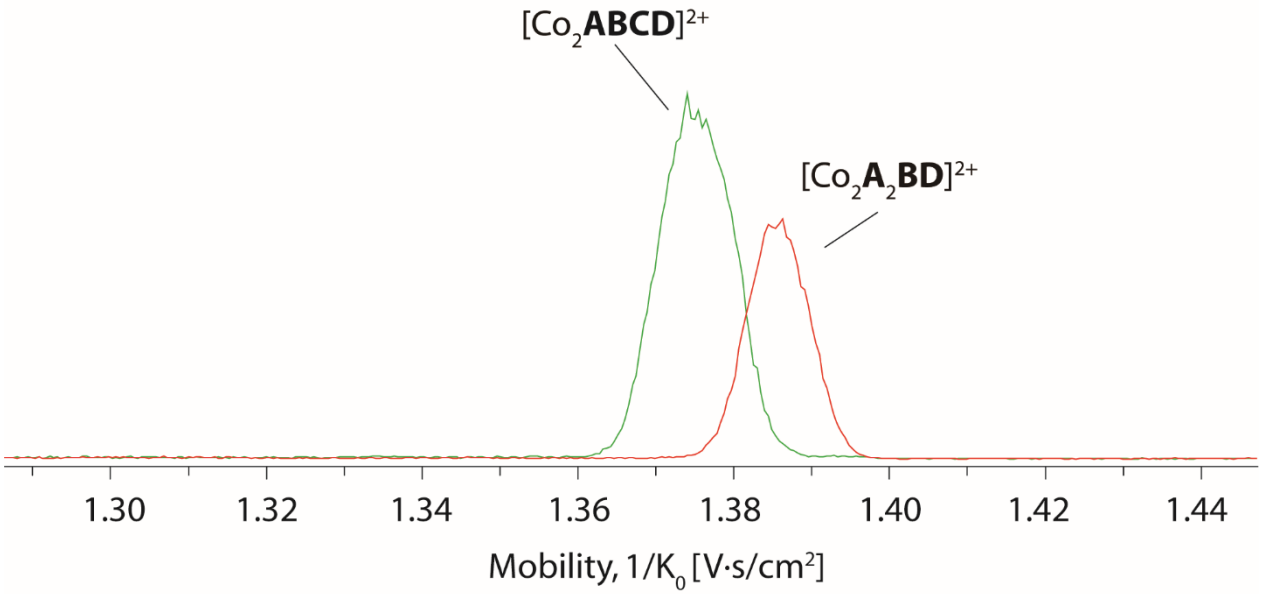

Figure S2.20. Superposition of mobilograms obtained by trapped ion mobility ESI-TOF mass spectrometry for cage complex $[Co_2\mathbf{ABCD}]^{2+}$ (CCS: 557.8 Å^2 at *m/z* 1086.4) and $[Co_2\mathbf{A}_2\mathbf{BD}]^{2+}$ (CCS: 562.4 Å^2 at *m/z* 1077.4). Both cages were mixed and co-injected for the measurement.

2.8.5.4 Self-assembly of cage $[Pd_2\mathbf{B}_2\mathbf{D}_2]^{4+}$

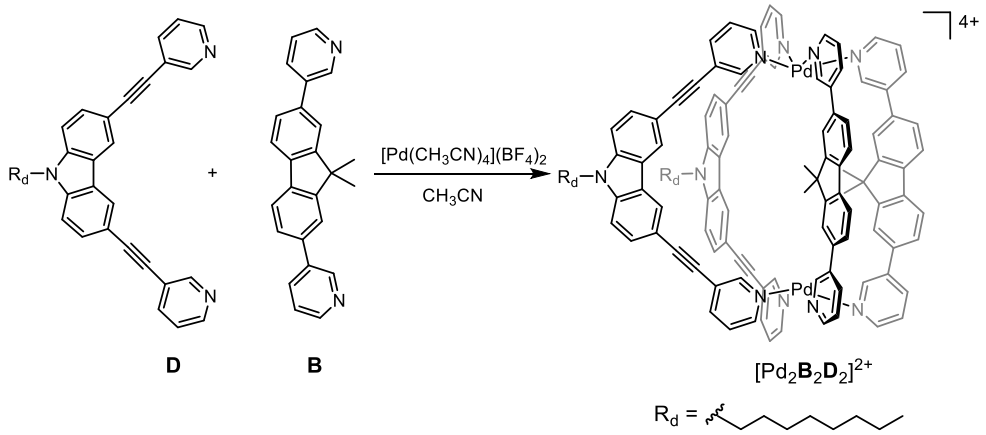

Ligand **D** (1.35 mg, 2.80 µmol, 1.0 equiv.) and ligand **B** (0.98 mg, 2.80 µmol 1.0 equiv.) were dissolved in 2 ml CD_3CN, a $[Pd(CH_3CN)_4](BF4)_2$ solution in CD_3CN (187 µl, 15 mM, 1.0 equiv.) was added and the mixture was heated to 70 °C for 2 h to afford $[Pd_2\mathbf{B}_2\mathbf{D}_2]^{4+}$ quantitatively.

^{1}H NMR (500 MHz, CD_3CN) δ 9.59 (s, 4H, H_a), 9.43 (s, 4H, H_I), 9.09 (d, *J* = 5.7 Hz, 4H, H_{II}), 9.03 (d, *J* = 5.9 Hz, 4H, H_b), 8.29 (s, 4H, H_{VII}), 8.23 (d, *J* = 7.9 Hz, 4H, H_d), 8.13 (d, *J* = 7.6 Hz, 4H, H_{IV}), 7.95 (d, *J* = 7.70 Hz, 4H, H_f), 7.72 (dd, *J* = 8.6, 1.6 Hz, 4H, H_V), 7.66 (td, *J* = 7.7, 6.8, 3.6 Hz, 8H, H_{III}, H_C), 7.61 (d, *J* = 1.7 Hz, 4H, H_g), 7.58 (d, *J* = 8.6 Hz, 4H, H_{VI}), 7.49 (dd, *J* = 7.7, 1.7 Hz, 4H, H_e), 4.34 (t, *J* = 7.1 Hz, 4H, H_{IX}), 1.77 (d, *J* = 7.3 Hz, 4H, CH_2), 1.67 (s, 6H, methyl groups from ligand **B**), 1.31 (s, 6H, methyl groups from ligand **B**), 1.34 – 1.09 (m, 20H, CH_2), 0.77 (t, *J* = 7.0 Hz, 6H, CH_3).

ESI-HRMS $[C_{118}H_{102}N_{10}Pd_2]^{4+}$: measured: 468.1596, calculated: 468.1597.

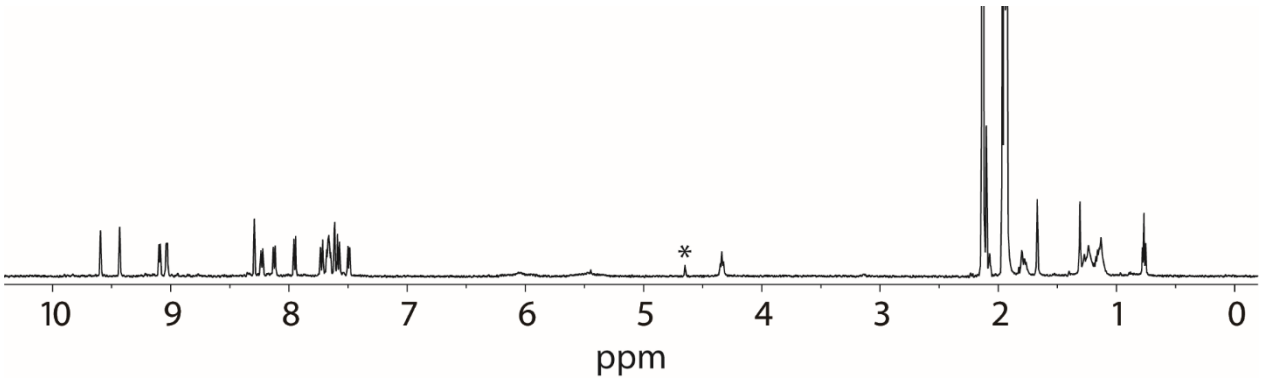

Figure S2.21. ^{1}H NMR spectrum (500 MHz/CD_3CN) of cage $[Pd_2\mathbf{B}_2\mathbf{D}_2]^{4+}$.

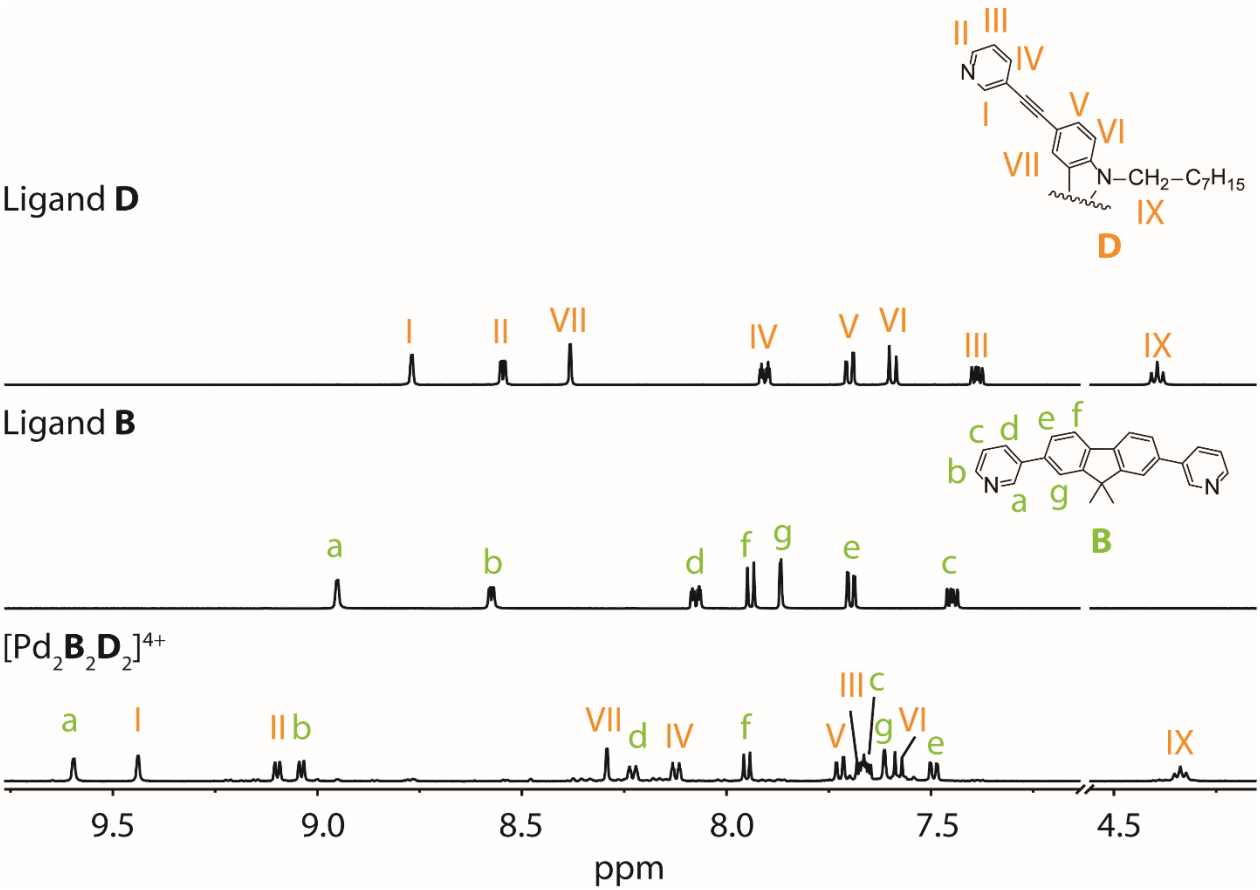

Figure S2.22. Partial ^{1}H NMR spectrum (500 MHz/CD_3CN) of cage $[Pd_2\mathbf{B}_2\mathbf{D}_2]^{4+}$ compared with spectra of free ligands **B** and **D**.

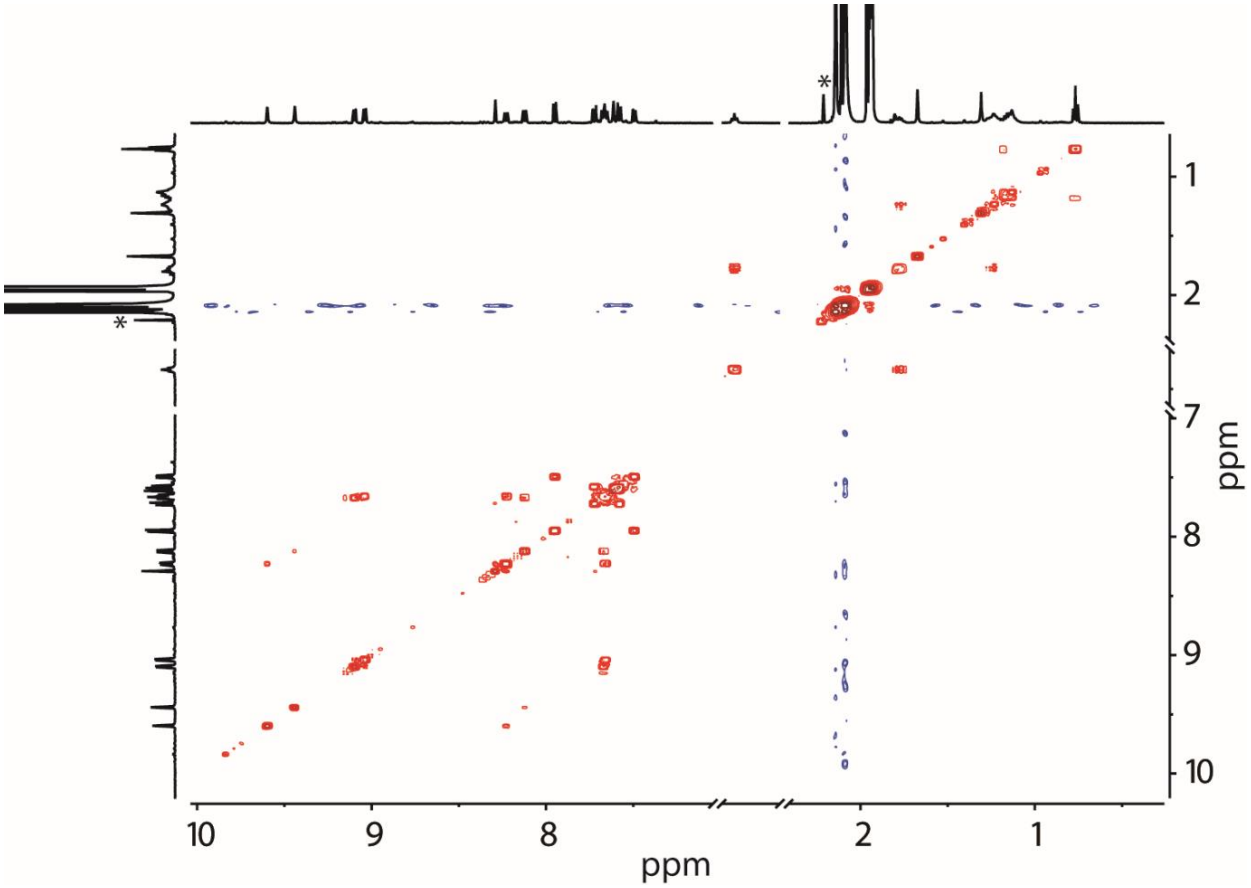

Figure S2.23. ^{1}H-^{1}H COSY spectrum (500 MHz/CD_3CN) of cage $[Pd_2\mathbf{B}_2\mathbf{D}_2]^{4+}$.

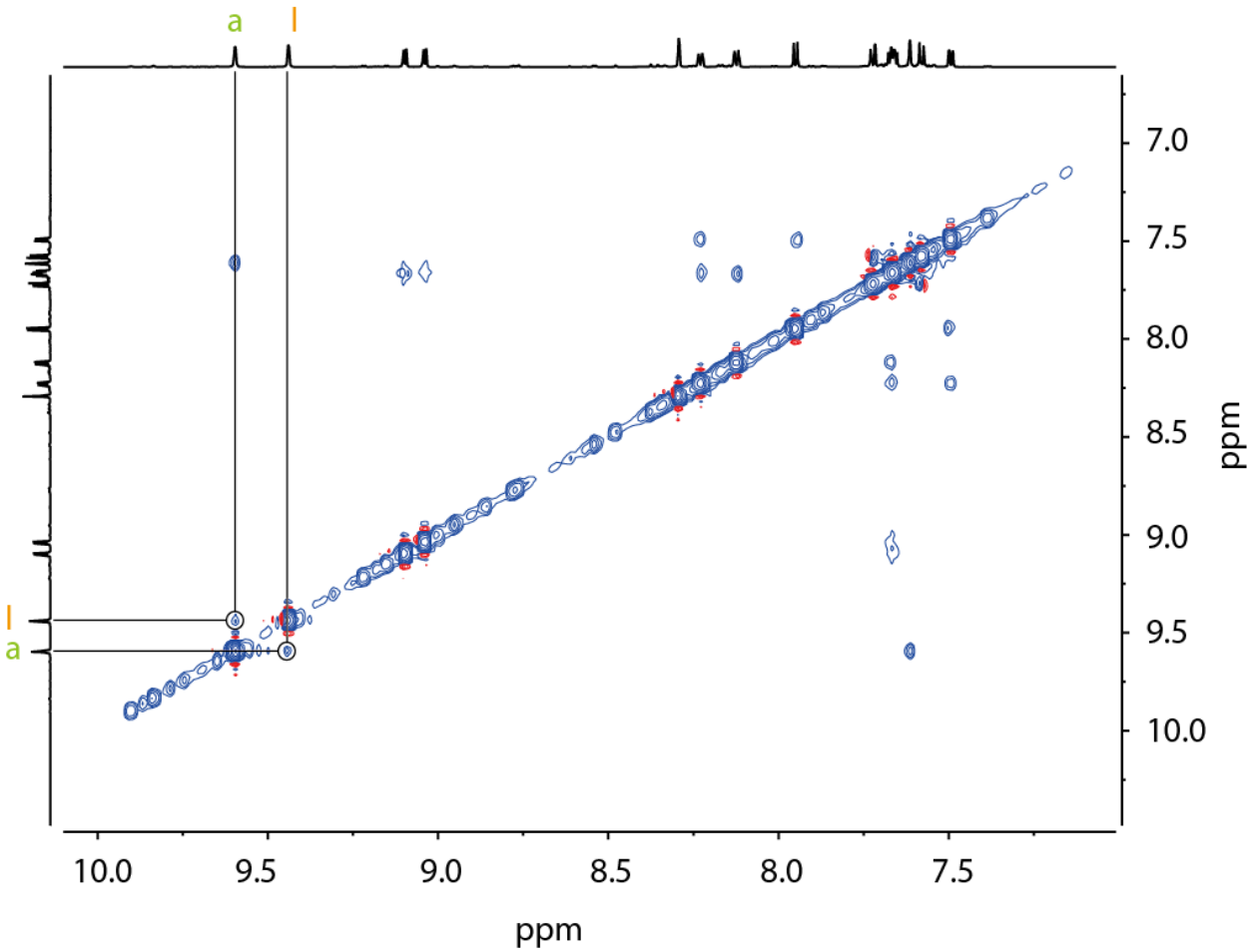

Figure S2.24. Partial ^{1}H-^{1}H NOESY spectrum (500 MHz/CD_3CN) of cage $[Pd_2\mathbf{B}_2\mathbf{D}_2]^{4+}$.

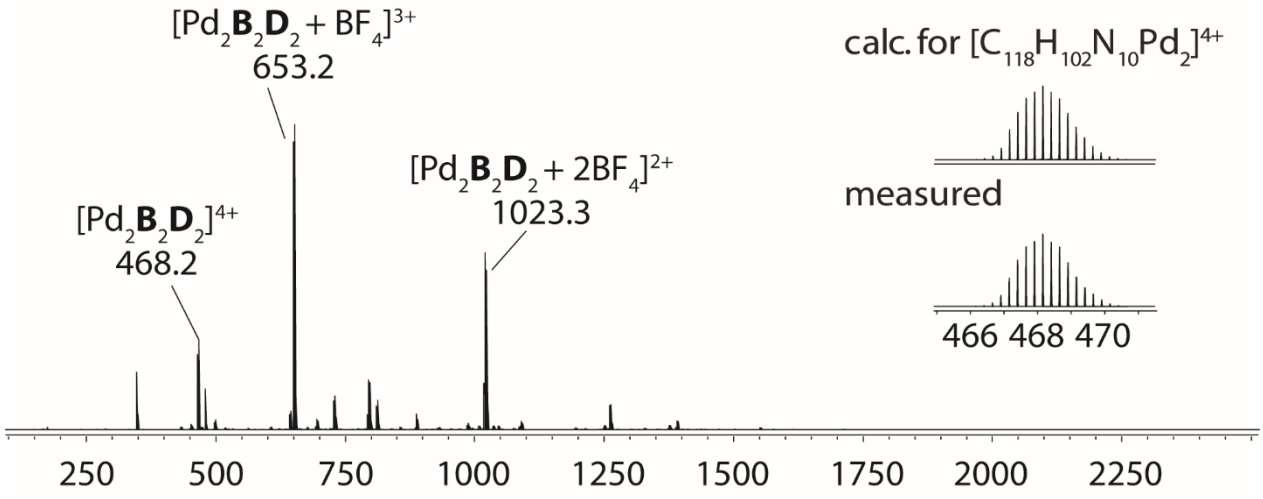

Figure S2.25 ESI mass spectrum of cage $[Pd_2\mathbf{B}_2\mathbf{D}_2]^{4+}$.

2.8.5.5 Self-assembly of $[Pd_2\mathbf{E}_4]^{4+}$ cage

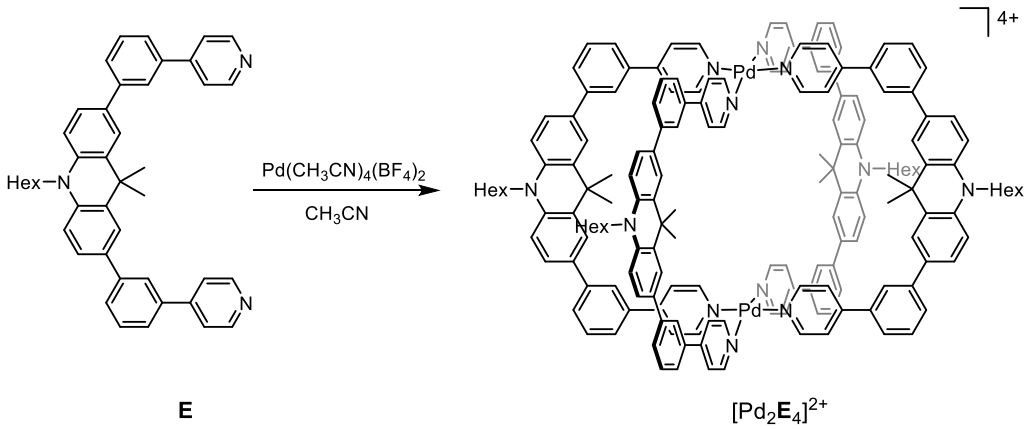

E $[Pd_2\mathbf{E}_4]^{2+}$

Ligand **E** (1.68mg, 2.80 µmol 1.0 equiv.) was dissolved in CD_3CN (1 ml), a $[Pd(CH_3CN)_4](BF_4)_2$ solution in CD_3CN (93 µl, 15 mM, 1.0 equiv.) was added and the mixture was heated to 70 °C for 30 min to afford $[Pd_2\mathbf{E}_4]^{4+}$.

^{1}H NMR (500 MHz, CD_3CN) δ 8.96 (d, *J* = 7.1 Hz 16H, H_A), 8.15 (t, *J* = 1.9 Hz, 8H, H_I), 8.08 (d, *J* = 8.0 Hz, 16H, H_B), 7.90 (d, *J* = 2.3 Hz, 8H, H_H), 7.82 (dt, *J* = 7.7, 1.4 Hz, 8H, H_E), 7.78 (ddd, *J* = 7.9, 1.8, 1.0 Hz, 8H, H_C), 7.61 (t, *J* = 7.8 Hz, 8H, H_D), 7.56 (dd, *J* = 8.6, 2.2 Hz, 8H, H_F), 7.15 (d, *J* = 8.6 Hz, 8H, H_G), 4.00 (t, *J* = 7.8 Hz, 8H, H_J), 1.83 –1.76 (m, 8H, CH_2), 1.66 (s, 24H, methyl groups from ligand **E**), 1.47 (q, *J* = 7.5 Hz, 8H, CH_2), 1.40 – 1.31 (m, 16H, CH_2), 0.88 (t, *J* = 6.9 Hz, 12H, CH_3).

ESI-HRMS $[C_{172}H_{164}N_{12}Pd_2]^{4+}$: measured: 652.7841, calculated: 652.7829.

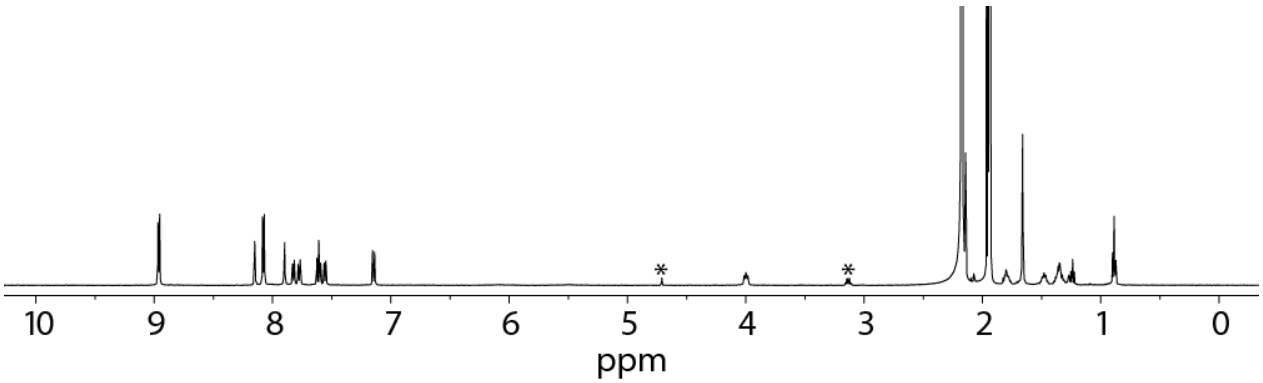

Figure S2.26. ^{1}H NMR spectrum (500 MHz/CD_3CN) of cage $[Pd_2\mathbf{E}_4]^{4+}$.

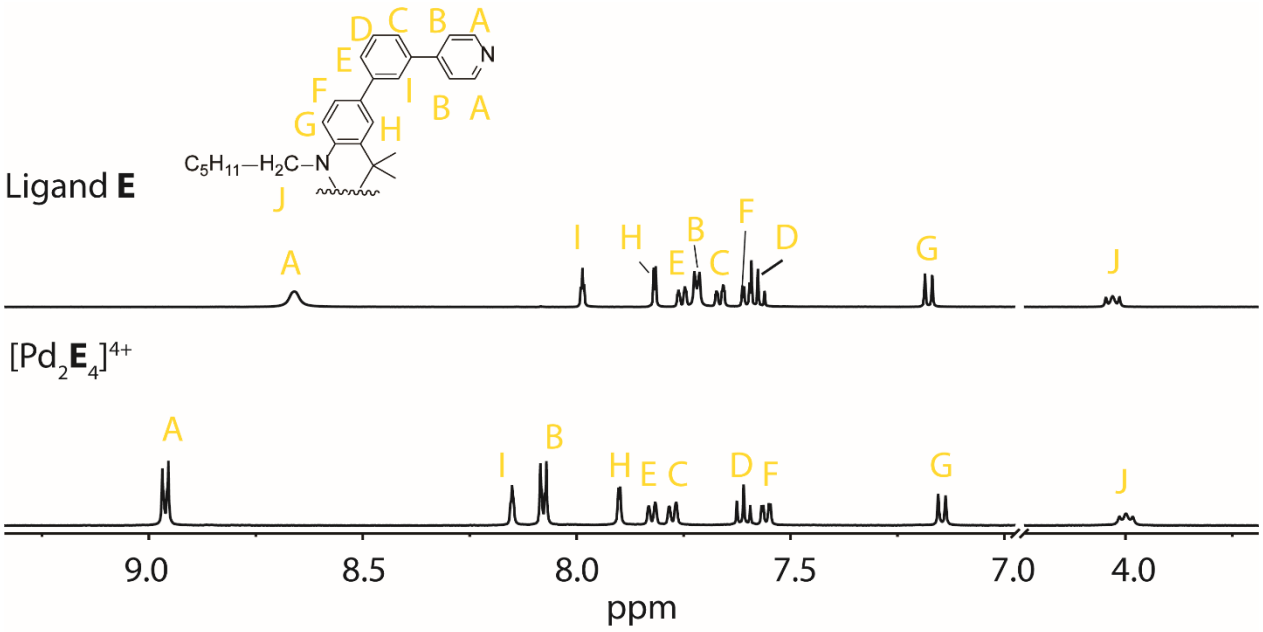

Figure S2.27. Partial ^{1}H NMR spectrum (500 MHz/CD_3CN) of cage [Pd_2**E**$_4$]$^{4+}$ compared with free ligand **E**.

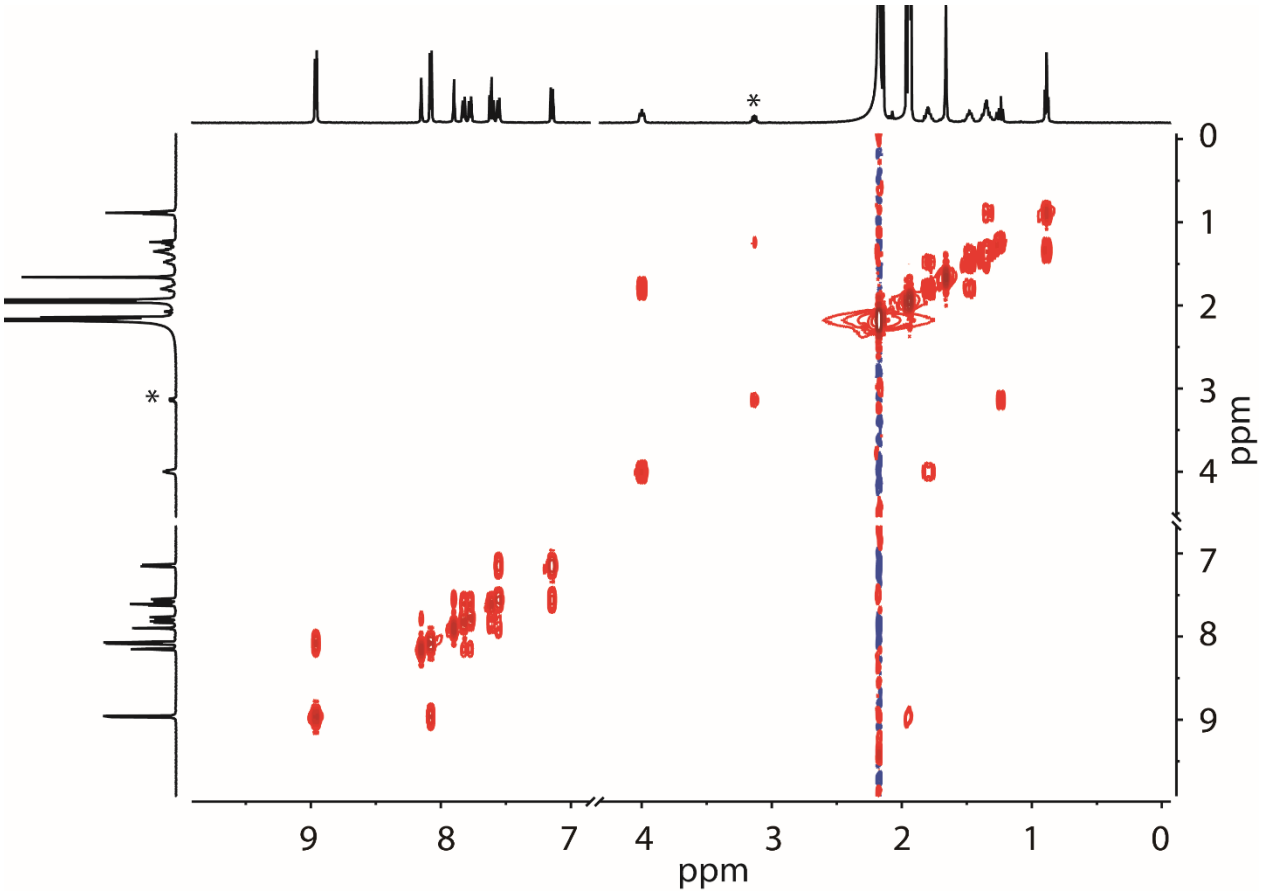

Figure S2.28. ^{1}H-^{1}H COSY spectrum (500 MHz/CD_3CN) of cage [Pd_2**E**$_4$]$^{4+}$.

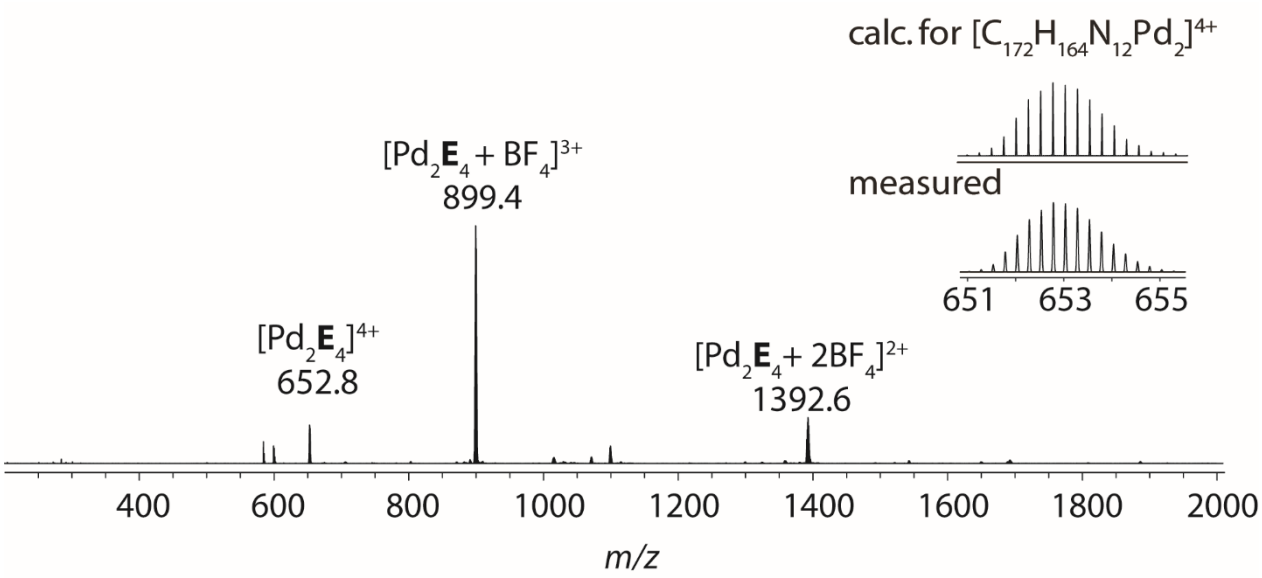

Figure S2.29. ESI mass spectrum of cage $[Pd_2\mathbf{E}_4]^{4+}$.

2.8.6 Self-sorting experiment

Route **a:** Macrocycle $\mathbf{A}_2$ (2.00 mg, 1.65 µmol, 1.0 equiv.) was dissolved in DMSO (2 ml). After addition of Co(acetate)$_2$ (0.58 mg, 3.30 µmol, 2.0 eq.), the mixture was stirred at room temperature for 30 min. Then ligand **B** (1.15 mg, 3.30 µmol, 2.0 equiv.) and NH_4PF_6 (0.54 mg, 3.30 µmol, 2.0 eq.) were added. The reaction mixture was subsequently heated to 70 °C for 19 h under air atmosphere.

Route **b**: The same procedure as described for a) was follwed. Macrocycle $\mathbf{A}_2$ (2.0 mg, 1.65 µmol, 1.0 equiv.) and ligand **D** (1.59 mg, 3.30 µmol, 2.0 eq.) were used for this experiment.

c, 500 µl of the samples from a) and b), respectively, were combined and the mixture was heated to 70 °C for 24h under air atmosphere.

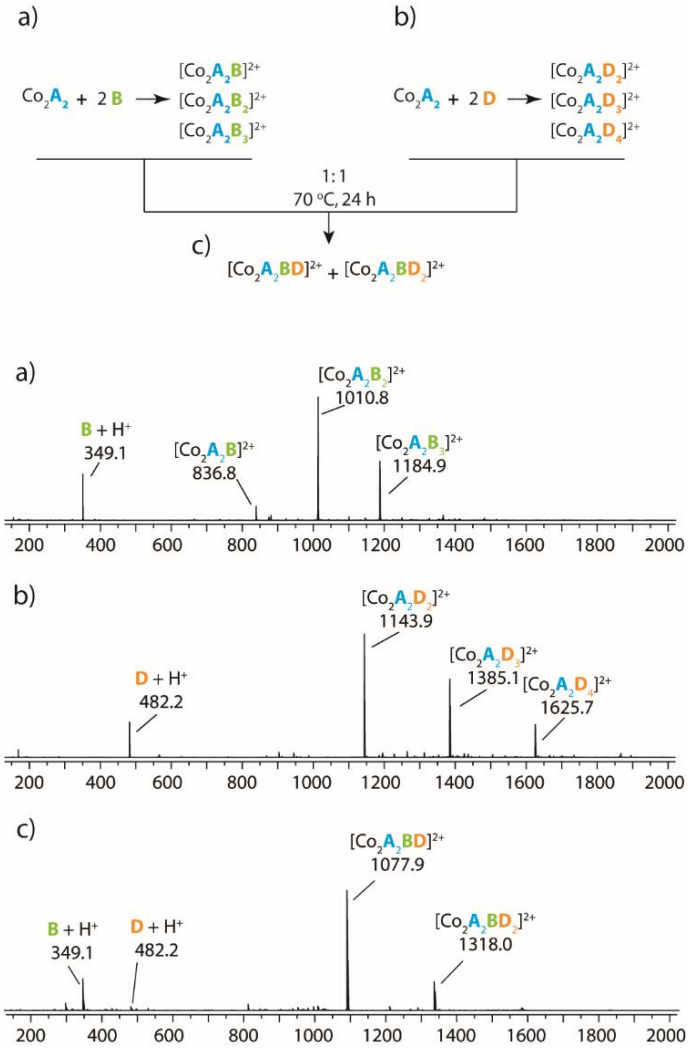

Figure S2.30. Self-sorting experiment monitored by ESI mass spectrometry: a) binuclear cobalt complex $[Co_2\mathbf{A}_2]^{2+}$ reacted with 2.0 equiv. of ligand **B**; b) binuclear Cobalt complex $[Co_2\mathbf{A}_2]^{2+}$ reacted with 2.0 equiv. of ligand **D**; c) samples from a) and b) mixed in a ratio of 1:1 and heated at 70 °C for 24 h.

2.8.7 Computational studies

Crystal structures of $[Co_2\mathbf{A}_2\mathbf{E}_2]^{2+}$ and $[Co_2\mathbf{A}_2\mathbf{BD}]^{2+}$ were used as starting structures for the calculations; other models were constructed using Wavefunction SPARTAN.[70] All structures were first geometry optimized on a PM6 or DFT (B3LYP/3-21g) level of theory using GAUSSAIN 09[71] (charge 2+ for all cobalt complexes; counter ions and side chains were removed to reduce computational costs). The resulting structures were further refined by DFT structure optimizations on B3LYP/LANL2DZ and B3LYP/DEF2SVP levels of theory.

Formation energies of all possible cage complexes that consist of ligands **A**, **B** and **D** with Co(III) cations were calculated according to equations 1-3, shown below. As a result, $[Co_2\mathbf{A}_2\mathbf{BD}]^{2+}$ was found to be the energetically most favorable species. In addition, complexes $[Co_2\mathbf{A}_2\mathbf{B}_2]^{2+}$ and $[Co_2\mathbf{A}_2\mathbf{D}_2]^{2+}$ were compared with $[Co_2\mathbf{A}_2\mathbf{E}_2]^{2+}$, whose formation energy was calculated through equation 4. All three complexes are formed from binuclear macrocycle $[Co_2\mathbf{A}_2]^{2+}$ and one of the banana-shaped ligands. According to the calculations, the formation of $[Co_2\mathbf{A}_2\mathbf{E}_2]^{2+}$ is much more favorable than that of $[Co_2\mathbf{A}_2\mathbf{B}_2]^{2+}$ and $[Co_2\mathbf{A}_2\mathbf{D}_2]^{2+}$.

1. $[Co_2A_2B_2]^{2+}$: $[Co_2A_2(DMSO)_4]^{2+}$ + 2 B → $[CoA_2B_2]^{2+}$ + 4 DMSO
2. $[Co_2A_2D_2]^{2+}$: $[Co_2A_2(DMSO)_4]^{2+}$ + 2 D → $[CoA_2D_2]^{2+}$ + 4 DMSO
3. $[Co_2A_2BD]^{2+}$: $[Co_2A_2(DMSO)_4]^{2+}$ + B + D → $[CoA_2BD]^{2+}$ + 4 DMSO
4. $[Co_2A_2E_2]^{2+}$: $[Co_2A_2\ (DMSO)_4]^{2+}$ + 2 E → $[CoA_2E_2]^{2+}$ + 4 DMSO

Table S2.1. DFT calculated cage formation energies using different calculation methods, unit: kJ/mol.

	$[Co_2A_2B_2]^{2+}$	$[Co_2A_2D_2]^{2+}$	$[Co_2A_2BD]^{2+}$	$[Co_2A_2E_2]^{2+}$
B3LYP/LANL2DZ	157.2	129.9	97.9	67.1
B3LYP/DEF2SVP	102.5	77.0	48.4	15.7

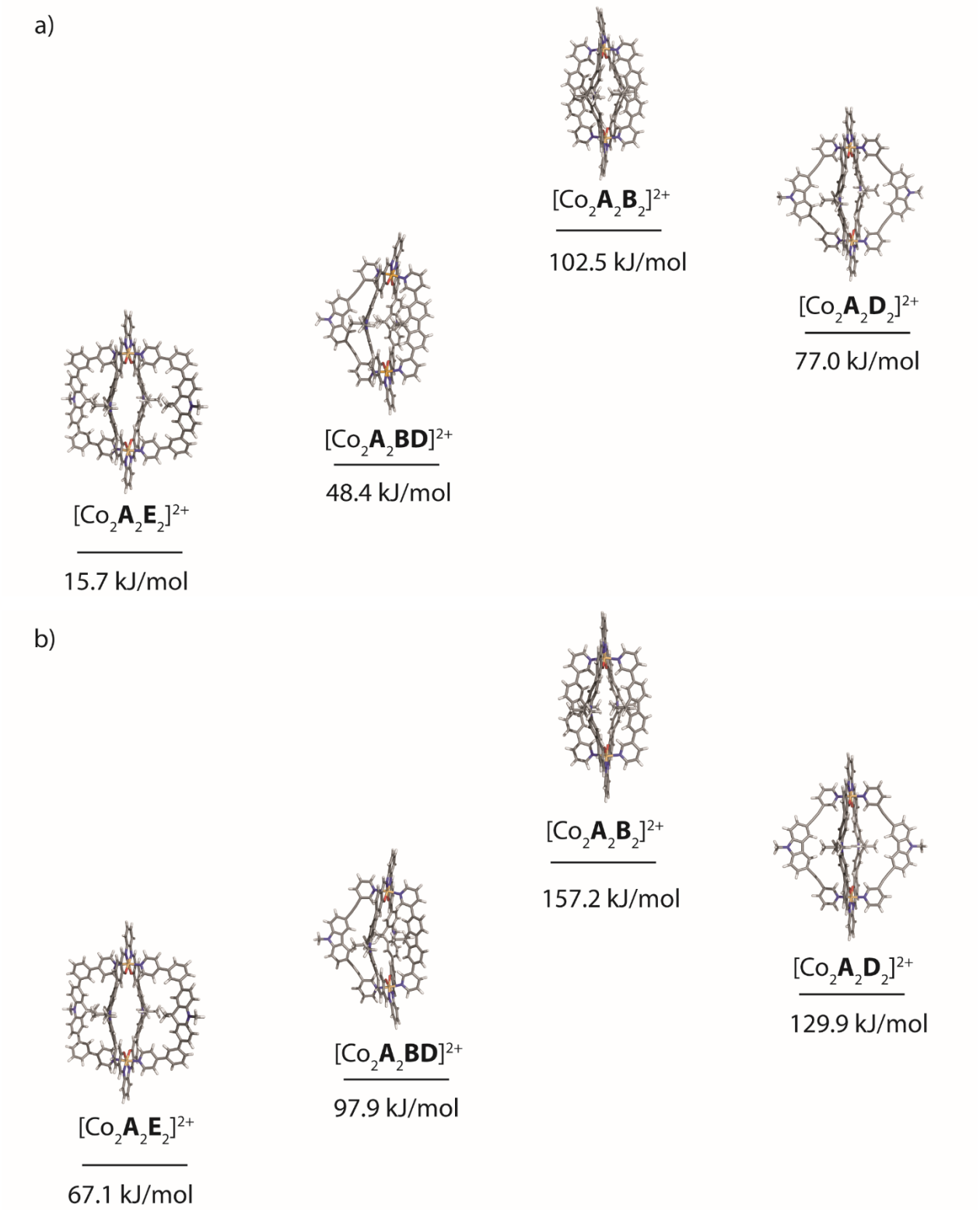

Figure S2.31. DFT calculated structures and relative energies of formation according to the equations in the text. a) B3LYP/DEF2SVP; b) B3LYP/LANL2DZ.

2.8.8 X-ray crystallography

General Methods

Crystals of supramolecular assemblies were extremely sensitive to loss of organic solvent. Gaining detailed structural insight thus required cryogenic crystal handling. Only crystals of **$[Pd_2E_4](BF_4)_4$** diffracted well enough to be studied on our in-house diffractometer using microfocussed CuKα radiation. The supramolecular assemblies of **$[Co_2A_2E_2](PF_6)_2$**, **$[Co_2A_2BD](PF_6)_2$**, **$[Pd_2B_2D_2](BF_4)_4$** and **$[Co_2ABCD](PF_6)_2$** required synchrotron radiation in order to be successfully determined by single crystal X-ray crystallography. Diffraction data of these four structures was collected during three beamtime shifts at macromolecular synchrotron beamline P11, PETRA III, DESY.[72] Even when using synchrotron radiation the analysis was further hampered by the limited scattering power due to very thin (down to 10 ym) plate- or needle-shaped crystals and the targeted resolution of 0.84 Å could not be reached in all cases. Modelling disorder of flexible side chains, disorder of a full cage over special position as well as counterion and solvent flexibility required carefully adapted macromolecular refinement protocols such as employing geometrical restraint dictionaries, local structural similarity restraints and restraints for anisotropic displacement parameters (ADPs). Analyzing morphologies and detailed geometries greatly enhanced the in-depth understanding of how these systems arrange in the solid state.

The data collection was performed by Dr. Julian Holstein, Dr. Witold Bloch, Dr. Rujin Li, Dr. Bin Chen, Irene Regeni and Philip Punt.

The crystal structures were solved and refined by Dr. Julian Holstein and Dr. Haeri Lee.

Table S2.2. Crystallographic data of $[Co_2\mathbf{A}_2\mathbf{E}_2](PF_6)_2$, $[Co_2\mathbf{A}_2\mathbf{BD}](PF_6)_2$ and $[Pd_2\mathbf{E}_4](BF_4)_4$.

Compound	$[Co_2\mathbf{A}_2\mathbf{E}_2](PF_6)_2$	$[Co_2\mathbf{A}_2\mathbf{BD}](PF_6)_2$	$[Pd_2\mathbf{E}_4](BF_4)_4$
CCDC number	1903507	1903508	1903509
Identification code	bz74c_sq	bz10a_sq	bz18a_sq
Empirical formula	$C_{168}H_{156}N_{12}O_4Co_2P_2F_{12}$	$C_{141}H_{125}N_{11}O_4Co_2P_2F_{12}$	$C_{172}H_{164}N_{12}Pd_2B_{2.5}F_{10}$
Formula weight	2814.84	2709.62	2828.97
Temperature (K)	80(2)	80(2)	100(2)
Wavelength (Å)	0.5636	0.6888	1.54178
Crystal system	Triclinic	Tetragonal	Triclinic
Space group	*P*-1	*I*41/a	*P*-1
a (Å)	18.488(4)	53.706(8)	21.3570(6)
b (Å)	20.406(4)	53.706(8)	22.1278(7)
c (Å)	24.338(5)	20.488(4)	22.2280(7)
α (°)	114.60(3)	90	102.876(2)
β (°)	92.08(3)	90	95.415(2)
γ (°)	90.35(3)	90	105.416(2)
Volume (Å^3)	8341(3)	59094(20)	9739.2(5)
Z	2	16	2
Density (calc.) (Mg/m^3)	1.121	1.218	0.965
Absorption coefficient (mm^{-1})	0.156	0.293	1.912
F (000)	2944	22656	2949
Crystal size (mm^3)	0.100 x 0.100 x 0.010	0.120 x 0.080 x 0.030	0.220 x 0.080 x 0.040
θ range for data collection (°)	0.730 to 15.568	0.735 to 26.875	2.144 to 54.436
Index ranges	-17<=h<=17 -19<=k<=19 -23<=l<=23	-70<=h<=70 -70<=k<=69 -26<=l<=26	-22<=h<=22 -23<=k<=23 -23<=l<=23
Reflections collected	51598	431020	175173
Independent reflections [R(int)]	14643 [0.0650]	34845 [0.0513]	23851 [0.0890]
Completeness to θ	97.00% (15.568°)	99.60% (24.411°)	99.50% (54.436°)
Absorption correction	None	None	Semi-empirical from equivalents
Refinement method	Full-matrix least-squares on F^2	Full-matrix least-squares on F^2	Full-matrix least-squares on F^2
Data / restraints / parameters	14643 / 3931 / 1906	34845 / 3443 / 1730	23851 / 6532 / 2596
Goodness-of-fit on F^2	1.705	1.365	1.455
Final R indices [I>2σ(I)]	R1 = 0.1388 *w*R2 = 0.4029	R1 = 0.0905 *w*R2 = 0.3102	R1 = 0.1189 *w*R2 = 0.3574
R indices (all data)	R1 = 0.1758 *w*R2 = 0.4318	R1 = 0.1065 *w*R2 = 0.3298	R1 = 0.1569 *w*R2 = 0.3899
Largest diff. peak and hole (e.Å^{-3})	1.100 and -0.555	1.832 and -0.761	1.473 and -0.618

Table S2.3. Crystallographic data of $[Pd_2\mathbf{B}_2\mathbf{D}_2](BF_4)_4$ and $[Co_2\mathbf{ABCD}](PF_6)_2$.

Compound	$[Pd_2B_2D_2](BF_4)_4$	$[Co_2ABCD](PF_6)_2$
CCDC number	1903510	1903511
Identification code	bz16a_sq	bz15a_sq
Empirical formula	$C_{118}H_{102}N_{10}Pd_2B_4F_{16}$	$C_{148}H_{139}N_{11}O_{10}Co_2P_2F_{12}$
Formula weight	2220.13	2639.49
Temperature (K)	80(2)	80(2)
Wavelength (Å)	0.6888	0.6888
Crystal system	Monoclinic	Tetragonal
Space group	*P*21/n	*I*41/a
a (Å)	23.149(5)	53.511(8)
b (Å)	43.375(9)	53.511(8)
c (Å)	26.764(5)	20.397(4)
α (°)	90	90
β (°)	104.22(3)	90
γ (°)	90	90
Volume ($Å^3$)	26050(10)	58405(20)
Z	8	16
Density (calc.) (Mg/m^3)	1.132	1.201
Absorption coefficient (mm^{-1})	0.313	0.295
F (000)	9088	22016
Crystal size (mm^3)	0.100 x 0.060 x 0.060	0.080 x 0.080 x 0.020
θ range for data collection (°)	0.886 to 16.969	0.738 to 18.776
Index ranges	-19<=h<=19 -36<=k<=36 -22<=l<=22	-48<=h<=48 -50<=k<=50 -19<=l<=19
Reflections collected	109603	162768
Independent reflections [R(int)]	16584 [0.0474]	12479 [0.0475]
Completeness to θ	99.90% (16.969°)	100.00% (18.776°)
Absorption correction	None	None
Refinement method	Full-matrix least-squares on F^2	Full-matrix least-squares on F^2
Data / restraints / parameters	16584 / 5720 / 2701	12479 / 3308 / 1666
Goodness-of-fit on F^2	2.732	1.728
Final R indices [I>2σ(I)]	R1 = 0.1971 *w*R2 = 0.5431	R1 = 0.1234 *w*R2 = 0.3628
R indices (all data)	R1 = 0.2160 *w*R2 = 0.5613	R1 = 0.1486 *w*R2 = 0.3969
Largest diff. peak and hole ($e.Å^{-3}$)	1.656 and -0.699	0.863 and -0.646

2.8.8.1 Data collection details of cage $[Co_2\boldsymbol{A}_2\boldsymbol{E}_2]^{2+}$

Red plated- shaped crystals of $[Co_2\mathbf{A}_2\mathbf{E}_2](PF_6)_2$ were grown by slow vapor diffusion of EtOAc into a solution of $[Co_2\mathbf{A}_2\mathbf{E}_2](PF_6)_2$ in DMSO. Four crystals, each mounted on a loop, were placed in UNI Pucks and stored at cryogenic temperature in a dry shipper, in which they were safely transported to macromolecular beamline P11 [72] at Petra III, DESY, Germany. UNI Pucks were transferred to the sample Dewar container and all samples were mounted using a StäubliTX60L robotic arm. A wavelength of 0.5636 Å was chosen using a liquid N_2 cooled double crystal monochromator. Single crystal X-ray diffraction data was collected at 80(2) K on a single axis goniometer, equipped with an Oxford Cryostream 800 and a Pilatus 6M detector. 720 diffraction images were collected in a 360° ϕ sweep at a detector distance of 300 mm, 100% filter transmission, 0.5° step width and 60 milliseconds exposure time per image. Data integration and reduction were undertaken using XDS. [73] The resolution was cut off at 0.93 Å, after which the signal to noise ratio has dropped below $I/\sigma(I) < 2.0$.The structures were solved by intrinsic phasing/direct methods using SHELXT[74] and refined with SHELXL [75] for full-matrix least-squares routines on F^2 and ShelXle [76] as a graphical user interface and the DSR program plugin was employed for modeling.

2.8.8.1.1 Refinement details of cage $[Co_2\boldsymbol{A}_2\boldsymbol{E}_2]^{2+}$

Stereochemical restraints for organic ligands in residues AHP and A24 were generated by the GRADE program using the GRADE Web Server (http://grade.globalphasing.org) and applied in the refinement. The GRADE dictionary contains target values and standard deviations for 1,2-distances (DFIX) and 1,3-distances (DANG), as well as restraints for planar groups (FLAT). Due to disorder of the flexibil hexyl chain and the ligand backboneof both residues A24, local structural similarity restraints (LSSR) for 1.4 distances were additionally employed to make geometries of ligands belonging to the same residue class similar to each other by employing non-crystallographic symmetry (NCSY). The anisotropic refinement for C, N, O atoms was enabled by a combination of similarity restraints (SIMU) and rigid bond restraints (RIGU).[77] The contribution of the electron density from solvent molecules, which could not be modelled with discrete atomic positions were handled using the SQUEEZE[78] routine in PLATON.[79] The solvent mask file (.fab) computed by PLATON were included in the SHELXL refinement via the ABIN instruction leaving the measured intensities untouched.

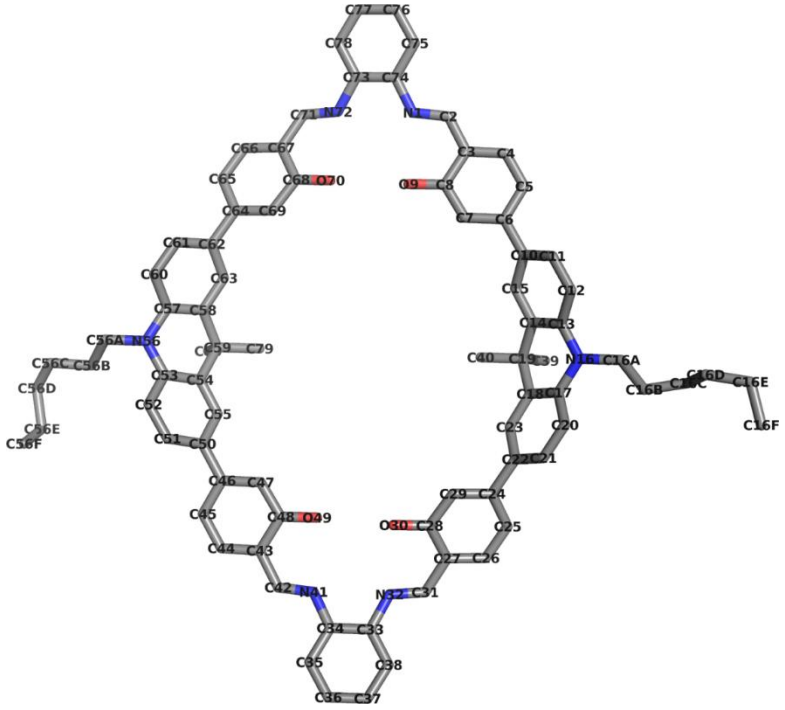

Figure S2.32. Atomic numbering scheme of residue AHP (ligand **A_2**)

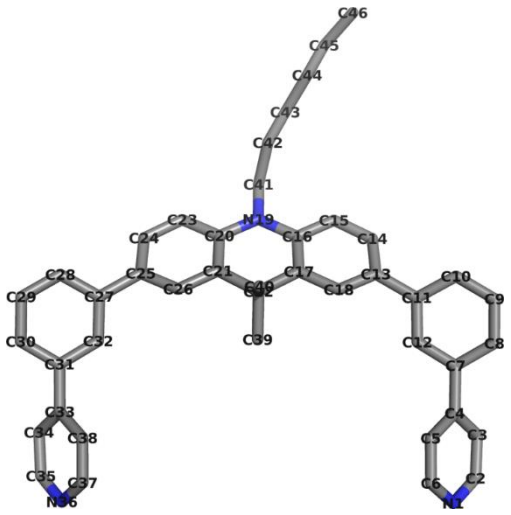

Figure S2.33. Atomic numbering scheme of residue A24 (ligand **E**)

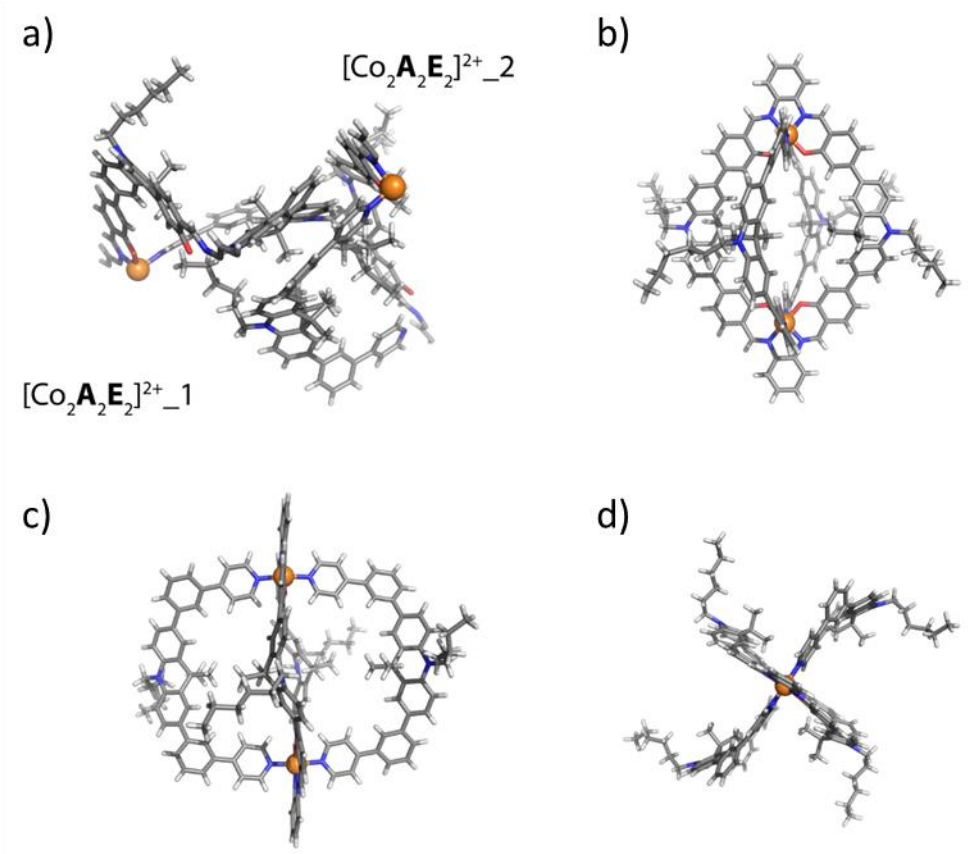

Figure S2.34. X-ray structure of $[Co_2\mathbf{A}_2\mathbf{E}_2]^{2+}$: a) the asymmetric unit contains two half cages; b) front view of cage $[Co_2\mathbf{A}_2\mathbf{E}_2]^{2+}$_1; c) side view $[Co_2\mathbf{A}_2\mathbf{E}_2]^{2+}$_1; d) top view $[Co_2\mathbf{A}_2\mathbf{E}_2]^{2+}$_1. Counterions ($PF_6^-$) were omitted for clarity. Color scheme: H, light grey; C, dark grey; N, blue; O, red; Co, orange.

2.8.8.2 Data collection details of cage $[Co_2\mathbf{A}_2\mathbf{BD}]^{2+}$

Red plate-shaped crystals of $[Co_2\mathbf{A}_2\mathbf{BD}](PF_6)_2$ were grown by slow layering of EtOAc into a solution of $[Co_2\mathbf{A}_2\mathbf{BD}](PF_6)_2$ in DCM. Five crystals, each mounted on a loop were placed in UNI Pucks and stored at cryogenic temperature in a dry shipper, in which they were safely transported to macromolecular beamline P11[72] at Petra III, DESY, Germany. UNI Pucks were transferred to the sample Dewar container and all samples were mounted using a StäubliTX60L robotic arm. A wavelength of 0.6888 Å was chosen using a liquid N_2 cooled double crystal monochromator. Single crystal X-ray diffraction data was collected at 80(2) K on a single axis goniometer, equipped with an Oxford Cryostream 800 and Pilatus 6M detector. 1800 diffraction images were collected in a 360° ϕ sweep at a detector distance of 156 mm, 60% filter transmission, 0.2° step width and 200 milliseconds exposure time per image. Data integration and reduction were undertaken using XDS. [73] The resolution was cut off at 0.75 Å, after which the signal to noise ratio has dropped below I/σ(I) < 2.0. The structures were solved by intrinsic phasing/direct methods using SHELXT [74] and refined with SHELXL [75]for full-matrix least-squares routines on F^2 and ShelXle[76] as a graphical user interface and the DSR program plugin was employed for modeling.

2.8.8.2.1 Refinement details of cage $[Co_2\mathbf{A}_2\mathbf{BD}]^{2+}$

Stereochemical restraints for organic ligands in residues COP, AHP and LFP and ethyl acetate solvent molecules (residue EEE) were generated by the GRADE program using the GRADE Web Server (http://grade.globalphasing.org) and applied in the refinement. The GRADE dictionary contains target values and standard deviations for 1,2-distances (DFIX) and 1,3-distances (DANG), as well as restraints for planar groups (FLAT). Due to the flexibility of Ethylacetate solvent molecules (residue EEE), local structural similarity restraints (LSSR) for 1.4 distances were employed to make geometries of Ethylactetate solvent molecules similar to each other by employing non-crystallographic symmetry (NCSY). The anisotropic refinement for C, N, O atoms was enabled by a combination of similarity restraints (SIMU) and rigid bond restraints (RIGU).[77] The contribution of the electron density from solvent molecules, which could not be modelled with discrete atomic positions were handled using the SQUEEZE[78] routine in PLATON.[79] The solvent mask file (.fab) computed by PLATON were included in the SHELXL refinement via the ABIN instruction leaving the measured intensities untouched.

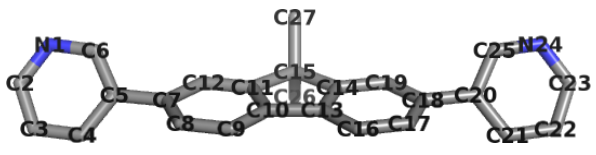

Figure S2.35. Atomic numbering scheme of residue LFP (ligand **B**)

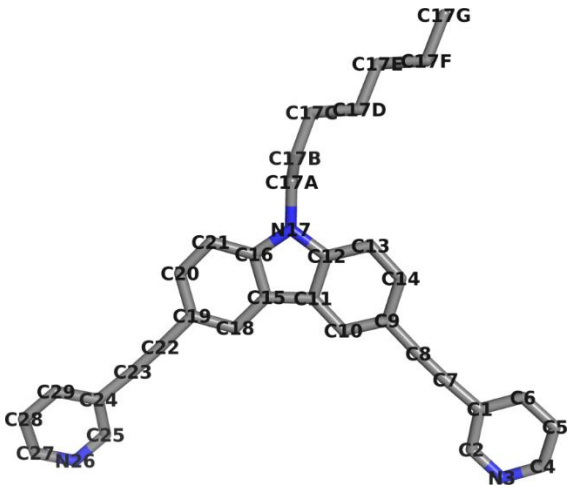

Figure S2.36. Atomic numbering scheme of residue COP (ligand **D**)

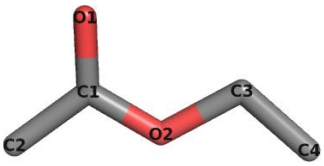

Figure S2.37. Atomic numbering scheme of residue EEE (Ethylacetate solvent molecule)

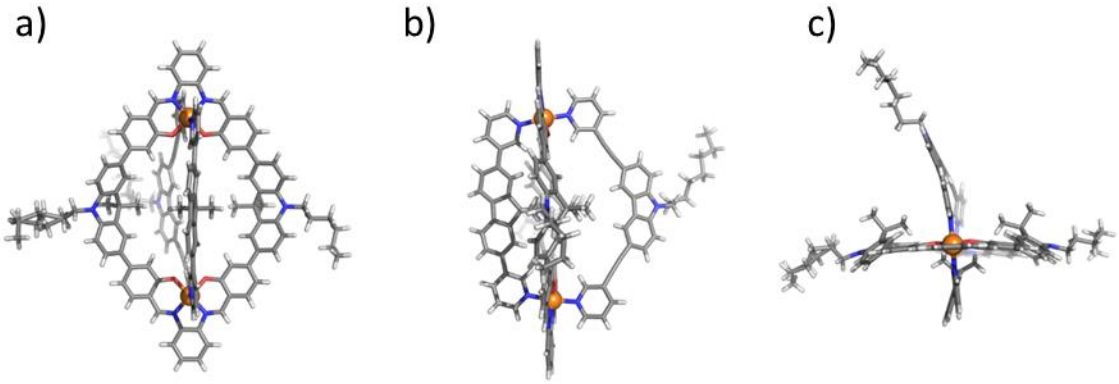

Figure S2.38. X-ray structure of $[Co_2\mathbf{A}_2\mathbf{BD}]^{2+}$: a) front view; b) side view; c) top view. Counterion (PF_6^-) and solvent molecule were omitted for clarity. Color scheme: H, light grey; C, dark grey; N, blue; O, red; Co, orange.

2.8.8.3 Data collection details of cage $[Pd_2\mathbf{E}_4]^{4+}$

Yellow cube-shaped crystals of $[Pd_2\mathbf{E}_4](BF_4)_4$ were grown by slow vapor diffusion of Et_2O into a solution of $[Pd_2\mathbf{E}_4](BF_4)_4$ in CD_3CN. Data was collected in-house on a Bruker D8 venture diffractometer equipped with an INCOATEC microfocus sealed tube (Iμs 3.0) using CuK_α radiation at 100 K. The resolution was cut off at 1.1 Å, after which the signal to noise ratio has dropped below I/σ(I) < 2.0. The data was integrated with APEX3. The structures were solved by intrinsic phasing/direct methods using SHELXT[74] and refined with SHELXL[75]for full-matrix least-squares routines on F^2 and ShelXle[76] as a graphical user interface and the DSR program plugin was employed for modeling.

2.8.8.3.1 Refinement details of cage $[Pd_2\mathbf{E}_4]^{4+}$

Stereochemical restraints for organic ligands (residue A24) were generated by the GRADE program using the GRADE Web Server (http://grade.globalphasing.org) and applied in the refinement. The GRADE dictionary contains target values and standard deviations for 1,2-distances (DFIX) and 1,3-distances (DANG), as well as restraints for planar groups (FLAT). For Tetrafluoroborate counterions (residue BF4) a restraints dictionary was generated manually using the Mogul program. One of the two symmetry independen cages including its palladium ions is disordered over a special position (inversion centre) and was therefore refined with 50% occupancy factor using negative parts (PART -1 and PART -2). Due to the flexibility of hexyl chain on ligand E (residue A24), local structural similarity restraints (LSSR) for 1.4 distances were additionally employed to make geometries of ligands (residue A24) belonging to the same residue class similar to each other by employing non-crystallographic symmetry (NCSY). The NCSY command was also employed to make geometries of Tetrafluoroborate counterions (residue BF4) similar to each other. The anisotropic refinement for C, N, and O atoms was enabled by a combination of similarity restraints (SIMU) and rigid bond restraints (RIGU).[77] The contribution of the electron density from solvent molecules and highly disordered anions, which could not be modelled with discrete atomic positions were handled using the SQUEEZE[78] routine in PLATON.[79] The solvent mask file (.fab) computed by PLATON were included in the SHELXL refinement via the ABIN instruction leaving the measured intensities untouched.

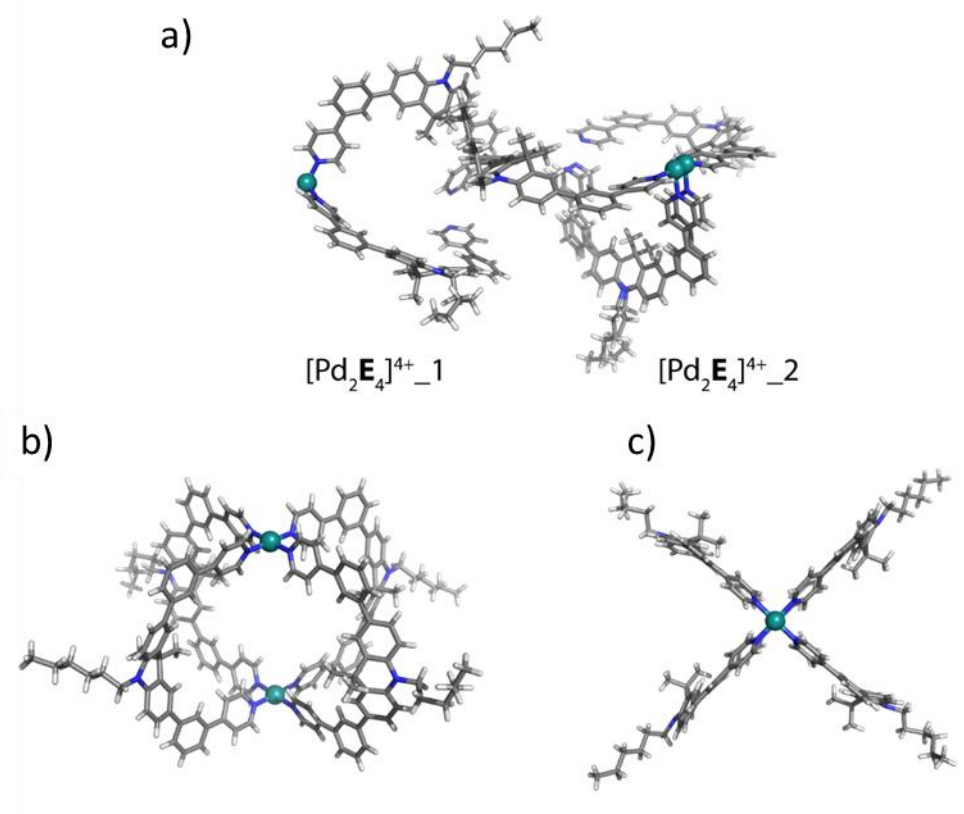

Figure S2.39. X-ray structure of $[Pd_2\mathbf{E}_2]^{4+}$: a) the asymmetric unit contains two crystallographically independent half cages; b) side view of $[Pd_2\mathbf{E}_2]^{4+}$_1; c) top view of $[Pd_2\mathbf{E}_2]^{4+}$_1. Counterion ($BF4^-$) and solvent molecule were omitted for clarity. Color scheme: H, light grey; C, dark grey; N, blue; Pd, dark green.

2.8.8.4 Data collection details of cage $[Pd_2\mathbf{B}_2\mathbf{D}_2]^{2+}$

Colouless needle-shaped crystals of $[Pd_2\mathbf{B}_2\mathbf{D}_2](BF_4)_4$ were grown by slow vapor diffusion of Et_2O into a solution of $[Pd_2\mathbf{B}_2\mathbf{D}_2](BF_4)_4$ in CD_3CN. Six crystals, each mounted on a loop were placed in UNI Pucks and stored at cryogenic temperature in a dry shipper, in which they were safely transported to macromolecular beamline P11[72] at Petra III, DESY, Germany. UNI Pucks were transferred to the sample Dewar container and all samples were mounted using a StäubliTX60L robotic arm. A wavelength of 0.6888 Å was chosen using a liquid N_2 cooled double crystal monochromator. Single crystal X-ray diffraction data was collected at 80(2) K on a single axis goniometer, equipped with an Oxford Cryostream 800 and a Pilatus 6M detector. 1800 diffraction images were collected in a 360° ϕ sweep at a detector distance of 255 mm, 100% filter transmission, 0.2° step width and 60 milliseconds exposure time per image. Data integration and reduction were undertaken using XDS.[73] The resolution was cut off at 1.18 Å, after which the signal to noise ratio has dropped below $I/\sigma(I) < 2.0$. The structures were solved by intrinsic phasing/direct methods using SHELXT[74] and refined with SHELXL[75] for full-matrix least-squares routines on F^2 and ShelXle[76] as a graphical user interface and the DSR program plugin was employed for modeling.

2.8.8.4.1 Refinement details of cage $[Pd_2\mathbf{B}_2\mathbf{D}_2]^{2+}$

Stereochemical restraints for organic ligand **B** and **D** in residues LFP and COP were generated by the GRADE program using the GRADE Web Server (http://grade.globalphasing.org) and applied in the refinement. The GRADE dictionary contains target values and standard deviations for 1,2-distances (DFIX) and 1,3-distances (DANG), as well as restraints for planar groups (FLAT). Due to the flexibility of octyl chains ligand **D** (residue COP**)**, local structural similarity restraints (LSSR) for 1.4 distances were employed to make geometries of ligands belonging to the same residue class similar to each other by employing non-crystallographic symmetry (NCSY). The anisotropic refinement for C, N, O atoms was enabled by a combination of similarity restraints (SIMU) and rigid bond restraints (RIGU).[77] ISOR restraints were additionally employed for Flurine and Boron atoms in Tetrafluroborate counterions (BF4) of residues 18, 19 and 20. The contribution of the electron density from solvent molecules, which could not be modelled with discrete atomic positions were handled using the SQUEEZE[78] routine in PLATON.[79] The solvent mask file (.fab) computed by PLATON were included in the SHELXL refinement via the ABIN instruction leaving the measured intensities untouched.

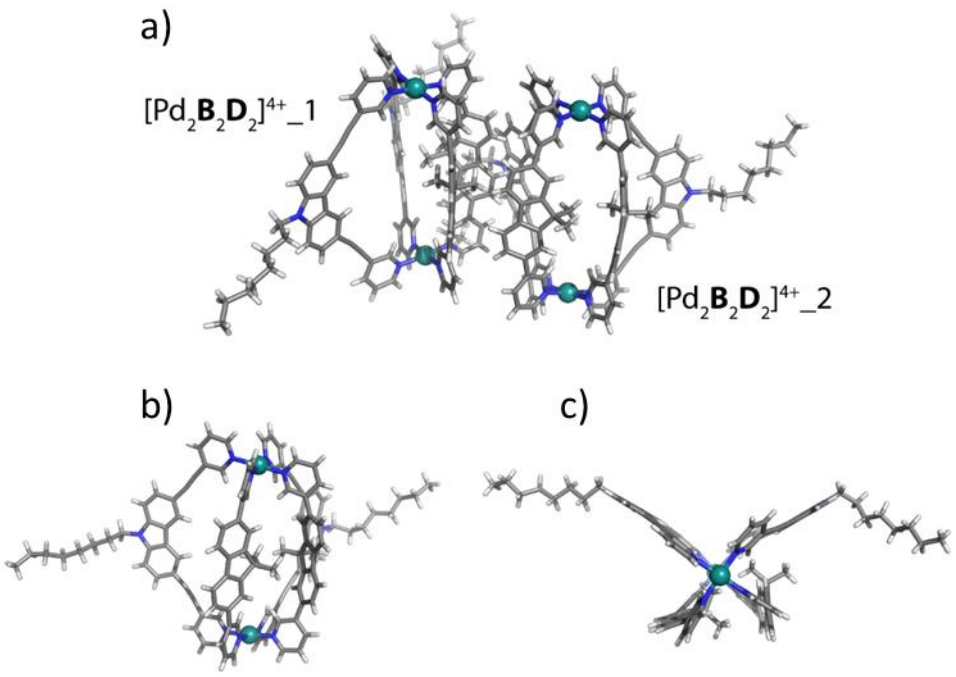

Figure S2.40. X-ray structure of $[Pd_2\mathbf{B}_2\mathbf{D}_2]^{4+}$: a) the asymmetric unit contains two crystallographically independent cages; b) side view of $[Pd_2\mathbf{B}_2\mathbf{D}_2]^{4+}$_1; c) top view of $[Pd_2\mathbf{B}_2\mathbf{D}_2]^{4+}$_1. Counterion ($BF4^-$) and solvent molecule were omitted for clarity. Color scheme: H, light grey; C, dark grey; N, blue; Pd, dark green.

*2.8.8.5 Data collection details of cage $[Co_2$**ABCD**$]^{2+}$*

Red plate crystals of $[Co_2$**ABCD**$](PF_6)_2$ were grown by slow layering of EtOAc into a solution of $[Co_2$**ABCD**$](PF_6)_2$ in DCM. Three crystals, each mounted on a loop were placed in UNI Pucks and stored at cryogenic temperature in a dry shipper, in which they were safely transported to macromolecular beamline P11[72] at Petra III, DESY, Germany. UNI Pucks were transferred to the sample Dewar container and all samples were mounted using a StäubliTX60L robotic arm. A wavelength of 0.6888 Å was chosen using a liquid N_2 cooled double crystal monochromator. Single crystal X-ray diffraction data was collected at 80(2) K on a single axis goniometer, equipped with an Oxford Cryostream 800 and a Pilatus 6M detector. 1800 diffraction images were collected in a 360° ϕ sweep at a detector distance of 200 mm, 100% filter transmission, 0.2° step width and 300 milliseconds exposure time per image. Data integration and reduction were undertaken using XDS.[73] The resolution was cut off at 1.07 Å, after which the signal to noise ratio has dropped below $I/\sigma(I) < 2.0$. The structures were solved by intrinsic phasing/direct methods using SHELXT[74] and refined with SHELXL[75] for full-matrix least-squares routines on F^2 and ShelXle[76] as a graphical user interface and the DSR program plugin was employed for modeling.

*2.8.8.5.1 Refinement details of cage $[Co_2$**ABCD**$]^{2+}$*

Stereochemical restraints for organic ligands **AC**, **B** and **D** in residue A1P, LFP and COP as well as ethyl acetate solvent molecules (residue EEE) were generated by the GRADE program using the GRADE Web Server (http://grade.globalphasing.org) and applied in the refinement. The GRADE dictionary contains target values and standard deviations for 1,2-distances (DFIX) and 1,3-distances (DANG), as well as restraints for planar groups (FLAT). As only the hexyl and the PEG side chain de-symmetrize the ligand **AC**, special care was taken during structural modeling. Both chains tend to disorder due to the high degree of freedom and distinguishing them from each other during the refinement was particularly tricky. Especially the PEG chains showed minor disordered. It was however not possible to model the PEG chain with a second discrete position at the experimental resolution of 1.07 Å despite using advanced macromolecular refinement protocols. Nevertheless, the model, which only includes the main conformer of the PEG chain is supported by the observed electron density (figure S2.42). The anisotropic refinement for C, N, O atoms was enabled by a combination of similarity restraints (SIMU) and rigid bond restraints (RIGU).[77] The contribution of the electron density from solvent molecules, which could not be modelled with discrete atomic positions were handled using the SQUEEZE[78] routine in PLATON.[79] The solvent mask file (.fab) computed by PLATON were included in the SHELXL refinement via the ABIN instruction leaving the measured intensities untouched.

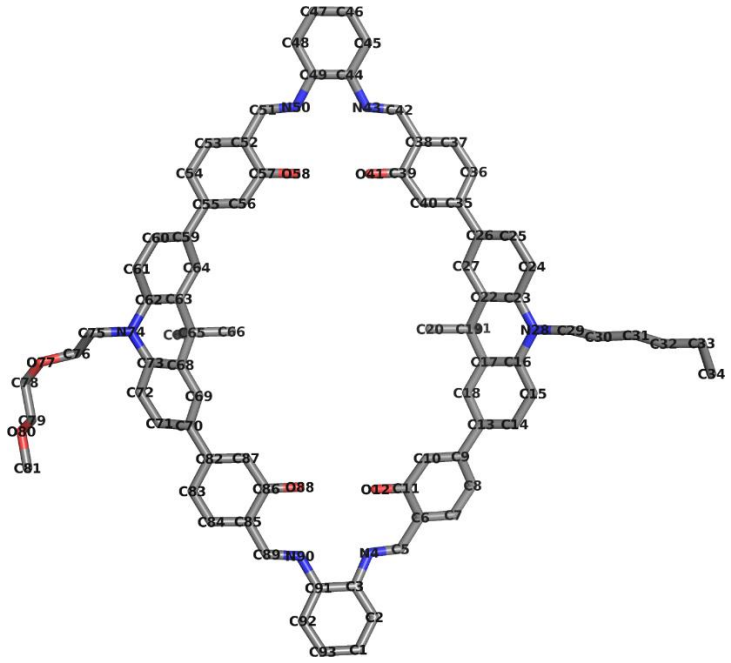

FigureS2.41. Atomic numbering scheme of residue A1P (ligand **AC**)

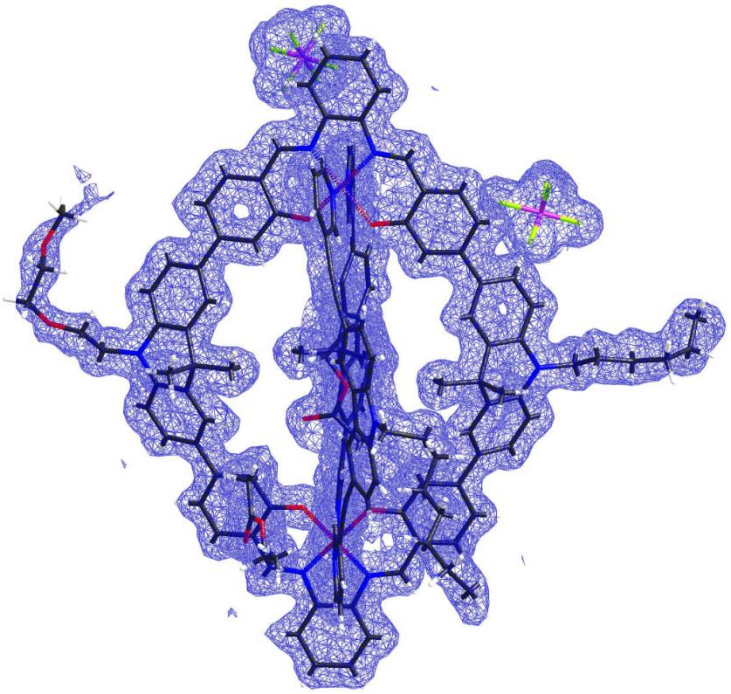

Figure S2.42. X-ray structure of $[Co_2\mathbf{ABCD}]^{2+}$: with iso mesh of observed electron density ($\boldsymbol{F_o}$) at 0.6 e/Å³ level.

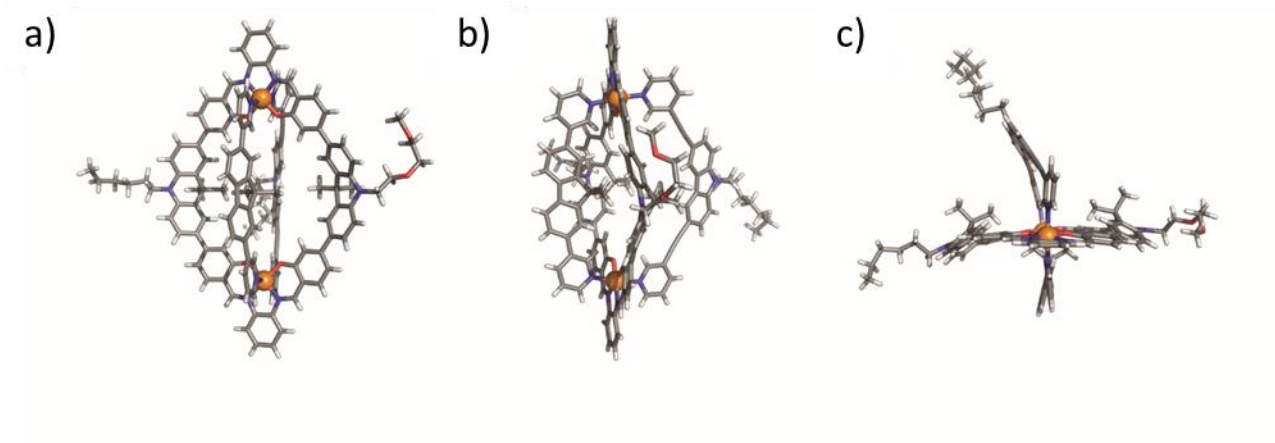

Figure S2.43. X-ray structure of $[Co_2\mathbf{ABCD}]^{2+}$: a) front view, b) side view, c) top view. Counterion (PF_6^-) and solvent molecule were omitted for clarity. Color scheme: H, light grey; C, dark grey; N, blue; O, red; Co, orange.

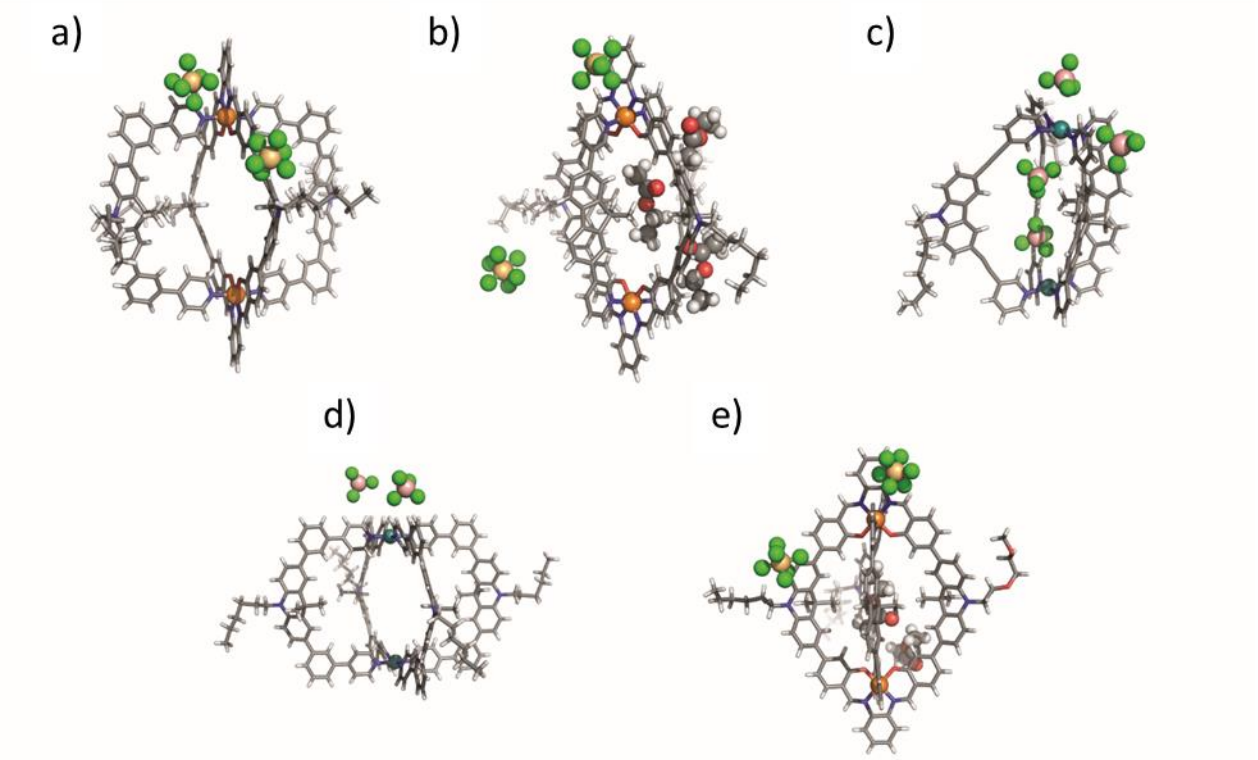

Figure S2.44. X-ray structures with counter ions and solvent molecules: a) X-ray structure of $[Co_2\mathbf{A}_2\mathbf{E}_2](PF_6)_2$; b) X-ray structure of $[Co_2\mathbf{A}_2\mathbf{BD}](PF_6)_2$ with solvent molecules (EtOAc); c) X-ray structure of $[Pd_2\mathbf{B}_2\mathbf{D}_2](BF_4)_4$; d) X-ray structure of $[Pd_2\mathbf{E}_4](BF_4)_4$.(only two of the BF_4^- have been found); e) X-ray structure of $[Co_2\mathbf{ABCD}](PF_6)_2$, with solvent molecules (EtOAc). Color scheme: H, light grey; C, dark grey; N, blue; O, red; F, green; P, light orange; B, pink Co, orange; Pd, dark green.

2.8.6. Structural comparisons of cobalt cages and palladium cages

Co – Co distances and angles between the two cobalt-salphen planes of cages $[Co_2\mathbf{A}_2\mathbf{E}_2]^{2+}$, $[Co_2\mathbf{A}_2\mathbf{BD}]^{2+}$ and $[Co_2\mathbf{ABCD}]^{2+}$ were calculated by ShleXle from the X-ray structures (Figure S2.45a). α is the angle formed by the coordination vectors of the pyridyl ligands sitting on the axial positions, which equals to the angle between two cobalt planes (Figure S2.45c).

Similarly, Pd – Pd distances and angles β between the two palladium planes of cages $[Pd_2\mathbf{B}_2\mathbf{D}_2]^{4+}$ and $[Pd_2\mathbf{E}_4]^{4+}$ were calculated by ShleXle from the X-ray structures. The Palladium plane is defended by Pd(II) and the four N atoms of the coordinating pyridines (Figure S2.45d).All values and estimated standard deviation were calculated directly from the full covariance matrix from SHELXL refinement using the MPLA command.

Table S2.4. Calculated metal – metal distance and angles with esd.

Cage	Metal – metal distance (Å)	Dihedral angle (°)
$[Co_2\mathbf{A}_2\mathbf{E}_2]^{2+}$_1	14.2492 ± 0.0050	α = 0.000 ± 0.502
$[Co_2\mathbf{A}_2\mathbf{E}_2]^{2+}$_2	14.1138 ± 0.0049	α = 0.000 ± 0.394
$[Co_2\mathbf{A}_2\mathbf{BD}]^{2+}$	14.3593 ± 0.0021	α = 18.586 ± 0.118
$[Pd_2\mathbf{E}_4]^{4+}$_1	12.5234 ± 0.0013	β = 0.000 ± 0.127
$[Pd_2\mathbf{E}_4]^{4+}$_2	12.0492 ± 0.0027	β = 0.570 ± 0.477
$[Pd_2\mathbf{B}_2\mathbf{D}_2]^{4+}$_1	13.5958 ± 0.0040	β = 21.473 ± 0.711
$[Pd_2\mathbf{B}_2\mathbf{D}_2]^{4+}$_1	13.5309 ± 0.0045	β = 21.716 ± 0.770
$[Co_2\mathbf{ABCD}]^{2+}$	14.3374 ± 0.0028	α = 19.277 ± 0.348

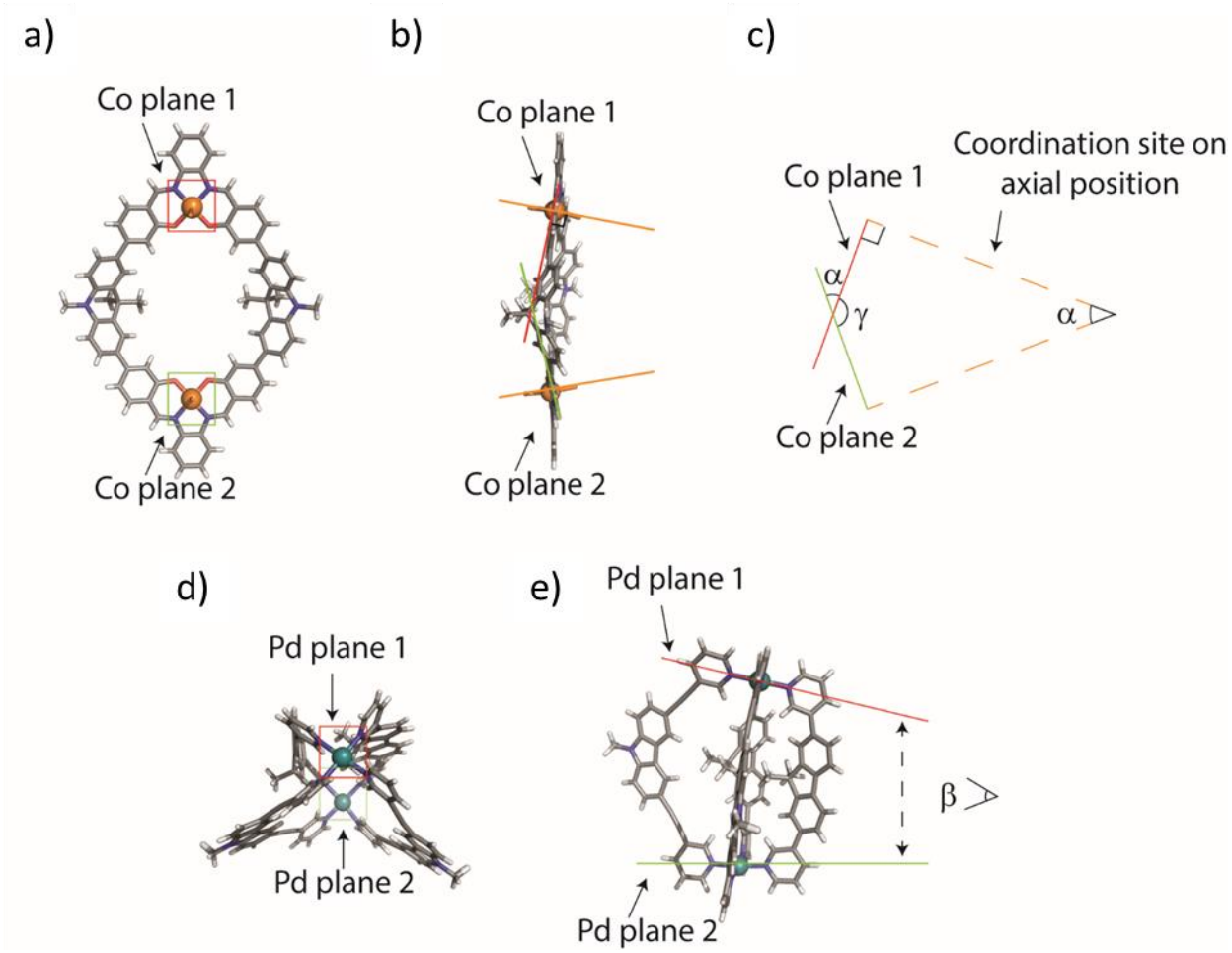

Figure S2.45. a) Cobalt planes are defined by the Co(III) cations and the coordinating O and N atoms from the salphen unit, b) artial X-ray structure of $[Co_2\mathbf{A}_2\mathbf{BD}]^{2+}$, c) schematic diagram of b, as the coordination vectors to the axially-positioned pyridyl ligands form an angel of 90° to the corresponding cobalt planes, the angle formed between the converging axial ligand vectors of the two coordination sites amount to 180° – γ = α; d) palladium planes are defined by Pd(II) and four N atoms from the coordinating pyridines; e) β is the angle formed by the two Pd-planes.

2.9. Reference

[1] V. Brega, M. Zeller, Y. He, H. P. Lu, J. K. Klosterman, *Chem. Commun.* **2015**, *51*, 5077-5080.

[2] S. Löffler, J. Lübben, L. Krause, D. Stalke, B. Dittrich, G. H. Clever, *J. Am. Chem. Soc.* **2015**, *137*, 1060-1063.

[3] N. Kishi, Z. Li, K. Yoza, M. Akita, M. Yoshizawa, *J. Am. Chem. Soc.* **2011**, *133*, 11438-11441.

[4] H. Wang, X. Qian, K. Wang, M. Su, W. W. Haoyang, X. Jiang, R. Brzozowski, M. Wang, X. Gao, Y. Li, B. Xu, P. Eswara, X. Q. Hao, W. Gong, J. L. Hou, J. Cai, X. Li, *Nat. Commun.* **2018**, *9*, 1815.

[5] T. Zhang, L. P. Zhou, X. Q. Guo, L. X. Cai, Q. F. Sun, *Nat. Commun.* **2017**, *8*, 15898.

[6] M. D. Ward, C. A. Hunter, N. H. Williams, *Acc. Chem. Res.* **2018**, *51*, 2073-2082.

[7] D. Fujita, Y. Ueda, S. Sato, N. Mizuno, T. Kumasaka, M. Fujita, *Nature* **2016**, *540*, 563-566.

[8] I. A. Bhat, D. Samanta, P. S. Mukherjee, *J. Am. Chem. Soc.* **2015**, *137*, 9497-9502.

[9] Q.-F. Sun, S. Sato, M. Fujita, *Nat. Chem.***2012**, *4*, 330-333.

[10] S. Pasquale, S. Sattin, E. C. Escudero-Adan, M. Martinez-Belmonte, J. de Mendoza, *Nat. Commun.* **2012**, *3*, 785.

[11] T. Beissel, R. E. Powers, K. N. *Angew. Chem. Int. Ed.* Raymond, **1996**, *35*, 1084-1086.

[12] Y. Ueda, H. Ito, D. Fujita, M. Fujita, *J. Am. Chem. Soc.* **2017**, *139*, 6090-6093.

[13] M. Otte, *ACS Catal.* **2016**, *6*, 6491-6510.

[14] C. J. Brown, F. D. Toste, R. G. Bergman, K. N. Raymond, *Chem. Rev.* **2015**, *115*, 3012-3035.

[15] W. Meng, B. Breiner, K. Rissanen, J. D. Thoburn, J. K. Clegg, J. R. Nitschke, *Angew. Chem. Int. Ed.* **2011**, *50*, 3479-3483.

[16] B. Roy, A. K. Ghosh, S. Srivastava, P. D'Silva, P. S. Mukherjee, *J. Am. Chem. Soc.* **2015**, *137*, 11916-11919.

[17] B. P. Burke, W. Grantham, M. J. Burke, G. S. Nichol, D. Roberts, I. Renard, R. Hargreaves, C. Cawthorne, S. J. Archibald, P. J. Lusby, *J. Am. Chem. Soc.* **2018**, *140*, 16877-16881.

[18] S. K. Samanta, D. Moncelet, V. Briken, L. Isaacs, *J. Am. Chem. Soc.* **2016**, *138*, 14488-14496.

[19] F. Schmitt, J. Freudenreich, N. P. Barry, L. Juillerat-Jeanneret, G. Suss-Fink, B. Therrien, *J. Am. Chem. Soc.* **2012**, *134*, 754-757.

[20] W. Y. Zhang, Y. J. Lin, Y. F. Han, G. X. Jin, *J. Am. Chem. Soc.* **2016**, *138*, 10700-10707.

[21] D. Fiedler, R. G. Bergman, K. N. Raymond, *Angew. Chem. Int. Ed.* **2006**, *45*, 745-748.

[22] P. Mal, B. Breiner, K. Rissanen, J. R. Nitschke, *Science* **2009**, *324*, 1697-1699.

[23] L. A. Wessjohann, O. Kreye, D. G. Rivera, *Angew. Chem. Int. Ed.* **2017**, *56*, 3501-3505.

[24] N. Christinat, R. Scopelliti, K. Severin, *Angew. Chem. Int. Ed.* **2008**, *47*, 1848-1852.

[25] M. Otte, M. Lutz, R. J. M. Klein Gebbink, *Eur. J. Org. Chem.* **2017**, *2017*, 1657-1661.

[26] S. Klotzbach, F. Beuerle, *Angew. Chem. Int. Ed.* **2015**, *54*, 10356-10360.

[27] W. M. Bloch, G. H. Clever, *Chem. Commun.* **2017**, *53*, 8506-8516.

[28] S. Pullen, G. H. Clever, *Acc. Chem. Res.* **2018**, *51*, 3052-3064.

[29] N. Kishi, Z. Li, K. Yoza, M. Akita, M. Yoshizawa, *J. Am. Chem. Soc.* **2011**, *133*, 11438-11441.

[30] M. Yamashina, T. Yuki, Y. Sei, M. Akita, M. Yoshizawa, *Chem. Eur. J.* **2015**, *21*, 4200-4204.

[31] A. M. Johnson, R. J. Hooley, *Inorg. Chem.* **2011**, *50*, 4671-4673.

[32] T. K. Ronson, D. A. Roberts, S. P. Black, J. R. Nitschke, *J. Am. Chem. Soc.* **2015**, *137*, 14502-14512.

[33] Q.-F. Sun, S. Sato, M. Fujita, *Angew. Chem. Int. Ed.* **2014**, *53*, 13510-13513.

[34] W. M. Bloch, Y. Abe, J. J. Holstein, C. M. Wandtke, B. Dittrich, G. H. Clever, *J. Am. Chem. Soc.* **2016**, *138*, 13750-13755.

[35] W. M. Bloch, J. J. Holstein, W. Hiller, G. H. Clever, **2017**, *56*, 8285-8289.

[36] D. Samanta, S. Shanmugaraju, S. A. Joshi, Y. P. Patil, M. Nethaji, P. S. Mukherjee, *Chem. Commun.* **2012**, *48*, 2298-2300.

[37] S. Prusty, K. Yazaki, M. Yoshizawa, D. K. Chand, *Chem. Eur. J.* **2017**, *23*, 12456-12461.

[38] J.-R. Li, H.-C. Zhou, *Nat. Chem.***2010**, *2*, 893-898.

[39] D. Preston, J. E. Barnsley, K. C. Gordon, J. D. Crowley, *J. Am. Chem. Soc.* **2016**, *138*, 10578-10585.

[40] R. Zhu, W. M. Bloch, J. J. Holstein, S. Mandal, L. V. Schafer, G. H. Clever, *Chem. Eur. J.* **2018**, *24*, 12976-12982.

[41] S. Mukherjee, P. S. Mukherjee, *Chem. Commun.* **2014**, *50*, 2239-2248.

[42] D. Bardhan, D. K. Chand, *Chem. Eur. J.* **2019**, *25*, 12241-12269.

[43] M. Yoshizawa, M. Nagao, K. Kumazawa, M. Fujita, *J. Org. Chem.***2005**, *690*, 5383-5388.

[44] V. Maurizot, M. Yoshizawa, M. Kawano, M. Fujita, *Dalton Trans.* **2006**, 2750-2756.

[45] Y.-R. Zheng, Z. Zhao, M. Wang, K. Ghosh, J. B. Pollock, T. R. Cook, P. J. Stang, *J. Am. Chem. Soc.* **2010**, *132*, 16873-16882.

[46] A. K. Bar, G. Mostafa, P. S. Mukherjee, *Inorg. Chem.* **2010**, *49*, 7647-7649.

[47] A. Company, L. Gómez, J. M. López Valbuena, R. Mas-Ballesté, J. Benet-Buchholz, A. Llobet, M. Costas, *Inorg. Chem.* **2006**, *45*, 2501-2508.

[48] L. Gomez, A. Company, X. Fontrodona, X. Ribas, M. Costas, *Chem. Commun.* **2007**, 4410-4412.

[49] C. Garcia-Simon, M. Garcia-Borras, L. Gomez, I. Garcia-Bosch, S. Osuna, M. Swart, J. M. Luis, C. Rovira, M. Almeida, I. Imaz, D. Maspoch, M. Costas, X. Ribas, *Chem. Eur. J.* **2013**, *19*, 1445-1456.

[50] C. García-Simón, R. Gramage-Doria, S. Raoufmoghaddam, T. Parella, M. Costas, X. Ribas, J. N. H. Reek, *J. Am. Chem. Soc.* **2015**, *137*, 2680-2687.

[51] C. Garcia-Simon, M. Garcia-Borras, L. Gomez, T. Parella, S. Osuna, J. Juanhuix, I. Imaz, D. Maspoch, M. Costas, X. Ribas, *Nat. Commun.* **2014**, *5*, 5557.

[52] S. Gaikwad, M. Lal Saha, D. Samanta, M. Schmittel, *Chem. Commun.* **2017**, *53*, 8034-8037.

[53] C. Baleizão, H. Garcia, *Chem. Rev.* **2006**, *106*, 3987-4043.

[54] P. G. Cozzi, *Chem. Soc. Rev.* **2004**, *33*, 410-421.

[55] C. T. L. Ma, M. J. MacLachlan, *Angew. Chem. Int. Ed.* **2005**, *44*, 4178-4182.

[56] Y. Sakata, S. Kobayashi, S. Akine, *Chem. Commun.* **2017**, *53*, 6363-6366.

[57] F. Mamiya, N. Ousaka, E. Yashima, *Angew. Chem. Int. Ed.* **2015**, *54*, 14442-14446.

[58] B. Doistau, A. Tron, S. A. Denisov, G. Jonusauskas, N. D. McClenaghan, G. Gontard, V. Marvaud, B. Hasenknopf, G. Vives, *Chem. Eur. J.* **2014**, *20*, 15799-15807.

[59] B. Doistau, J.-L. Cantin, L.-M. Chamoreau, V. Marvaud, B. Hasenknopf, G. Vives, *Chem. Commun.* **2015**, *51*, 12916-12919.

[60] J. Dong, C. Tan, K. Zhang, Y. Liu, P. J. Low, J. Jiang, Y. Cui *J. Am. Chem. Soc.* **2017**, *139*, 1554-1564.

[61] S. Akine, M. Miyashita, T. Nabeshima, *J. Am. Chem. Soc.* **2017**, *139*, 4631-4634.

[62] S. Akine, M. Miyashita, T. Nabeshima, *Chem. Eur. J.* **2019**, *25*, 1432-1435.

[63] P. R. Symmers, M. J. Burke, D. P. August, P. I. T. Thomson, G. S. Nichol, M. R. Warren, C. J. Campbell, P. J. Lusby, *Chem. Sci.* **2015**, *6*, 756-760.

[64] S. Akine, M. Miyashita, T. Nabeshima, *J. Am. Chem. Soc.* **2017**, *139*, 4631-4634.

[65] P. D. Frischmann, J. Jiang, J. K. H. Hui, J. J. Grzybowski, M. J. MacLachlan, *Org. Lett.* **2008**, *10*, 1255-1258.

[66] A. M. Castilla, S. Curreli, E. C. Escudero-Adán, M. M. Belmonte, J. Benet-Buchholz, A. W. Kleij, *Org. Lett.* **2009**, *11*, 5218-5221.

[67] T. L. Andrew, T. M. Swager, *J. Org. Chem.***2011**, *76*, 2976-2993.

[68] F. Mamiya, N. Ousaka, E. Yashima, *Angew. Chem. Int. Ed.* **2015**, *54*, 14442-14446.

[69] S.-J. Su, D. Tanaka, Y.-J. Li, H. Sasabe, T. Takeda, J. Kido, *Org. Lett.***2008**, *10*, 941-944.

[70] R. Zhu, J. Lubben, B. Dittrich, G. H. Clever, *Angew. Chem. Int. Ed.* **2015**, *54*, 2796-2800.

[71] W. Spartan '08 Version 1.2.0, Wavefunction, Inc., Irvine, CA, **2009**.

[72] G. W. T. M. J. Frisch, H. B. Schlegel, G. E. Scuseria, M. A. Robb, J. R. Cheeseman, G. Scalmani, V. Barone, B. Mennucci, G. A. Petersson, H. Nakatsuji, M. Caricato, X. Li, H. P. Hratchian, A. F. Izmaylov, J. Bloino, G. Zheng, J. L. Sonnenberg, M. Hada, M. Ehara, K. Toyota, R. Fukuda, J. Hasegawa, M. Ishida, T. Nakajima, Y. Honda, O. Kitao, H. Nakai, T. Vreven, J. A. Montgomery, Jr., J. E. Peralta, F. Ogliaro, M. Bearpark, J. J. Heyd, E. Brothers, K. N. Kudin, V. N. Staroverov, R. Kobayashi, J. Normand, K. Raghavachari, A. Rendell, J. C. Burant, S. S. Iyengar, J. Tomasi, M.

Cossi, N. Rega, J. M. Millam, M. Klene, J. E. Knox, J. B. Cross, V. Bakken, C. Adamo, J. Jaramillo, R. Gomperts, R. E. Stratmann, O. Yazyev, A. J. Austin, R. Cammi, C. Pomelli, J. W. Ochterski, R. L. Martin, K. Morokuma, V. G. Zakrzewski, G. A. Voth, P. Salvador, J. J. Dannenberg, S. Dapprich, A. D. Daniels, Ö. Farkas, J. B. Foresman, J. V. Ortiz, J. Cioslowski, and D. J. Fox, Gaussian, Inc., Wallingford, CT, USA, **2009**.

[73] A. Burkhardt, T. Pakendorf, B. Reime, J. Meyer, P. Fischer, N. Stübe, S. Panneerselvam, O. Lorbeer, K. Stachnik, M. Warmer, P. Rödig, D. Göries, A. Meents, *Eur. Phys. J. Plus.* **2016**, *131*.

[74] W. Kabsch, *Acta Crystallogr*. *Sect. D* **2010**, *66*, 125-132.

[75] G. M. Sheldrick, *Acta Crystallogr*. *Sect. A* **2015**, *71*, 3-8.

[76] G. M. Sheldrick, *Acta Crystallogr*. *Sect. C* **2015**, *71*, 3-8.

[77] C. B. Hubschle, G. M. Sheldrick, B. Dittrich, *J Appl Crystallogr*. **2011**, *44*, 1281-1284.

[78] A. Thorn, B. Dittrich, G. M. Sheldrick, *Acta Crystallogr. Sect. A* **2012**, *68*, 448-451.

[79] A. L. Spek, *Acta Crystallogr. Sect. C* **2015**, *71*, 9-18.

[80] A. L. Spek, *Acta Crystallogr. Sect. D* **2009**, *65*, 148-155.

3. Multifunctional Coordination Complexes

3.1. Introduction

We have developed the methodology for the coordination-driven self-assembly of cages with up to four different organic ligands on determined positions, which to the best of our knowledge is the structurally most complicated lantern-shaped coordination cage to date. The emphasis of our next studies is now smoothly shifting from multicomponent to multifunction self-assemblies. In the following part of this chapter, I would like to elaborate on some of the undergoing projects, which relate to the theme “cobalt-salphen based heteroleptic self-assemblies”.

3.2. Multifunctional cages

Utilizing almost the same procedure for the synthesis of cage $[Co_2\mathbf{A}_2\mathbf{E}_2]^{2+}$, a chiral multifunctional heteroleptic cage $[Co_2\mathbf{A}_2\mathbf{F}_2\mathbf{G}_2]^{2+}$ was obtained (Figure 4.1). The ligand precursor **A** reacted with chiral diamine **G** in a ratio of 1 : 1, at 60 °C overnight, providing a yellow precipitate as the product. However, even after purification, hardly a clean the NMR spectrum of the new macrocycle $\mathbf{A}_2\mathbf{G}_2$ can be obtained. The yellow solid was then used directly for the next step without further purification. After addition of Co(acetate)$_2$ in 1,4-dioxane, the colour of the solvent slowly turned to dark brown. The mixture was heated at 60 °C overnight before the phenothiazine-based ligand **F** and NH_4PF_6 was added. Finally, by adding saturated aqueous solution of KPF_6 into the reaction mixture, the target complex $[Co_2\mathbf{A}_2\mathbf{F}_2\mathbf{G}_2]^{2+}$ was collected as dark brown precipitate and further purified by the described method to give 57 % isolated yield (synthesis detail see experimental section). The ^{1}H NMR characterization of $[Co_2\mathbf{A}_2\mathbf{F}_2\mathbf{G}_2]^{2+}$ revealed a single species featuring signals consist of the **A**, **F** and **G** substructures in a 1 : 1 :1 ratio. Also, the ^{1}H-^{1}H NOESY experiment shows clear cross signals, indicating the close contact between the different components. The high-resolution ESI-TOF mass spectrum confirmed cage formation by showing a prominent signal at *m/z*= 1442.6 which perfectly matches with the calculated mass for the formula of $[Co_2\mathbf{A}_2\mathbf{F}_2\mathbf{G}_2]^{2+}$. Since a chiral diamine was introduced to the cage compound, we expected the chirality could be induced to the entire structure. Evidence comes from circular dichroism (CD) spectra, not only in the UV region, but also signal in visible light area has been found, indicated an asymmetric cage is formed.

The successful synthesis of cage $[Co_2\mathbf{A}_2\mathbf{F}_2\mathbf{G}_2]^{2+}$ confirmed our strategy could be a universal approach for producing hetroleptic assemblies. Phenothiazine derivates have been applied for photoredox reactions, [1][2] electron transfer[3] and guest recognition.[4] In combination with chirality provided by component **G**, cage $[Co_2\mathbf{A}_2\mathbf{F}_2\mathbf{G}_2]^{2+}$ exhibits promise to act as asymmetric catalyst and chiral molecular sensor.

In addition, our colleague Qianqian Yan is currently working on the synthesis of multifunctionally $[Co_2\mathbf{A}_2\mathbf{BD}]^{2+}$ type cage equipped with catalytic reactive moieties.

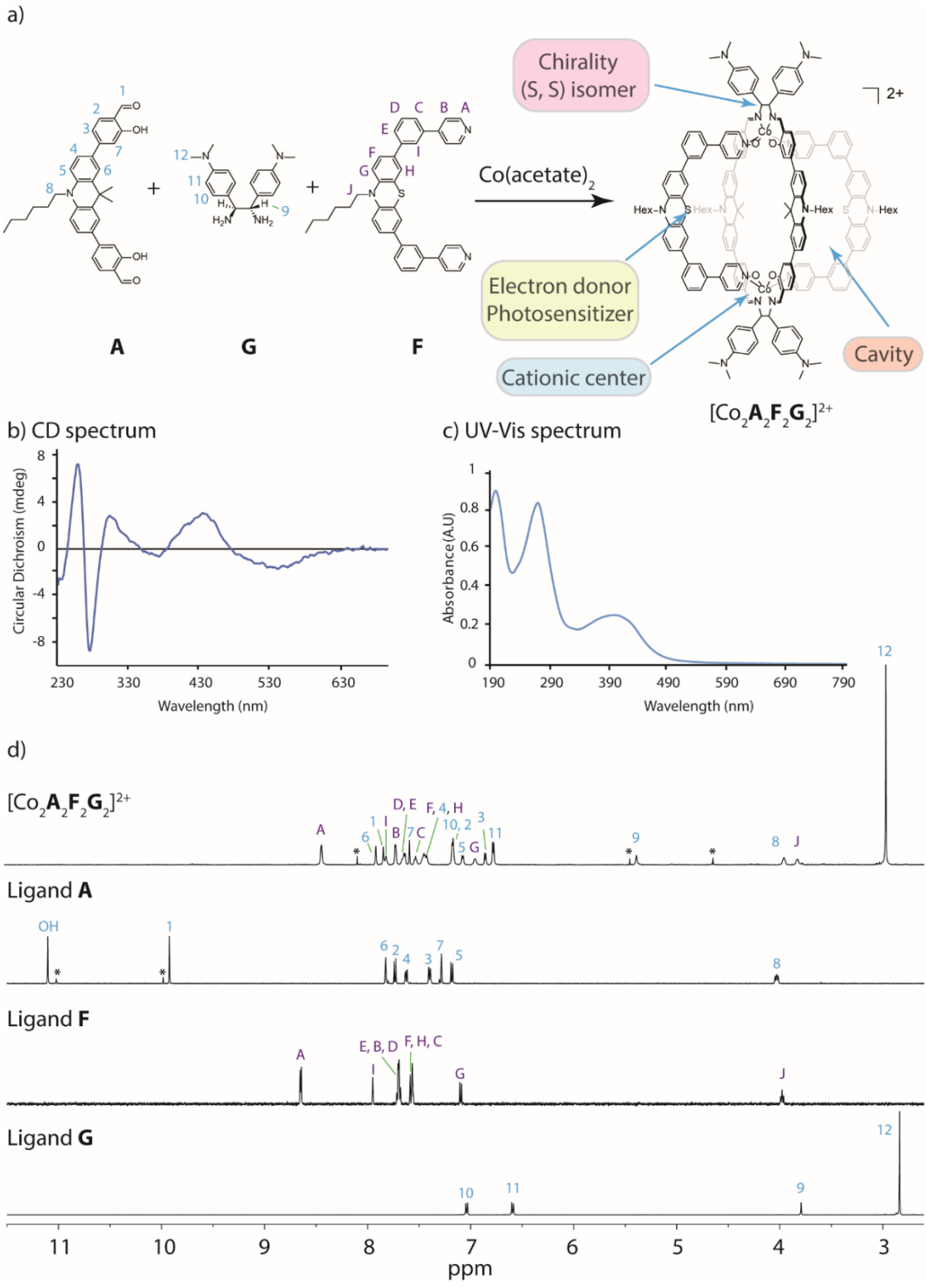

Figure 3.1. a) Synthesis of multifunctional coordination cage $[Co_2\mathbf{A}_2\mathbf{F}_2\mathbf{G}_2]^{2+}$, b) CD spectrum of cage $[Co_2\mathbf{A}_2\mathbf{F}_2\mathbf{G}_2]^{2+}$, c) UV-Vis spectrum of cage $[Co_2\mathbf{A}_2\mathbf{F}_2\mathbf{G}_2]^{2+}$, both c) and d) are measured in CD_3CN, concentration: 0.05 mM, at ambition temperature, d) comparation of ^1H NMR of cage $[Co_2\mathbf{A}_2\mathbf{F}_2\mathbf{G}_2]^{2+}$ with free ligands, all NMR was measured in DCM at ambition temperature.

3.3. Coordination-driven formation of mechanically interlocked molecule.

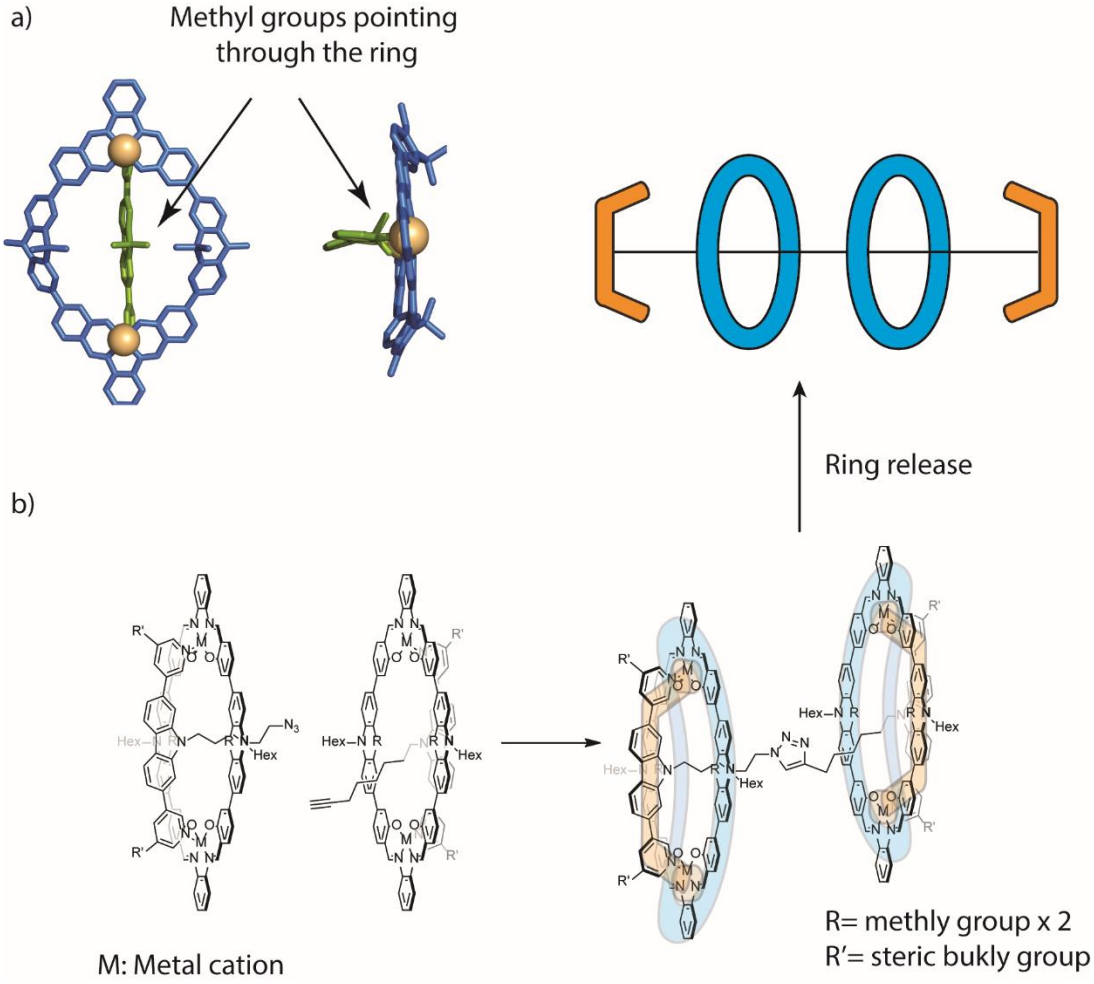

Figure 3.2. a) Partial X-ray structure of $[Co_2\mathbf{A}_2\mathbf{BD}]^{2+}$ revealing the methyl groups on ligand **B** pointing through the macrocycle $\mathbf{A}_2$, b) the proposed synthesis route for making salphen complex based [3] rotaxane.

As we have shown in chapter 2, macrocycle $\mathbf{A}_2$ has a strong preference to bind fluorene-based ligand **B** on one site of the ring, indicating the possibility for formation of bowl-shaped complex $[Co_2\mathbf{A}_2\mathbf{B}]^{2+}$. Based on the X-ray structure (Figure 3.2a), the methyl groups on **B** are pointing through the centre of $\mathbf{A}_2$, inspired by which, we propose that an elongated group on the same position could be forced to cross the macrocycle. If two of this kind of complexes could be connect, for example via click chemistry, a novel [3] rotaxane could be produced by removing the coordinating metal ion or by addition of a competing ligand to displace the ring from ligand **B** (Figure 3.2b), which would be a new approach for synthesis of mechanically interlocked molecules.

3.4. Experimental section

3.4.1. Synthesis of cage $[Co_2A_2F_2G_2]^{2+}$

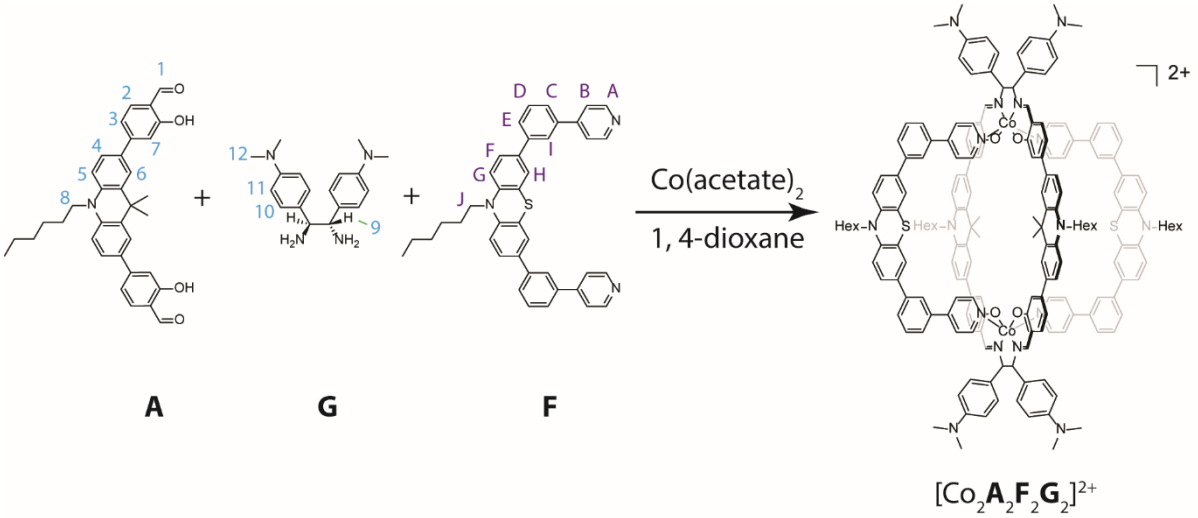

Ligand **A** (2.00 mg**,** 3.75 µmol**,** 1.0 equiv.) and diamine **G** (2.24 mg. 7.50 µmol, 2.0 equiv.) were dissolved in 3ml solvent mixture ($CHCl_3$: MeOH = 2 : 1). The reaction was stirred at 55 °C overnight. Then, the solvent was removed under reduced pressure. The residue was washed with anhydrous methanol (3 × 1 ml) and dried in high vacuum and used directly for the next step without further purification.

The yellow powder produced in the final step was suspended in 2 ml anhydrous 1, 4-dioxane. Combined with $Co(acetate)_2$ (0.67 mg, 3.75 µmol, 1.0 equiv.), the reaction was stirred in ambient atmosphere at 55 °C for 10 h. Subsequently, ligand **F**[8] (2.21mg, 3.75 µmol, 1.0 equiv.,) were added. After reacting for 4 h, the solution was cooled to room temperature. The crude product was precipitated by saturated KPF_6 aqua solution. The brown precipitation was collected and dried under high vacuum. Then, the crude product was dissolved in a minimal amount of DCM and precipitated with Et_2O, this step was repeated for three to four times to provide 3.33 mg (56% yield) of the product as a dark brown solid.

^{1}H NMR (700 MHz, CD_3CN) δ 8.43 (d, *J* = 6.0 Hz, 8H, H_A), 7.91 (s, 4H, H_6), 7.83 (s, 4H, H_1), 7.81 (s, 4H, H_I), 7.72 (d, *J* = 6.0 Hz, 8H, H_B), 7.63 (m, 8H, H_D, H_E), 7.58 (s, 4H, H_7), 7.53 (d, *J* = 8.0 Hz, 4H, H_C), 7.49 – 7.39 (m, 12H, H_F, H_4, H_H), 7.16 (d, *J* = 8.1 Hz, 12H, H_{10}, H_2), 7.06 (d, *J* = 8.5 Hz, 4H, H_5), 6.94 (s, 4H, H_G), 6.85 (d, *J* = 8.2 Hz, 4H, H_3), 6.77 (d, *J* = 8.2 Hz, 8H, H_{11}), 5.38 (s, 4H, H_9), 3.96 (br, 4H, H_8), 3.83 (br, 4H, H_J), 2.97 (s, 24H, H_{12}), 1.76 – 1.70 (m, 8H, CH_2), 1.66 (s, 12H, methyl groups on macrocycle), 1.46 – 1.37 (m, 8H, CH_2), 1.28 (m, 16H, CH_2), 0.82 (q, *J* = 6.8 Hz, 12H, CH_3 on hexyl chain).

ESI-HRMS $[C_{186}H_{180}Co_2N_{16}O_4S_2]^{2+}$: measured: 1442.6192, calculated: 1442.6263.

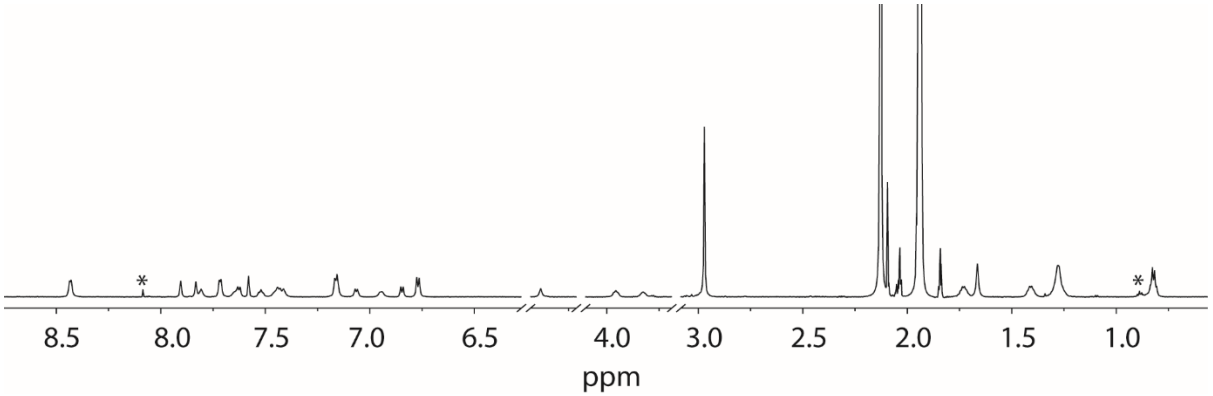

Figure S3.1. ^{1}H NMR spectrum (700 MHz/CD_2Cl_2) of cage $[Co_2\mathbf{A}_2\mathbf{F}_2\mathbf{G}_2]^{2+}$.

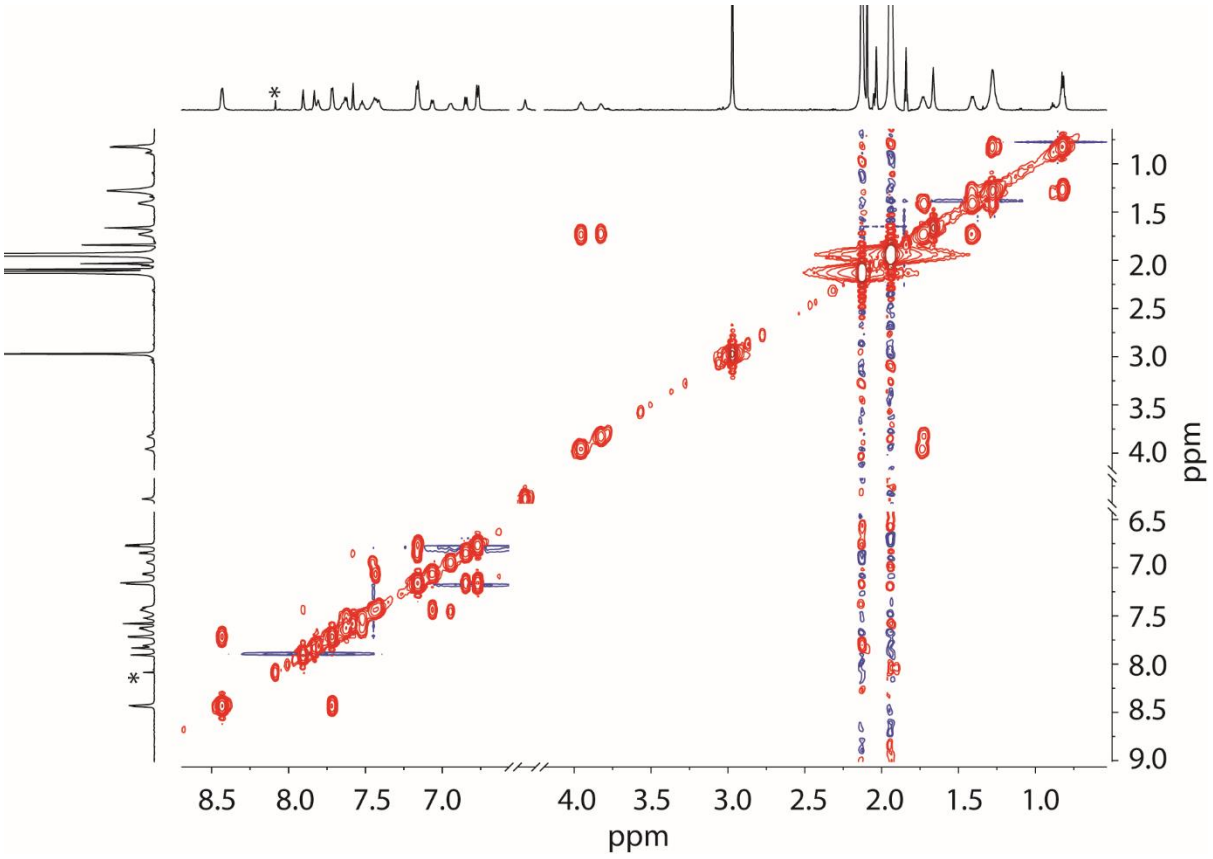

Figure S3.2. ^{1}H-^{1}H COSY spectrum (700 MHz/CD_2Cl_2) of cage $[Co_2\mathbf{A}_2\mathbf{F}_2\mathbf{G}_2]^{2+}$.

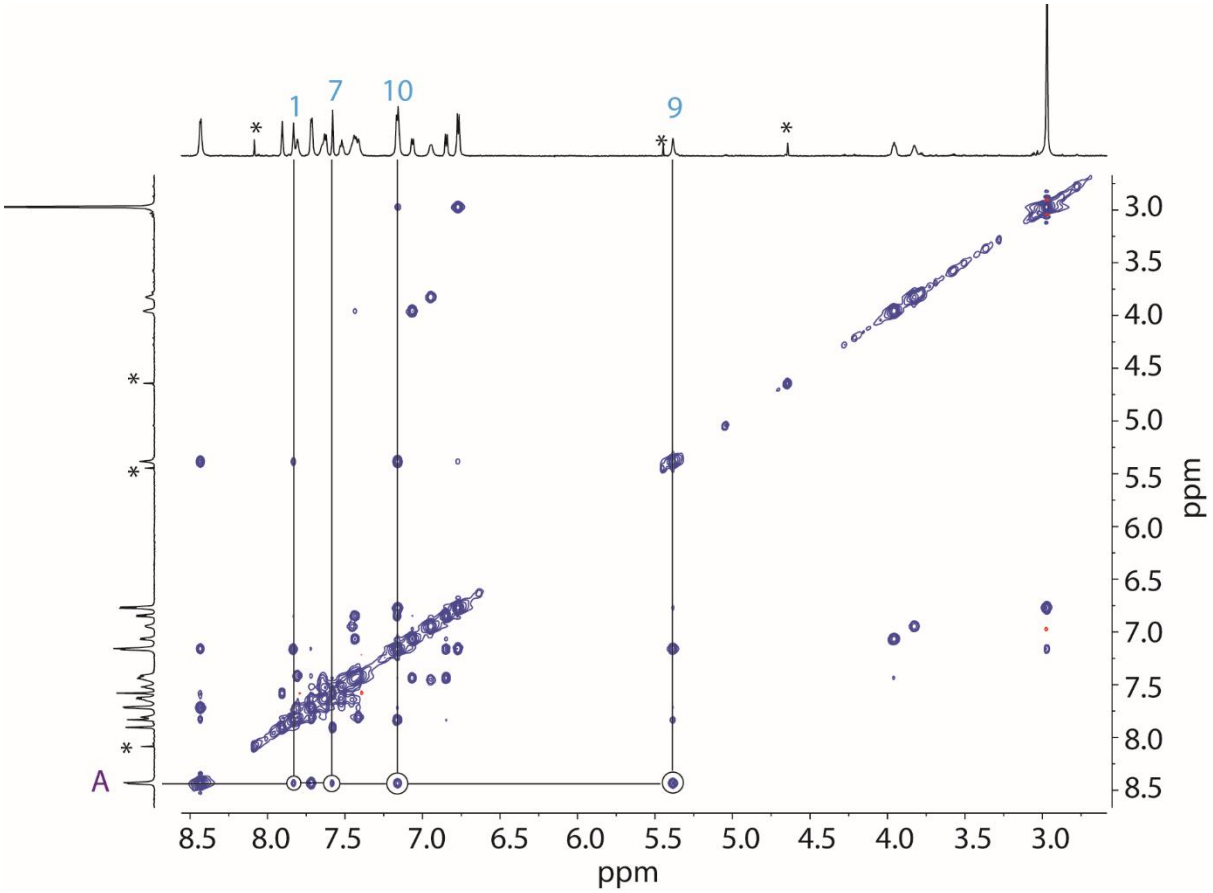

Figure S3.3. Partial ^{1}H-^{1}H NOESY spectrum (700 MHz/CD_2Cl_2) of cage $[Co_2\mathbf{A}_2\mathbf{F}_2\mathbf{G}_2]^{2+}$.

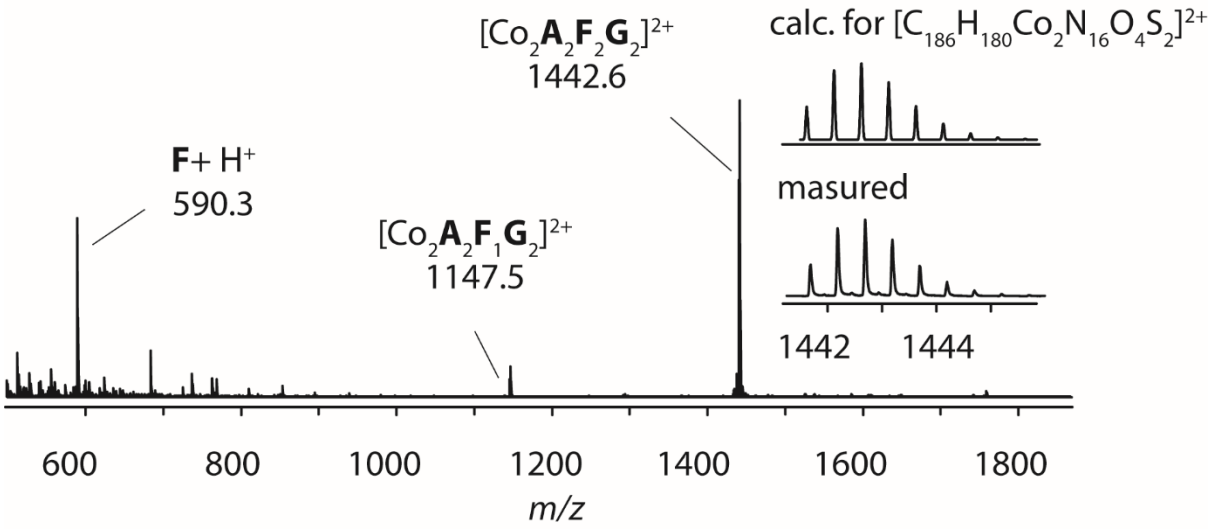

Figure S3.4 HRMS of cage $[Co_2\mathbf{A}_2\mathbf{F}_2\mathbf{G}_2]^{2+}$.

3.5. Reference.

[1] E. H. Discekici, N. J. Treat, S. O. Poelma, K. M. Mattson, Z. M. Hudson, Y. Luo, C. J. Hawker, J. Read de Alaniz, *Chem. Commun.* **2015**, *51*, 11705-11708.

[2] X. Pan, C. Fang, M. Fantin, N. Malhotra, W. Y. So, L. A. Peteanu, A. A. Isse, A. Gennaro, P. Liu, K. Matyjaszewski, *J. Am. Chem. Soc.* **2016**, *138*, 2411-2425.

[3] M. Frank, J. Ahrens, I. Bejenke, M. Krick, D. Schwarzer, G. H. Clever, *J. Am. Chem. Soc.* **2016**, *138*, 8279-8287.

[4] B. Mondal, P. S. Mukherjee, *J. Am. Chem. Soc.* **2018**, *140*, 12592-12601.

[5] K. E. Ebbert, L. Schneider, A. Platzek, C. Drechsler, B. Chen, R. Rudolf, G. H. Clever, *Dalton Trans.* **2019**, *48*, 11070-11075.

[6] S. A. Ewing, M. T. Donor, J. W. Wilson, J. S. Prell, J. Am. Soc. Mass Spectrom. Chem. **2017**, *28*, 587-596.

[7] C. Bannwarth, S. Ehlert, S. Grimme, *J. Chem. Theory Comput.* **2019**, *15*, 1652-1671.

[8] R. Li, *Supramolecular Coordination Cages Based on Light-Switchable Diarylethene Ligands,* Ph.D diss., Technische Universität Dortmund, **2019**.

4. Control of London Dispersion Interactions in Self-Assembled Supramolecular Host-Guest Systems

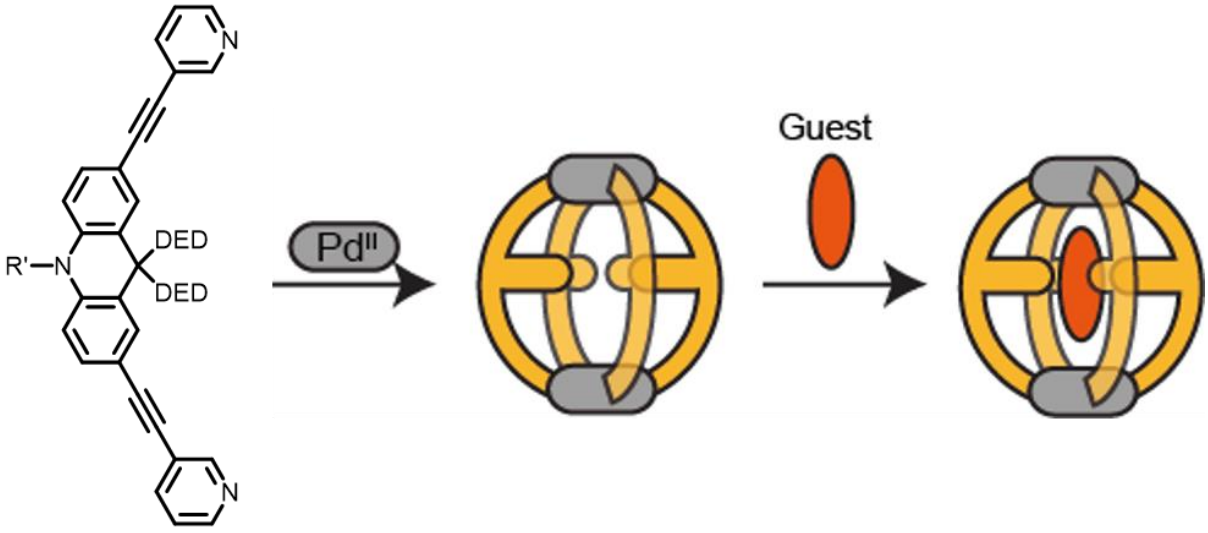

$\mathbf{L}^{Me}$: DED = Methyl
$\mathbf{L}^{Bu}$: DED = *n*-Butyl
$\mathbf{L}^{Ph}$: DED = Phenyl

(DED: dispersion energy donor)

Extra stability?

4.1. Introduction

4.1.1. The nature of London dispersion forces

London dispersion forces belong to the attractive part of the van der Waals force. These interactions are named after the German-American physicist Fritz London, who was the first person to propose the concept.[1][2] London dispersion forces exist everywhere, they can be found in polar or nonpolar molecules, in atoms , huge supramolecular structures and polymers, in gases, liquids and solids. Nature utilizes London dispersion effects to build up spherical bilayer biological membrane, without dispersion effects, noble gases would be never in liquid state, no matter how the temperature or pressure changed, also, it would be impossible for a gecko to walk up a wall (Figure 4.1).[3]

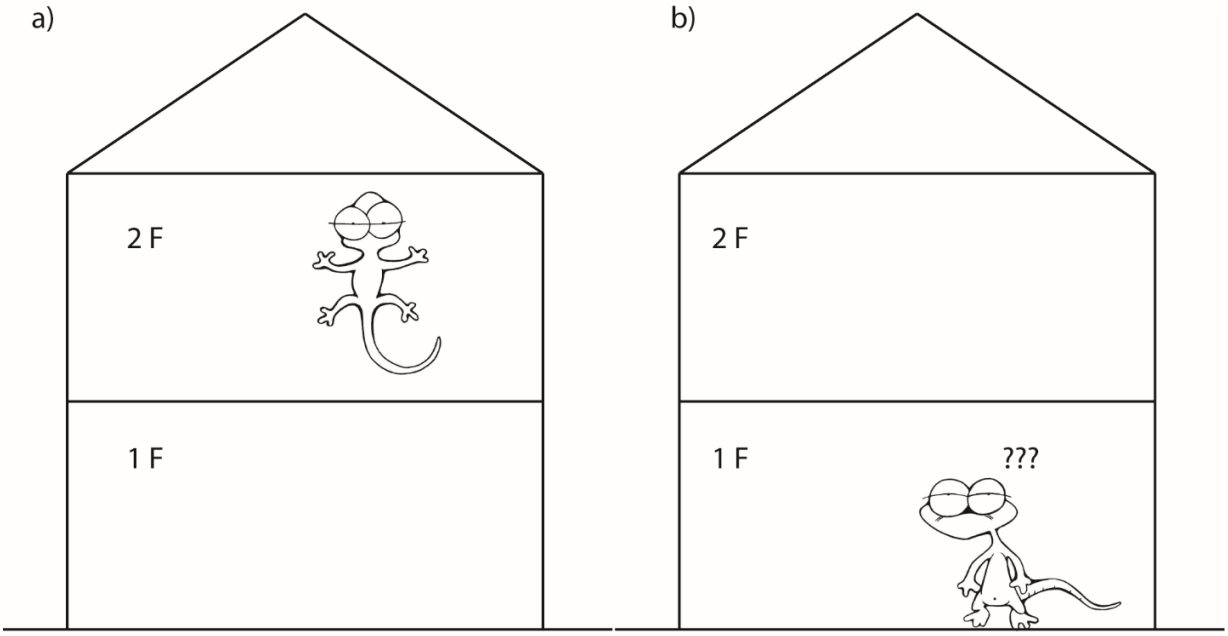

Figure 4.1. Benefitting from the adhesion in the millions of setae on the toes, a gecko can walk stably on a surface of glass or a wall, the mechanism of this phenomenon has attracted a lot of interests in scientists. After being studied for over a century, the secret is unlocked as van der Waals forces,[3] of which London dispersion interactions belong to the attractive part. a) With the help of London dispersion effects, the gecko is walking on a wall; b) without London dispersion forces, the gecko can only walk on the ground.

Owning to non-uniform distributions of negative and positive charges on a molecule, a dipole moment can be formed. The instantaneous dipole formed in atoms or molecules is the reason to cause dispersion effect. The electrons around atom or molecule are moving constantly, this movement can lead to an unsymmetrically distribution of electrons and produce a temporary dipole of the atom or molecule. Then the neighbouring atom or molecule is influenced by the dipole and induces a redistribution of electrons, which enable an attractive interaction between the two moieties, namely, London dispersion force (Figure 4.2). London dispersion forces together with Keesom forces

(permanent–permanent dipoles interaction) and Debye forces (permanent-induced interaction) are known as van der Waals forces.

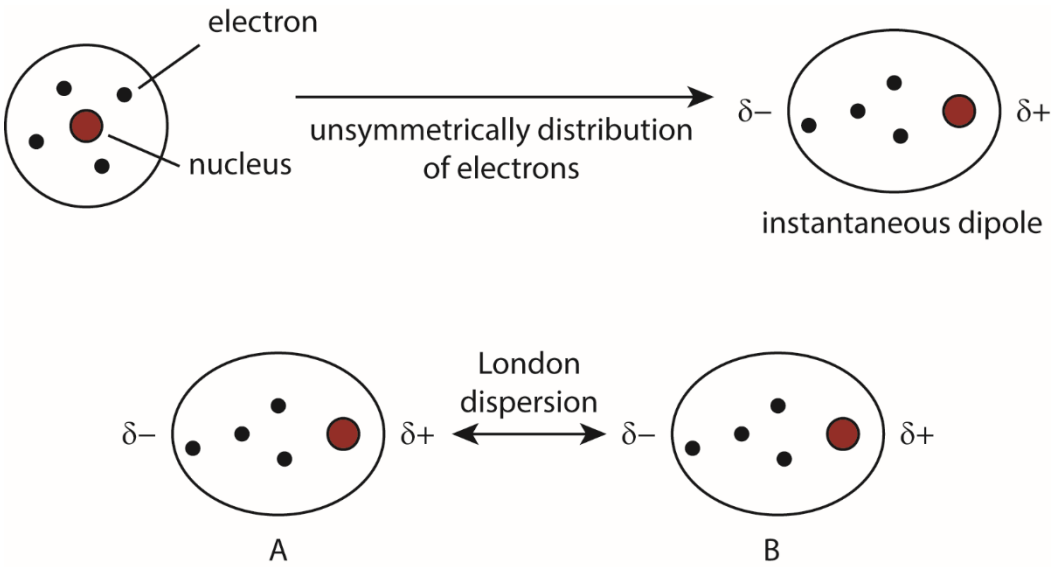

$$E_{\text{disp}} = -\sum_{AB}^{atom\ pairs} \frac{C_6^{AB}}{R_{AB}^6}$$

Figure 4.2. The generation of London dispersion (LD) interaction between two adjacent atoms. The equation at the bottom is a semiclassical approximation for the description of LD force between the atom A and B. R_{AB} is the distance between atom A and B. C_6 is an average dipole-dipole dispersion coefficient (for light elements), which roughly equal to 10 E_h $Bohr^6$ (E_h = Hartree).[4]

There are several factors that can increase the strength of London dispersion forces.[1][2] The dispersion energy can be described with the semiclassical approximation (Figure 4.2 bottom),[4] which shows that London dispersion is highly distance dependent. Polarizability is also directly related to the strength of London dispersion forces. Compared to relatively small atoms, large and heavy atoms are easier to be polarized and form instantaneous dipoles, thus benefit more from London dispersion interactions. The strength of London dispersion forces is in direct proportion to the number of interacting atoms. For a long time, London dispersion forces have not drawn enough attention of chemists, especially in the field of synthetic organic chemistry and inorganic chemistry, because they are the weakest noncovalent interactions. Nevertheless, as the number of pairwise interactions between atoms of two or more molecules increases, the strength of the attractive forces could be equal or even surpass the strong forces like covalent or electrostatic interactions (Figure 4.3).[4] The last factor is the contact area between molecules. It has been shown that polyhedral and branched alkanes are more likely to benefit from dispersion interactions.[5][6]

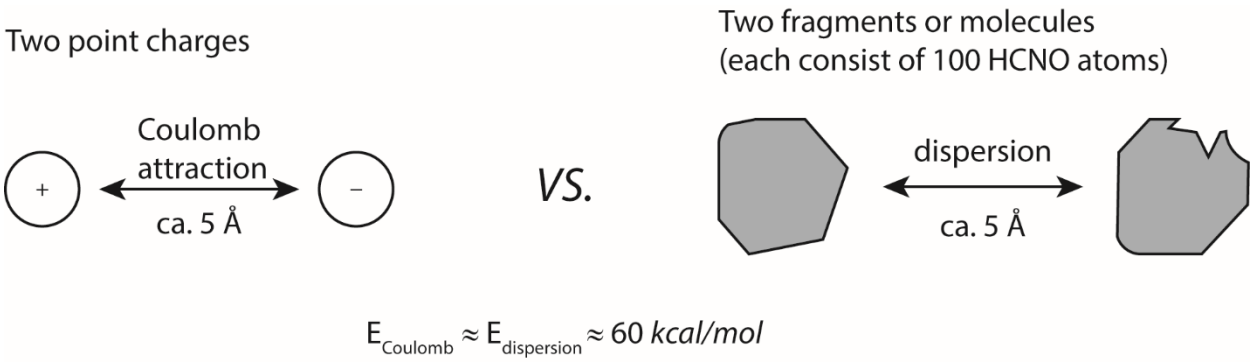

Figure 4.3. The coulomb interaction energy (E) of two interacting point charges (left) has the same magnitude compared to dispersion interaction energy produced by the system on the right side at a distance around 5 Å, in which each of the two fragments has 100 dispersion interacting atoms. Adapted from Ref[4].

4.1.2. Repulsion versus stabilization

Sterically bulky substituents, like *t*-butyl or adamantyl groups, are usually used to provide steric hindrance to hinder a reaction or to block a reactive site. However, these large groups could also help to stabilize structures with their London dispersion contributions and provide unexpected results. For example, hexaphenylethane (Figure 4.4a) is unstable and all the attempts to synthesize this molecule are unsuccessful due to the steric repulsion provide by the phenyl groups. On the other hand, a sterically much more crowded derivate of hexaphenylethane (Figure 4.4b) was successfully synthesized. This compound is stable at room temperature and the crystal structure has been resolved by X-ray, providing a C-C bond with a remarkable length of 1.670 Å (Figure 4.4b).[7] According to recent studies, the structure is mainly stabilized by London dispersion forces coming from the twelve *t*-butyl substituents.[8][9]

In the year 2011, Schreiner et al. reported the syntheses of a series of diamondoid ethane derivates.[10] Among all the products, the adduct produced by coupling of triamantane and diamantane (Figure 4.4c) has a C-C bond as long as 1.704 Å, which is the longest reported C-C bond in alkanes. Despite the extreme length of the C-C bond, the compound is very stable, showing decomposition only when temperatures reach over 200 °C. On the basis of DFT calculations, this high stability a result of the dispersive interactions between the intramolecular contact surface.

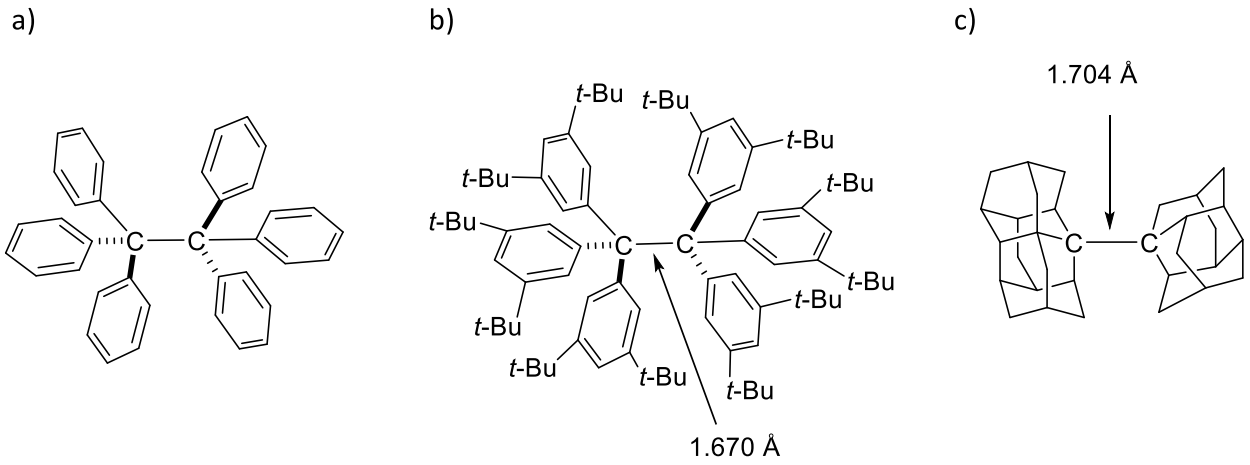

Figure 4.4. Very long carbon-carbon bond stabilized by London dispersion forces, a) hexaphenylethane, not stable due to the steric repulsion from the phenyl groups. b) all-*meta*-*tert*-butyl derivate of hexaphenylethane, stable at room temperature,[7] c) diamondoid ethane derivate formed by coupling of triamantane and diamantane moieties, provide the longest carbon-carbon bond in alkanes.[10]

In the former work of our group, a sterically overcrowded supramolecular cage $[Pd_2\mathbf{L}^{4.1}{}_4]^{4+}$ was obtained by self-assembly of adamantly group functionalized banana-shaped ligands with square-planar Pd(II) ions (Figure 4.5).[11] Due to the steric hindrance provide by the bulky group, the adamantly substituent bends sideways out of the ligand surface and is flipping rapidly from side to side. These dynamics has been studied comprehensively, not only for the ligand, but also in the self-assembled cage. Interestingly, the cage can bind relatively big anionic guests into its cavity and tune the flipping dynamic with the encapsulation. A prominent dispersion contribution between the guests and adamantly groups has been confirmed by the electronic structure calculations, which helps stabilizing of the host-guest complexes.

Unexpected results like the cases mentioned above lead to a revaluation of the role that sterically bulky groups play in the chemical structure. Appropriate adjusting of the balance between steric repulsion and attractive dispersion interactions, gives new points of view for the consideration of molecular structure design, stability and reactivity.[12][13]

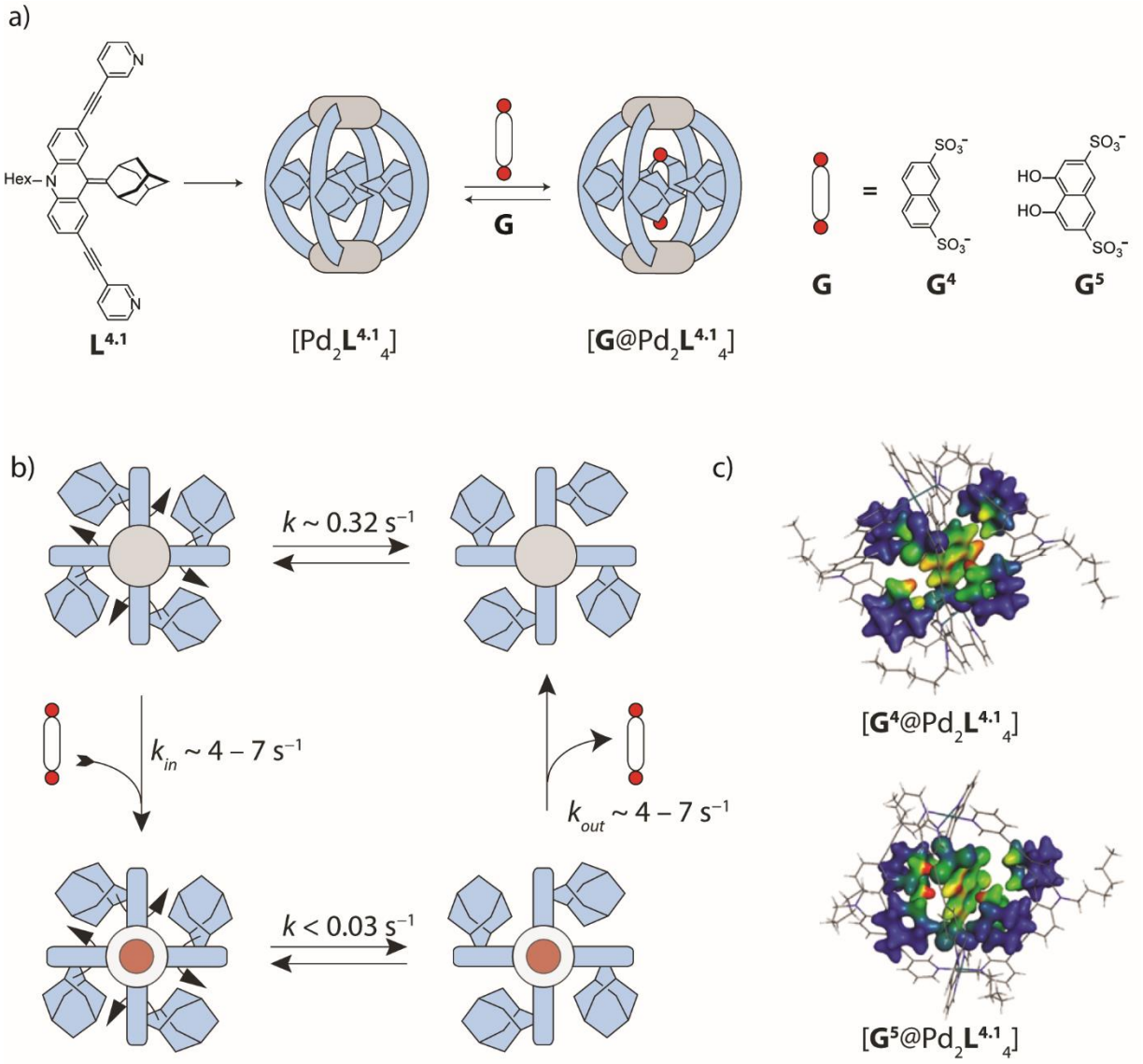

Figure 4.5. Sterically overcrowded self-assembled cage, a) cage formation with adamantyl group functionalized banana-shaped ligand and anionic guest encapsulation, b) flipping dynamics in the cage tuning by guest binding and releasing, c) map of dispersion interaction densities (DID) for host-guest complexes. Red means high DID and blue means low DID. Adapted from Ref[11]. © The Royal Society of Chemistry

4.1.3. London dispersion interactions in host-guest chemistry in organic solvents

In the field of supramolecular chemistry, the importance of dispersive interactions has drawn considerable attention. Since interactions like π-π stacking and edge-to-face attraction are proven to be driven mainly by dispersion interactions,[14][15][16] it is not difficult to find examples about utilizing London dispersion forces in self-assembly or guest binding. [16][17][18][19]

For instance, owing to the unique physical and chemical properties, C_{60} and its derivates have shown versatile applications in material science. It also attracts a lot of interests of supramolecular chemists to study the development of fullerenes binder for different prospers. In the year of 2011, a cubic cage was reported by the group of Nitschke, which can bind C_{60} into its cavity through π-π interactions between the porphyrin walls and the guests (Figure 4.6a).[20] According to their further investigation, the cubic cage also binds C_{70} with a significantly higher binding affinity due to a larger contact area of C_{70} compared to C_{60}. In the same year, Yoshizawa group successfully made a fullerene binder using an anthracene based-ligand coordinating to $Pd_2(NO_3)_4$ in DMSO (Figure 4.6b).[21] In addition, Fujita and co-workers utilize a coronene functionalized self-assembled supramolecular sphere for C_{60} encapsulation (Figure 4.6c).[22] Later, in 2013, Yoshizawa and co-workers developed a new generation of their anthracene ligand based on the former work, which forms a peanut-shaped cage by self-assembly and successfully binds two fullerene molecules (Figure 4.6d).[23] Furthermore, in 2017, Nitschke's group published a novel tetrahedral cage able to encapsulate up to four C_{60} into the cavity in $PhNO_2$ solution (Figure 4.6e).[24] Recently, our group reported a self-assembled system for fullerene binding.[25] By engineering the coordination site, we are able to prepare a $[Pd_2L_4]^{4+}$ type cage, which only selectively binds C_{60}; a $[Pd_2L_3]^{4+}$ bowl-shaped structure, which can encapsulate both C_{60} and C_{70} and were used as a protecting group for C_{60} selective functionalization. The bowl-shaped structure can also be bridged by sterically low-demanding dicarboxylate ligands to form pill-shaped dimers that able to bind two fullerenes (Figure 4.6f).

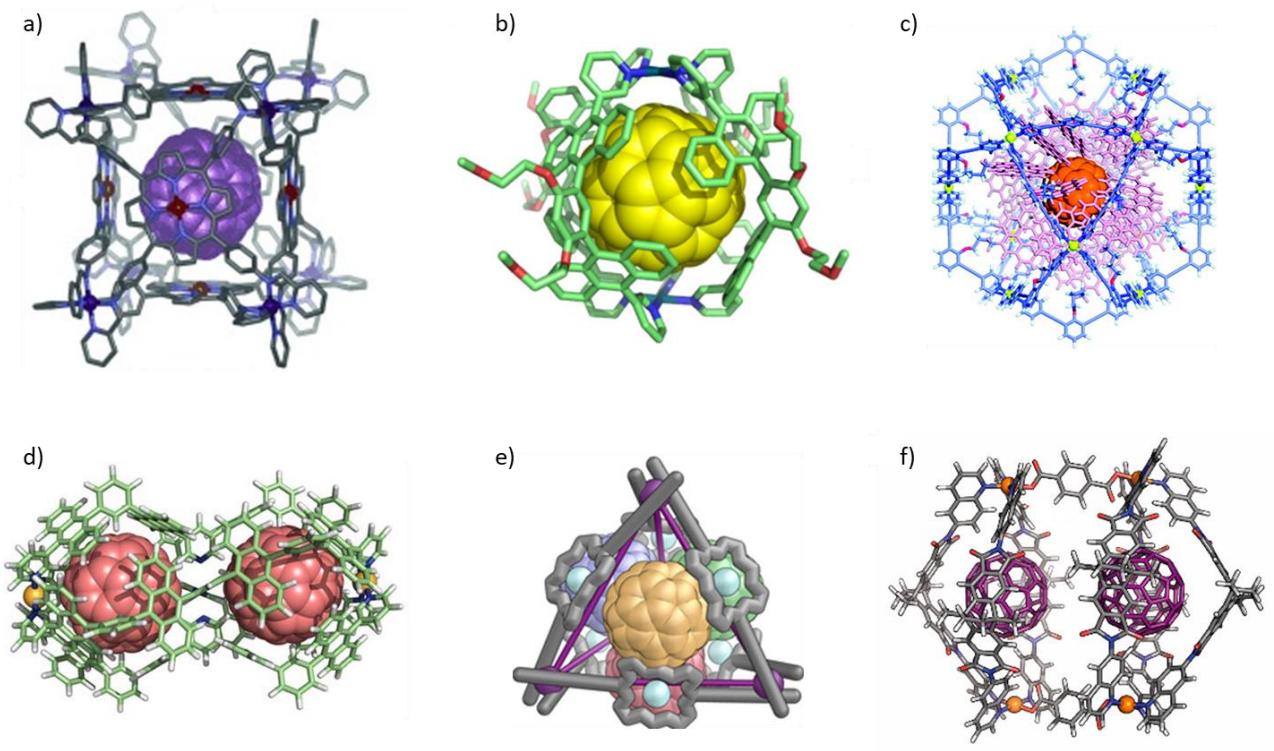

Figure 4.6. Artificial fullerene binders, a) cubic cage functionalized with Ni-porphyrin binding C_{60}, reported by Nitschke group, adapted from Ref[20]. © Wiley-VCH Verlag GmbH & Co. KGaA, Weinheim. b) X-ray structure of anthracene based $[Pd_2L_4]^{4+}$ cage from Yoshizawa group binding C_{60}, adapted from Ref[21]. © American Chemical Society. c) self-assembled supramolecular $[Pd_{12}L_{24}]^{24+}$ sphere from Fujita group binding C_{60}, adapted from Ref[22]. © American Chemical Society; d) force-field calculation optimized structure of peanut cage encapsulating two fullerenes reported by Yoshizawa group, adapted from Ref[23]. © Springer Nature; e) Ni-porphyrin based tetrahedral cage binds four C_{60} inside of the cavity, reported from Nitschke group, adapted from Ref[24]. © American Chemical Society; f) PM6-optimized structure of bridged pill-shaped dimer with two fullerenes from Clever group, adapted from Ref[25]. © American Chemical Society.

Beside stabilization of host-guest complexes using π interactions in various aromatic systems, there are only a handful of systems that have been reported able to enclose small nonaromatic neutral guests in organic solvent. As the size of the guest molecules getting smaller, the strength of dispersion forces decreases rapidly due to lack of interacting pairs. This makes it more challenging to design a system able to encapsulate neutral guests taking advantage of London dispersion effects. In such a case, to increase the intensity of London dispersion, a matched shape of guest molecule to host cavity is particularly important.[26]

Cryptophanes are a class of organic host, which consist of two cyclotriveratrylene units connect by three aliphatic linkers. Since 1980s, this artificial host has been synthesized and studied to capture small noncovalent neutral guests, such as xenon, methane and chloroform, in organic solvents, where the hydrophobic effect does not exist.[27–31] Based on a series of investigations, the association affinities were found to be highly related to the shape complementarity between the host cavity and the guest molecules. For example, all three cryptophanes in Figure 4.7 are able to encapsulate chloroform as

guest. The association constant measured at 300 K using 1,1,2,2,-tetrachloroethane as solvent for cryptophane-A is 230 M^{-1},[30] for cryptophane-E the binding is slightly stronger (K_a= 470 M^{-1}) because of the larger cavity size.[29] However, for the modified marine cyclopeptides, the binding constants increased dramatically to 140,000 M^{-1}.[32] The extremely high affinity is supposed to be related to dispersion interactions since the shape of the cavity perfectly fits the geometry of the chloroform molecule. Meanwhile, in the case of cryptophane-A and E, it has been believed that the solvent molecules, which could exist in the host cavity, are responsible for the relatively low binding affinity.

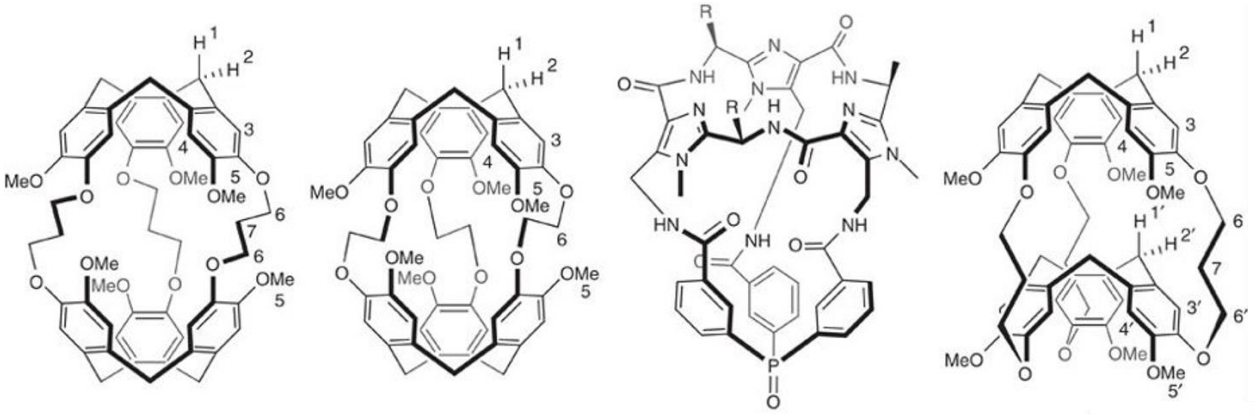

4.2 (cryptophane-E) **4.3** (cryptophane-A) **4.4** R = *i*Pr *Impl*-**4.2** (imploded cryptophane-E)

Host	Solvent	K_a (M^{-1})	ΔG (kcal/mol)
Cryptophane-E (**4.2**)	$C_2D_2Cl_4$	250 ± 50	− 3.3
	C_6D_5Cl	870 ± 50	− 4.0
	C_6D_5Br	940 ± 50	− 4.1
	$C_6D_4Cl_2$	26,000 ± 4,000	− 6.0

Figure 4.7. Top: chemical structure of cryptophanes; bottom**:** experimental results from NMR titration using $CHCl_3$ as guest. All experiments were performed at 298 K. Adapted from Ref[33]. © The Royal Society of Chemistry.

To prove this view of point, in 2014, Bandmann and co-workers investigated the association constants of cryptophane-E, with $CHCl_3$ as guest, in different solvents.[33] As a result, in larger solvent like 1,2-dichlorobenzene, the binding constant (K_a) increase to 26,000 M^{-1}, which is two orders of magnitudes higher compare to K_a in 1,1,2,2,-tetrachloroethane. Based on DFT simulation, the strong binding is mainly dominated by London dispersion forces. It has been confirmed through theoretical calculation, despite all the solvent molecules are able to go inside of the host cavity, the large solvent molecules bind less effectively, which helps increasing the binding affinity of $CHCl_3$ (Figure 4.7 bottom). Interestingly, the calculation also shows that empty cryptophane-E is an unstable species, it will either

turn into the imploded form (Figure 4.7 *Impl*-**4.2**) because of intramolecular dispersion effects between two cyclotriveratrylene units, or it will capture a guest into its cavity immediately.

Not long ago, the Clever group has developed a unique system, which could encapsulate various natural guests in organic solvent.[34] By coordination of square planar Pd(II) with acridone-based banana-shaped ligands in CD_3CN, an interpenetrated double cage was formed, through a monomeric cage as intermediate, with three cavities, all filled with BF_4^-, which is the counter ion of the palladium salt. The two outer pockets show extremely high binding affinity to halide anions. Surprisingly, after addition of Cl^-, the middle pocket was found able to take up neutral guests like benzene and cyclohexane, which cannot happen if the double cage is not previously activated by the binding of Cl^-. In other words, the neutral guest encapsulation is triggered by the addition of chloride anions (Figure 4.8a). According to X-ray structures, by binding of Cl^-, the size of the outer pockets is shrinking and meanwhile the volume of the middle pocket is increased, which is supposed to be responsible for neutral guest binding (Figure 4.8b).

Subsequently, to have a comprehensive understanding of the system, the authors have studied the binding behaviour with over 50 small neutral guests.[35] As result, the three-dimensional guest DABCO shows the strongest binding, 6-membered rings with heteroatoms on the para-position are favourable to bind in the cavity; Furthermore, the bridged 6-rings also form relatively stable host-guest complexes. The packing coefficient (PC) of the guest also plays a role on the strength of the association constant. On the base of calculation, the optimized packing coefficient for the guests is around 56%. Both decrease or increase the size of the guests can lead to a lower association constant, which could be the explanation of the weakly binding for the 5-membered ring guests. Besides, guests with one methyl substituent show relatively low binding affinity, two substituents and noncyclic guests cannot be encapsulated at all (Figure 4.8d). Most importantly, electronic structure calculations indicate the neutral guest encapsulation is highly stabilized by London dispersion forces. For instance, by enclosing of DABCO, the calculated dispersive interaction energy contributions are up to –134.4 kJ/mol. For a number of guests, the binding constants are in direct proportion to the calculated contributions of dispersive energy (Figure 4.8e).

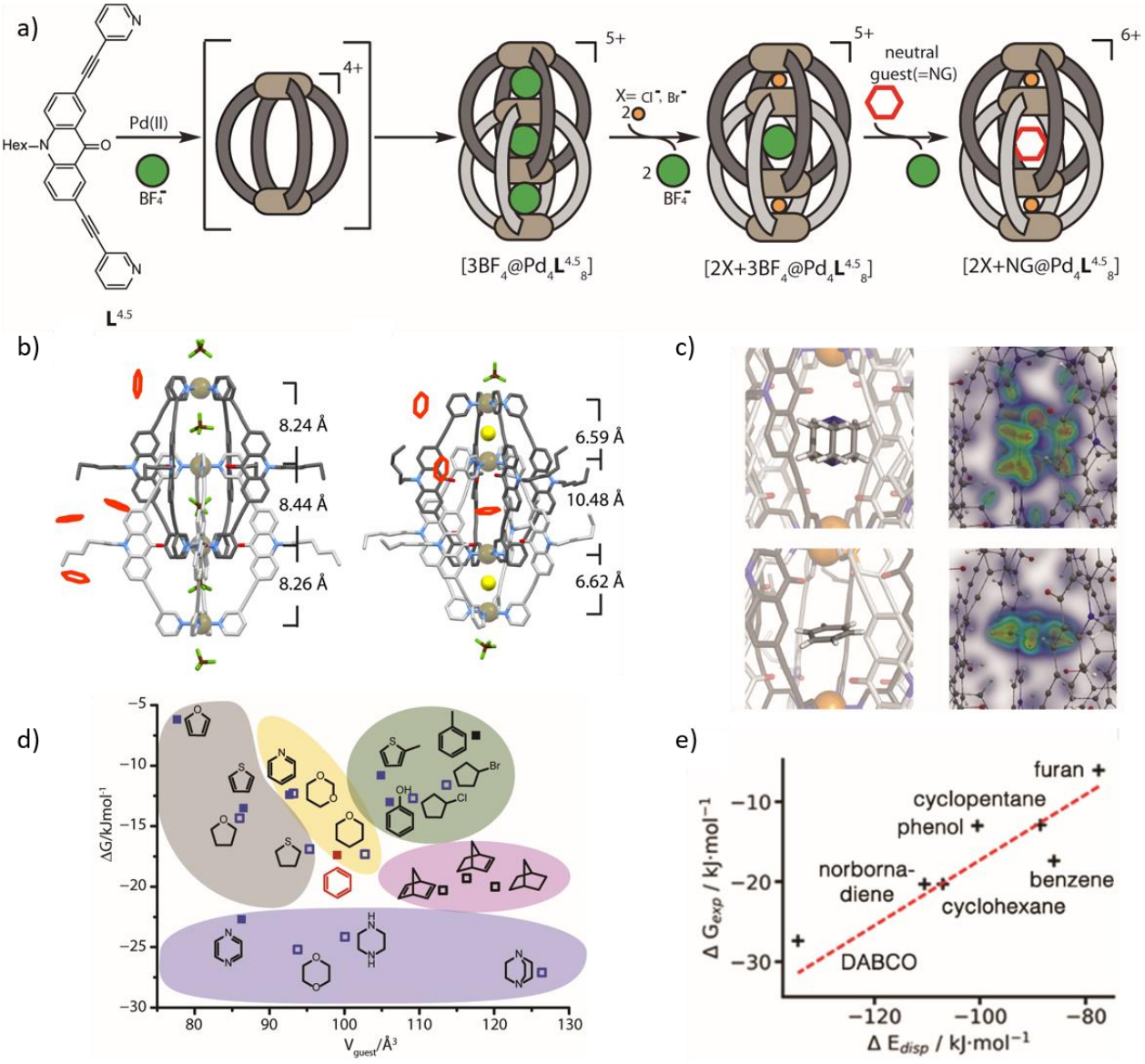

Figure 4.8. a) Schematic diagram of interpenetrated double cage self-assembly and neutral guest binding triggered by addition of halide anions; b) X-ray structures of interpenetrated double cages $[3BF_4@Pd_4\mathbf{L^{4.5}}_8]^{5+}$ (left) and $[2Cl+BF_4@Pd_4\mathbf{L^{4.5}}_8]^{5+}$ (right), with Cl^- binding in the two outer pockets, the Pd-Pd distances shrank from 8.2 Å to 6.6 Å, while the Pd-Pd distance for the middle pocket expanded to 10.5 Å; c) X-ray structures of DABCO (top) and benzene (bottom) binding inside of the middle cavity and the calculated dispersion interaction densities (DID), red means high DID and blue means low DID; d) experimental binding free energy against the volume of different guests with heteroatoms, substituents, ring-size; e) experimental binding free energy against calculated dispersive energy contributions, which shows the stronger binding are relevant to larger dispersion interactions. Adapted from Ref[34][35]. © American Chemical Society, The Royal Society of Chemistry.

4.2. Aims and objectives

In recent years, the importance of London dispersion forces for the stabilization of self-assembled structures is becoming increasingly clear. However, it is still challenging to control dispersion effects in an efficient way, especially in organic solvent, since solvent molecules can strongly quench dispersion interactions.[36] To increase the strength of London dispersion interactions, usually a large number of atoms are demanded. As a disadvantage this could destabilize the system due to the growing steric repulsion. Thus, a careful adjustment of the balance between London dispersion and repulsion is required, about which there is still lot of room for improvement. In this project, we attempted to utilize London dispersion interactions for providing host-guest complexes with extra stability. Therefore, three endohedrally functionalized banana-shaped ligands with nonpolar substituents, such as methyl, *n*-butyl and phenyl groups, were synthesized. Those substituents are supposed to work as dispersion energy donors (DED). All the ligands are designed to form coordination-driven self-assembled monomeric cages, which are able to encapsulate small anionic guests. Because of London dispersion interactions, thermodynamically more stable host-guest complexes are expected to form by the more crowded cages. The stabilities of the host-guest complexes were evaluated by means of association constants that can be determined by different methods, including NMR titrations and ITC experiments. In combination with theoretical calculations, we expected to get a better understanding about the control of London dispersion forces in supramolecular assemblies.

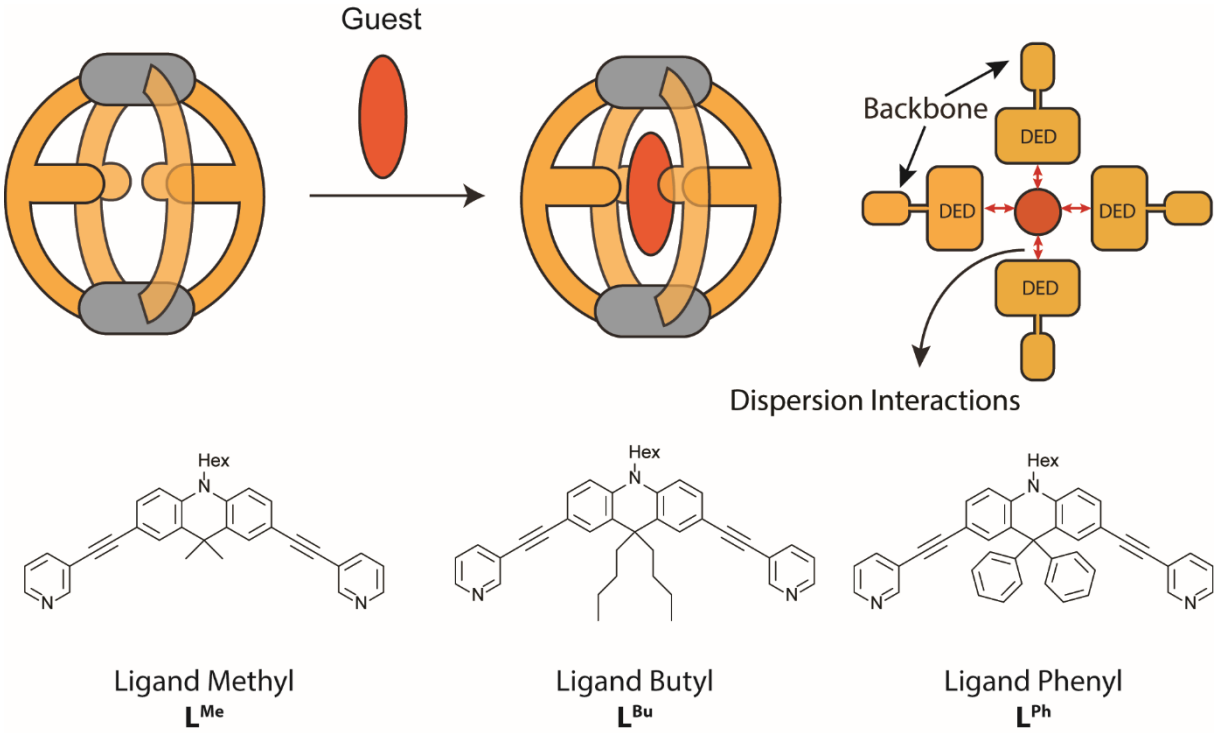

Figure 4.9. Schematic diagram of dispersion effect working on the coordination-driven self-assembled cages and dispersion energy donor groups functionalized banana-shaped ligands.

4.3. Ligand synthesis and cage assembly

The banana-shaped ligands were synthesized following the route shown in Figure 4.10. The DED group functionalized acridine derivates (**9a**-**9c**) were produced by Grignard reaction followed by ring-closure reaction using concentrated phosphoric acid. In order to increase solubility of the final products, an *n*-hexyl chain was attached by nucleophilic substitution (**10a**-**10c**). The products were then halogenated using NBS (**11a**-**11c**). The final ligands (**12a**-**12c**) were synthesized by a Sonogashira coupling reaction. All ligands were further purified by GPC before cage assembly.

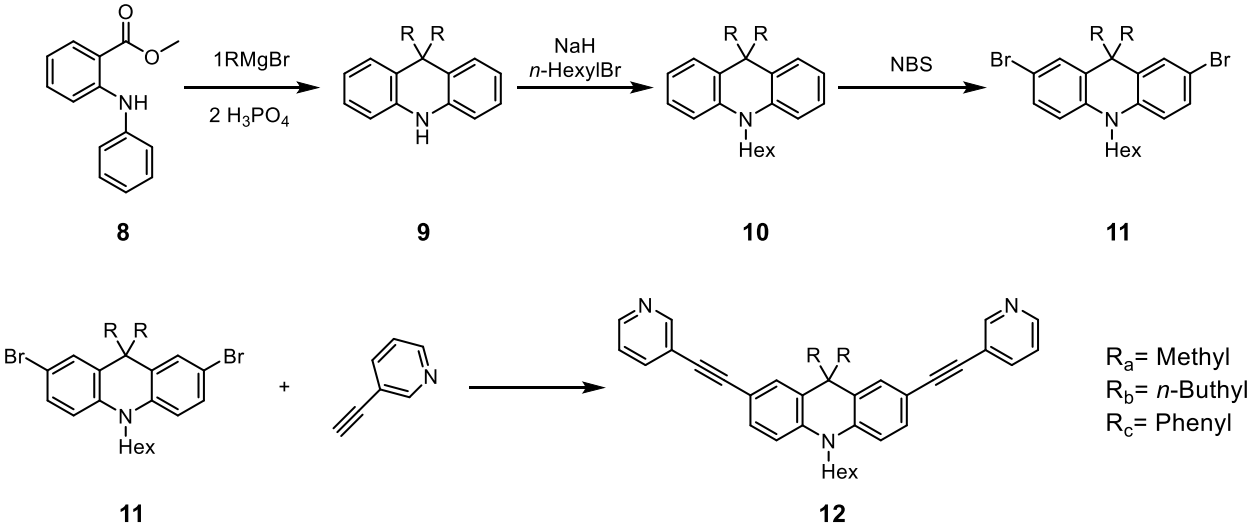

Figure 4.10. Synthetic route towards DED group-functionalized banana-shaped ligands.

After the successful syntheses of the ligands, their ability to form supramolecular cage complexes was examined. For instance, for the self-assembly of cage $[Pd_2\mathbf{L}^{\mathbf{Bu}}{}_4](BF_4)_4$, $\mathbf{L}^{\mathbf{Bu}}$ was first dissolved in CD_3CN (2.8 mM, 1.0 eq., 1 ml), then 0.5 eq. of $[Pd(CH_3CN)_4](BF_4)_2$ (15 mM stock solution in CD_3CN) was added. After heating at 70 °C for 1 h, coordination cage $[Pd_2\mathbf{L}^{\mathbf{Bu}}{}_4]^{4+}$ was formed. The structure was characterized by NMR spectroscopy and HRMS. Comparison to free ligand $\mathbf{L}^{\mathbf{Bu}}$, an obvious down field shifting of protons H_a and H_b has been observed due to coordination with Pd(II). The high-resolution ESI-TOF mass spectrum showed a strong signal at m/z = 632.8 for a 4+ species which is in excellent agreement with the calculated mass for $[Pd_2\mathbf{L}^{\mathbf{Bu}}{}_4]^{4+}$(Figure 4.11). Cage complexes $[Pd_2\mathbf{L}^{\mathbf{Me}}{}_4]^{4+}$ and $[Pd_2\mathbf{L}^{\mathbf{Ph}}{}_4]^{4+}$ were synthesized according to the same procedure. Although $\mathbf{L}^{\mathbf{Bu}}$ and $\mathbf{L}^{\mathbf{Ph}}$ are functionalized with sterically quite bulky groups, the NMR analysis showed very clean spectra, indicating quantitative cage formation. As we expect, all three ligands are able to form monomeric cage, with square-planar Pd(II).

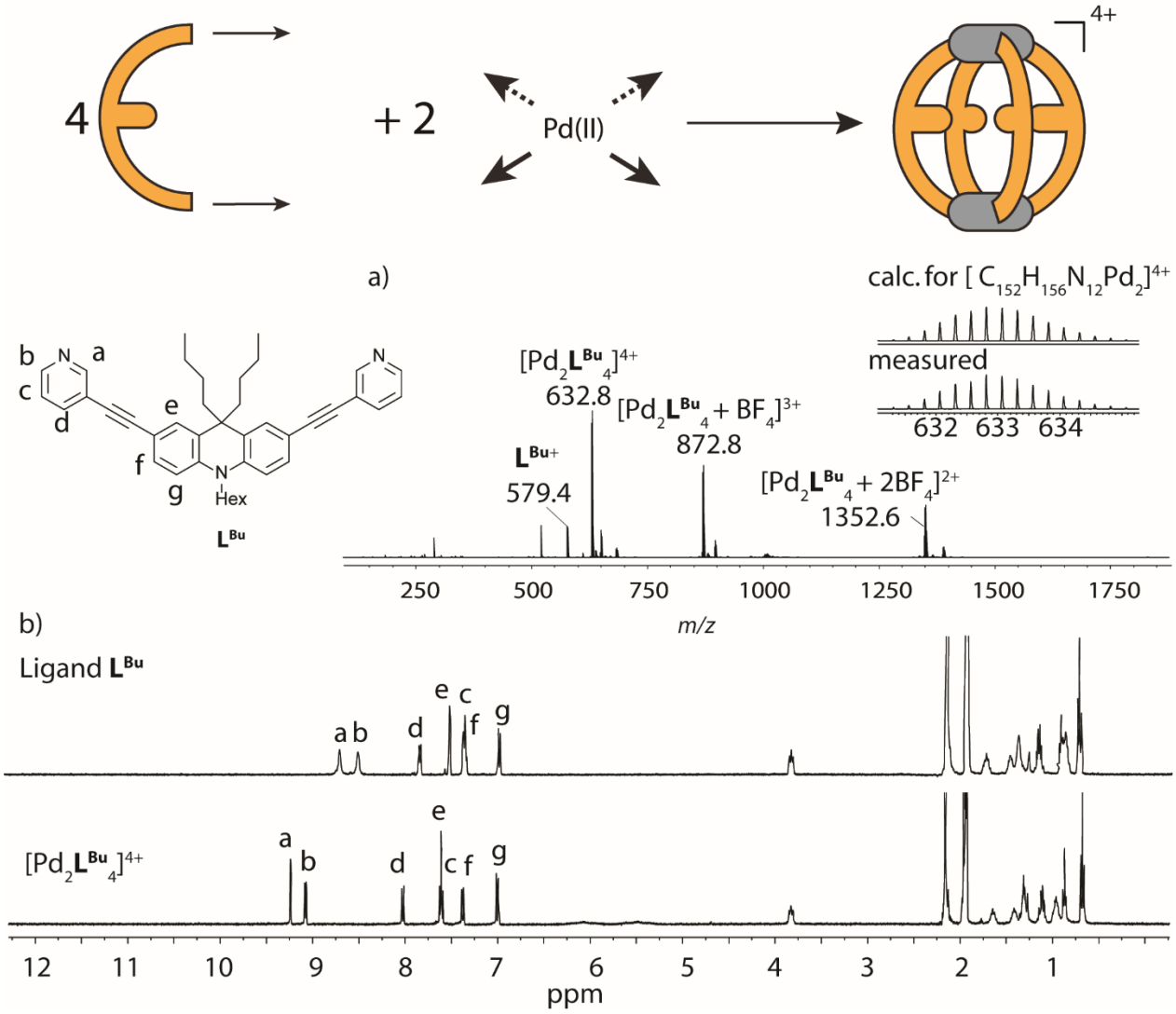

Figure 4.11. Self-assembly and characterization of coordination-driven supramolecular cage $[Pd_2\mathbf{L^{Bu}}_4](BF_4)_4$. a) ESI high-resolution mass spectrum, b) ^{1}H NMR of ligand $\mathbf{L^{Bu}}$ and cage $[Pd_2\mathbf{L^{Bu}}_4](BF_4)_4$.

Crystals of cage $[Pd_2\mathbf{L^{Me}}_4]^{4+}$ that are suitable for X-ray structure determination were grown via slow evaporation of diethyl ether into a cage solution in acetonitrile, having BF_4^- as counter ion. With the same crystallization condition, single crystals of cage $[Pd_2\mathbf{L^{Ph}}_4]^{4+}$ were successfully obtained. In the latter case, the anion of the cage complex is PF_6^-. According to the X-ray structure, for cage $[Pd_2\mathbf{L^{Ph}}_4]^{4+}$, one of the two phenyl groups on each ligand $\mathbf{L^{Ph}}$ is pointing inside of $[Pd_2\mathbf{L^{Ph}}_4]^{4+}$, while the other shows out of the cavity, similar orientation has also been observed for the methyl substituents in $[Pd_2\mathbf{L^{Me}}_4]^{4+}$ (Figure 4.12). Compared with cage $[Pd_2\mathbf{L^{Me}}_4]^{4+}$, the backbones of cage $[Pd_2\mathbf{L^{Ph}}_4]^{4+}$ are highly bended (bend angle 154°, figure 4.12f) and twisted (torsion angle 118°, figure 4.12d) due to the steric hindrance from the phenyl groups, in case of $[Pd_2\mathbf{L^{Me}}_4]^{4+}$ the Pd-Pd is 16.9 Å, while the $[Pd_2\mathbf{L^{Ph}}_4]^{4+}$ cage have a slightly short distance of 16.7 Å. The cavity of cage $[Pd_2\mathbf{L^{Ph}}_4]^{4+}$ was separated by the inward pointing phenyl groups into two parts according to the X-ray structure (Figure 4.12f). Each part was

occupied by a tetrahedra guest molecule, which was supposed to be $PF_2O_2^-$ anion converted by PF_6^-. Despite several attempts, crystals of $[Pd_2\mathbf{L}^{\mathbf{Bu}}{}_4]^{4+}$ that could be measured with X-ray methods could not be obtained. The possible reason could be the high flexibility on the alkyl chains, which makes crystallization very difficult.

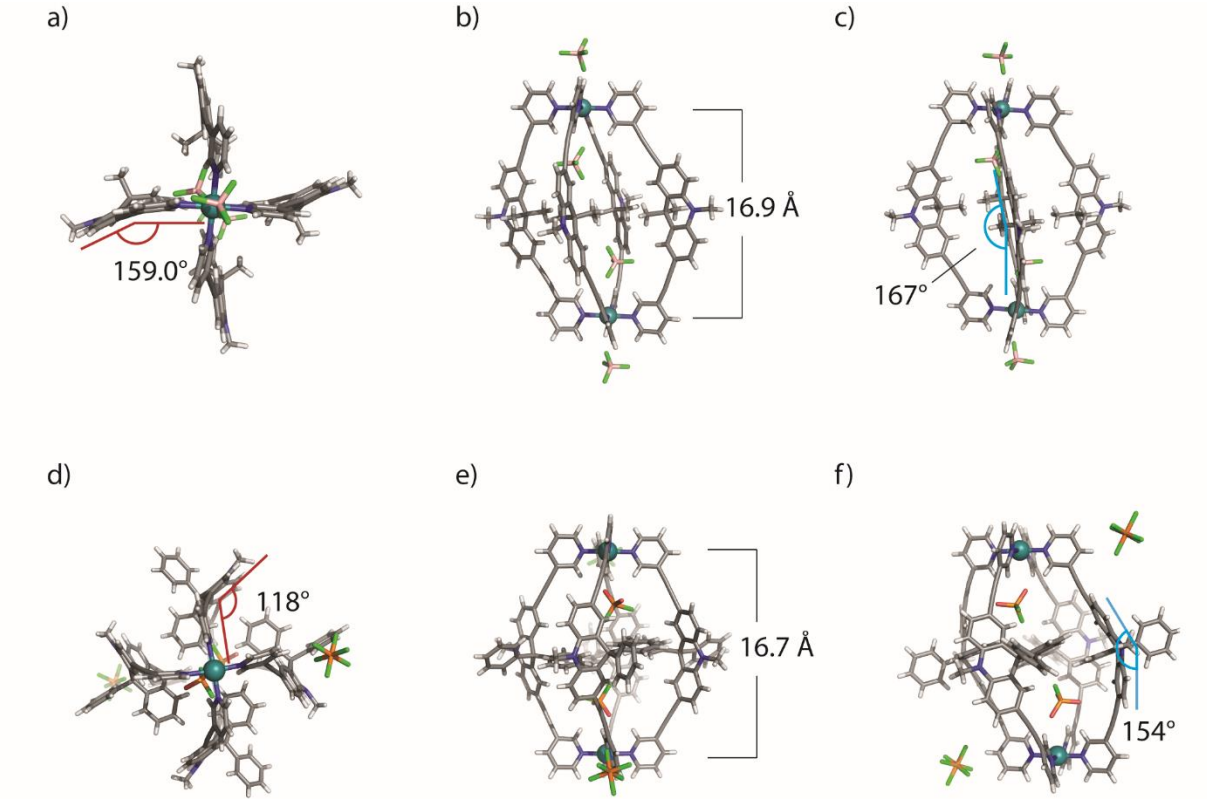

Figure 4.12. X-ray structures of (a-c) cage $[Pd_2\mathbf{L}^{\mathbf{Me}}{}_4](BF_4)_4$ and (d-f) cage $[Pd_2\mathbf{L}^{\mathbf{Ph}}{}_4](PF_6)_2(PF_2O_2)_2$ (Pd(II), deep teal; C, gray; N, blue; H, white; B, pink; O, red; P, orange; F, light green. Torsion angle, red; bend angle, blue; solvent molecules and side chains were omitted for the clarity).

4.4. Anionic guest binding

A series of small anions, i.e. ClO_4^-, IO_4^- and ReO_4^- were chosen as guest molecules. All three guests have a tetrahedral structure and single negative charge, on the other hand, the central atoms are quite different in size, polarizability and number of electrons, which was deemed of particular interest for our study to focus on the effects of London dispersion.

According to NMR experiments, all three guests are able to bind inside the cavity of all three cages. For example, by adding ReO_4^- as guest into a solution of cage $[Pd_2\mathbf{L}^{\mathbf{Me}}{}_4](BF_4)_4$, shifting of inside pointing protons H_a and H_e was observed, which hints a encapsulation and fast exchange between host and guest. In addition, chemical shift of the signal of methyl groups from $\mathbf{L}^{\mathbf{Me}}$ indicated that the DED group also interact with the guest molecule ReO_4^- (Figure 4.13b).

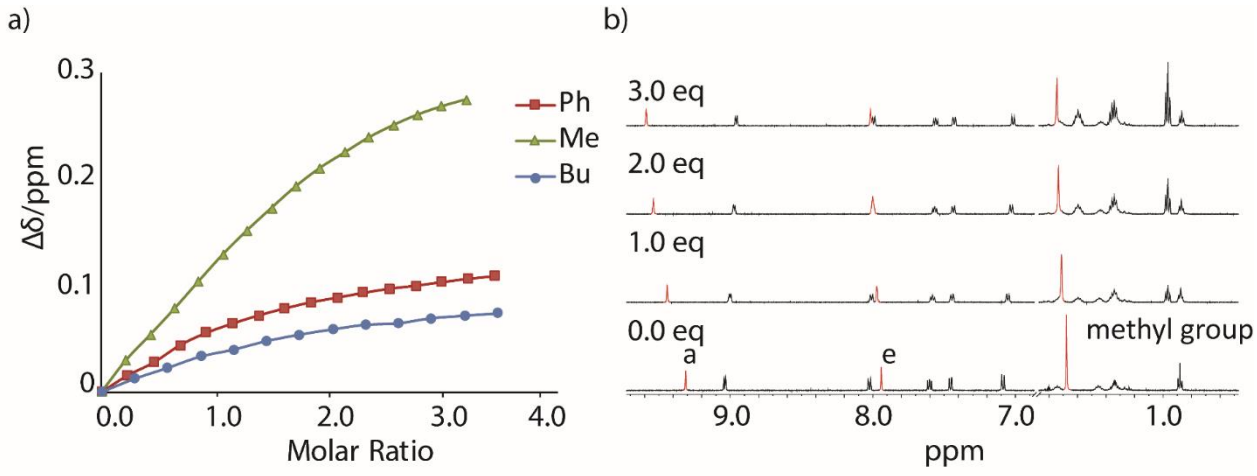

Figure 4.13, a) Change of chemical shift of proton *a* in cages $[Pd_2\mathbf{L}^{\mathbf{Ph}}{}_4]^{4+}$, $[Pd_2\mathbf{L}^{\mathbf{Me}}{}_4]^{4+}$ and $[Pd_2\mathbf{L}^{\mathbf{Bu}}{}_4]^{4+}$ upon binding ReO_4^-, b) NMR titration of cage $[Pd_2\mathbf{L}^{\mathbf{Me}}{}_4]^{4+}$ with ReO_4^-, chemical shifts of protons *a*, *e* and methyl group (highlighted in red) indicate the guest is binding inside the cage.

Because of the limitation and the inaccuracy of the "Job plot" method in the stoichiometry determination for supramolecular systems,[37] in this project, the stoichiometry of the host-guest system was determined additionally by ITC together with high resolution ESI-MS analysis. Based on the results of ITC, the host-guest complexes formed by cage $[Pd_2\mathbf{L}^{\mathbf{Bu}}{}_4]^{4+}$ and cage $[Pd_2\mathbf{L}^{\mathbf{Ph}}{}_4]^{4+}$ have a stoichiometry of 1 : 1, while cage $[Pd_2\mathbf{L}^{\mathbf{Me}}{}_4]^{2+}$ shows a 1 : 2 binding (see experimental section). The samples after ITC experiments were further analysed by ESI-HRMS. As a result, prominent signals of $[IO_4@Pd_2\mathbf{L}^{\mathbf{Bu}}{}_4]^{3+}$ and $[IO_4@Pd_2\mathbf{L}^{\mathbf{Ph}}{}_4]^{3+}$ have been observed (Figure 4.14b, 4.14c), confirming a 1 : 1 binding in both cases. A strong signal assigned to $[(IO_4)_2@Pd_2\mathbf{L}^{\mathbf{Me}}{}_4]^{2+}$ proves that cage $[Pd_2\mathbf{L}^{\mathbf{Me}}{}_4]^{4+}$ can bind two guest molecules (Figure 4.14a). Steric hindrance provided by the DED groups is supposed to be responsible for the difference, since *n*–butyl and phenyl groups are much bulkier compared to methyl groups, hence occupying more space in the cavities of cages $[Pd_2\mathbf{L}^{\mathbf{Bu}}{}_4]^{4+}$ and $[Pd_2\mathbf{L}^{\mathbf{Ph}}{}_4]^{4+}$. Thus, the resulting confined space is big enough for encapsulating only one guest molecule.

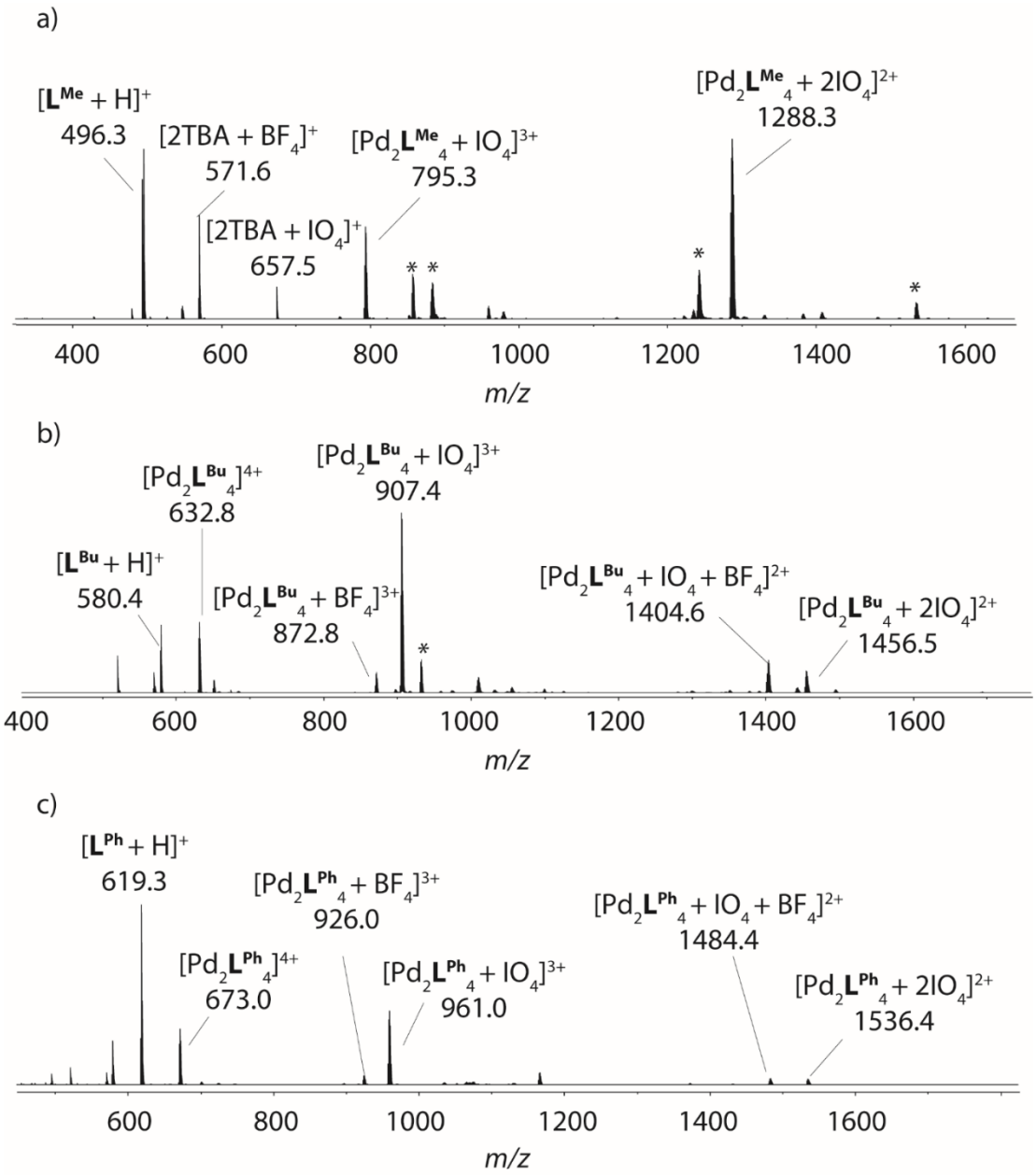

Figure 4.14. ESI-HRMS spectrum of a) cage $[Pd_2\mathbf{L}^{\mathbf{Me}}{}_4](BF_4)_4$ with IO_4^-, b) cage $[Pd_2\mathbf{L}^{\mathbf{Bu}}{}_4](BF_4)_4$ with IO_4^-, c) cage $[Pd_2\mathbf{L}^{\mathbf{Ph}}{}_4](BF_4)_4$ with IO_4^-.

The association constants of anionic guests were first investigated by NMR titrations. For each titration, at least ten data points were collected. All the titration experiments were performed in CD_3CN at 298 K with BF_4^- as counterion of the host molecules. Tetra-*n*-butylammonium (TBA) salts were used as the source of anionic guests. The accurate concentration of the host complex was determined by comparing the NMR integral values of the host and TBA signals after addition of 1.0 eq. TBA as reference. The data were fitted with the free online software "Bindfit" for global analysis. Data related to cage $[Pd_2\mathbf{L}^{\mathbf{Me}}{}_4]^{4+}$ were fitted using a 1 : 2 statistical model[37] for this was the only model that gives physically meaningful binding constants.

Table 4.1. Data fitting of NMR titration of $[Pd_2L^{Me}_4](BF_4)_4$ with ReO_4^- with different binding model provide by Bindfit. K_a is association constant (M^{-1}), δ is NMR resonance of complex. Only statistical model provided physically meaningful binding constants. (The experiments were performed at 298 K in CD_3CN, cage concentration was 0.60 mM.). Please refer to Ref[37] for more information about binding model.

Stoichiometry	Full $K_{a1} \neq 4K_{a2}$ $\delta_{\Delta HG} \neq \delta_{\Delta HG2}$	Non-cooperative $K_{a1} = 4K_{a2}$ $\delta_{\Delta HG} \neq \delta_{\Delta HG2}$	Additive $K_{a1} \neq 4K_{a2}$ $\delta_{\Delta HG} \neq \delta_{\Delta HG2}$	Statistical $K_{a1} = 4K_{a2}$ $\delta_{\Delta HG} \neq \delta_{\Delta HG2}$
1:2	K_{a1}= 0.15 K_{a2}= 646189	K_{a1}= 136 K_{a2}= 34	K_{a1}= 161 K_{a2}= −80	K_{a1}= 5882 K_{a2}= 1471

In general, binding in cage $[Pd_2\mathbf{L}^{\mathbf{Ph}}_4]^{4+}$ is slightly stronger than in cage $[Pd_2\mathbf{L}^{\mathbf{Bu}}_4]^{4+}$. However, cage $[Pd_2\mathbf{L}^{\mathbf{Me}}_4]^{4+}$ exhibits the highest overall binding affinity among all three cages (Table 4.2). For instance, ReO_4^- shows a binding constant of K_{a1}= 5882 M^{-1} with cage $[Pd_2\mathbf{L}^{\mathbf{Me}}_4]^{4+}$, while the association constants with cages $[Pd_2\mathbf{L}^{\mathbf{Bu}}_4]^{4+}$ and $[Pd_2\mathbf{L}^{\mathbf{Ph}}_4]^{4+}$ are 1830 M^{-1} and 2024 M^{-1}, respectively. According to these results, the DED group-functionalized cages do not form more stable host-guest complexes. On the contrary, the steric repulsion provided by these bulky groups hinder the encapsulation of the anionic guests into the self-assembled cages.

Table 4.2 Results of NMR titrations. All experiments were performed at 298 K in CD_3CN. All the data were fitted using Bindfit v0.5 (http://app.supramolecular.org/bindfit/). *a*: using statistical 1:2 binding model, K_{a1}=4K_{a2}. Unit of ΔG: kJ/mol; unit of association constant K_a: M^{-1}

	Stoichiometry	ClO_4^-	IO_4^-	ReO_4^-
Cage $[Pd_2\mathbf{L}^{\mathbf{Me}}_4]^{4+}$	1:2[a]	K_{a1}= 792 ΔG_1= −16.54 K_{a2}= 198 ΔG_2= −13.10	K_{a1}= 7021 ΔG_1= −21.95 K_{a2}= 1755 ΔG_2= −18.51	K_{a1}= 5882 ΔG_1= −21.51 K_{a2}= 1471 ΔG_2= −18.07
Cage $[Pd_2\mathbf{L}^{\mathbf{Bu}}_4]^{4+}$	1:1	K_a= 374 ΔG= −14.68	K_a = 1455 ΔG= −18.05	K_a = 1830 ΔG= −18.61
Cage $[Pd_2\mathbf{L}^{\mathbf{Ph}}_4]^{4+}$	1:1	K_a = 813 ΔG= −16.63	K_a = 1911 ΔG= −18.72	K_a = 2024 ΔG= −18.86

From the aspect of the anionic guests: ClO_4^- binds to all three cages with the weakest binding constants, roughly one order of magnitude weaker, compared to the other anions. The other guests, by contrast, show much stronger binding affinities (Table 4.2). These results are in line with our prediction. The periodate anion is larger in size (Figure 4.15) has a and higher polarizability compared to the perchlorate anion, therefore, the binding affinity is supposed to benefit from London dispersion effects to a larger extent. Similarly, although perchlorate anion and perrhenate anion, are much different in size, rhenium is a relatively heavy element (Figure 4.15) and consequently London dispersion forces tend to be stronger when forming host-guest complexes.

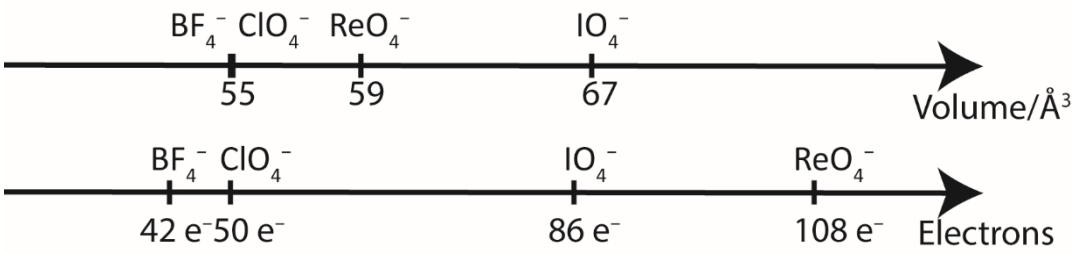

Figure 4.15. Comparison of guests in size and number of electrons. CPK volume of EDF2/6-31G* optimized model.

The system was then studied by ITC (Isothermal titration calorimetry), which is another technique that is commonly used for determination of thermodynamic parameters of host-guest systems. While NMR titration was utilized for measuring binding constants and monitoring changes on certain signals caused by adding guest to provide information about binding position (inside binding or outside binding), ITC experiments are able to offer important information such as the stoichiometry, binding affinity and enthalpy change (ΔH) by a single experiment at a fixed temperature. Accordingly, free energy change (ΔG) and entropy change (ΔS) can be calculated, which help to get a better understanding of binding mechanisms. Here need to note, the binding constants determined by NMR and ITC are not necessarily the same, because the two methods are measuring different physical parameters: for NMR titration, changes on chemical shift (fast exchange) or on integration of signals (slow exchange) would be used for determining of binding constant, ITC measured directly the heat generated or absorbed by formation of host-guest complex. Combination of the two analysis technics was expected to give a full picture about the binding behavior for the host-guest system.[38]

ITC experiments of $[Pd_2L^{Bu}_4](BF_4)_4$ with:

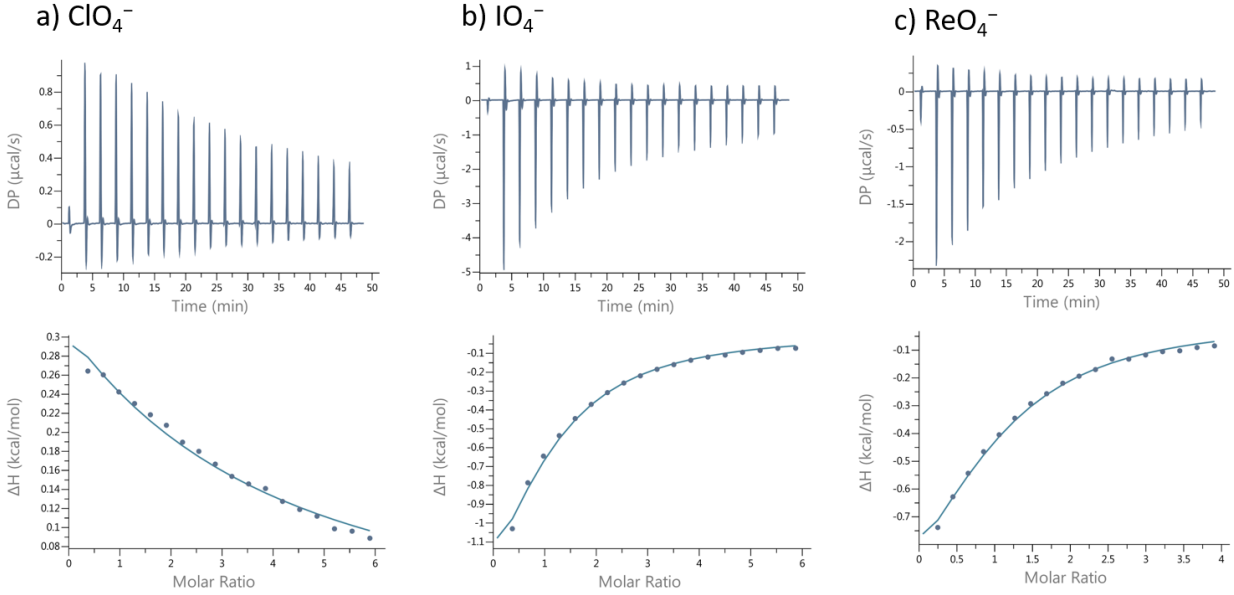

Figure 4.16. Titration curves and fitting of ITC experiment results of cage $[Pd_2\mathbf{L}^{\mathbf{Bu}}_4]^{4+}$ with a) ClO_4^-; b) IO_4^-; c) ReO_4^-; all experiments were performed in CD_3CN at 298 K.

Table 4.3. Results of ITC. All experiments were performed at 298 K in CD_3CN. Unit of ΔG, ΔH and –TΔS is kJ/mol. *a*: fitted using one set of sites model, which means K_{a1}=K_{a2}; *b*: the data was analyzed by AFFINImeter (https://www.affinimeter.com/site/) using two set of sites binding model.

	Stoichiometry	ClO_4^-	IO_4^-	ReO_4^-
Cage $[Pd_2\mathbf{L}^{\mathbf{Me}}{}_4]^{4+}$	1:2	K_{a1} = K_{a2}= 163 [a] ΔG= −12,64 ΔH= 6.52 −TΔS= −19.16	K_{a1}= 6635 [b] ΔG_1= −21.81 ΔH_1= −3.60 $-T\Delta S_1$= −18.21 K_{a2}= 2808; ΔG_2= −19.67 ΔH_2= −10.67 $-T\Delta S_2$= −9.00	K_{a1} = K_{a2}= 10131 [a] ΔG= −22.89 ΔH= −2.95 −TΔS=−19.92
Cage $[Pd_2\mathbf{L}^{\mathbf{Bu}}{}_4]^{4+}$	1:1	K_a= 233 ΔG= −13.51 ΔH= 11.88 −TΔS= −25.40	K_a= 1757 ΔG= −18.54 ΔH= −9.71 −TΔS= −8.83	K_a= 2288 ΔG= −19.16 ΔH= −6.32 −TΔS= −12.84
Cage $[Pd_2\mathbf{L}^{\mathbf{Ph}}{}_4]^{4+}$	1:1	K_a= 328 ΔG= −14.35 ΔH= 3.03 −TΔS= −17.41	K_a= 1689 ΔG= −18.45 ΔH= −4.81 −TΔS= −13.60	K_a= 3984 ΔG= −20.59 ΔH= −2.44 −TΔS= −18.12

Compared to NMR titrations, ITC experiments provide a similar trend in terms of binding constants for all guests. Due to the weak binding affinity of ClO_4^-, the titration curves using this guest are quite flat. However, it was possible to obtain binding constants and binding enthalpy in a reliable way.[39,40] Surprisingly, upwards peaks were observed in the titration experiments with ClO_4^- (Figure 4.16a), which means that the binding of ClO_4^- with all the cages is an endothermic reaction driven by entropic effects. Again, IO_4^- and ReO_4^- show stronger binding affinities compared to the relatively smaller guest ClO_4^-.

The ITC results for cage $[Pd_2\mathbf{L}^{\mathbf{Bu}}{}_4]^{4+}$ and cage $[Pd_2\mathbf{L}^{\mathbf{Ph}}{}_4]^{4+}$ are in good agreement with NMR titration results. By encapsulation of the same guest, both cages have similar binding free energies ΔG. Nevertheless, the driving force of guest binding are different. The binding enthalpy for encapsulation of IO_4^- inside cage $[Pd_2\mathbf{L}^{\mathbf{Ph}}{}_4]^{4+}$ is −4.81 kJ/mol, while the entropy change at 298 K is −13.60 kJ/mol, which means the reaction is mainly driven by entropic effects. On the other hand, when $[Pd_2\mathbf{L}^{\mathbf{Bu}}{}_4]^{4+}$ is used, over 50% contribution of the total ΔG comes from the enthalpy term (−9.71 kJ/mol), suggesting that dispersion contributions donated by *n*-butyl groups play an important role, since London dispersion effects are enthalpy related (Figure 4.16).

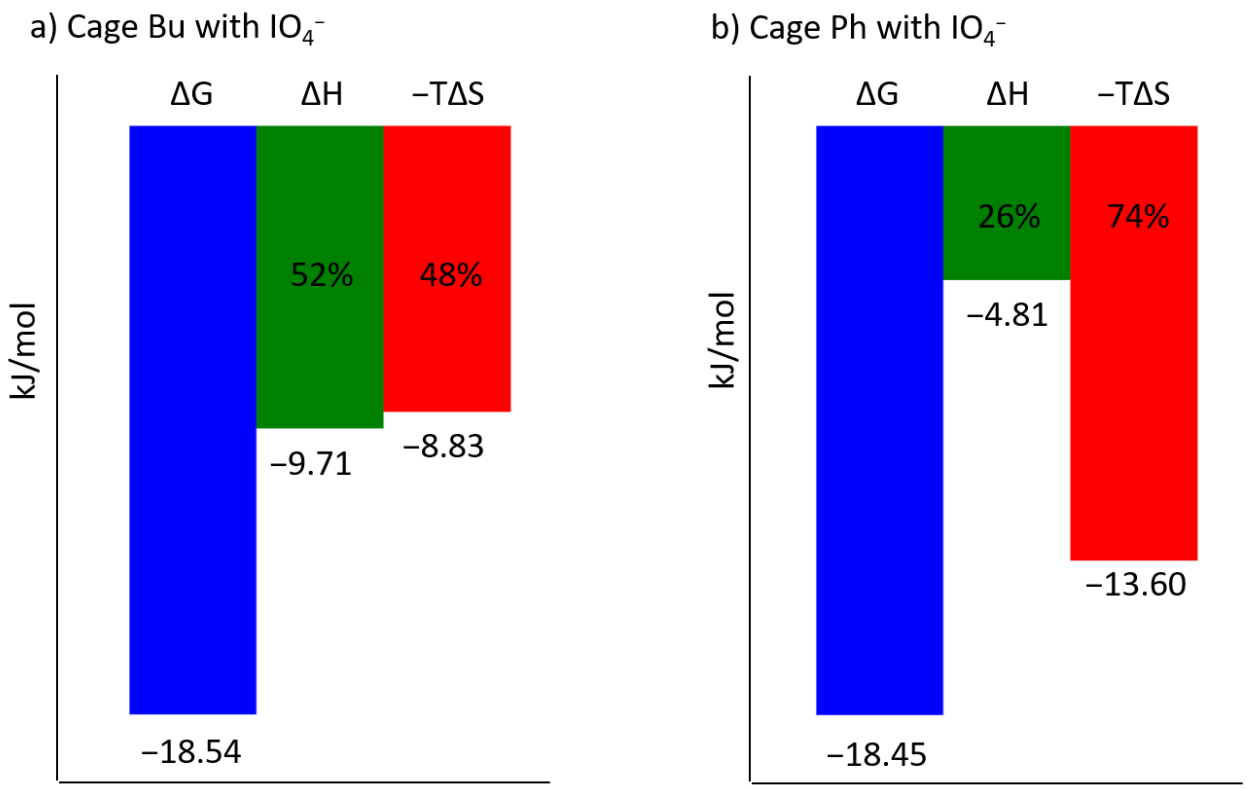

Figure 4.17. Thermodynamic signatures (measured at 298K) of cage $[Pd_2\mathbf{L}^{\mathbf{Bu}}{}_4]^{4+}$(left) and cage $[Pd_2\mathbf{L}^{\mathbf{Ph}}{}_4]^{4+}$ (right) upon interaction with IO_4^-.

The situation for cage $[Pd_2\mathbf{L}^{\mathbf{Me}}{}_4]^{4+}$ is more complicated. According to the results of the ITC experiments, binding with ReO_4^- provides a sigmoidal titration curve that indicates a one set of site binding. However, when IO_4^- is added as the guest, a hook-shaped curve was obtained. This result was then fitted with the "Affinimeter" software, using a stepwise two sets of site binding model: H + G ⟶ HG, HG + G ⟶ HG_2 (H= host, G= guest). Finally, ITC also confirmed that cage $[Pd_2\mathbf{L}^{\mathbf{Me}}{}_4]^{4+}$ has the strongest binding affinity for IO_4^- and ReO_4^-.

4.5. Conclusion

In this project, research emphasis was focused on experimental insights into dispersion interactions in self-assembled supramolecular host-guest systems. Therefore, three banana-shaped organic ligands, functionalized with dispersion energy donor groups, were synthesized and used to self-assemble monomeric $[Pd_2L_4]^{4+}$ cages by coordination with square planar Pd(II) ions, providing three hosts with different DED groups in the cavity. To reduce the variables and simplify the system as much as possible, three anionic molecules (ClO_4^-, $IO_4^-$and ReO_4^-) with same geometry and charge have been chosen as guests. Since IO_4^- and ReO_4^- are larger in size and composed of heavier elements than ClO_4^-, they are more likely to benefit from London dispersion interactions. The system has been analysed using orthogonal analytical techniques: NMR and ITC titrations. On the basis of the obtained results, IO_4^- and

ReO_4^- show a stronger binding to the self-assembled cages than guest ClO_4^-, coherently with the hypothesis of a strong contribution derived by London dispersion interactions. Nevertheless, other possible factors that could influence the strength of binding affinities like charge distribution of the guests should also be considered, which would be evaluate in next by theoretical calculations.

On the other hand, sterically bulky substituents, such as *n*-butyl and phenyl groups, are expected to help stabilize host-guest complexes by their dispersion contribution. However, these DED group-functionalized cages do not form host-guest complexes with extra stability. Their binding affinities are weaker compared to the methyl functionalized cage $[Pd_2\mathbf{L}^{\mathbf{Me}}{}_4]^{4+}$, which indicates that steric repulsion provided by the bulky groups hindered the encapsulation of guest molecules. The low binding constants does not necessarily mean less dispersion contributions, as shown in our former work, since the prominent contributions of dispersion can be counterweighted by unfavourable effects.[34,35] In addition, ITC shows that even with a similar binding affinity, the cages with different functionalities go through different pathways for guest encapsulations. Since more enthalpy contribution to guest binding has been observed with the relatively flexible *n*-butyl group functionalization, London dispersion effects are supposed to play a more important role in case of cage $[Pd_2\mathbf{L}^{\mathbf{Bu}}{}_4]^{4+}$.

In summary, according to our experimental investigations, promising new insights into London dispersion effects were obtained, showing that the contribution of the London dispersion effect can be related to both the host and the guest species. Subsequently, we collaborate with the group of Prof. Mata from University of Göttingen for computation of dispersion interaction density (DID), influence of charge distribution and trend of binding affinity with or without dispersion contributions to get a clearer and deeper understanding of the system.

4.6. Experimental section

4.6.1. Materials and methods

Unless otherwise stated, all chemicals were obtained from commercial sources and used as received. Syntheses of compounds **9a**, **10a**, **11a** have been described in the last chapter. Compound **9c** was synthesized according to literature procedures.[41]. Dry solvents were purchased or purified and dried over absorbent-filled columns on a GS-Systems solvent purification system (SPS). Reactions were monitored with thin layer chromatography (TLC) using silica coated aluminium plates (Merck, silica 60, fluorescence indicator F254, thickness 0.25 mm). For column chromatography, silica (Merck, silica 60, 0.02 – 0.063 mesh ASTM) was used as the stationary phase, if not mentioned otherwise. Flash chromatography was performed on a Biotage Isolera One fraction collector with Biotage SNAP Ultra columns. Recycling gel permeation chromatography (GPC) was performed on Japan Analytical Industry NEXT and LaboACE instruments using JAIGEL 1-HH and 2-HH 20 mm x 600 mm columns with a flowrate of 7 mL/min.

The NMR spectroscopic data was measured on Bruker AV 500 Avance NEO, Bruker AV 700 Avance III HD and Agilent Technologies DD2 spectrometers. For ^{1}H NMR spectra, the chemical shifts were calibrated on the lock signals of the solvents ($CDCl_3$: 7.26 ppm, CD_3CN: 1.94 ppm, CD_2Cl_2: 5.32 ppm). For ^{13}C NMR spectra, solvent signals were used as internal standards (CD3CN: 1.32, 118.26 ppm, CD_2Cl_2: 54.00 ppm, $CDCl_3$: 77.00 ppm). Chemical shifts δ are given in ppm, coupling constants *J* in Hz. All spectra were recorded in standard 5 mm NMR tubes at 25 °C.

Mass spectrometry data were measured on Bruker timsTOF, Bruker Compact, Bruker Apex IV FTICR or Waters Synapt G2 ESI-MS instruments (positive mode). Trapped ion mobility data were measured on Bruker ESI-timsTOF. For calibration of the TIMS and TOF devices, Agilent ESI Tuning Mix was used. Signals in the NMR spectra and HRMS spectrum assigned to minor impurities are marked with an asterisk (*).

ITC experiments were performed on a Malvern MicroCal PEAQ-ITC instrument.

Single crystal X-ray diffraction data was collected at macromolecular beamline P11, Petra III, DESY, Germany, or on our in-house diffractometer Bruker D8 venture equipped with an INCOATEC microfocus sealed tube (Iμs 3.0) using CuK_α radiation at 100 K. For further details, see experimental section on X-ray crystallography in each chapter.

4.6.2. Ligand synthesis

4.6.2.1. Synthesis of *9,9-dibutyl-9,10-dihydroacridine (**9b**)*

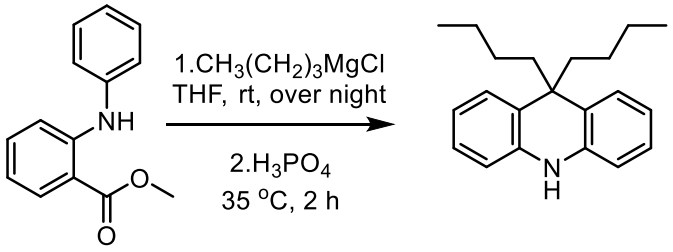

8 **9b**

A flame-dried Schleck flask was charged with compound **8** (1.0 g, 4.40 mmol, 1.0 eq.) and anhydrous THF (40 ml). The mixture was cooled to 0 °Cin an ice bath. *N*-butylmagnesium chloride (1.80 g, 15.40 mmol, 3.5 eq.) was added dropwise into the mixture over a period of 15 min. The reaction was stirred at rt. for 18 h. After the reaction finished, saturated NH_4Cl solution (aq.) was added to quench the reaction. Next, the mixture was extracted with DCM, then washed with saturated NaCl solution (aq.) three times. The organic phase was dried over Na_2SO_4. Solvent was removed under reduce pressure to provide a brown oily liquid as the raw product which was used directly for the next step without further purification.

Under N_2 atmosphere, 3 ml H_3PO_4 (85% wt.) was added to the crude product from the last step. The mixture was stirred at 35 °C for 3 h. Subsequently, the mixture was poured into ice, a white precipitate formed and collected by filtration. After purification by column chromatography (pentane : DCM=20:1), 647 mg (50 %) clean compound **9b** was obtained as white solid.

^{1}H NMR (500 MHz, CD_3CN) δ 7.25 (dd, *J* = 8.0, 1.4 Hz, 2H), 7.03 (ddd, *J* = 7.9, 7.2, 1.4 Hz, 2H), 6.80 (ddd, *J* = 7.9, 7.2, 1.3 Hz, 2H), 6.64 (dd, *J* = 7.9, 1.3 Hz, 2H), 1.91 – 1.85 (m, 4H), 1.12 (p, *J* = 7.7 Hz, 4H), 0.94 – 0.79 (m, 4H), 0.70 (t, *J* = 7.4 Hz, 6H).

^{13}C NMR (126 MHz, CD_3CN) δ 140.77, 127.62, 127.46, 125.63, 120.67, 113.83, 46.36, 45.06, 28.31, 23.70, 14.26.

ESI-MS ($C_{21}H_{27}N + H^+$): measured: 294.2101, calculated: 294.2216

*4.6.2.2. Synthesis of 9,9-dibutyl-10-hexyl-9,10-dihydroacridine (**10b**)*

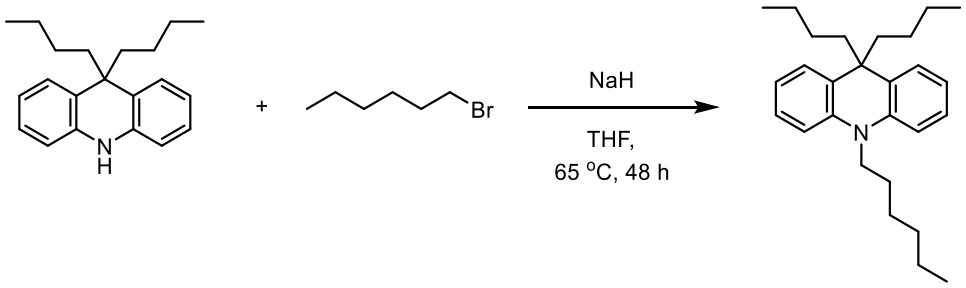

9b **10b**

A flame-dried Schlenk flask was charged with compound **1** (500 mg, 1.7 mmol, 1.0 equiv.) and anhydrous THF (28 ml) under nitrogen atmosphere. Then NaH (136 mg, 3.41 mmol, 2.0 equiv. 60% dispersion in mineral oil) was added slowly at 0 °C. After stirring for 1 hour at room temperature, 1-bromohexane was added. The reaction was finished after heating at 65 °C for 48 h. The excess of NaH was quenched by addition of NH_4Cl (aq.) and the reaction mixture was extracted with dichloromethane (3 × 50 ml). Organic phases were combined and dried over Na_2SO_4. After evaporating the solvent under reduced pressure, the crude product was purified by column chromatography with pentane to provide 548 mg of the product as a colourless solid (85% yield).

^{1}H NMR (500 MHz, CD_3CN) δ 7.31 (dd, *J* = 7.8, 1.6 Hz, 2H), 7.14 (m, 2H), 6.91 (dd, *J* = 8.4, 1.2 Hz, 2H), 6.89 – 6.83 (m, 2H), 3.78 (t, *J* = 8.1 Hz, 2H), 1.91 – 1.84 (m, 4H), 1.76 – 1.66 (m, 2H), 1.50 – 1.42 (m, 2H), 1.38 (m, 4H), 1.12 (h, *J* = 7.4 Hz, 4H), 0.95 – 0.89 (m, 3H), 0.89 – 0.81 (m, 4H), 0.70 (t, *J* = 7.4 Hz, 6H).

^{13}C NMR (126 MHz, CD_3CN) δ 142.14, 128.18, 127.79, 127.42, 120.63, 113.00, 46.67, 45.61, 44.69, 32.30, 27.98, 27.16, 26.72, 23.70, 23.38, 14.28, 14.24.

ESI-MS ($C_{27}H_{39}N + H^+$): measured: 378.3008, calculated:.378.3155

*4.6.2.3. Synthesis of 10-hexyl-9,9-diphenyl-9,10-dihydroacridine (**10c**)*

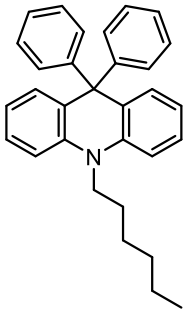

10c

Compound **10c** was synthesized following the same procedure as described for **10b**. Compound **9b** (500 mg, 1.5 mmol) was used for the reaction. The crude product was purified by column chromatography with DCM: pentane = 1:10 to yield the product as a white oil (417 mg, 79%).

^{1}H NMR (700 MHz, CD_2Cl_2) δ 7.25 (m, 2H), 7.22 – 7.18 (m, 6H), 7.02 (dd, *J* = 8.2, 1.2 Hz, 2H), 6.89 – 6.84 (m, 6H), 6.80 (dd, *J* = 7.7, 1.6 Hz, 2H), 3.82 (t, *J* = 7.3 Hz, 2H), 1.58 – 1.55 (m, 2H), 1.22 – 1.13 (m, 4H), 1.04 (m, 2H), 0.84 (t, *J* = 7.1 Hz, 3H).

^{13}C NMR (176 MHz, CD_2Cl_2) δ 146.44, 141.49, 131.33, 130.28 (2C), 130.11, 127.43 (2C), 127.06, 126.22, 119.45, 112.70, 56.91, 45.53, 31.52, 26.34, 25.93, 22.50, 13.78.

ESI-MS ($C_{31}H_{31}N + H^+$): measured: 418.2362, calculated: 418.2529

*4.6.2.4. Synthesis of 2,7-dibromo-9,9-dibutyl-10-hexyl-9,10-dihydroacridine (**11b**)*

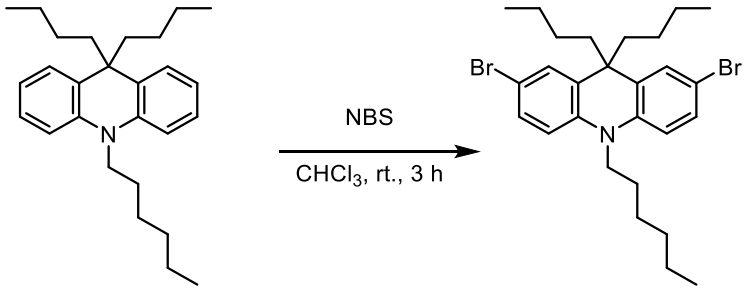

10b **11b**

Compound **10b** (298 mg, 0.80 mmol, 1.0 equiv.) and NBS (281 mg, 1.58 mmol. 2.0 equiv.) were dissolved in $CHCl_3$ (8 ml) and stirred for 3 h. Afterwards, the solvent was removed under reduced pressure and the residues were purified by column chromatography with pentane to yield the product as a colorless solid (387.5 mg, 92%).

^{1}H NMR (500 MHz, CD_3CN) δ 7.43 (d, *J* = 2.4 Hz, 2H), 7.30 (dd, *J* = 8.9, 2.4 Hz, 2H), 6.87 (d, *J* = 8.9 Hz, 2H), 3.76 (t, *J* = 8.1 Hz, 2H), 1.90 – 1.85 (m, 4H), 1.73 – 1.65 (m, 2H), 1.44 (m, 2H), 1.42 – 1.34 (m, 4H), 1.17 (h, *J* = 7.3 Hz, 4H), 0.96 – 0.91 (m, 3H), 0.91 – 0.82 (m, 4H), 0.75 (t, *J* = 7.4 Hz, 6H).

^{13}C NMR (151 MHz, CD_3CN) δ 140.65, 130.32, 130.10, 129.64, 114.94, 112.41, 46.50, 45.54, 44.91, 31.86, 27.53, 26.65, 26.00, 23.16, 22.97, 13.89, 13.80.

ESI-MS ($C_{27}H_{37}Br_2N + H^+$): measured: 536.1131, calculated: 536.1347

*4.6.2.5. Synthesis of 2,7-dibromo-10-hexyl-9,9-diphenyl-9,10-dihydroacridine (**11c**)*

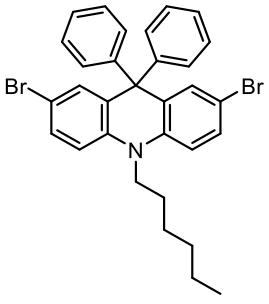

11c

Compound 11c was synthesized following the same procedure as described for **11b**. Compound **10c** (200 mg, 0.57 mmol) was used for the reaction. The crude product was purified by column chromatography with pentane to yield the product as a brown oil (256 mg, 93%).

^{1}H NMR (600 MHz, CD_2Cl_2) δ 7.29 (dd, *J* = 8.8, 2.4 Hz, 2H), 7.18 – 7.15 (m, 6H), 6.82 (dd, *J* = 7.5, 4.5 Hz, 2H), 6.79 (d, *J* = 2.4 Hz, 2H), 6.76 (m, 1.7 Hz, 4H), 3.70 – 3.66 (t, *J* = 7.2 Hz, 2H), 2H), 1.38 (m, 2H), 1.12 – 1.00 (m, 4H), 0.89 – 0.84 (m, 2H), 0.76 – 0.73 (m, 3H).

^{13}C NMR (151 MHz, CD_2Cl_2) δ 144.79, 140.42, 132.41, 130.10 (2C), 130.06, 127.83 (2C), 127.63, 126.87, 114.68, 112.36, 56.93, 45.75, 31.43, 26.17, 25.84, 22.43, 13.76.

ESI-MS ($C_{27}H_{37}Br_2N + H^+$): measured: 576.0492, calculated: 576.0722

*4.6.2.6.. Synthesis of 9,9-dibutyl-10-hexyl-2,7-bis(pyridin-3-ylethynyl)-9,10-dihydroacridine (**L^{Bu}**)*

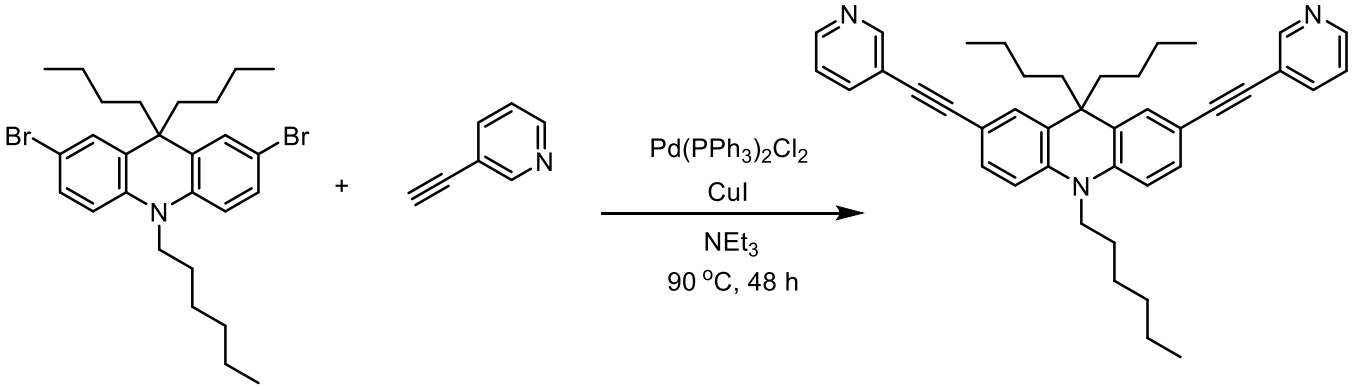

11c **L^{Bu}**

Compound **11c** (350 mg, 0.65 mmol, 1.0 equiv.), 3-ethynylpyridine (202 mg, 1.96 mmol, 3.0 equiv.), $Pd(PPh_3)_2Cl_2$ (22.9 mg, 32.7 µmmol, 5 mol%) and CuI (14.9 mg. 0.78 mmol, 12 mol%) were suspended in triethylamine (4 ml). After degassing (via freeze-thaw cycles), the mixture was heated to 90 °C and stirred for 48 h. Subsequently, the mixture was cooled to ambient temperature. The solvent was removed under reduced pressure. The crude product was purified by column chromatography (DCM: EtOAc=1:4) and then further purified by GPC to provide the clean **L^{Bu}** as a light-yellow solid (154 mg, 41 % yield).

^{1}H NMR (700 MHz, CD_3CN) δ 8.75 (dd, *J* = 2.2, 1.0 Hz, 2H), 8.55 (dd, *J* = 4.8, 1.7 Hz, 2H), 7.88 (dt, *J* = 7.8, 1.9 Hz, 2H), 7.56 (d, *J* = 2.0 Hz, 2H), 7.43 – 7.37 (m, 4H), 7.03 (d, *J* = 8.6 Hz, 2H), 3.87 (t, *J* = 8.0 Hz, 2H), 1.79 – 1.71 (m, 2H), 1.50 (p, *J* = 7.2 Hz, 2H), 1.46 – 1.37 (m, 4H), 1.22 – 1.14 (m, 4H), 0.95 (t, *J* = 7.1 Hz, 3H), 0.93 – 0.88 (m, 4H), 0.75 (t, *J* = 7.3 Hz, 6H).

^{13}C NMR (176 MHz, CD_3CN) δ 152.24, 148.99, 141.71, 138.55, 131.25, 130.62, 128.34, 123.96, 121.20, 114.31, 113.48, 93.59, 85.35, 46.45, 46.13, 44.54, 31.89, 27.67, 26.67, 26.30, 23.28, 23.00, 13.90, 13.88

ESI-HRMS ($C_{41}H_{45}N_3^+$): measured: 579.3607, calculated: 579.3608

*4.6.2.7. Synthesis of 10-hexyl-9,9-diphenyl-2,7-bis(pyridin-3-ylethynyl)-9,10-dihydroacridine (**L^{Ph}**)*

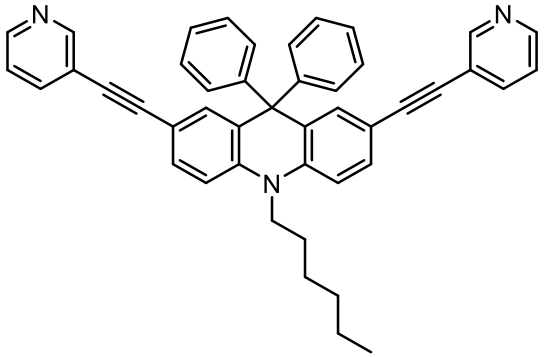

L^{Ph}

Ligand **L^{Ph}** was synthesized following the same procedure as described for **L^{Bu}**. Compound **11c** (200 mg, 0.35 mmol) was used for the reaction. The crude product was purified by column chromatography with DCM to yield the product as a brown oil (110 mg, 51%).

^{1}H NMR (700 MHz, CD_3CN) δ 8.66 (d, *J* = 2.8 Hz, 2H), 8.52 (dd, *J* = 4.8, 1.7 Hz, 2H), 7.81 (dt, *J* = 7.9, 1.9 Hz, 2H), 7.54 (dd, *J* = 8.5, 2.0 Hz, 2H), 7.37 – 7.30 (m, 8H), 7.22 (d, *J* = 8.6 Hz, 2H), 6.96 (d, *J* = 1.9 Hz, 2H), 6.94 – 6.88 (m, 4H), 3.94 (t, *J* = 7.3 Hz, 2H), 1.56 (p, *J* = 7.7 Hz, 2H), 1.22 – 1.14 (m, 5H), 1.02 (p, *J* = 7.6 Hz, 2H), 0.86 (t, *J* = 7.1 Hz, 3H).

^{13}C NMR (176 MHz, CD_3CN) δ 152.22, 149.07, 145.84, 141.90, 138.61, 133.54, 131.84, 131.78, 130.57, 128.60, 127.61, 123.89, 120.90, 114.50, 114.27, 93.11, 85.77, 57.20, 45.94, 31.77, 26.51, 26.40, 22.77, 13.89.

ESI-HRMS ($C_{45}H_{37}N_3^+$): measured: 619.2740, calculated: 619.2982

*4.6.2.8. Synthesis of 10-hexyl-9,9-dimethyl-2,7-bis(pyridin-3-ylethynyl)-9,10-dihydroacridine (**L^{Me}**)*

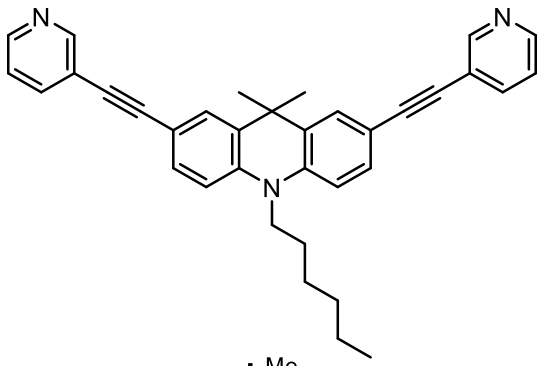

L^{Me}

Ligand **L^{Me}** was synthesized following the same procedure as described for **L^{Bu}**. Compound **11a** (200 mg, 0.44 mmol) was used for the reaction. The crude product was purified by column chromatography with EtOAc:Pentan=2:1 to yield the product as a brown oil (107 mg, 49%).

^{1}H NMR (500 MHz, Acetonitrile-d_3) δ 9.31 (d, *J* = 1.8 Hz, 2H), 9.03 (d, *J* = 5.9 Hz, 2H), 8.02 (dt, *J* = 8.1, 1.6 Hz, 2H), 7.94 (d, *J* = 1.9 Hz, 2H), 7.60 (dd, *J* = 8.0, 5.8 Hz, 2H), 7.46 (dd, *J* = 8.5, 1.9 Hz, 2H), 7.09 (d, *J* = 8.6 Hz, 2H), 3.92 (t, *J* = 8.0 Hz, 2H), 1.75 (m, 2H), 1.67 (s, 6H), 1.45 (m, 2H), 1.34 (m, 4H), 0.88 (t, *J* = 7.0 Hz, 4H).

^{13}C NMR (151 MHz, CD_3CN) δ 152.23, 149.00, 140.98, 138.58, 132.66, 131.08, 128.75, 123.97, 121.17, 114.77, 114.06, 93.56, 85.49, 46.46, 36.55, 31.82, 29.05, 26.89, 26.16, 22.98, 13.90.

ESI-HRMS ($C_{35}H_{33}N_3^+$): measured: 495.2669, calculated: 495.2669

4.6.3. Cage self-assembly

4.6.3.1. General procedure

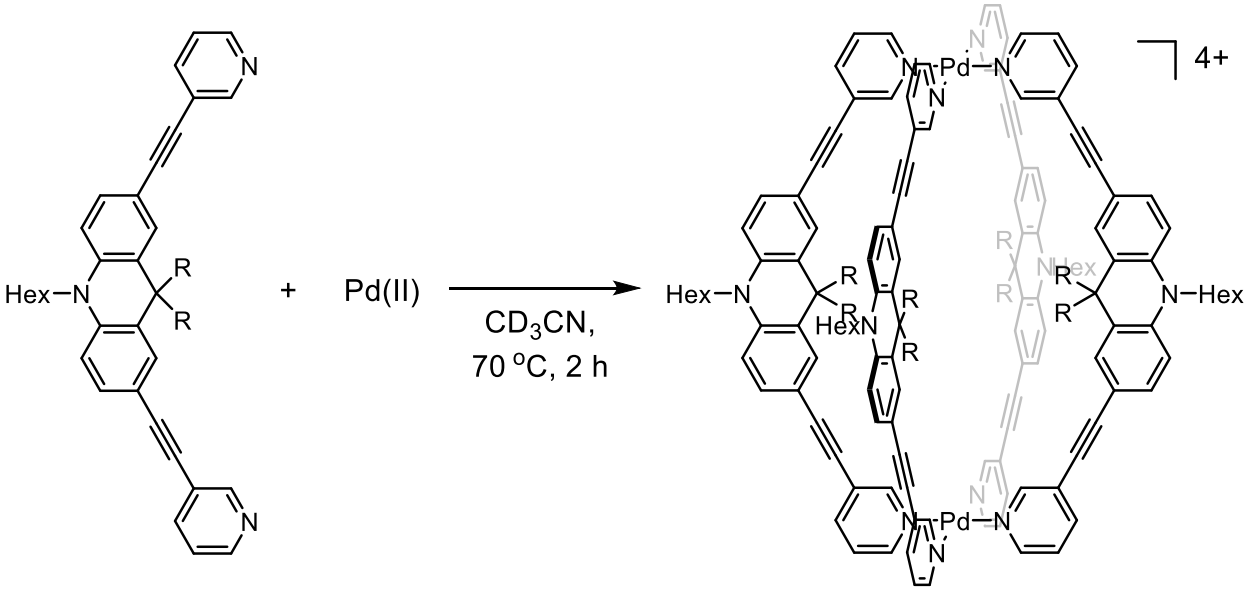

R= Methly, *n*-Butyl or Phenly

Banana-shaped ligand (1.0 equiv., 2.8 µmol) was suspended or dissolved in 1ml CD_3CN. Subsequently, $[Pd(CH_3CN)_4](BF_4)_2$ (0.5 equiv., 1.4 µmol, stock solution 15 mM in CD_3CN) was added. The mixture was heated at 70 °C for 2 h to provide $[Pd_2\mathbf{L}_4](BF_4)_4$ cage quantitatively.

3.6.3.2. Characterization of self-assembled cage $[Pd_2L^{Me}{}_4](BF_4)_4$.

^{1}H NMR (500 MHz, CD_3CN) δ 9.31 (d, *J* = 1.8 Hz, 2H), 9.03 (d, *J* = 5.9 Hz, 2H), 8.07 – 7.91 (m, 4H), 7.60 (dd, *J* = 8.0, 5.8 Hz, 2H), 7.46 (dd, *J* = 8.5, 1.9 Hz, 2H), 7.09 (d, *J* = 8.6 Hz, 2H), 3.92 (t, *J* = 8.0 Hz, 2H), 1.78 – 1.70 (m, 2H), 1.67 (s, 6H), 1.45 (q, *J* = 7.3 Hz, 2H), 1.38 – 1.30 (m, 4H), 0.88 (t, *J* = 7.0 Hz, 3H).

ESI-HRMS $[C_{140}H_{132}N_{12}Pd_2]^{4+}$: measured: 548.7193, calculated: 548.7201

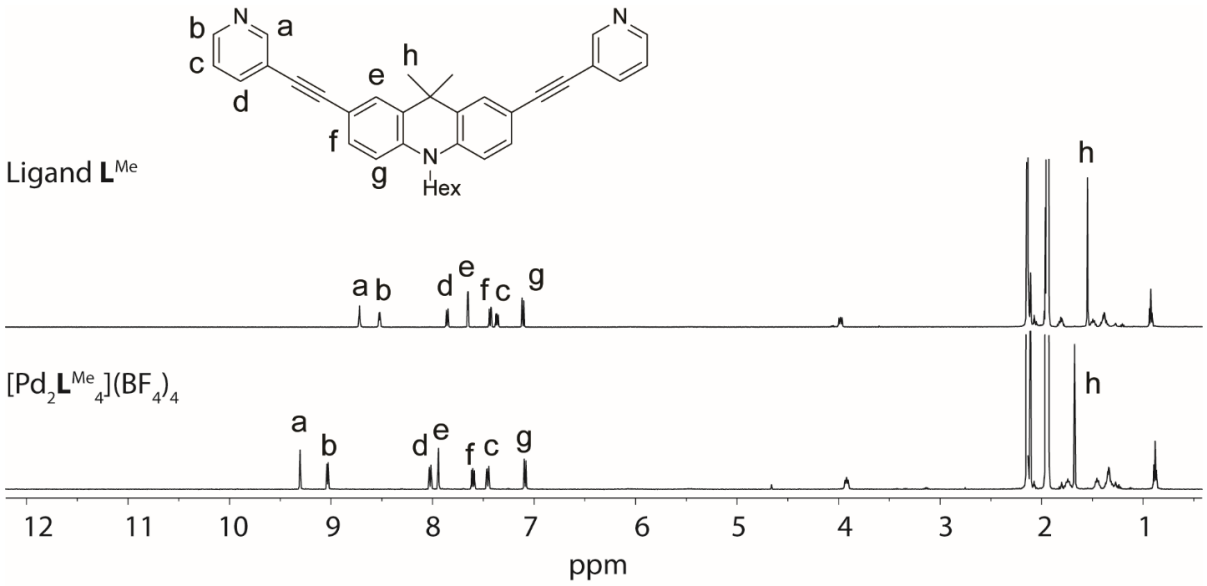

Figure S4.1. ^{1}H NMR spectrum (500 MHz/CD_3CN) of cage $[Pd_2\mathbf{L}^{Me}{}_4](BF_4)_4$ compared with free ligand $\mathbf{L}^{Me}$

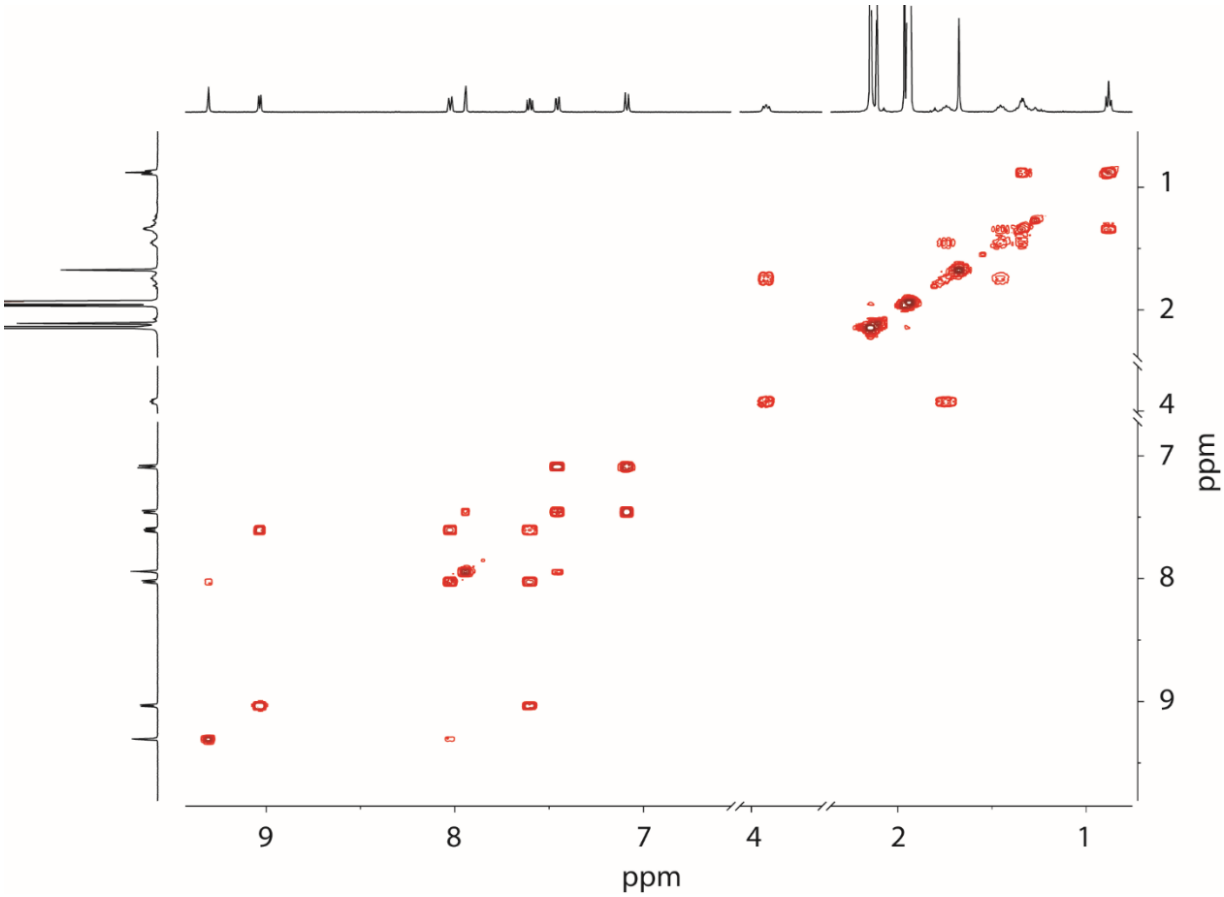

Figure S4.2. COSY NMR of cage $[Pd_2\mathbf{L}^{Me}{}_4](BF_4)_4$ (500 MHz, CD_3CN).

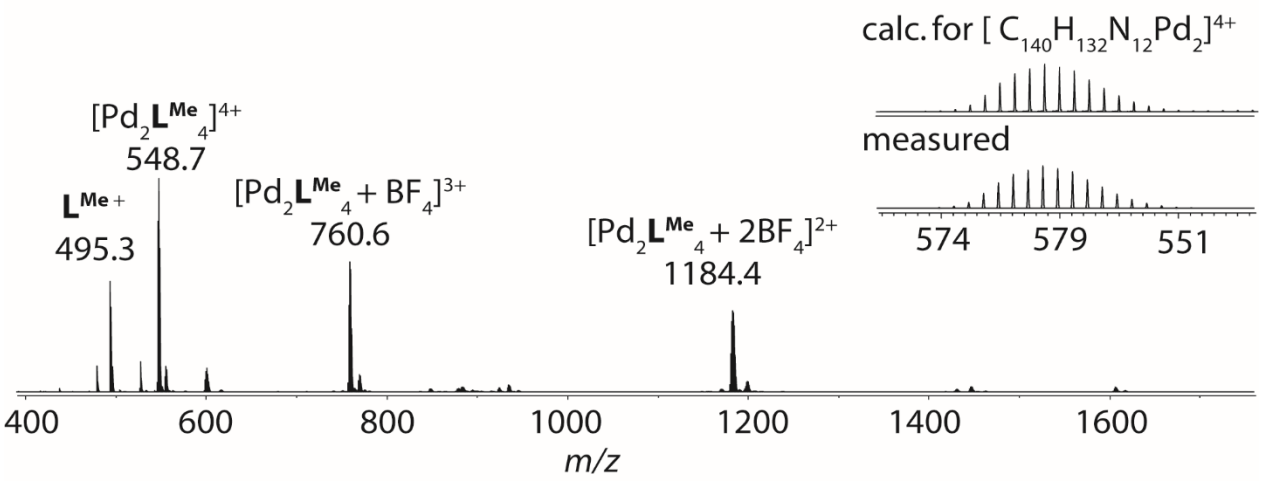

Figure S4.3. HRMS of cage $[Pd_2\mathbf{L}^{Me}_4](BF_4)_4$

4.6.3.3. Characterization of self-assembled cage $[Pd_2L^{Bu}{}_4](BF_4)_4$.

^{1}H NMR (500 MHz, CD_3CN) δ 9.28 (d, *J* = 1.9 Hz, 2H), 9.10 (dd, *J* = 5.9, 1.3 Hz, 2H), 8.05 (dt, *J* = 8.0, 1.6 Hz, 2H), 7.70 – 7.59 (m, 5H), 7.40 (dd, *J* = 8.5, 1.9 Hz, 2H), 7.03 (d, *J* = 8.7 Hz, 2H), 3.85 (t, *J* = 8.0 Hz, 2H), 1.67 (m, 2H), 1.45 (d, *J* = 7.8 Hz, 2H), 1.32 (d, *J* = 19.0 Hz, 6H), 1.14 (h, *J* = 7.8 Hz, 4H), 1.04 – 0.96 (m, 4H), 0.90 (t, *J* = 7.0 Hz, 3H), 0.70 (t, *J* = 7.2 Hz, 6H). (signal of one of the CH_2 group on the n-hexyl chain is over lapped with the signal of CD_3CN).

ESI-HRMS $[C_{152}H_{156}N_{12}Pd_2]^{4+}$: measured: 632.8133, calculated: 632.8142

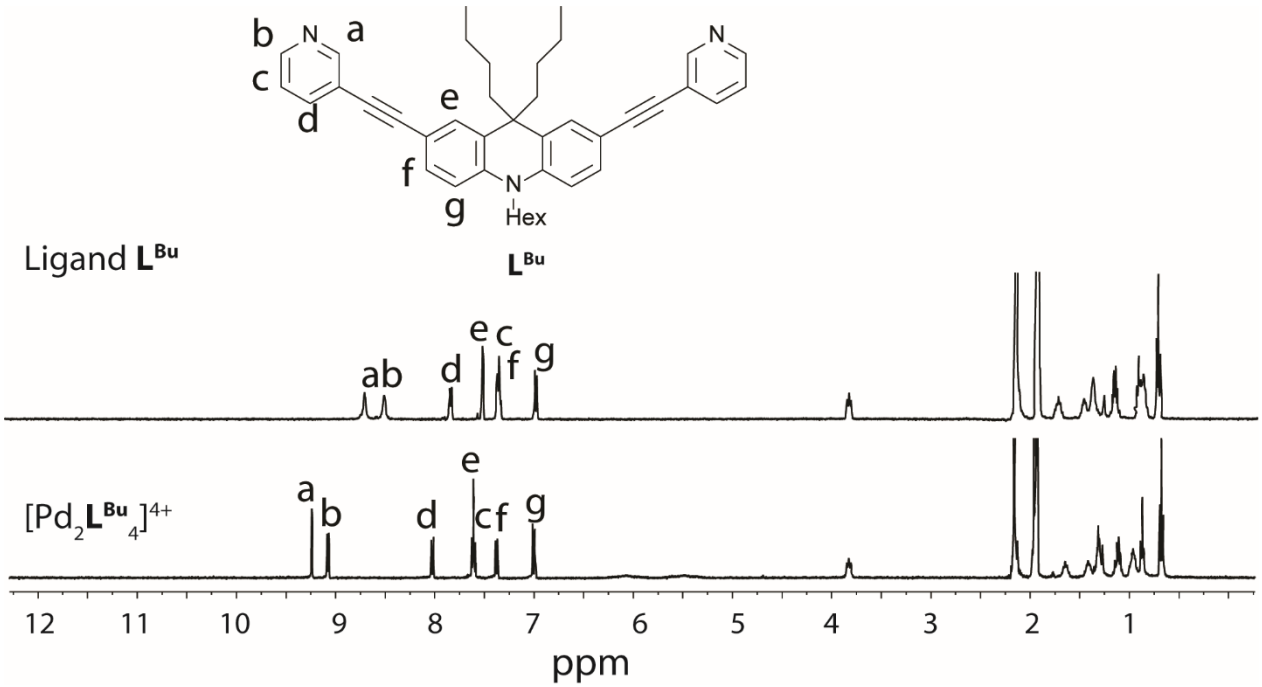

Figure S4.4. ^{1}H NMR spectrum (500 MHz/CD_3CN) of cage $[Pd_2\mathbf{L}^{\mathbf{Bu}}{}_4](BF_4)_4$ compared with free ligand $\mathbf{L}^{\mathbf{Bu}}$.

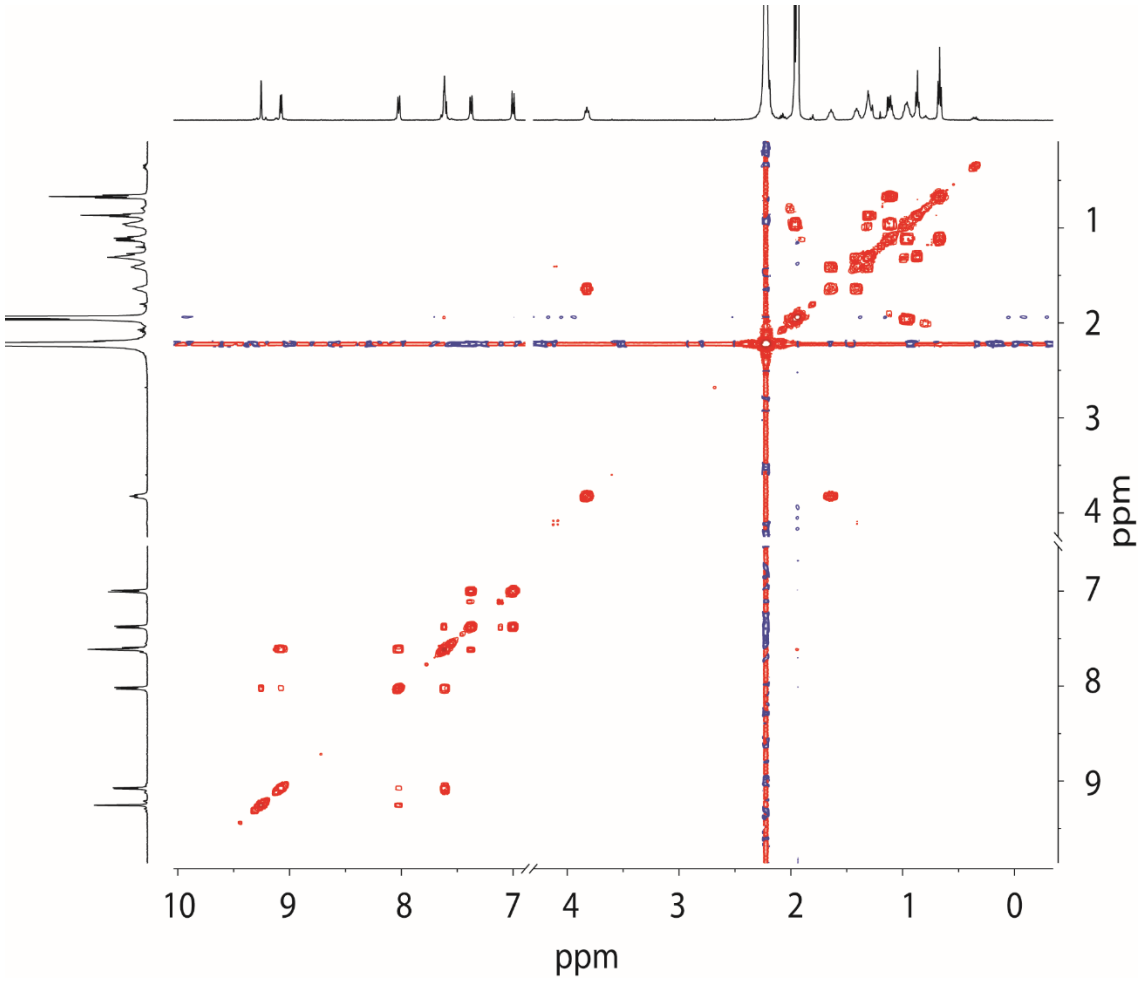

Figure S4.5. COSY NMR of cage $[Pd_2\mathbf{L}^{\mathbf{Bu}}{}_4](BF_4)_4$ (500 MHz, CD_3CN)

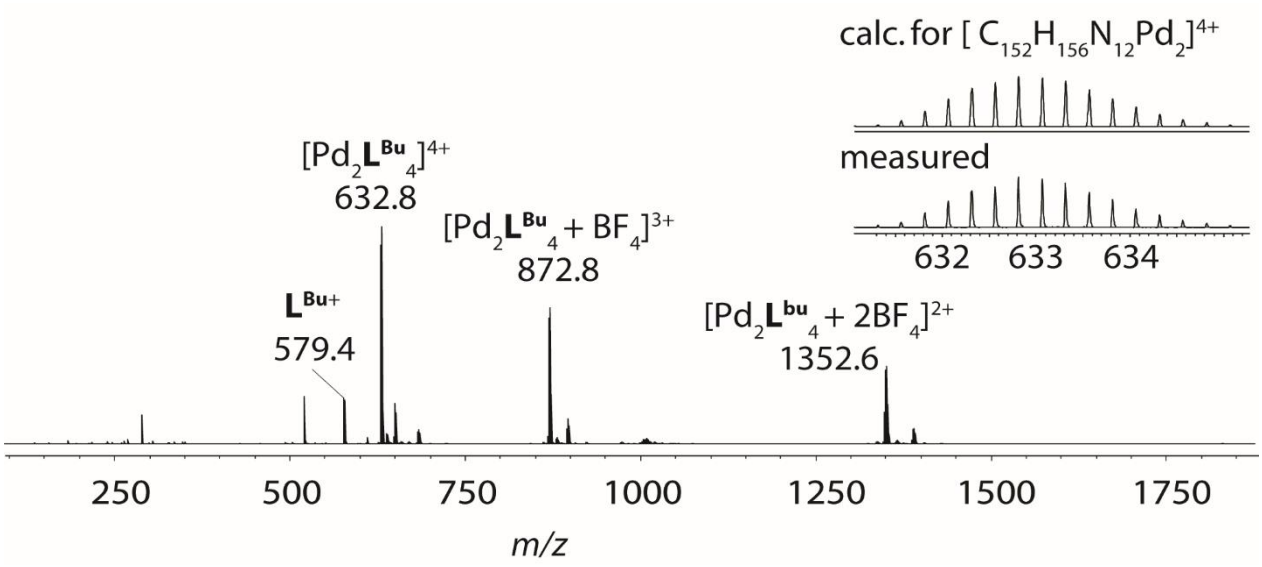

Figure S4.6. HRMS of cage $[Pd_2\mathbf{L}^{\mathbf{Bu}}{}_4](BF_4)_4$

4.6.3.4. Characterization of self-assembled cage $[Pd_2L^{Ph}{}_4](BF_4)_4$.

^{1}H NMR (500 MHz, CD_3CN) δ 8.82 (d, *J* = 1.8 Hz, 2H), 8.80 – 8.73 (m, 2H), 7.98 (dt, *J* = 8.1, 1.5 Hz, 2H), 7.56 – 7.45 (m, 4H), 7.23 (d, *J* = 8.6 Hz, 2H), 7.15 (t, *J* = 7.7 Hz, 4H), 6.95 (d, *J* = 2.0 Hz, 2H), 6.92 (t, *J* = 7.4 Hz, 2H), 6.80 (d, *J* = 7.9 Hz, 4H), 3.91 (t, *J* = 7.4 Hz, 2H), 1.41 (p, *J* = 7.4 Hz, 2H), 1.14 – 1.00 (m, 4H), 0.88 (p, *J* = 7.5 Hz, 2H), 0.78 (t, *J* = 7.2 Hz, 3H).

ESI-HRMS $[C_{180}H_{148}N_{12}Pd_2]^{4+}$: measured: 672.9980, calculated: 673.0019

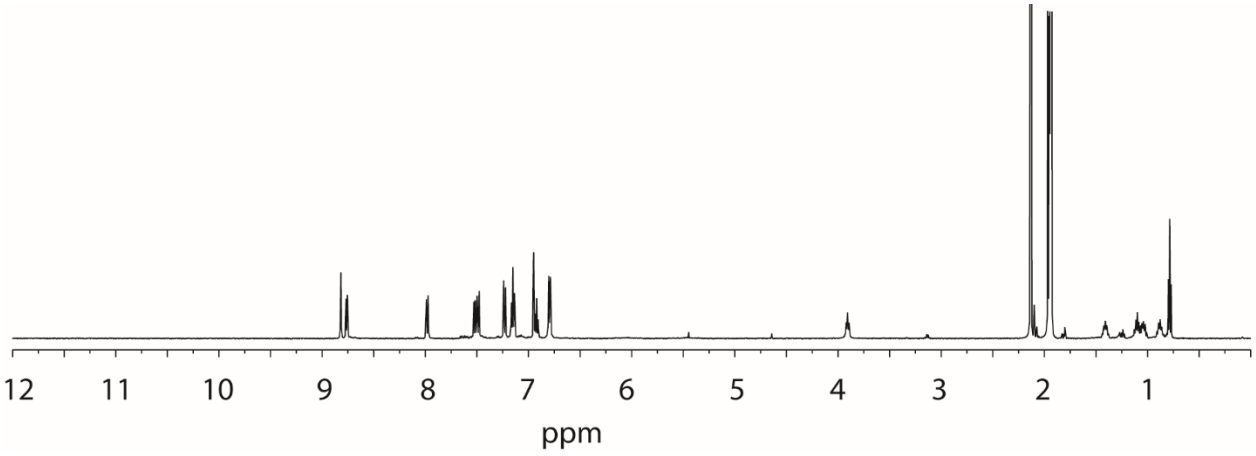

Figure S4.7. ^{1}H NMR spectrum (500 MHz/CD_3CN) of cage $[Pd_2\mathbf{L}^{Ph}{}_4](BF_4)_4$.

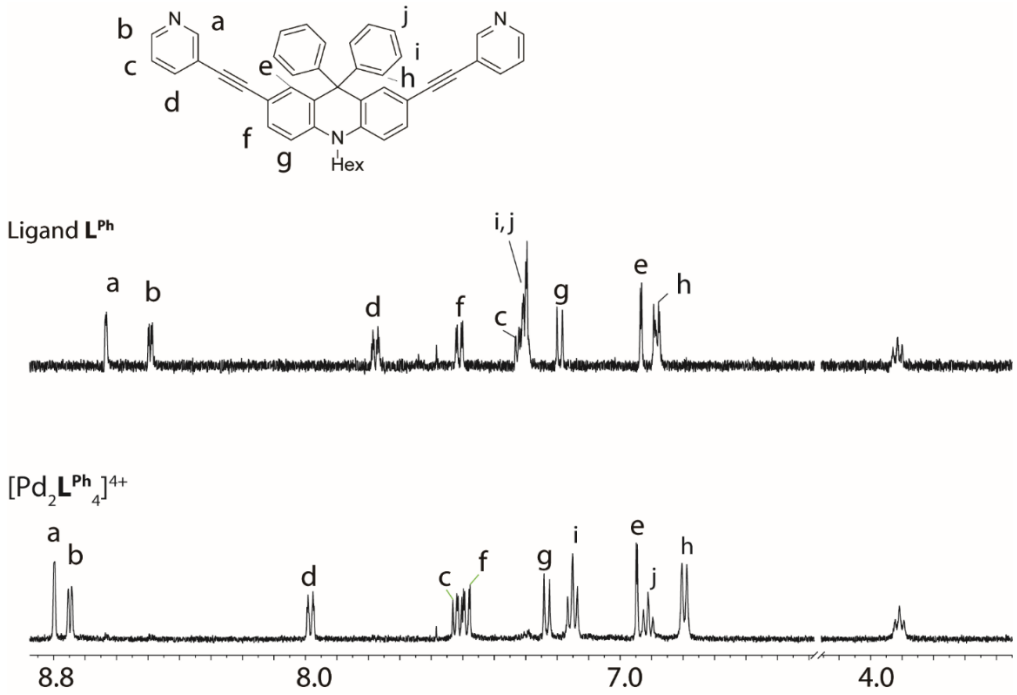

Figure S4.8. Partial ^{1}H NMR spectrum (500 MHz/CD_3CN) of cage $[Pd_2\mathbf{L}^{Bu}{}_4](BF_4)_4$ compared with free ligand $\mathbf{L}^{Ph}$.

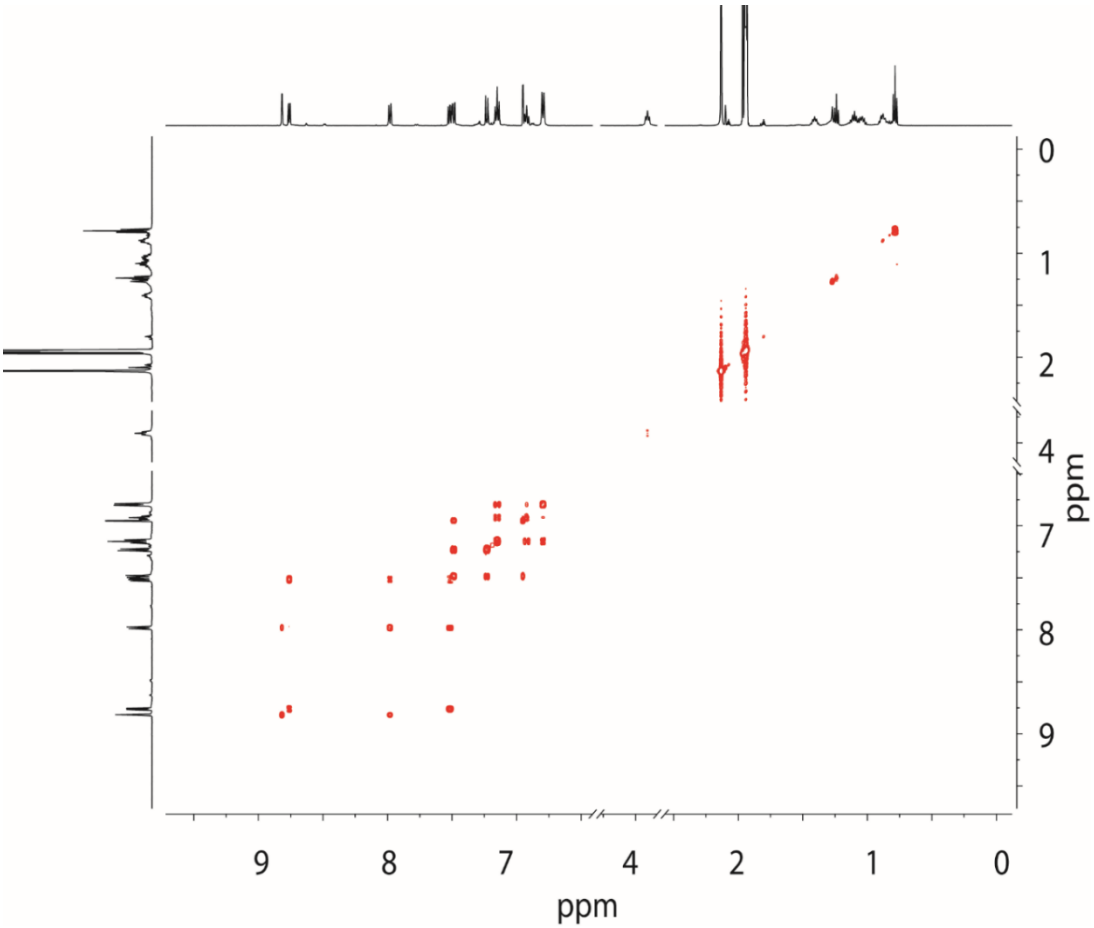

Figure S4.9. COSY NMR of cage $[Pd_2\mathbf{L}^{Ph}{}_4](BF_4)_4$ (500 MHz, CD_3CN).

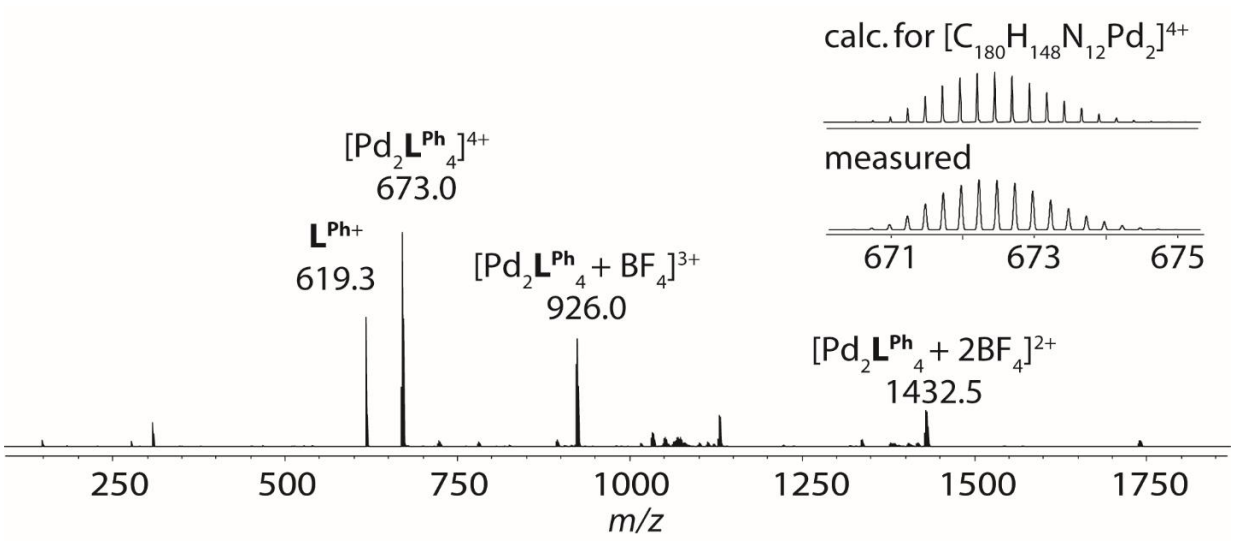

Figure S4.10. HRMS of cage $[Pd_2\mathbf{L}^{Ph}{}_4](BF_4)_4$

4.6.4. NMR titration experiments

All the titration experiments were performed on a Bruker AV 500 Avance NEO spectrometer at 298 K in CD_3CN using BF_4^- as counterion of cage complexes. Tetrabutylammonium salts were used as source of anionic guests. The accurate concentrations of self-assembled cages were determined by adding 1.0 equiv. tetrabutylammonium (TBA) salt as reference. At least 10 datapoints were collected for each titration experiment. All the results were fitting by the software Bindfit (http://app.supramolecular.org/).

4.6.4.1. $[Pd_2\mathbf{L}^{Ph}_4](BF_4)_4$ with ReO_4^-

Table S4.1 Tabulated signal shifts of inward pointing protons *a* and *e*, concentration of $[Pd_2\mathbf{L}^{Ph}_4]^{4+}$ is 0.557 mM, the association constants K_a was calculated using a 1:1 mode.

Guest (eq.)	a (ppm)	e (ppm)	j (ppm)
0.0	8.8168	6.9523	6.9203
0.2	8.8325	6.9562	6.9226
0.5	8.8448	6.9583	6.9240
0.7	8.8610	6.9641	6.9267
0.9	8.8726	6.9671	6.9283
1.1	8.8814	6.9692	6.9294
1.4	8.8891	6.9712	6.9303
1.6	8.8957	6.9727	6.9313
1.8	8.9015	6.9741	6.9322
2.1	8.9059	6.9752	6.9327
2.3	8.9104	6.9761	6.9335
2.5	8.9143	6.9769	6.9341
2.8	8.9172	6.9775	6.9344
3.0	8.9205	6.9781	6.9349
3.2	8.9236	6.9787	6.9354
3.4	8.9261	6.9791	6.9358
K_a = 2024.05 ± 1.41%			

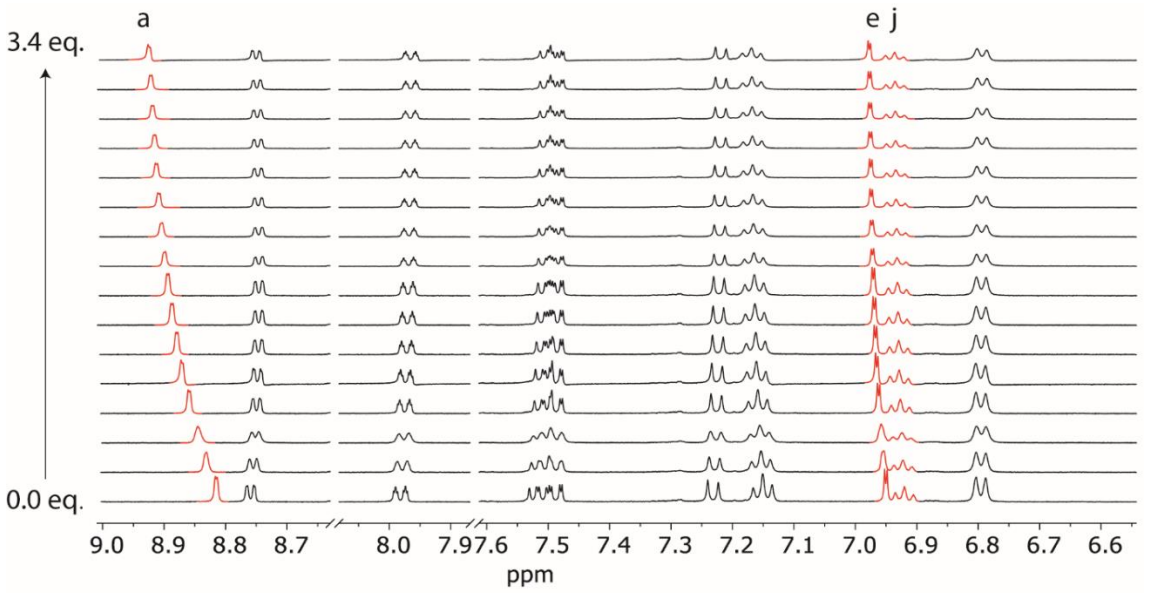

Figure S4.11. ^{1}H NMR-monitored titrations of ReO_4^- with $[Pd_2\mathbf{L}^{\mathbf{Ph}}_4]^{4+}$, signals of inward pointing proton *a, e* and *j* are highlighted with red color.

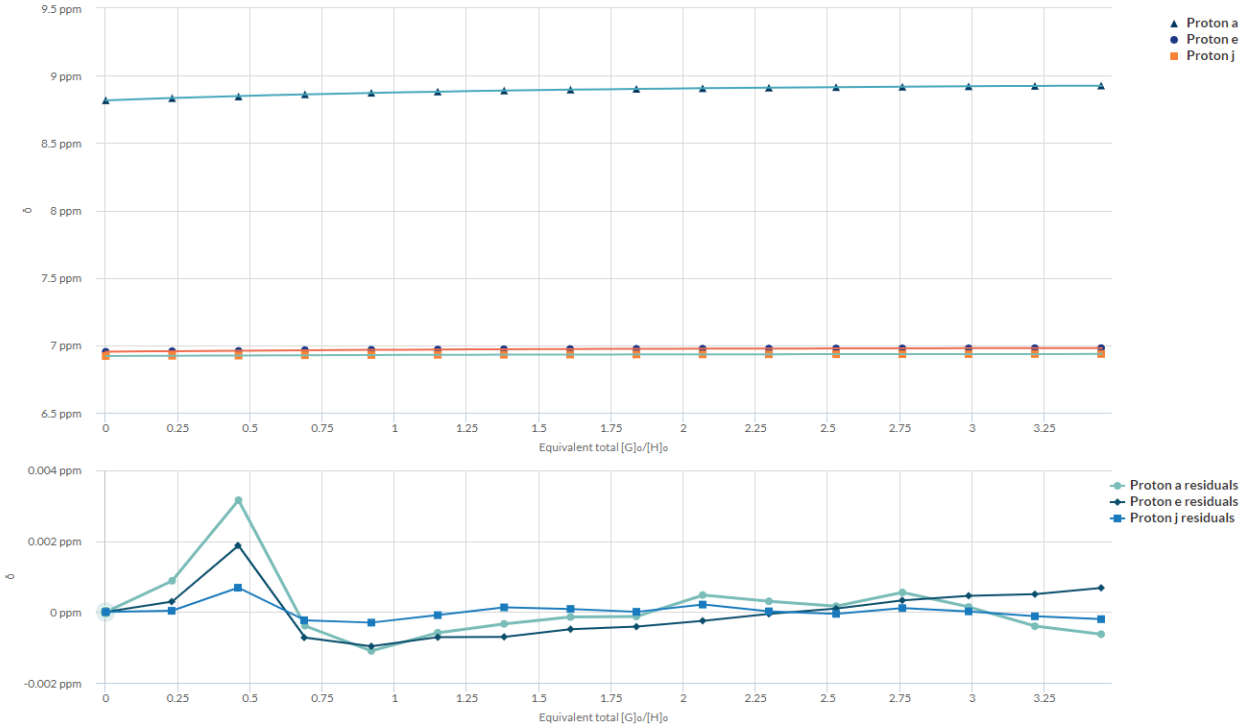

Figure S4.12 Global fitting plot and residual distributions of proton a, e and j for the titration experiment ReO_4^- with $[Pd_2\mathbf{L}^{\mathbf{Ph}}_4]^{4+}$ using 1:1 mode.

4.6.4.2. $[Pd_2\mathbf{L}^{Ph}_4](BF_4)_4$ with IO_4^-

Table S4.2. Tabulated signal shifts of inward pointing protons *a e* and *j*, concentration of $[Pd_2\mathbf{L}^{Ph}_4]^{4+}$ is 0.500 mM, the association constants K_a was calculated using 1:1 mode.

Guest (eq.)	a (ppm)	e (ppm)	j (ppm)
0.0	8.8612	6.9748	6.9280
0.3	8.8803	6.9782	6.9241
0.5	8.8951	6.9819	6.9209
0.8	8.9076	6.9833	6.9186
1.0	8.9198	6.9856	6.9159
1.3	8.9294	6.9872	6.9143
1.5	8.9370	6.9886	6.9182
1.8	8.9443	6.9899	6.9115
2.0	8.9504	6.9909	6.9105
2.3	8.9558	6.9918	6.9095
2.6	8.9606	6.9926	6.9087
3.2	8.9690	6.9939	6.9075
3.8	8.9761	6.9951	6.9065
K_a = 1910.68 ± 1.94%			

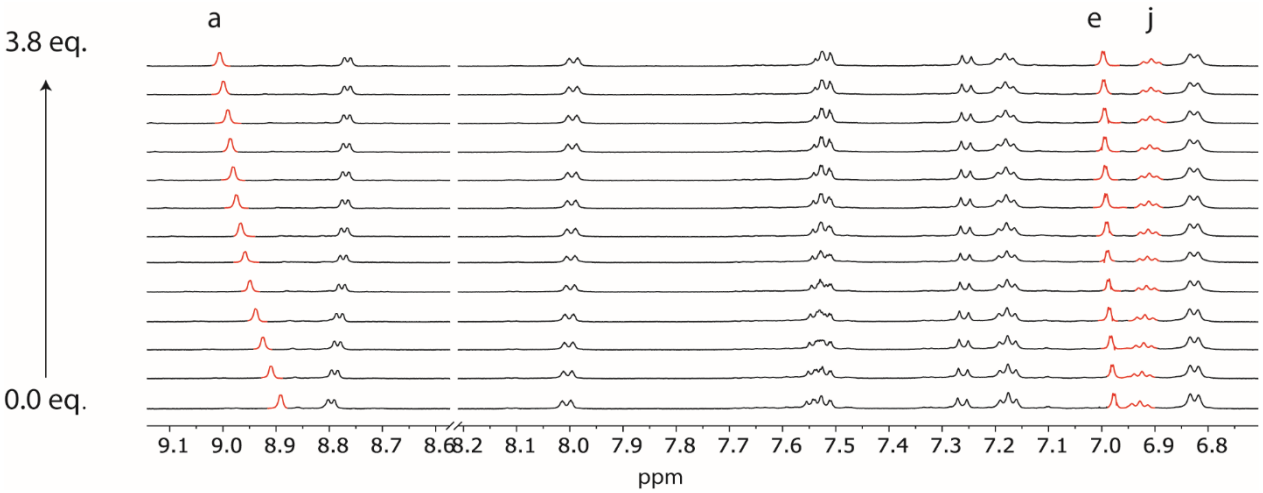

Figure S4.13. ^{1}H NMR-monitored titrations of IO_4^- with $[Pd_2\mathbf{L}^{Ph}_4]^{4+}$, signals of inward pointing proton *a e* and *j* are highlighted with red color.

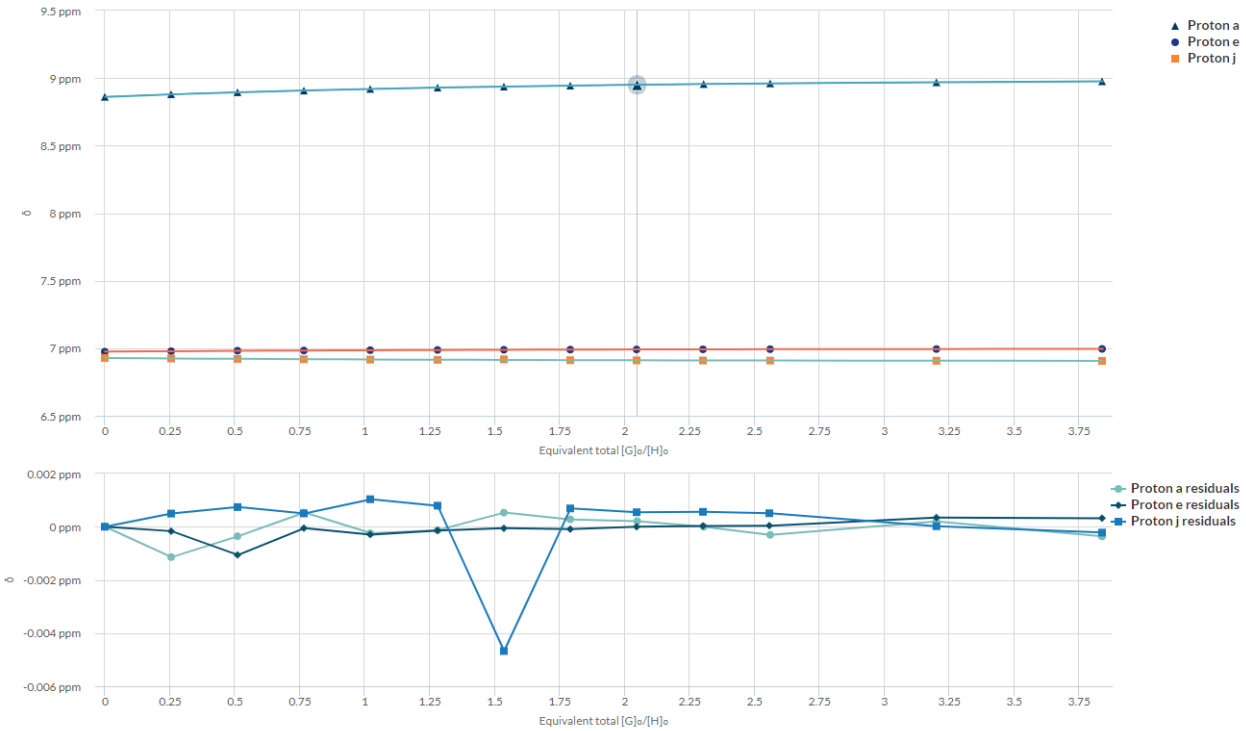

Figure S4.14 Global fitting plot and residual distributions of proton a, e and j for the titration experiment IO_4^- with $[Pd_2\mathbf{L}^{\mathbf{Ph}}_4]^{4+}$ using 1:1 mode.

4.6.2.3. $[Pd_2\mathbf{L}^{Ph}_4](BF_4)_4$ with ClO_4^-

Table S4.3 Tabulated signal shifts of inward pointing protons *a* e and *j*, concentration of $[Pd_2\mathbf{L}^{Ph}_4]^{4+}$ is 0.557 mM, the association constants K_a was calculated using 1:1 mode.

Guest (eq.)	a (ppm)	e (ppm)	j (ppm)
0.0	8.8216	6.9485	6.9212
0.2	8.8323	6.9498	6.9245
0.5	8.8427	6.951	6.9273
0.7	8.8514	6.9521	6.9295
0.9	8.8592	6.953	6.9316
1.1	8.8663	6.9539	6.9335
1.4	8.8733	6.9497	6.9351
1.8	8.8845	6.9559	6.9379
2.3	8.8944	6.9596	6.9401
2.8	8.9029	6.9679	6.9272
3.2	8.9100	6.9587	6.9436
3.7	8.9166	6.9594	6.9447
4.6	8.9221	6.96	6.9459
5.7	8.9335	6.9611	6.9482
K_a = 823.23 ± 5.53%			

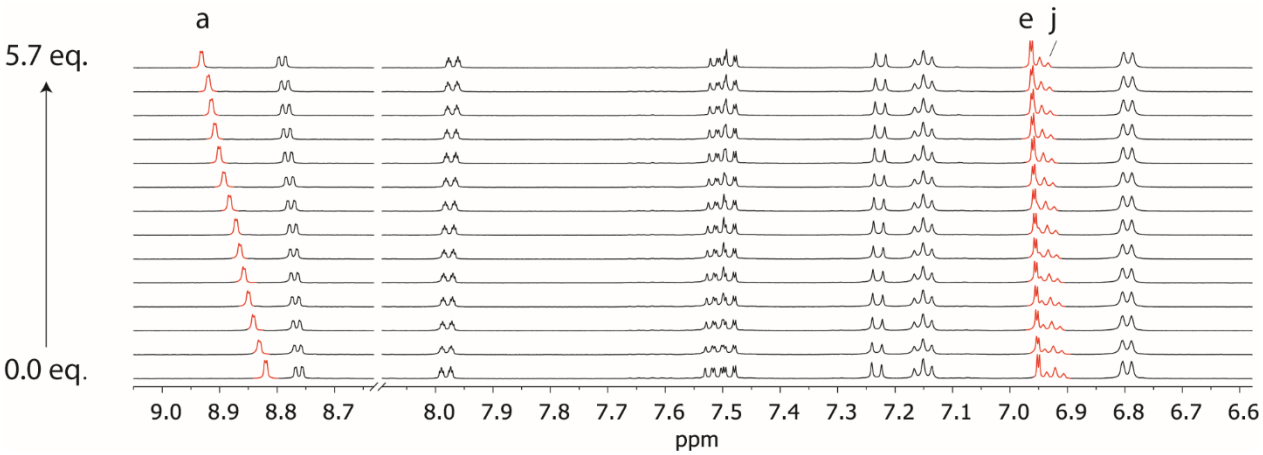

Figure S4.15. ^{1}H NMR-monitored titrations of ClO_4^- with $[Pd_2\mathbf{L}^{Ph}_4]^{4+}$, signals of inward pointing proton *a e* and *j* are highlighted with red color.

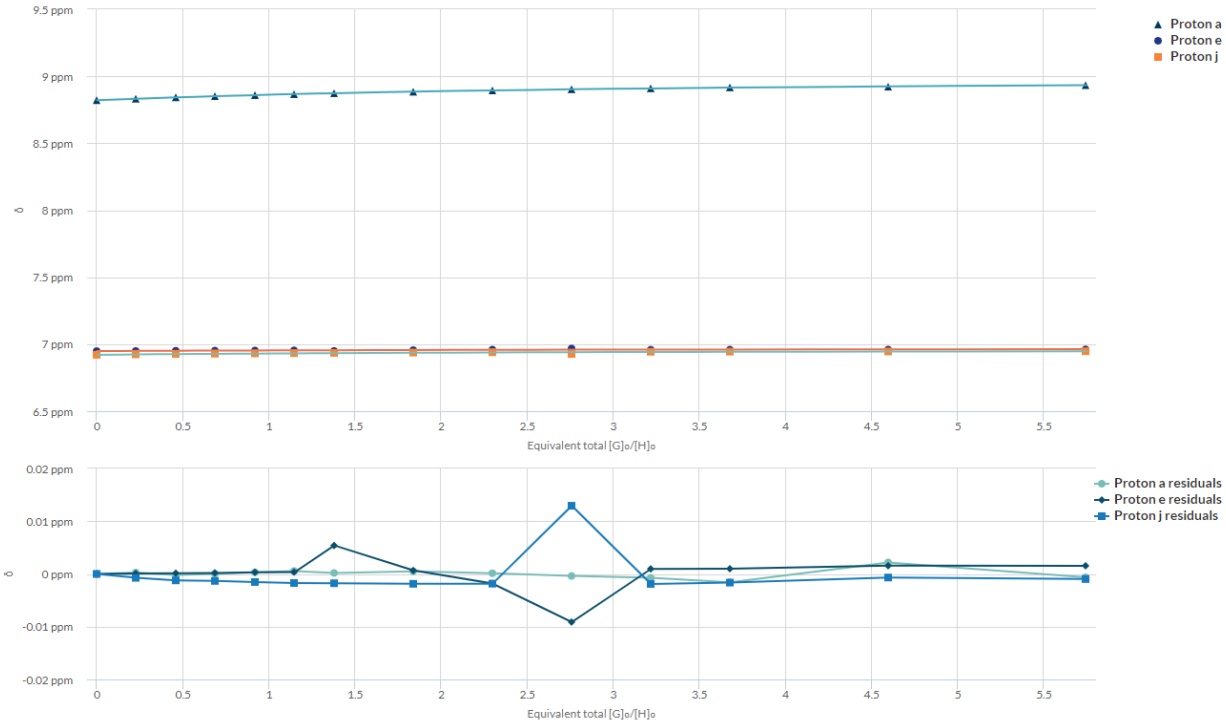

Figure S4.16 Global fitting plot and residual distributions of proton a, e and j for the titration experiment ClO_4^- with $[Pd_2\mathbf{L}^{\mathbf{Ph}}_4]^{4+}$ using 1:1 mode.

4.6.2.4. $[Pd_2\mathbf{L}^{\mathbf{Bu}}{}_4](BF_4)_4$ with ReO_4^-

Table S4.4. Tabulated signal shifts of inward pointing protons *a* *e*, concentration of $[Pd_2\mathbf{L}^{\mathbf{Bu}}{}_4]^{4+}$ is 0.442 mM, the association constants K_a was calculated using 1:1 mode.

Guest (eq.)	a (ppm)	e (ppm)
0.00	9.2371	7.6074
0.29	9.2496	7.6075
0.58	9.2599	7.6114
0.87	9.2706	7.6147
1.16	9.2772	7.6135
1.45	9.2852	7.6178
1.74	9.2913	7.6189
2.03	9.2963	7.6202
2.32	9.3006	7.6209
2.61	9.3021	7.62
2.90	9.3068	7.6224
3.19	9.3092	7.6229
3.48	9.3114	7.6232
3.76	9.3135	7.6239
4.05	9.3151	7.6244
4.34	9.3167	7.6247
4.63	9.3182	7.6249
4.92	9.3195	7.6254
5.21	9.3208	7.6258
5.50	9.3218	7.6262
5.79	9.3227	7.6263
6.23	9.324	7.6265
6.66	9.325	7.627
7.10	9.326	7.6273
K_a = 1829.73 $\pm$ 1.71%		

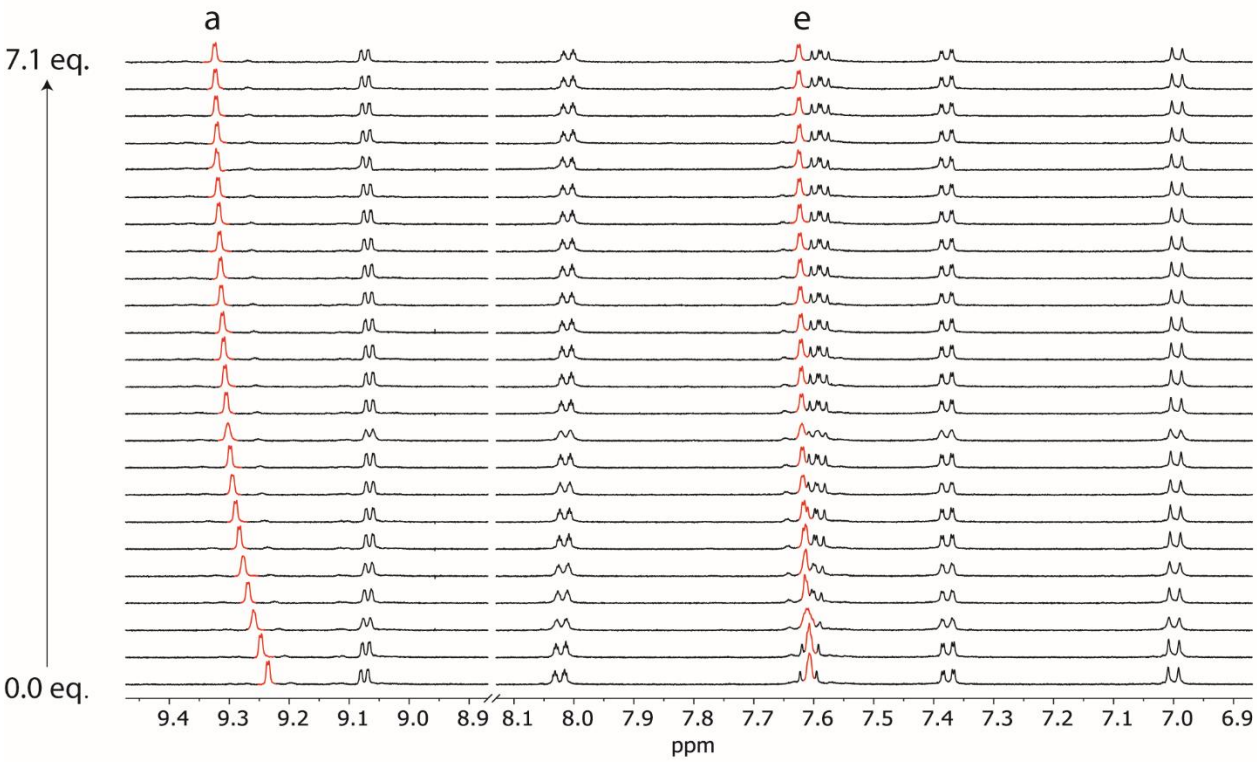

Figure S4.17. ^{1}H NMR-monitored titrations of ReO_4^- with $[Pd_2\mathbf{L}^{\mathbf{Bu}}{}_4]^{4+}$, signals of inward pointing proton *a* and *e* are highlighted with red color.

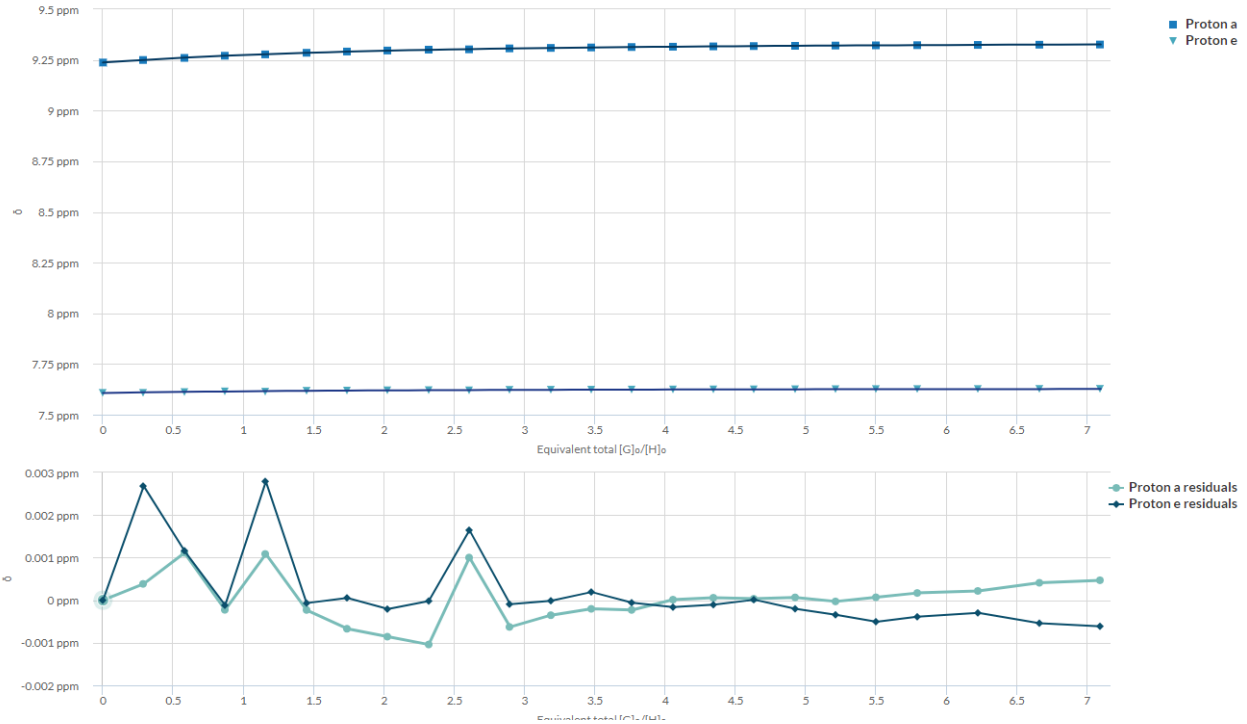

Figure S4.18 Global fitting plot and residual distributions of proton a and e for the titration experiment ReO_4^- with $[Pd_2\mathbf{L}^{\mathbf{Bu}}{}_4]^{4+}$ using 1:1 mode.

4.6.2.5. $[Pd_2\mathbf{L}^{\mathbf{Bu}}{}_4](BF_4)_4$ with IO_4^-

Table S4.5. Tabulated signal shifts of inward pointing protons *a* *e*, concentration of $[Pd_2\mathbf{L}^{\mathbf{Bu}}{}_4]^{4+}$ is 0.408 mM, the association constants K_a was calculated using 1:1 mode.

Guest (eq.)	a (ppm)	e (ppm)
0.0	9.2177	7.5955
0.3	9.2382	7.5973
0.6	9.255	7.6016
0.9	9.2703	7.6035
1.3	9.2834	7.6046
1.6	9.2968	7.6059
1.9	9.3053	7.6063
2.2	9.3134	7.6072
2.5	9.3211	7.6079
2.8	9.3271	7.608
3.1	9.3317	7.6084
3.5	9.3362	7.6089
3.8	9.3419	7.6089
4.1	9.3445	7.6093
4.4	9.3481	7.6102
4.7	9.3528	7.6105
K_a = 1455.54 ± 1.28%		

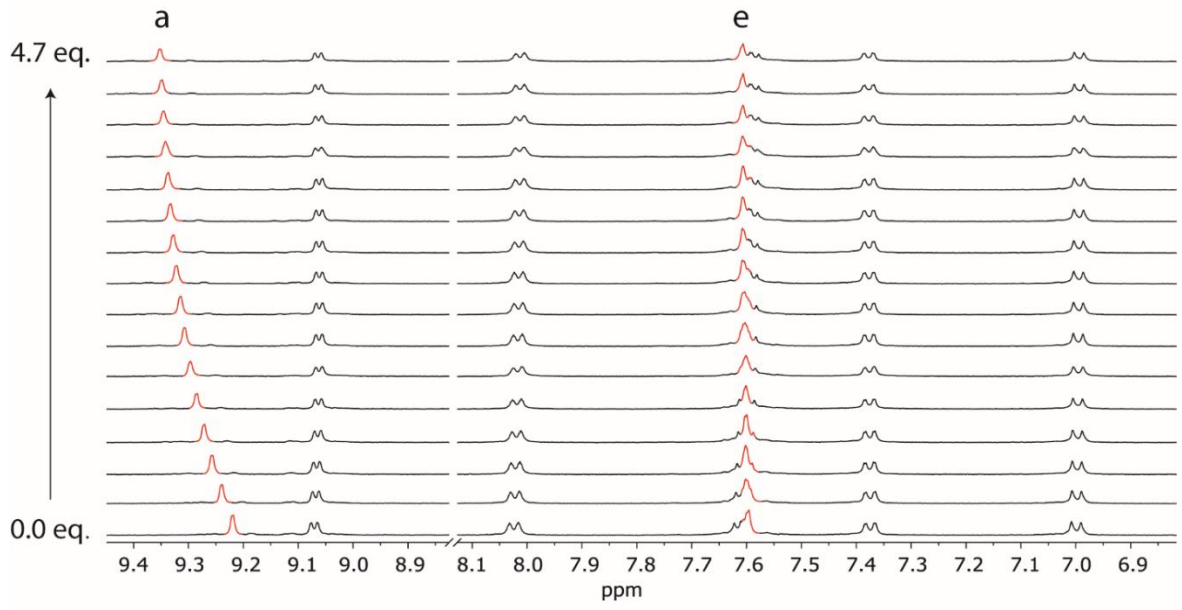

Figure S4.19. ^{1}H NMR-monitored titrations of IO_4^- with $[Pd_2\mathbf{L}^{\mathbf{Bu}}{}_4]^{4+}$, signals of inward pointing proton *a* and *e* are highlighted with red color.

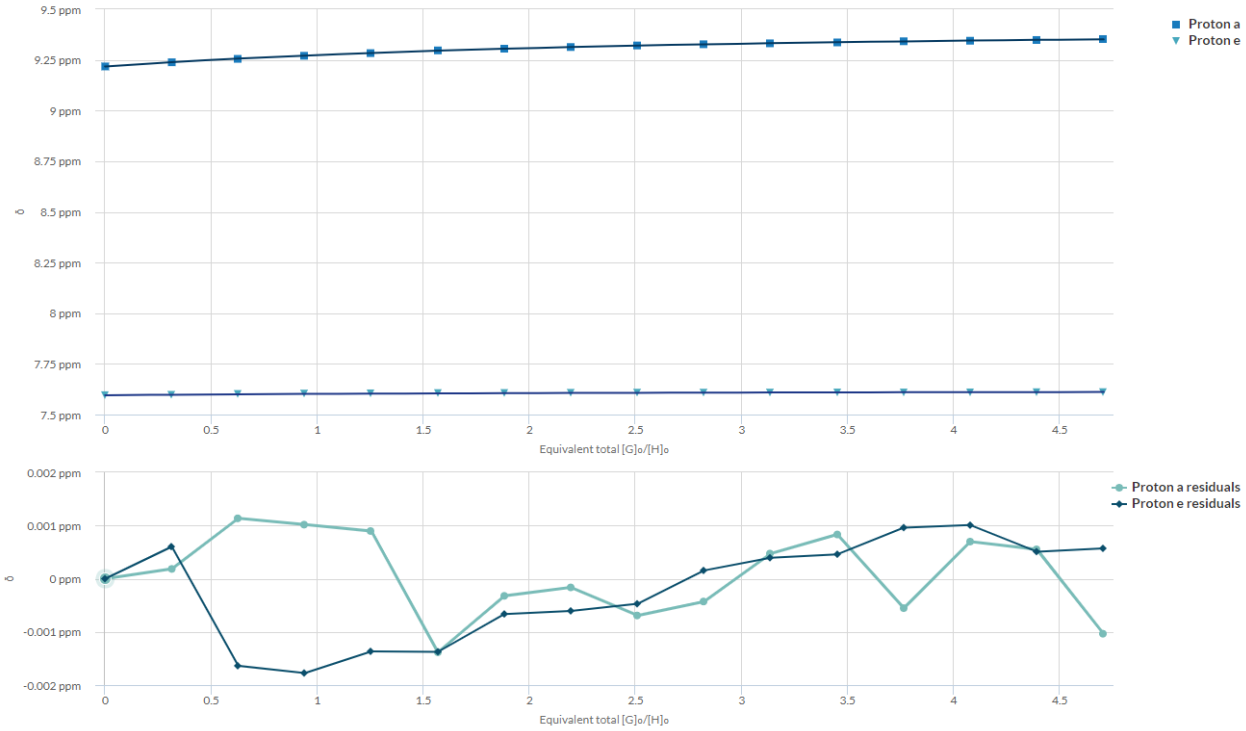

Figure S4.20 Global fitting plot and residual distributions of proton a and e for the titration experiment IO_4^- with $[Pd_2\mathbf{L}^{\mathbf{Bu}}{}_4]^{4+}$ using 1:1 mode.

4.6.2.6. $[Pd_2L^{Bu}_4](BF_4)_4$ with ClO_4^-

Table S4.6. Tabulated signal shifts of inward pointing protons *a* *e*, concentration of $[Pd_2L^{Bu}_4]^{4+}$ is 0.516 mM, the association constants K_a was calculated using 1:1 mode.

Guest (eq.)	a (ppm)	e (ppm)
0.0	9.2203	7.5959
0.2	9.2253	7.5953
0.5	9.2303	7.5947
0.7	9.235	7.594
1.0	9.2397	7.5935
1.2	9.2439	7.5927
1.5	9.2482	7.5924
2.0	9.2552	7.5914
2.5	9.2615	7.5905
3.0	9.2668	7.5892
3.5	9.2718	7.5886
4.0	9.2764	7.5881
5.0	9.2845	7.5872
6.2	9.2925	7.5865
K_a = 374.19 ± 0.59%		

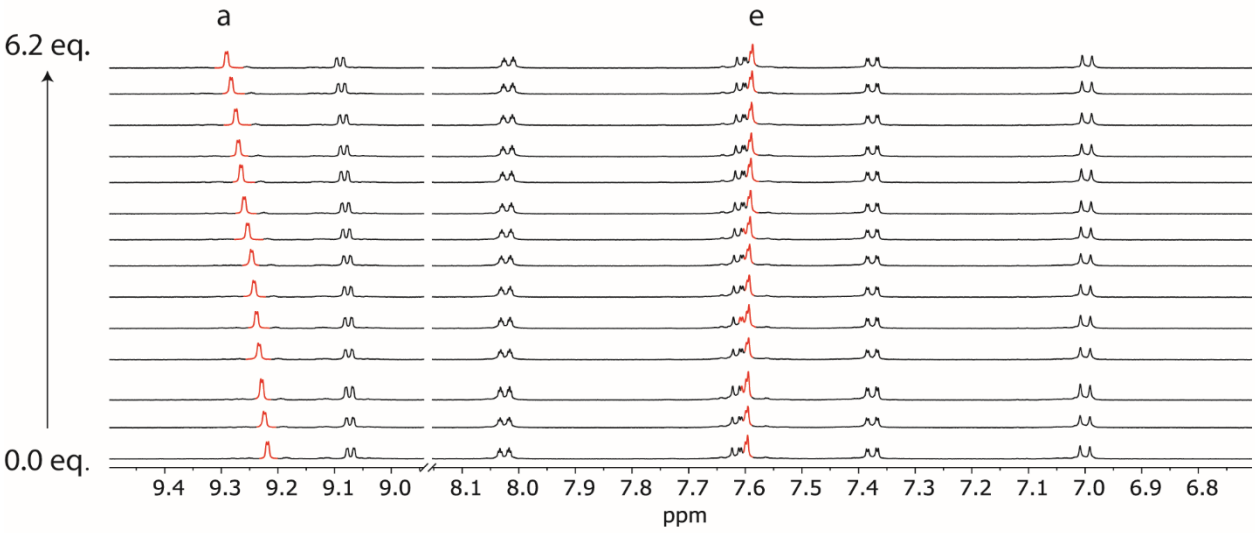

Figure S4.21. ^{1}H NMR-monitored titrations of ClO_4^- with $[Pd_2L^{Bu}_4]^{4+}$, signals of inward pointing proton *a* and *e* are highlighted with red color.

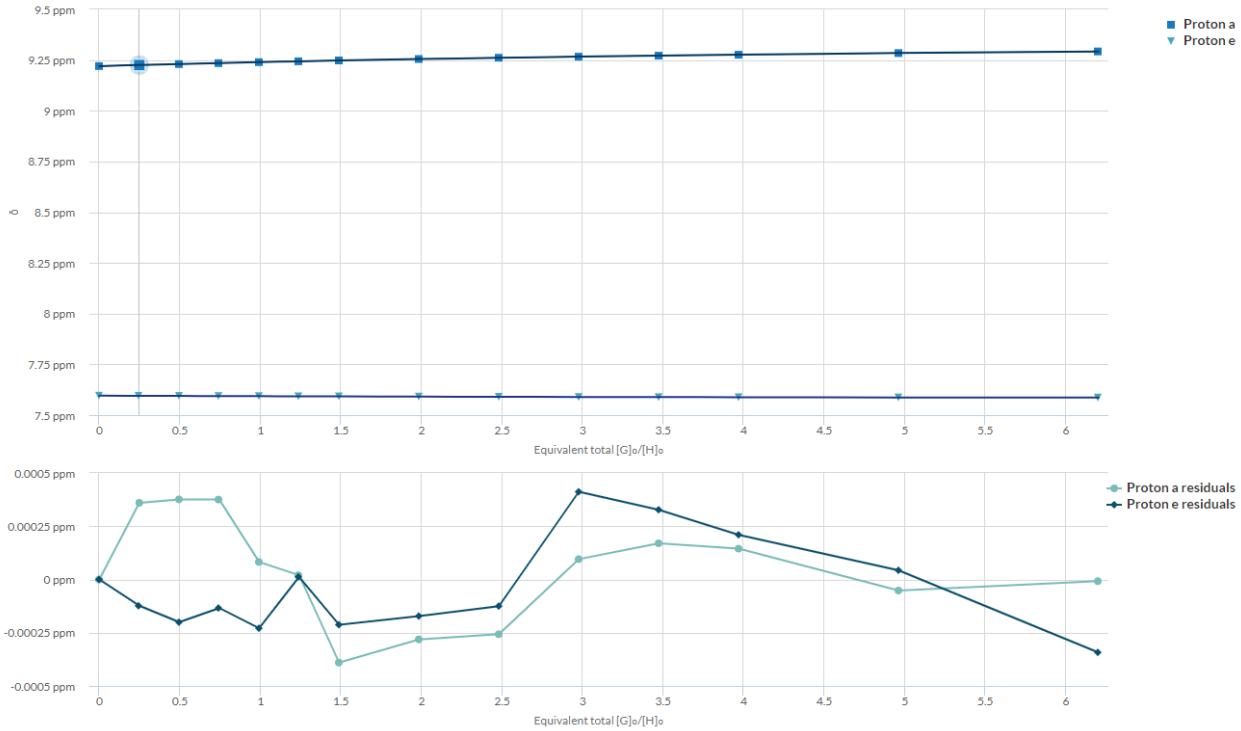

Figure S4.22 Global fitting plot and residual distributions of proton a and e for the titration experiment ClO_4^- with $[Pd_2\mathbf{L}^{\mathbf{Bu}}{}_4]^{4+}$ using 1:1 mode.

4.6.2.7. $[Pd_2\mathbf{L}^{Me}{}_4](BF_4)_4$ with ReO_4^-

Table S4.7. Tabulated signal shifts of inward pointing protons *a e* and *h* concentration of $[Pd_2\mathbf{L}^{Me}{}_4]^{4+}$ is 0.600 mM, the association constants K_a was calculated using 1:2 statistical binding mode, $K_{a2} = K_{a1}/4$.

Guest (eq.)	a (ppm)	e (ppm)	h (ppm)
0.0	9.3132	7.9429	1.6767
0.2	9.3429	7.9486	1.6851
0.4	9.3670	7.9549	1.6929
0.6	9.3916	7.9597	1.6994
0.9	9.4175	7.9663	1.7057
1.1	9.4428	7.9732	1.7121
1.3	9.4655	7.9798	1.7177
1.5	9.4865	7.9862	1.7228
1.7	9.5068	7.9916	1.7270
1.9	9.5242	7.9942	1.7307
2.1	9.5385	8.0020	1.7339
2.3	9.5527	8.0059	1.7369
2.6	9.5642	8.0083	1.7392
2.8	9.5741	8.0129	1.7410
3.0	9.5820	8.0154	1.7426
3.2	9.5885	8.0173	1.7442
3.4	9.5962	8.0186	1.7455
3.6	9.6021	8.0218	1.7465
3.8	9.6061	8.0232	1.7475
4.1	9.609	8.0228	1.7483
4.3	9.6125	8.0256	1.7490
4.6	9.6175	8.0271	1.7498
4.9	9.6223	8.0279	1.7505
5.2	9.6229	8.0288	1.7511
$K_{a1} = 5882.57 \pm 2.34\%$			

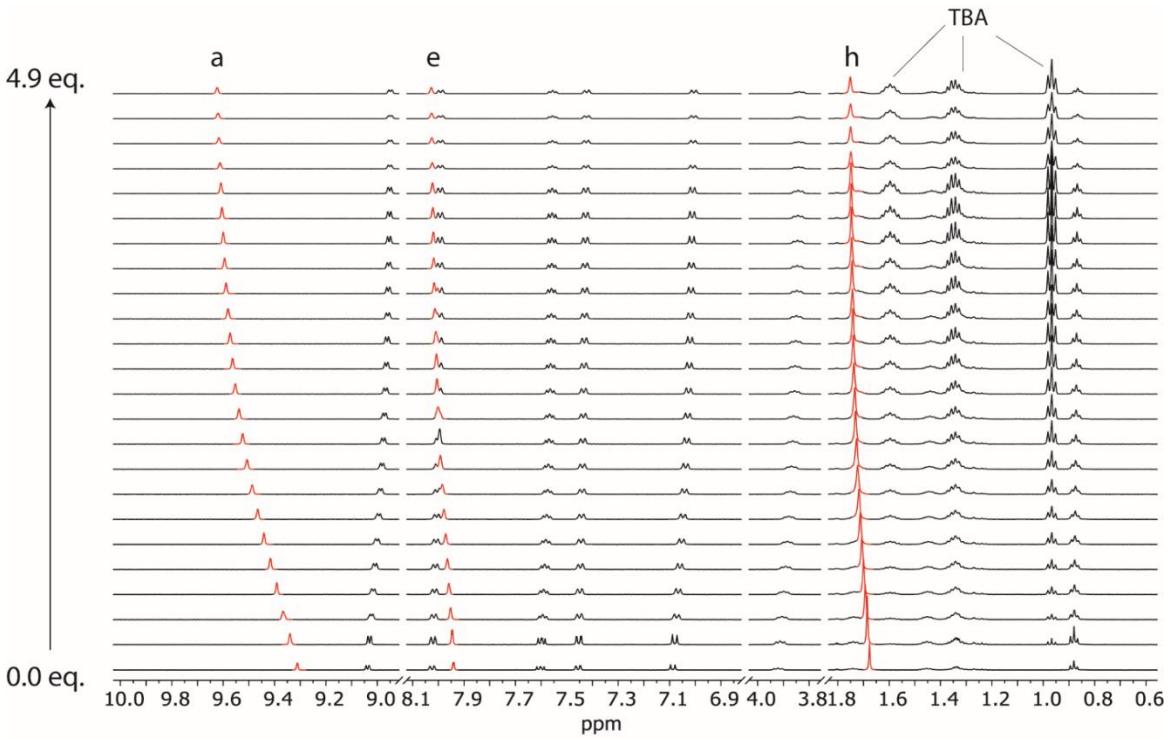

Figure S4.23. ^{1}H NMR-monitored titrations of ReO_4^- with $[Pd_2\mathbf{L}^{\mathbf{Me}}_4]^{4+}$, signals of inward pointing proton *a e* and *h* are highlighted with red color.

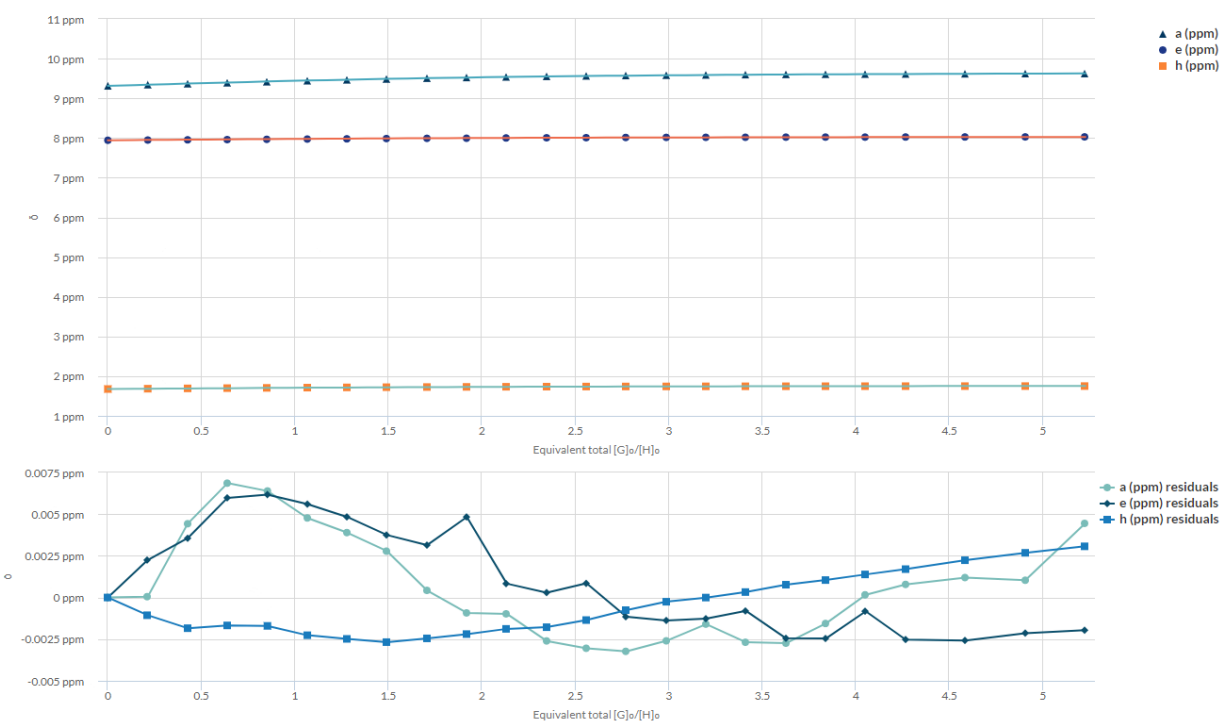

Figure S4.24 Global fitting plot and residual distributions of proton a, e and h for the titration experiment ReO_4^- with $[Pd_2\mathbf{L}^{\mathbf{Me}}_4]^{4+}$ using 1:2 statistical binding mode.

4.6.2.8. $[Pd_2\mathbf{L}^{Me}_4](BF_4)_4$ with IO_4^-

Table S4.8. Tabulated signal shifts of inward pointing protons *a e* and *h* concentration of $[Pd_2\mathbf{L}^{Me}_4]^{4+}$ is 0.512 mM, the association constants K_a was calculated using 1:2 statistical binding mode, $K_{a2} = K_{a1}/4$.

Guest (eq.)	a (ppm)	b (ppm)	h (ppm)
0.0	9.3067	7.9409	1.6752
0.3	9.3471	7.9463	1.6840
0.5	9.3899	7.9531	1.6932
0.8	9.4340	7.9606	1.7025
1.0	9.4733	7.9681	1.7111
1.3	9.5131	7.9755	1.7186
1.5	9.5493	7.9834	1.7262
1.8	9.5843	7.9908	1.7326
2.0	9.6148	7.9975	1.7383
2.3	9.6397	8.0030	1.7430
2.5	9.6605	8.0076	1.7469
2.8	9.6757	8.0111	1.7498
3.0	9.6895	8.0143	1.7522
3.3	9.6988	8.0168	1.7542
3.5	9.7081	8.0190	1.7560
3.8	9.7162	8.0208	1.7573
4.4	9.7293	8.0239	1.7595
5.0	9.7380	8.0260	1.7610
$K_{a1} = 7021.47 \pm 3.61\%$			

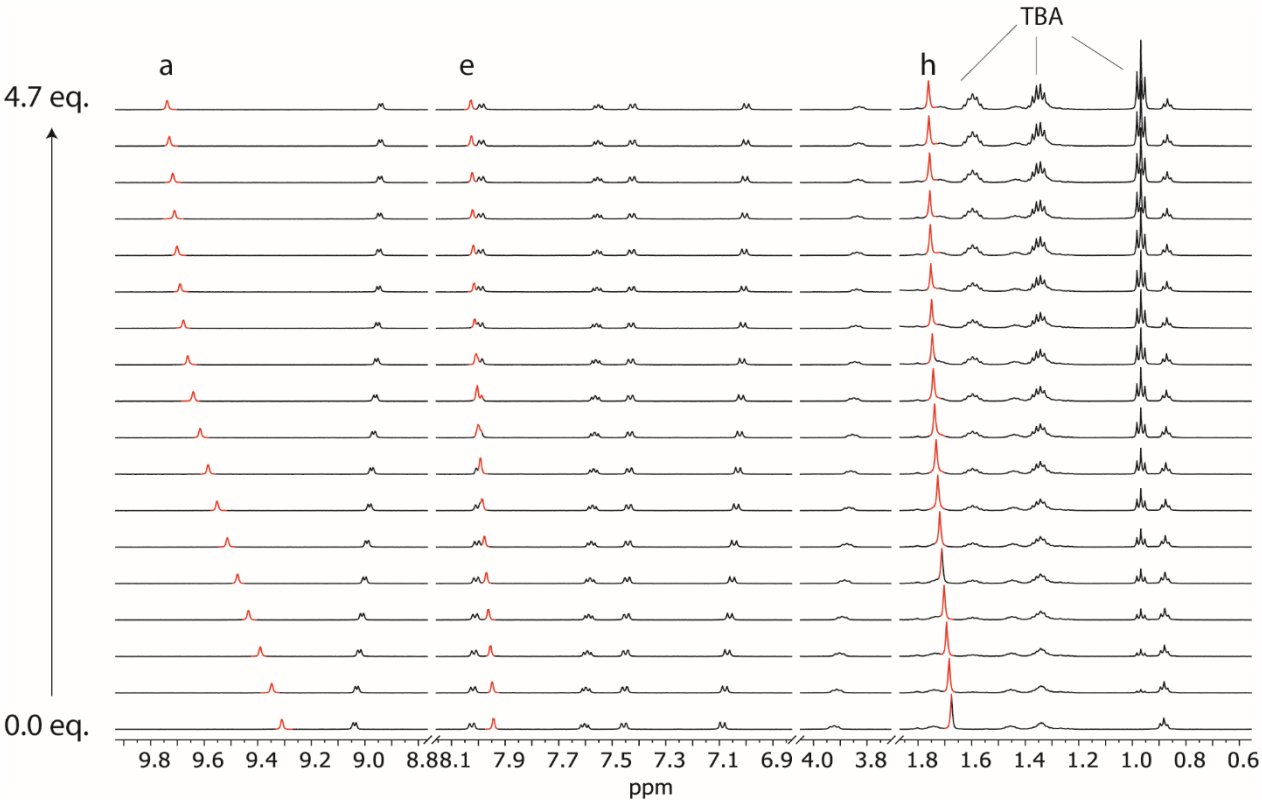

Figure S4.25. ^{1}H NMR-monitored titrations of IO_4^- with $[Pd_2\mathbf{L}^{\mathbf{Me}}{}_4]^{4+}$, signals of inward pointing proton *a* *e* and *h* are highlighted with red color.

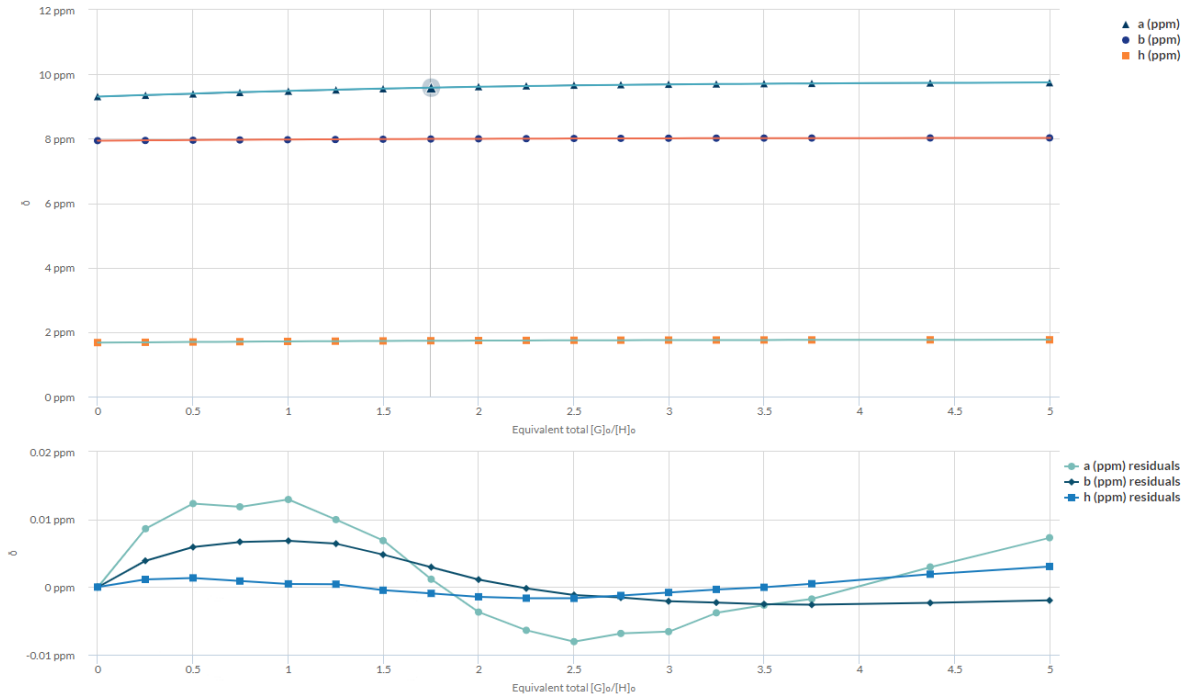

Figure S4.26 Global fitting plot and residual distributions of proton a, e and h for the titration experiment IO_4^- with $[Pd_2\mathbf{L}^{\mathbf{Me}}{}_4]^{4+}$ using 1:2 statistical binding mode.

4.6.4.9. $[Pd_2\mathbf{L}^{Me}{}_4](BF_4)_4$ with ClO_4^-

Table S4.9. Tabulated signal shifts of inward pointing protons *a e* and *h* concentration of $[Pd_2\mathbf{L}^{Me}{}_4]^{4+}$ is 0.538 mM, the association constants K_a was calculated using 1:2 statistical binding mode, $K_{a2} = K_{a1}/4$.

Guest (eq.)	a (ppm)	b(ppm)	h (ppm)
0.0	9.3112	7.9422	1.6764
0.2	9.3174	7.9391	1.6767
0.5	9.3234	7.9363	1.6771
0.7	9.3291	7.9337	1.6774
1.0	9.3355	7.9310	1.6776
1.2	9.3402	7.9282	1.6771
1.4	9.3464	7.9269	1.6781
1.9	9.3565	7.9230	1.6787
2.4	9.3652	7.9196	1.6796
2.9	9.3733	7.9172	1.6803
3.3	9.3806	7.9144	1.6804
3.8	9.3872	7.9121	1.6811
4.8	9.3986	7.9081	1.6817
6.0	9.4104	7.9040	1.6823
$K_{a1} = 792.17 \pm 1.23\%$			

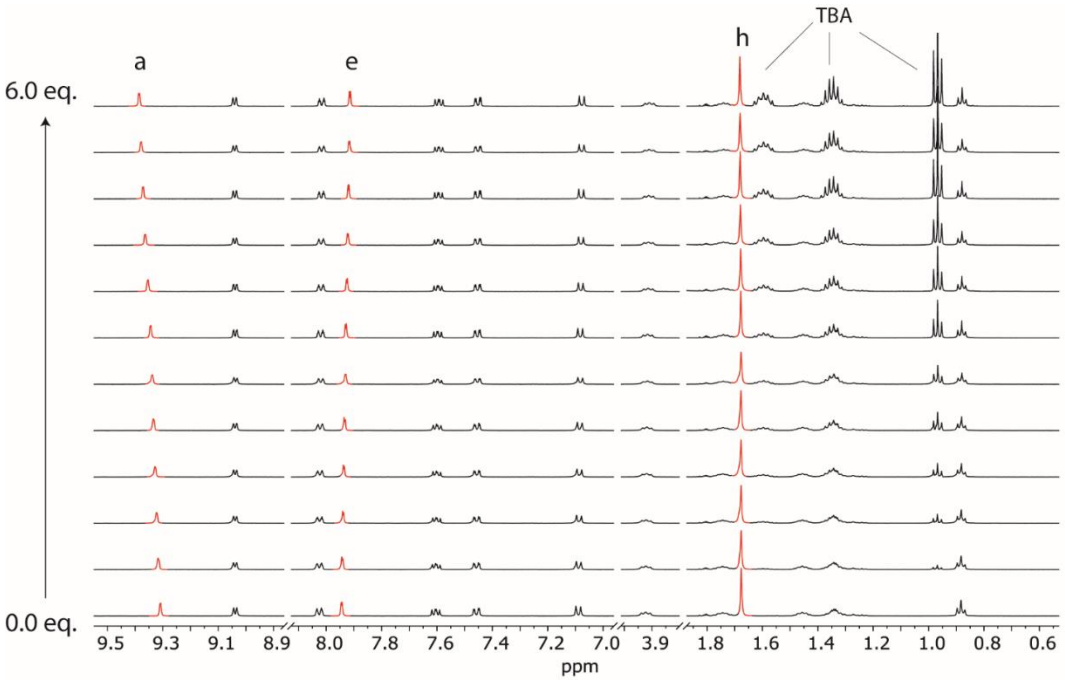

Figure S4.27. ^{1}H NMR-monitored titrations of ClO_4^- with $[Pd_2\mathbf{L}^{\mathbf{Me}}{}_4]^{4+}$, signals of inward pointing proton *a e* and *h* are highlighted with red color.

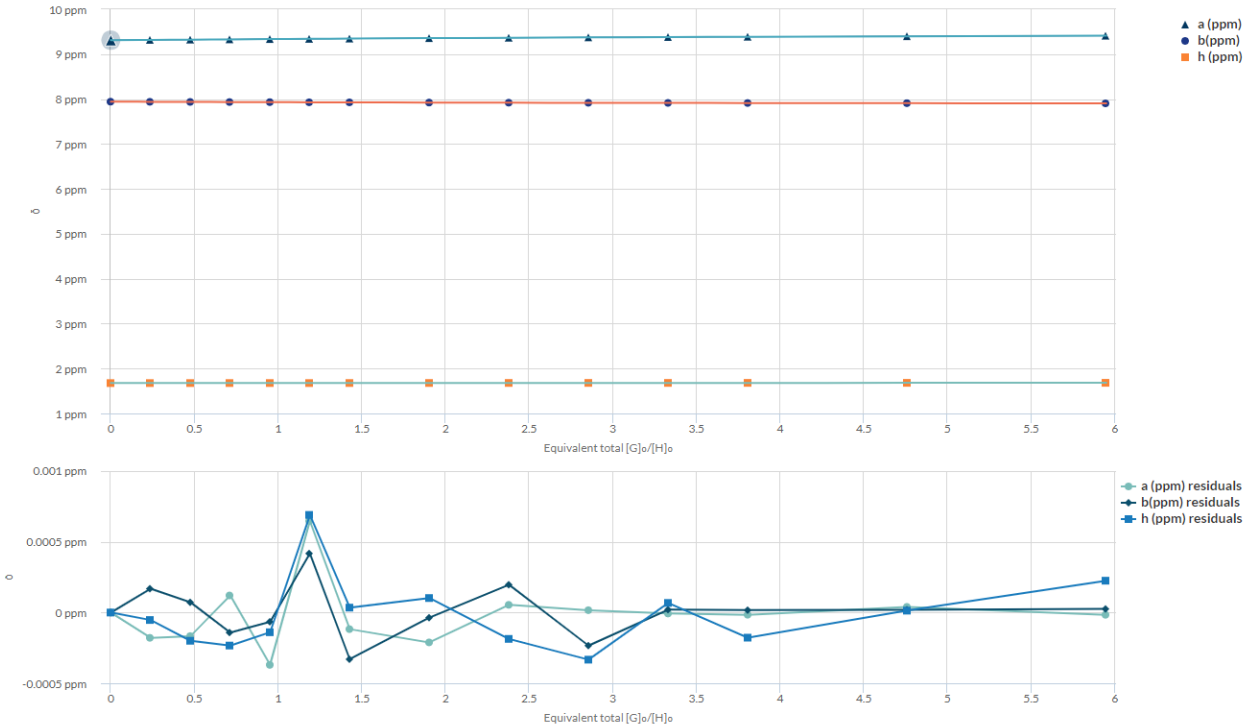

Figure S4.28 Global fitting plot and residual distributions of proton a, e and h for the titration experiment ClO_4^- with $[Pd_2\mathbf{L}^{\mathbf{Me}}{}_4]^{4+}$ using 1:2 statistical binding mode.

4.6.5 Isothermal titration calorimetry (ITC).

All the ITC experiments were performed at 298 K in CD_3CN on Malvern MicroCal PEAQ-ITC., the accurate concentrations of cage complexes were determined by NMR with adding 1.0 eq. tetrabutylammonium tetrafluoroborate as reference. The splitting of peaks is caused by the dilution effect when the concentrated guest solution goes into sample cell, which has been corrected as background for data analysis.

4.6.5.1. Raw data of reference experiments

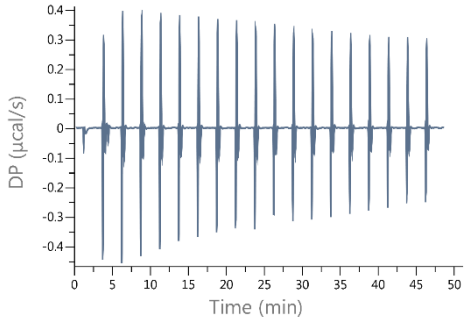

Figure S4.29. Reference titration experiment, TBA(ReO_4) (10 mM) into CD_3CN.

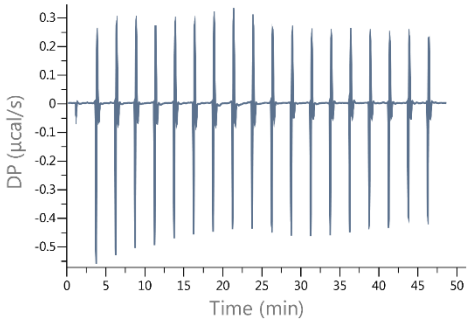

Figure S4.30. Reference titration experiment, TBA(IO_4) (15 mM) into CD_3CN

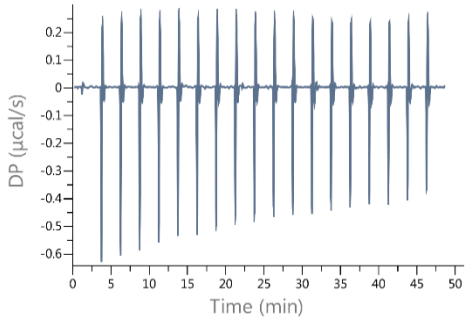

Figure S4.31. Reference titration experiment, TBA(ClO_4) (15 mM) into CD_3CN

4.6.5.2. Microcalorimetric titration of $[Pd_2\mathbf{L}^{Ph}_4](BF_4)_4$ with ReO_4^-

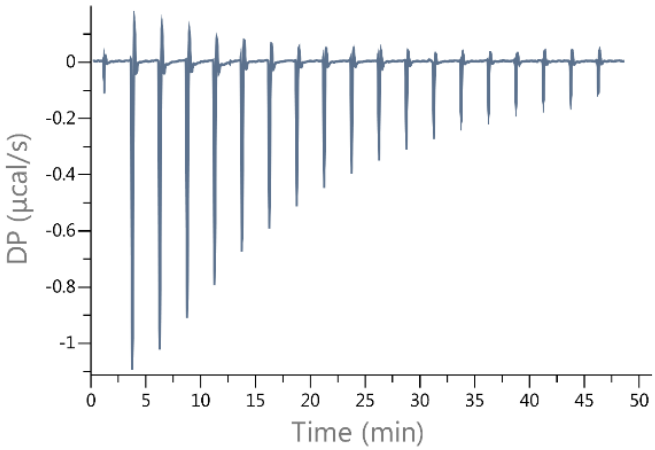

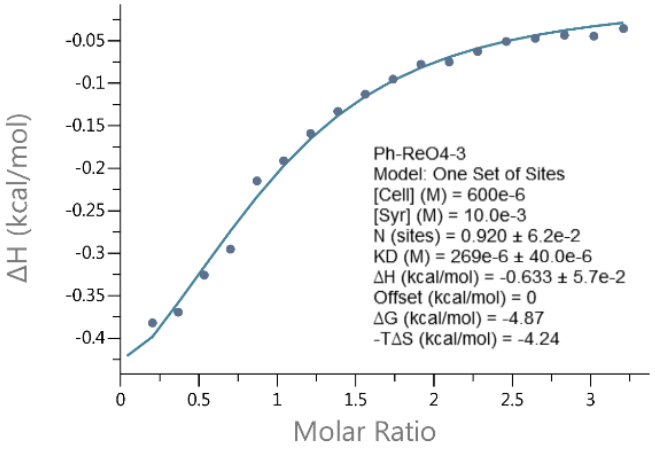

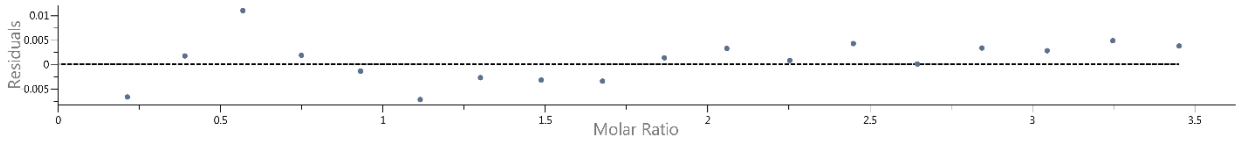

4.6.5.3. Microcalorimetric titration of $[Pd_2\mathbf{L}^{Ph}_4](BF_4)_4$ with IO_4^-

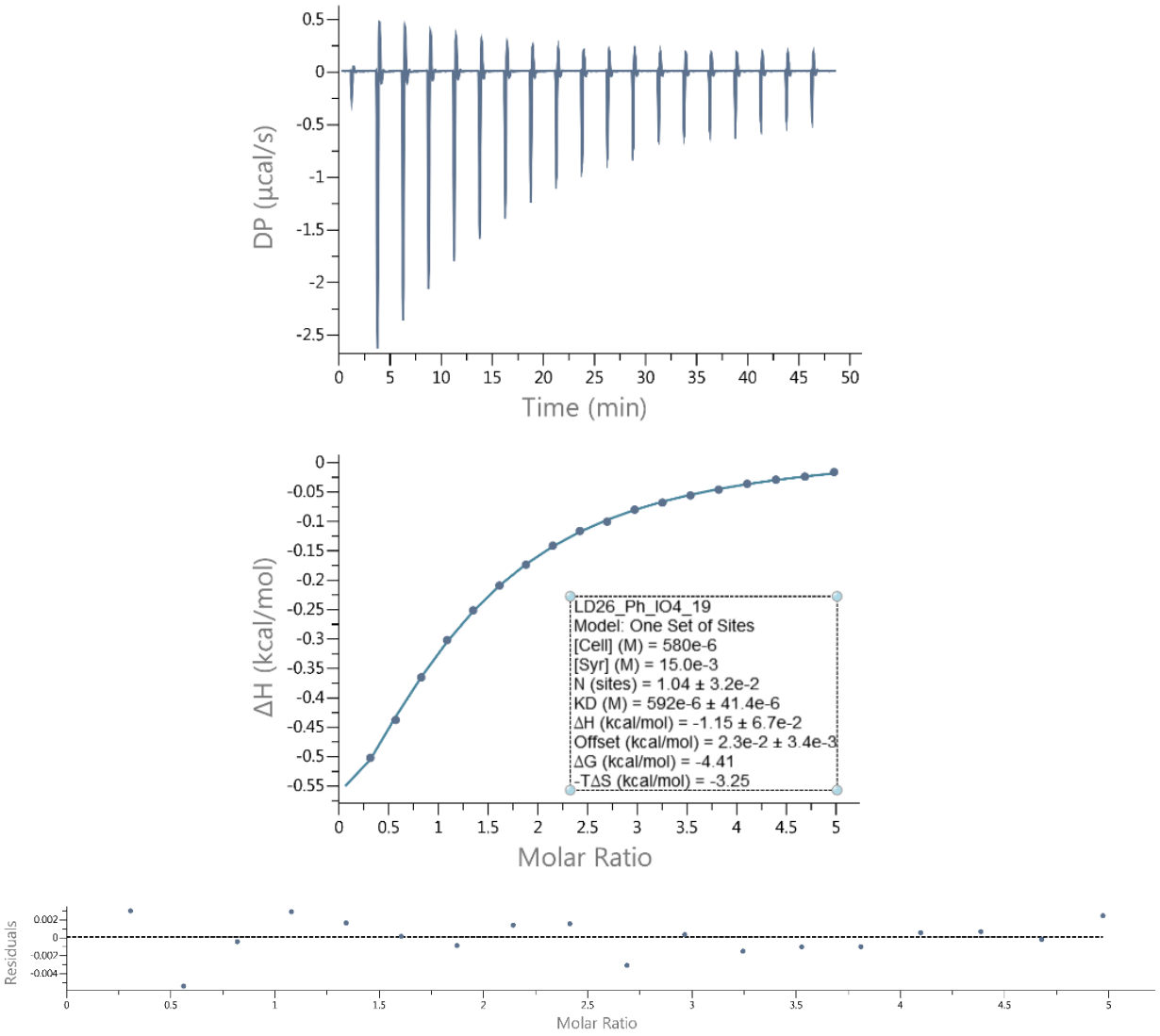

4.6.5.4. Microcalorimetric titration of $[Pd_2\mathbf{L}^{Ph}_4](BF_4)_4$ with ClO_4^-

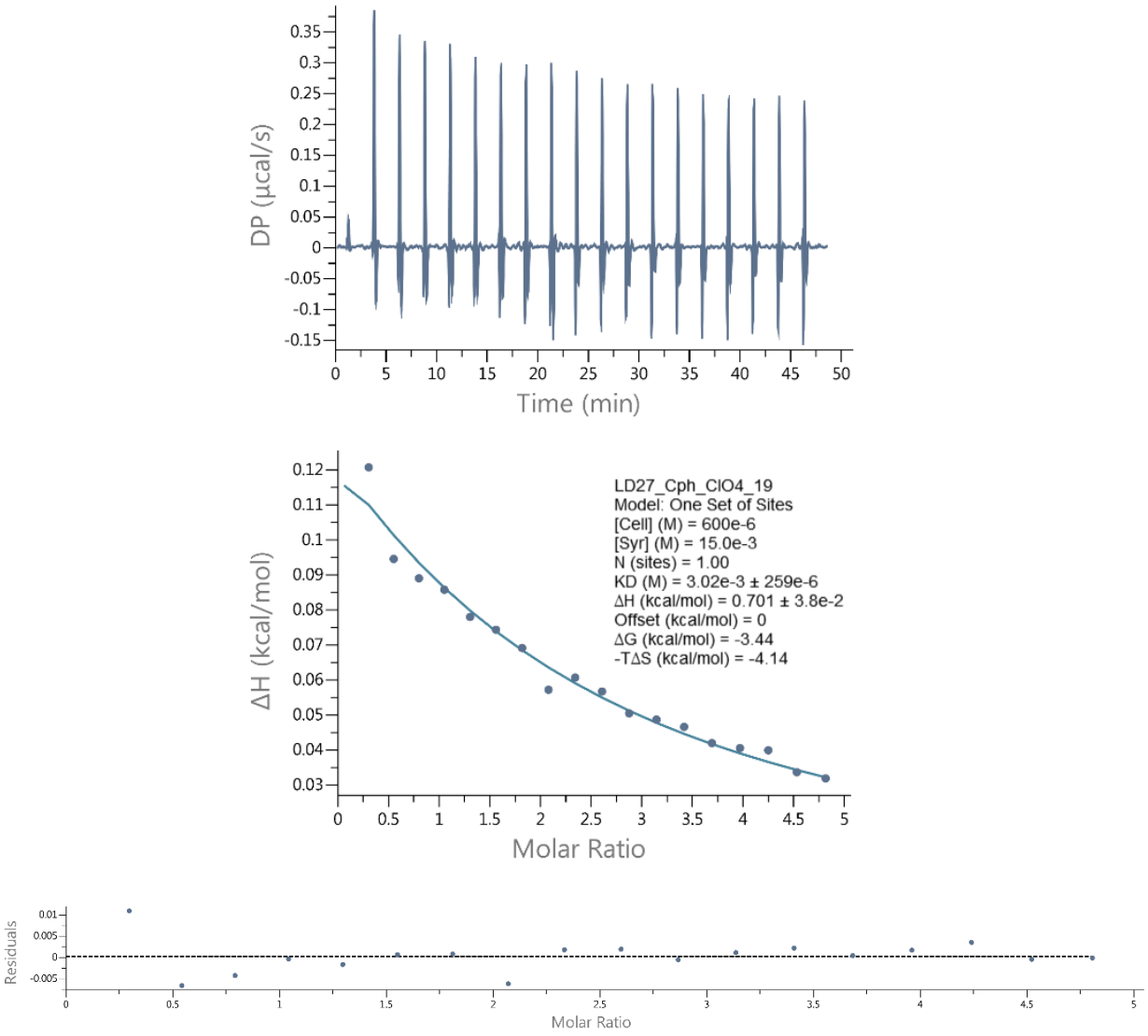

4.6.5.5. Microcalorimetric titration of $[Pd_2\mathbf{L}^{\mathbf{Bu}}{}_4](BF_4)_4$ with ReO_4^-

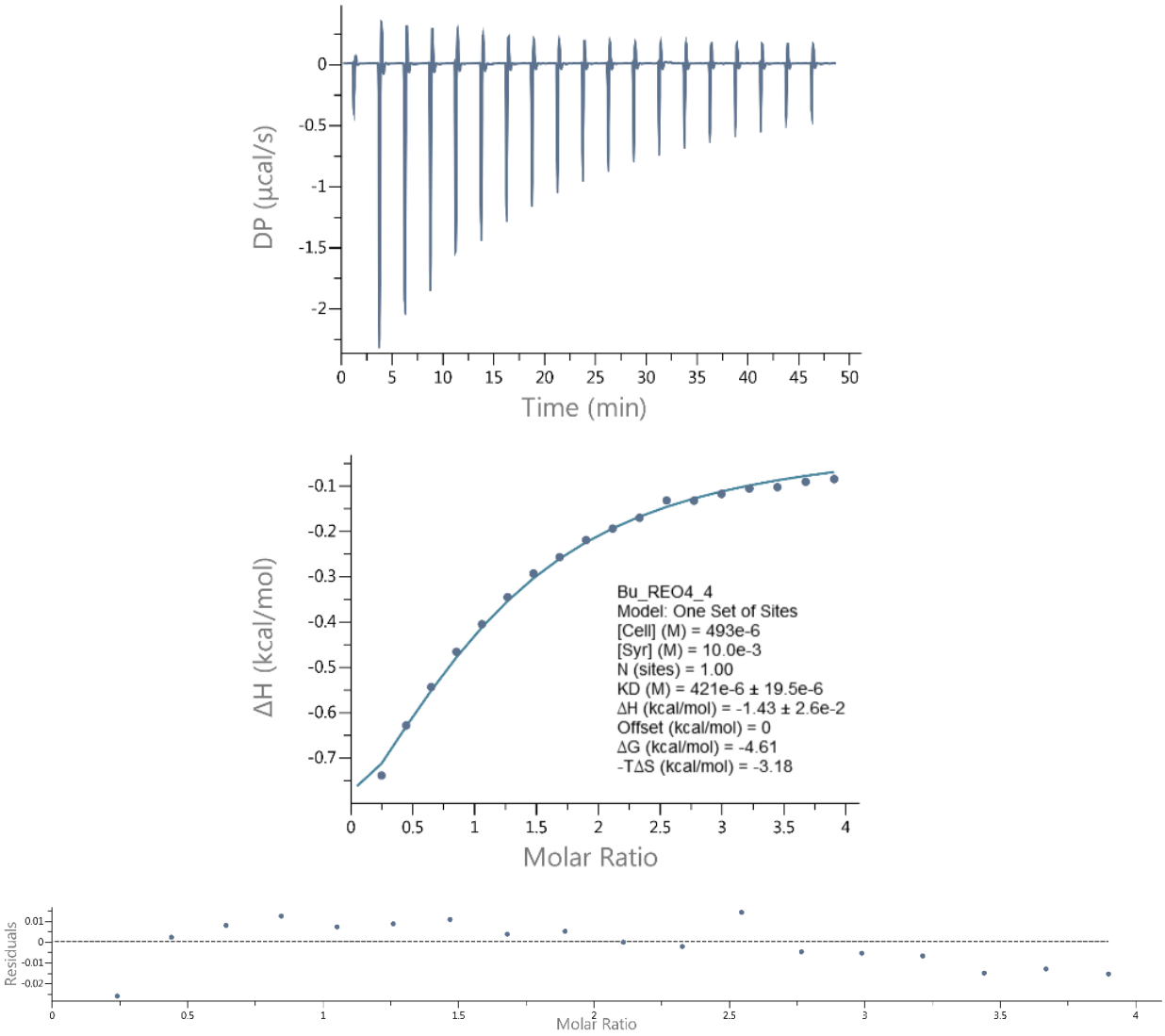

4.6.5.6. Microcalorimetric titration of $[Pd_2\mathbf{L}^{\mathbf{Bu}}{}_4](BF_4)_4$ with IO_4^-

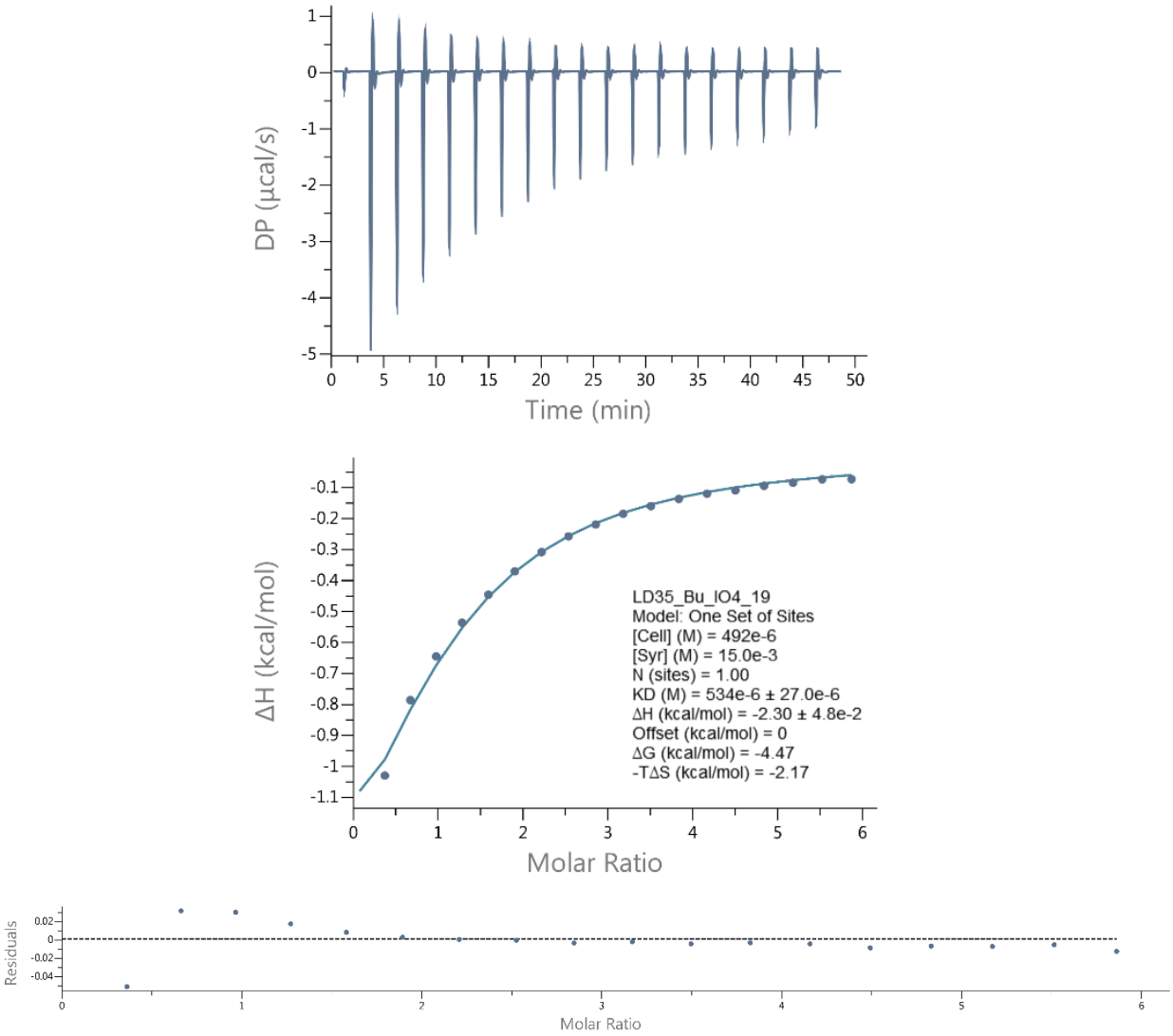

4.6.5.7. Microcalorimetric titration of $[Pd_2\mathbf{L}^{\mathbf{Bu}}{}_4](BF_4)_4$ with ClO_4^-

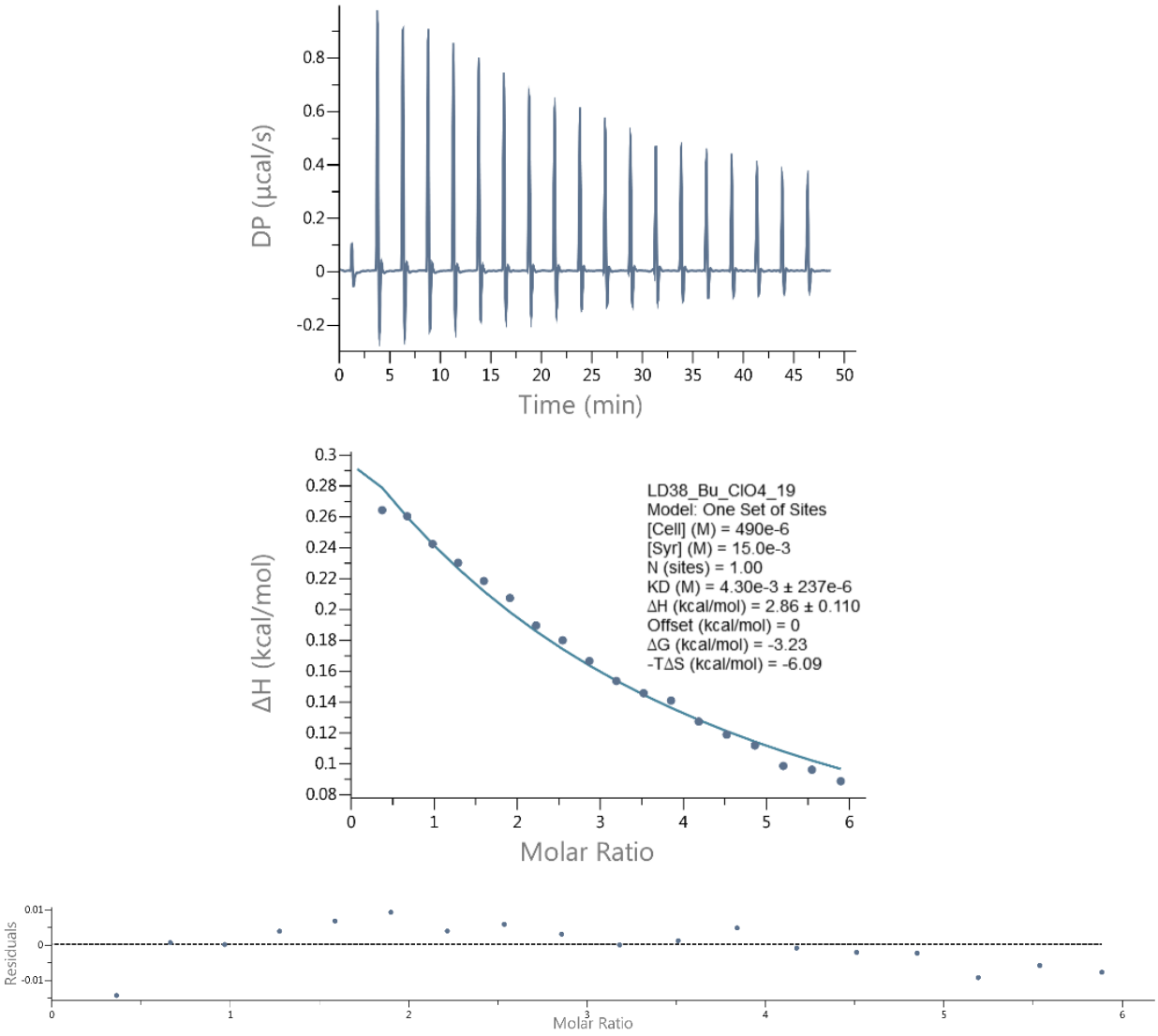

4.6.5.8. Microcalorimetric titration of $[Pd_2\mathbf{L}^{\mathbf{Me}}{}_4](BF_4)_4$ with ReO_4^-

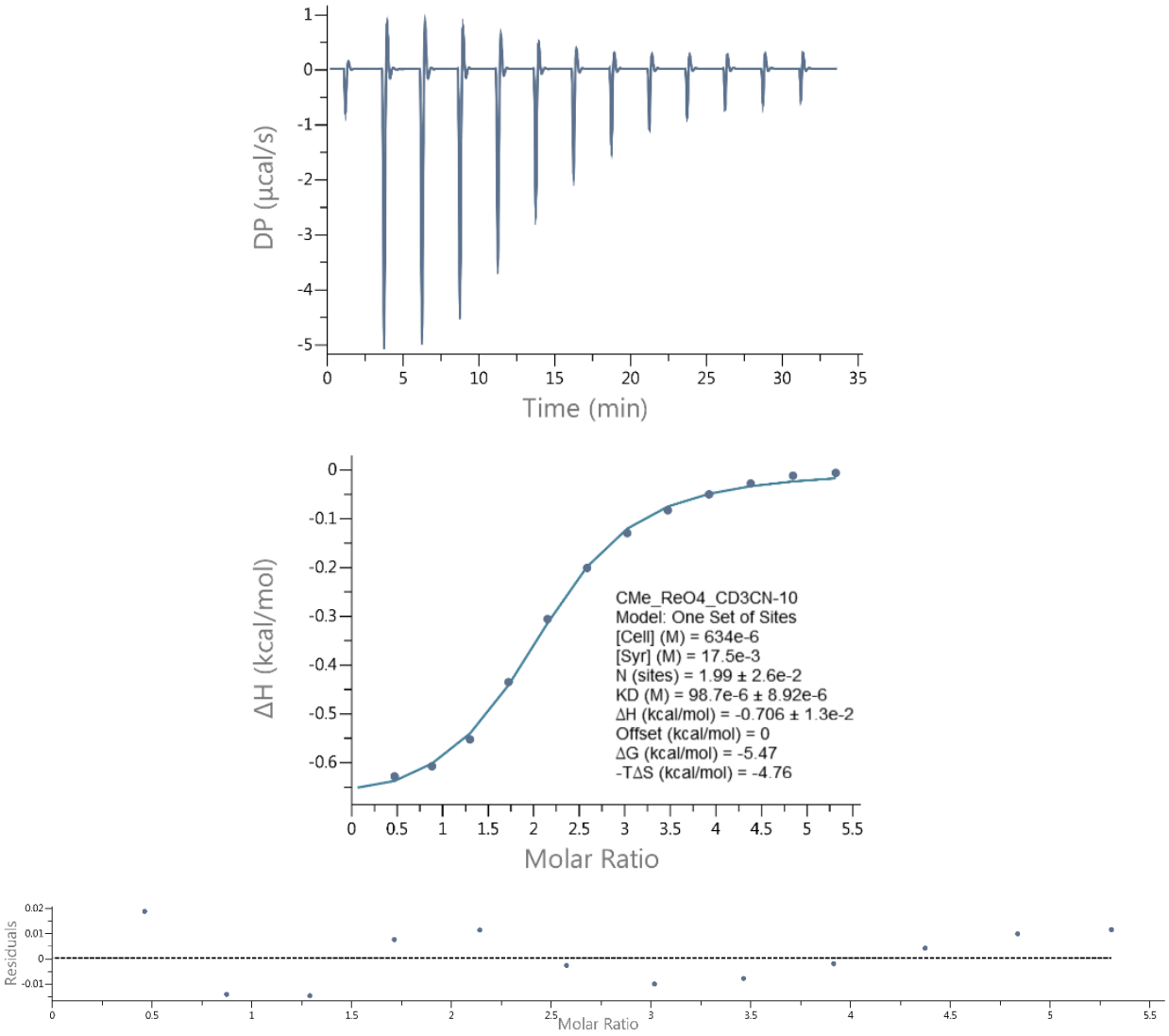

4.6.5.9. Microcalorimetric titration of $[Pd_2L^{Me}_4](BF_4)_4$ with ClO_4^-

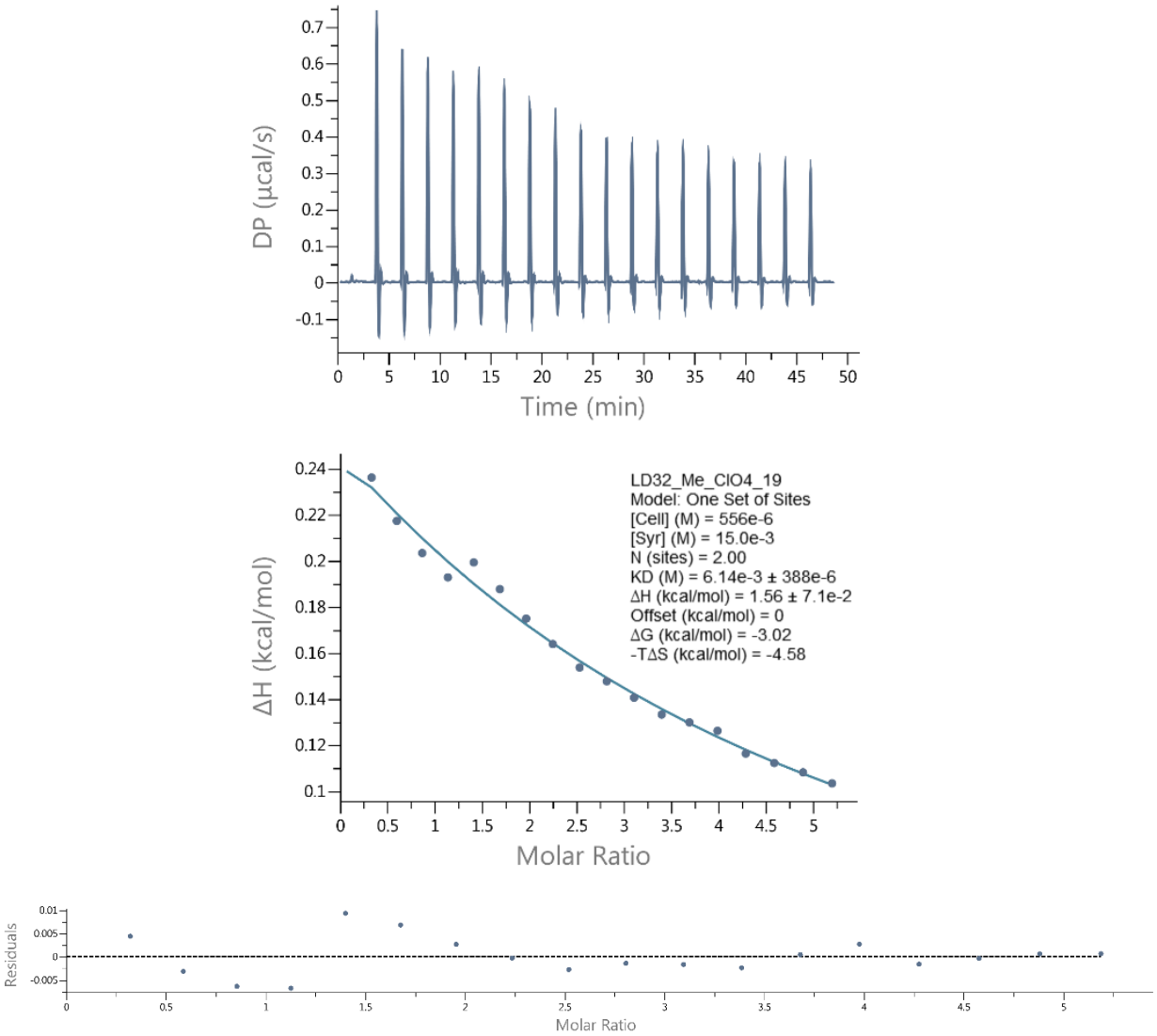

4.6.5.10. Microcalorimetric titration of $[Pd_2L^{Me}_4](BF_4)_4$ with IO_4^-

a)

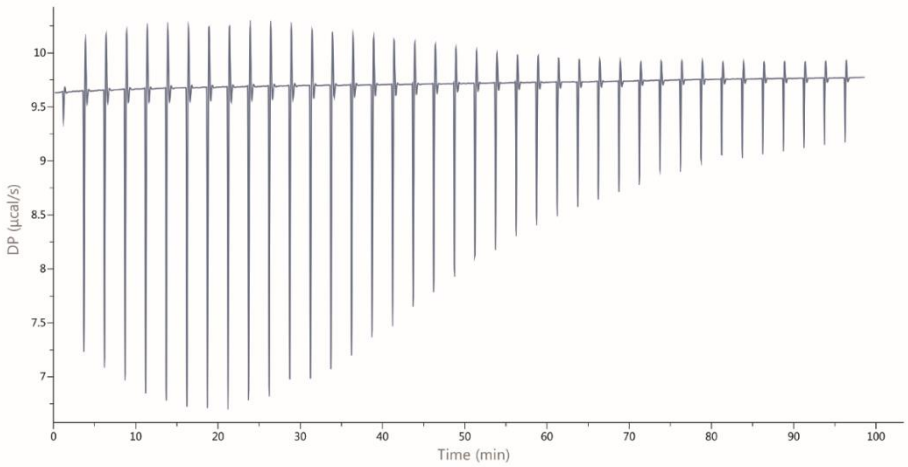

b)

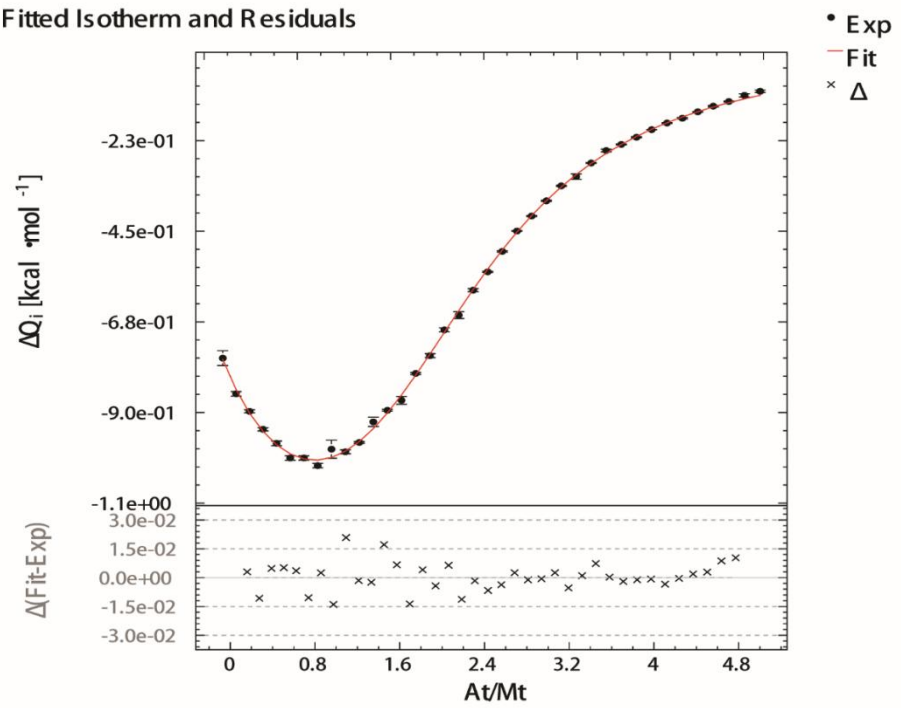

Reaction	K [M^{-n}]	ΔH [cal · mol^{-1}]
[1] Free species ↔ MA	(6.6353 ± 0.1768) e+03	(−8.6175 ± 0.0394) e+02
[2] MA ↔ MA_2	(2.8080 ± 0.0972) e+03	(−2.5494 ± 0.0128) e+03

a) Raw ITC data for 39 injections of IO_4^- solution into the solution of $[Pd_2L^{Me}_4]^{4+}$, b) the data was fitted with software Affinimeter (https://www.affinimeter.com/site/itc/).

.

4.6.6. High resolution mass spectrometric analysis of host-guest complexes.

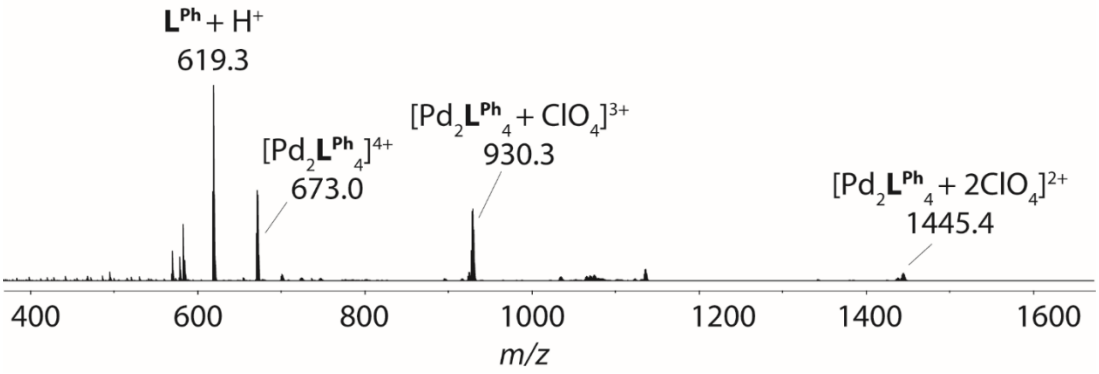

Figure S4.32. ESI mass spectrum of cage $[Pd_2\mathbf{L}^{Ph}_4](BF_4)_4$ with TBA(ClO_4).

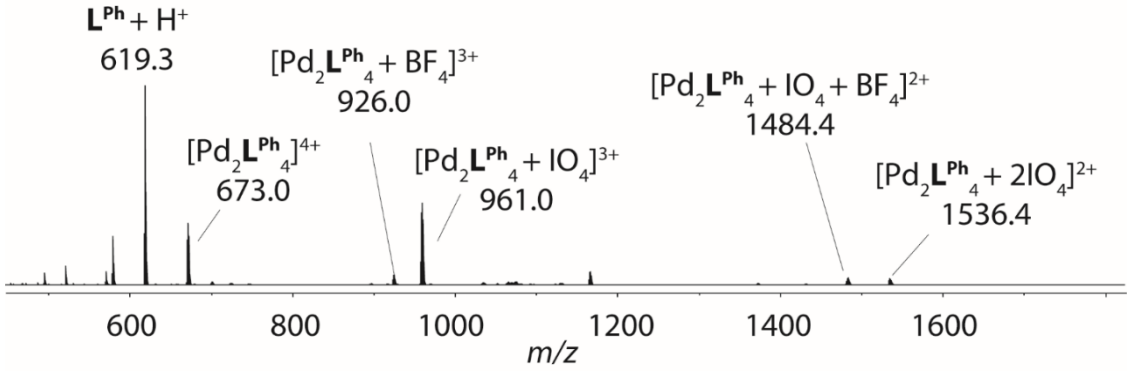

Figure S4.33. ESI mass spectrum of cage $[Pd_2\mathbf{L}^{Ph}_4](BF_4)_4$ with TBA(IO_4).

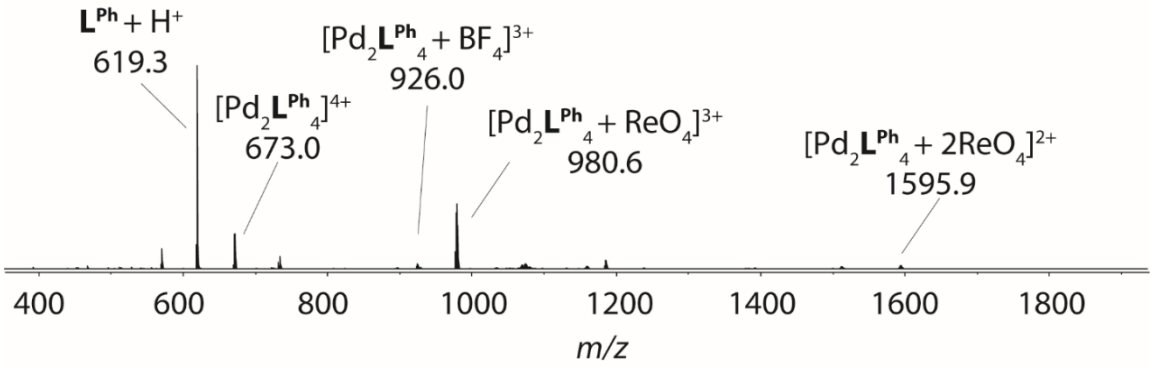

Figure S4.34. ESI mass spectrum of cage $[Pd_2\mathbf{L}^{Ph}_4](BF_4)_4$ with TBA(ReO_4).

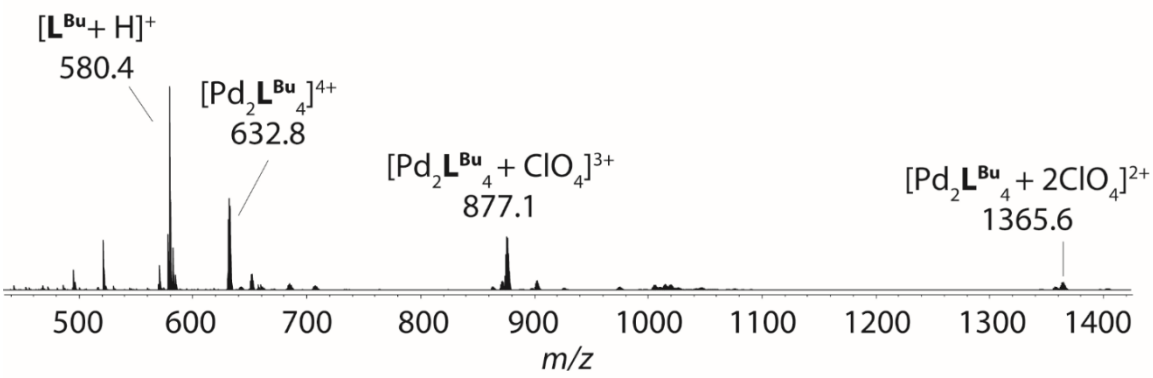

Figure S4.35. ESI mass spectrum of cage $[Pd_2\mathbf{L}^{\mathbf{Bu}}{}_4](BF_4)_4$ with TBA(ClO_4).

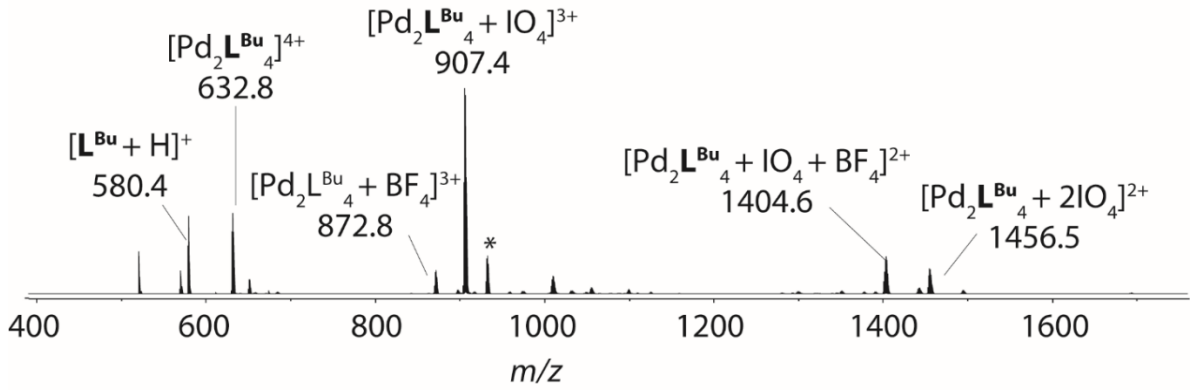

Figure S4.36. ESI mass spectrum of cage $[Pd_2\mathbf{L}^{\mathbf{Bu}}{}_4](BF_4)_4$ with TBA(IO_4).

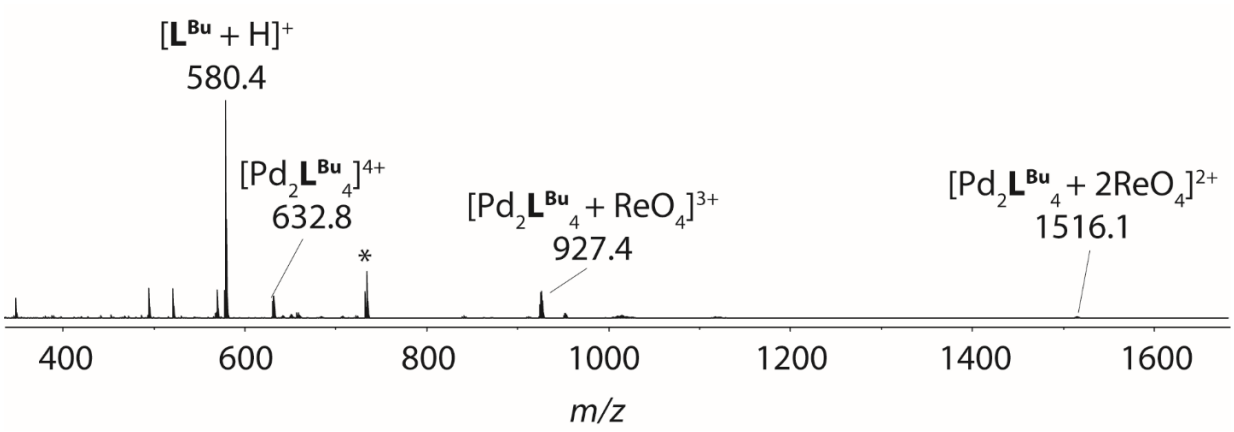

Figure S4.37. ESI mass spectrum of cage $[Pd_2\mathbf{L}^{\mathbf{Bu}}{}_4](BF_4)_4$ with TBA(ReO_4).

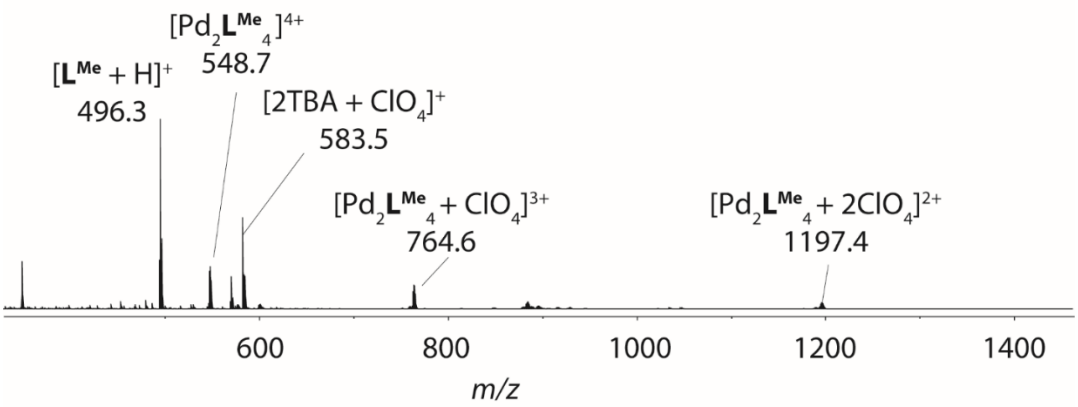

Figure S4.38. ESI mass spectrum of cage $[Pd_2\mathbf{L}^{Me}_4](BF_4)_4$ with TBA(ClO_4).

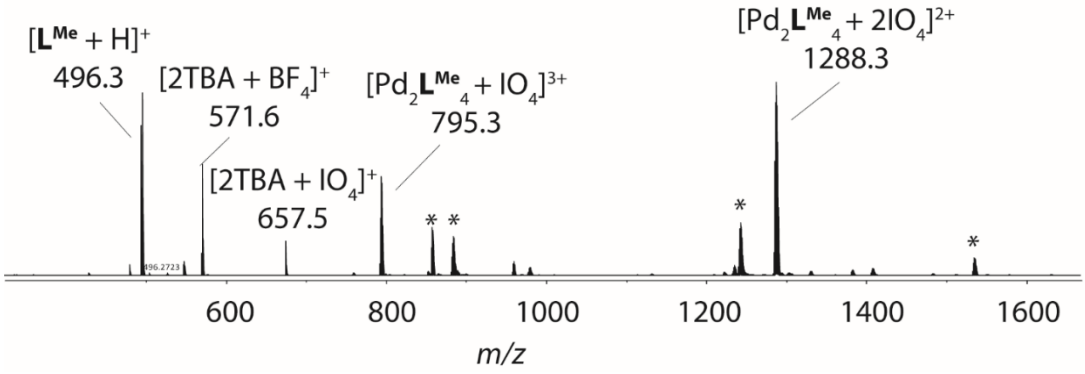

Figure S4.39. ESI mass spectrum of cage $[Pd_2\mathbf{L}^{Me}_4](BF_4)_4$ with TBA(IO_4).

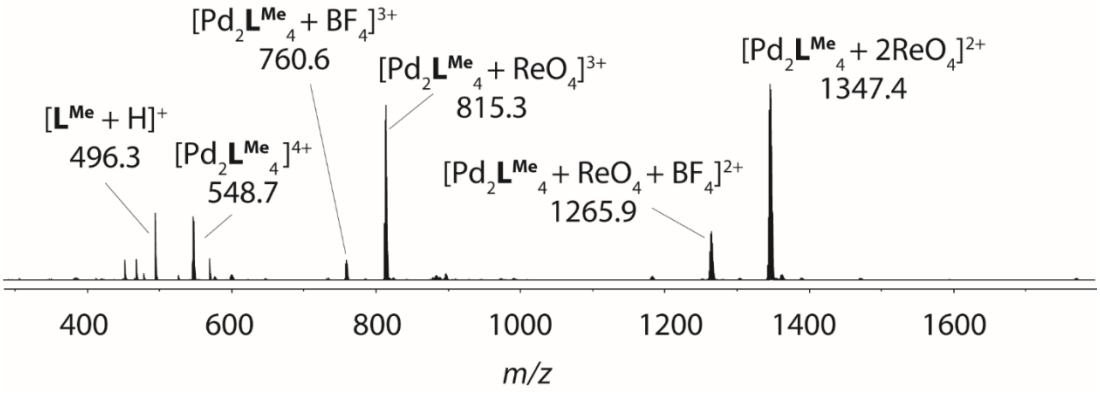

Figure S4.40. ESI mass spectrum of cage $[Pd_2\mathbf{L}^{Me}_4](BF_4)_4$ with TBA(ReO_4).

3.6.7. X-ray crystallography

General Methods

Crystals of supramolecular assemblies were extremely sensitive to loss of organic solvent. The supramolecular assemblies of **$[Pd_2L^{Me}_4](BF_4)_4$** and **$[Pd_2L^{Ph}_4](PF_6)_2(PO_2F_2)_2$**were successfully determined by single crystal X-ray crystallography. Diffraction data was collected during two beamtime shifts at macromolecular synchrotron beamline P11, PETRA III, DESY.[73] Using synchrotron radiation enabled us to reach a sub-atomic resolution of 0.70 Å. Nevertheless, modelling disorder of flexible side chains counterion ions and solvent molecules required carefully adapted macromolecular refinement protocols such as employing geometrical restraint dictionariesand restraints for anisotropic displacement parameters (ADPs) were employed. Analyzing morphologies and detailed geometries greatly enhanced the in-depth understanding of how these systems arrange in the solid state.

Data collection and crystal refinement were performed by Dr. Julian Holstein.

Table S3.10 Crystallographic data of $[Pd_2\mathbf{L}^{\mathbf{Me}}{}_4](BF_4)_4$ and $[Pd_2\mathbf{L}^{\mathbf{Ph}}{}_4](PF_6)_2(PO_2F_2)_2$.

Compound	$[Pd_2\mathbf{L}^{\mathbf{Me}}{}_4](BF_4)_4$	$[Pd_2\mathbf{L}^{\mathbf{Ph}}{}_4](PF_6)_2(PO_2F_2)_2$
Identification code	bz14a_sq	bz1a_sq
Empirical formula	$C_{314}H_{327}B_8F_{32}N_{35}O_3Pd_4$	$C_{196}H_{172}F_{10}N_{20}O_4P_3Pd_2$
Formula weight	5759.17	3367.24
Temperature [K]	80(2)	80(2)
Crystal system	monoclinic	monoclinic
Space group (number)	$P2_1/c$ (14)	$C2/c$ (15)
a [Å]	19.604(4)	35.558(7)
b [Å]	25.896(5)	27.815(6)
c [Å]	15.512(3)	18.500(4)
α [Å]	90	90
β [Å]	112.27(3)	100.51(3)
γ [Å]	90	90
Volume [Å^3]	7287(3)	17990(6)
Z	1	4
ρ_{calc} [g/cm^3]	1.312	1.243
μ [mm^{-1}]	0.297	0.164
F(000)	2992	6988
Crystal size [mm^3]	0.200×0.180×0.130	0.200×0.100×0.010
Radiation	synchrotron (λ=0.6888)	synchrotron (λ=0.5636)
2Θ range [°]	2.18 to 48.41	1.48 to 47.48
Index ranges	-23 ≤ h ≤ 23 -30 ≤ k ≤ 29 -18 ≤ l ≤ 18	-50 ≤ h ≤ 50 -39 ≤ k ≤ 39 -26 ≤ l ≤ 26
Reflections collected	79900	181501
Independent reflections	12840 R_{int} = 0.0240 R_{sigma} = 0.0161	26815 R_{int} = 0.0428 R_{sigma} = 0.0236
Completeness to θ = 24.205°	99.70	98.70
Data / Restraints / Parameters	12840/1537/1052	26815/3464/1481
Goodness-of-fit on F^2	1.024	1.029
Final R indexes [I≥2σ(I)]	R_1 = 0.0469 wR_2 = 0.1287	R_1 = 0.0611 wR_2 = 0.1799
Final R indexes [all data]	R_1 = 0.0477 wR_2 = 0.1295	R_1 = 0.0665 wR_2 = 0.1864
Largest peak/hole [eÅ^3]	0.98/-1.93	2.77/-1.45

3.6.7.1. Data collection details of cage $[Pd_2\mathbf{L}^{\mathbf{Me}}{}_4](BF_4)_4$

Orange block- shaped crystals of $[Pd_2\mathbf{L}^{Me}_4](BF_4)_4$ were grown by slow vapor diffusion of Et_2O into a solution of $[Pd_2\mathbf{L}^{Me}_4](BF_4)_4$ in CD_3CN. Seven crystals, each mounted on a loop, were placed in UNI Pucks and stored at cryogenic temperature in a dry shipper, in which they were safely transported to macromolecular beamline P11[42] at Petra III, DESY, Germany. UNI Pucks were transferred to the sample Dewar container and all samples were mounted using a StäubliTX60L robotic arm. A wavelength of 0.6888 Å was chosen using a liquid N_2 cooled double crystal monochromator. Single crystal X-ray diffraction data was collected at 80(2) K on a single axis goniometer, equipped with an Oxford Cryostream 800 and a Pilatus 6M detector. 1800 diffraction images were collected in a 360° ϕ sweep at a detector distance of 156 mm, 10% filter transmission, 0.2° step width and 200 milliseconds exposure time per image. Data integration and reduction were undertaken using XDS.[43] The maximum resolution of 0.70 Å was reached. The structures were solved by intrinsic phasing/direct methods using SHELXT[44] and refined with SHELXL[45] for full-matrix least-squares routines on F^2 using ShelXle[46] as a graphical user interface. DSR program pluginp[47][48] was employed for modeling.

3.6.7.2. Refinement details of cage $[Pd_2\mathbf{L}^{Me}_4](BF_4)_4$

The Co-crystallized diethyl ether solvent molecule is disordered over special position (inversion center) in the center of the cage cavity. Both Tetrafluoroborate counterions are disordered over two positions. To achieve a stable refinement of disordered and highly flexible solvents parts, stereochemical restraints for diethyl ether and acetonitrile solvent molecules in residue classes ETO and ACN were generated by the GRADE program using the GRADE Web Server (http://grade.globalphasing.org) and applied in the refinement. GRADE dictionaries contains target values and standard deviations for 1,2-distances (DFIX) and 1,3-distances (DANG), as well as restraints for planar groups (FLAT). Stereochemical restraints for Tetrafluoroborate counterions in residue class BF4 were generated from the Cambridge CSD using the Mogul program in manual mode. The anisotropic refinement for C, N, O atoms was enabled by a combination of similarity restraints (SIMU) and rigid bond restraints (RIGU).[49]

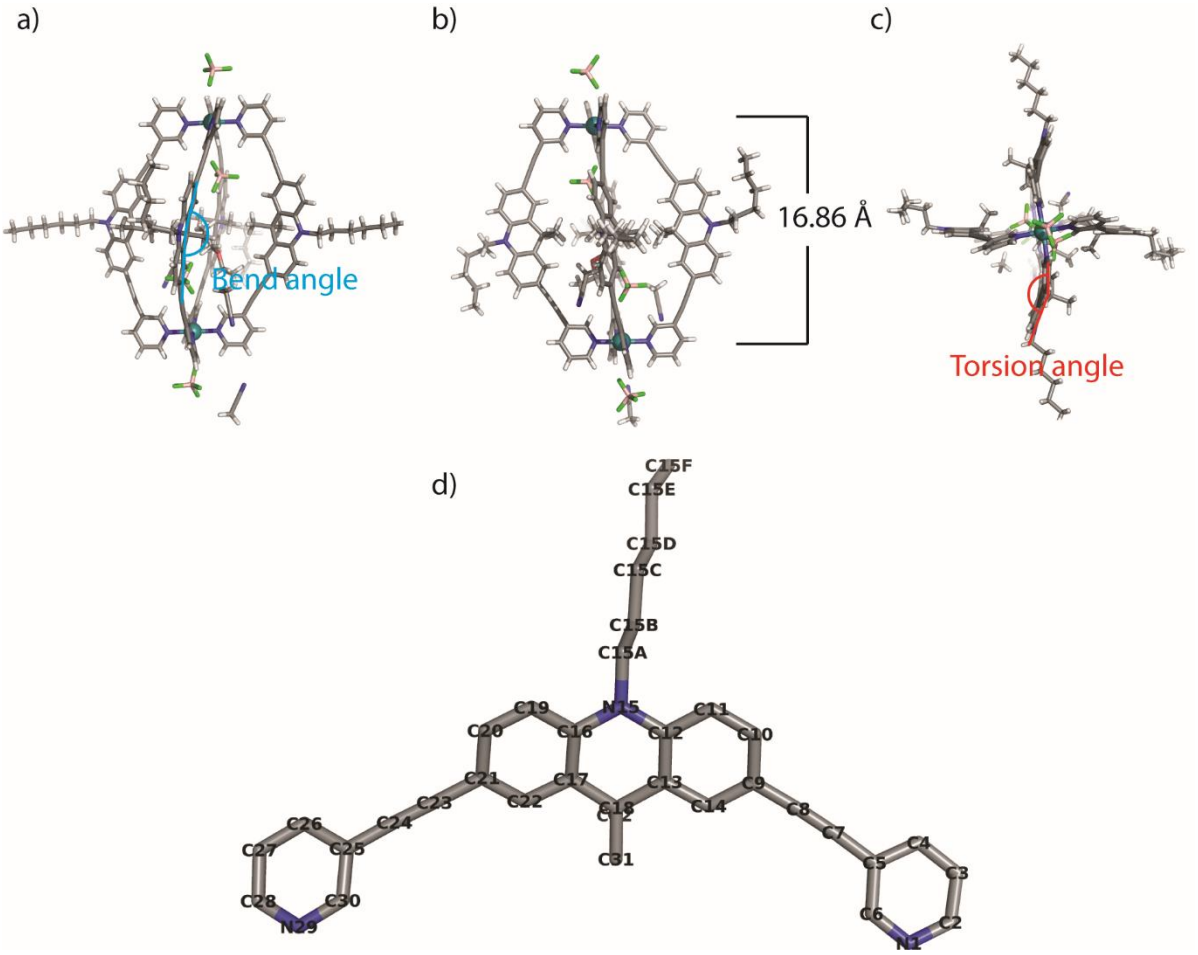

Figure S4.41 X-ray structure of $[Pd_2\mathbf{L}^{Me}_4](BF_4)_4$, a) front view, bend angle is defined as the obtuse angle formed by two benzene planes, b) side view, Pd-Pd distance 16.8574 (0.0046) Å, c) top view, torsion angle is determined by line C11-C14 and C4-N1, d) atomic naming scheme of $\mathbf{L}^{Me}$ (residue class AMP, residue number 2 and 3).Color code: Pd, deep teal; C, gray; N, blue; H, white; B, pink; F, light green.

Table S4.12 Calculated bend angle and torsion angle of $\mathbf{L}^{Me}$ in $[Pd_2\mathbf{L}^{Me}_4](BF_4)_4$.

Residues No.	Dihedral angle (°) between the benzene planes (bend angle) C16-C17-C19-C20-C21-C22 and C9-C10-C11-C12-C13-C14	Esd	Torsion angel (°) between C11-C14 and C4-N1 or C19-C22 and C26-N29	Esd
2	161.34	0.16	158.52	0.11
			146.66	0.13
3	172.97	0.14	159.16	0.11
			171.10	0.13
Average	167.15		158.86	

3.6.7.3. Data collection details of cage $[Pd_2\mathbf{L}^{Ph}{}_4](PF_6)_2(PO_2F_2)_2$

Colorless plate- shaped crystals of $[Pd_2\mathbf{L}^{Ph}{}_4](PF_6)_4$ were grown by slow vapor a solution of $[Pd_2\mathbf{L}^{Me}{}_4](PF_6)_4$ in CD_3CN. Five crystals, each mounted on a loop, were placed in UNI Pucks and stored at cryogenic temperature in a dry shipper, in which they were safely transported to macromolecular beamline P11 [42] at Petra III, DESY, Germany. UNI Pucks were transferred to the sample Dewar container and all samples were mounted using a StäubliTX60L robotic arm. A wavelength of 0.5636 Å was chosen using a liquid N_2 cooled double crystal monochromator. Single crystal X-ray diffraction data was collected at 80(2) K on a single axis goniometer, equipped with an Oxford Cryostream 800 and a Pilatus 6M detector. 720 diffraction images were collected in a 360° ϕ sweep at a detector distance of 200 mm, 100% filter transmission, 0.5° step width and 100 milliseconds exposure time per image. Data integration and reduction were undertaken using XDS.[43] The maximum resolution of 0.70 Å was reached. The structures were solved by intrinsic phasing/direct methods using SHELXT[44] and refined with SHELXL[45] for full-matrix least-squares routines on F^2 using ShelXle[46] as a graphical user interface. DSR program plugin[47][48] was employed for modeling.

3.6.7.3. Refinement details of cage $[Pd_2\mathbf{L}^{Ph}{}_4](PF_6)_2(PO_2F_2)_2$

The coordinating ligands $\mathbf{L}^{Ph}$ is disordered over special position (inversion center). Co-crystallized hexafluorophosphate counterion is disordered over two positions, difluorophosphate counterion is disordered over three positions. To achieve a stable refinement of disordered and the highly flexible solvents parts, stereochemical restraints for coordinating ligands $\mathbf{L}^{Ph}$ and Acetonitrile solvent molecules in residue classes APP and ACN, were generated by the GRADE program using the GRADE Web Server (http://grade.globalphasing.org) and applied in the refinement. GRADE dictionaries contains target values and standard deviations for 1,2-distances (DFIX) and 1,3-distances (DANG), as well as restraints for planar groups (FLAT). Additional similarity restraints (SADI) for 1.2 and 1.3 distances were required to model the highly flexible and disordered hexyl chains of the coordinating ligands $\mathbf{L}^{Ph}$ in residues class APP. Stereochemical restraints for hexafluorophosphate and difluorophosphate in residue classes PF6 and POF were derived from semi-empirical quantum mechanics calculation using the XTB program.[50] For each orientation of the difluorophosphate counterion the occupancy factors were freely refined using a free variable and the sum of all three free variables was restrained to 100% using the SUMP command. The anisotropic refinement for C, N, O atoms was enabled by a combination of similarity restraints (SIMU) and rigid bond restraints (RIGU).[49]

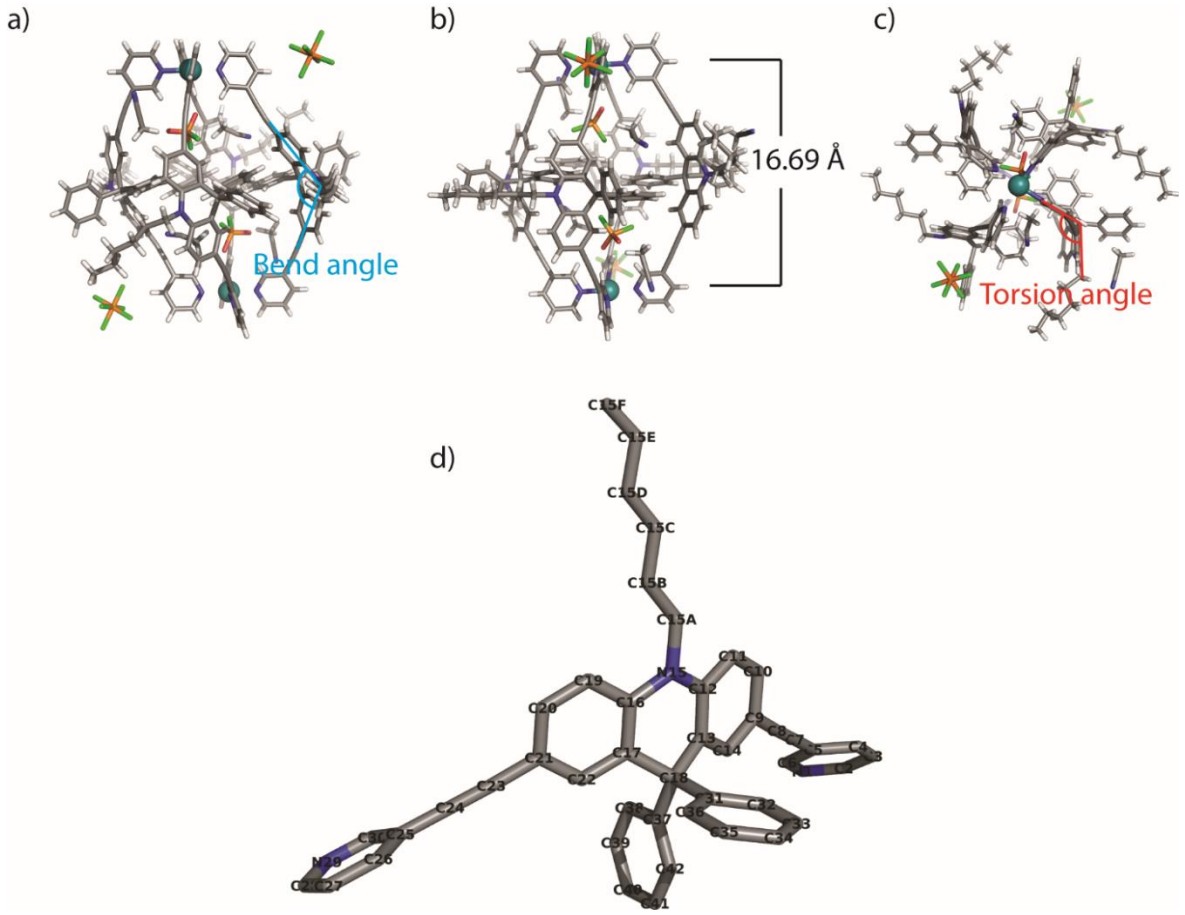

Figure S4.42 X-ray structure of $[Pd_2\mathbf{L}^{Ph}_4](PF_6)_2(PO_2F_2)_2$, a) front view, bend angle is defined as the obtuse angle formed by two benzene planes, b) side view, Pd-Pd distance 16.6049 (0.0033) Å, c) top view, torsion angle is determined by line C11-C14 and C4-N1, d) atomic naming scheme of $\mathbf{L}^{Ph}$ (residue class APP, residue number 2 and 3).Color code: Pd, deep teal; C, gray; N, blue; H, white; B, pink; F, light green, O, red; P. orange.

Table S4.13 Calculated bend angle and torsion angle of $\mathbf{L}^{ph}$ in $[Pd_2\mathbf{L}^{Ph}_4](PF_6)_2(PO_2F_2)_2$.

Residues No.	Dihedral angle (°) between the benzene planes (bend angle) C16-C17-C19-C20-C21-C22 and C9-C10-C11-C12-C13-C14	Esd	Torsion angel (°) between C11-C14 and C4-N1 or C19-C22 and C26-N29	Esd
2	150.03	0.10	122.06	0.14
			126.38	0.15
3	157.37	0.25	119.50	0.10
			103.35	0.09
Average	153.70		117.82	

4.7. Reference

[1] R. Eisenschitz, F. London, Zeitschrift Für Physik **1930**, 60, 491–527.

[2] F. London, Trans. Faraday Soc. **1937**, 33, 8b – 26.

[3] K. Autumn, M. Sitti, Y. A. Liang, A. M. Peattie, W. R. Hansen, S. Sponberg, T. W. Kenny, R. Fearing, J. N. Israelachvili, R. J. Full, PANS. **2002**, 99, 12252–12256.

[4] S. Grimme, The Chemical Bond (Eds.: G. Frenking, S.Shaik), Wiley-VCH, Weinheim, **2014**, 477–500.

[5] S. Grimme, Angew. Chem. Int. Ed. **2006**, 45, 4460–4464.

[6] M. D. Wodrich, C. S. Wannere, Y. Mo, P. D. Jarowski, K. N. Houk, P. Schleyer, Chem. Eur. J. **2007**, 13, 7731–7744.

[7] B. Kahr, D. Engen, K. Mislow, J. Am. Chem. Soc. **1986**, 108, 8305–8307.

[8] S. Rösel, C. Balestrieri, P. R. Schreiner, Chem. Sci. **2016**, 8, 405–410.

[9] S. Grimme, P. R. Schreiner, Angew. Chem. Int. Ed. **2011**, 50, 12639–12642.

[10] P. R. Schreiner, L. V. Chernish, P. A. Gunchenko, E. Tikhonchuk, H. Hausmann, M. Serafin, S. Schlecht, J. E. Dahl, R. M. Carlson, A. A. Fokin, Nature **2011**, 477, 308.

[11] S. Löffler, J. Lübben, A. Wuttke, R. A. Mata, M. John, B. Dittrich, G. H. Clever, Chem. Sci. **2016**, 7, 4676–4684.

[12] P. J. Wagner, P. R. Schreiner, Angew. Chem. Int. Ed. **2017**, 54, 12274–12296.

[13] D. J. Liptrot, P. P. Power, Nat. Rev. Chem.**2017**, 1, 0004.

[14] K. E. Riley, P. Hobza, Acc. Chem. Res. **2013**, 46, 927–936.

[15] S. Ehrlich, J. Moellmann, S. Grimme, Acc. Chem. Res. **2013**, 46, 916–926.

[16] D. C. Sherrill, Acc. Chem. Res. **2013**, 46, 1020–1028.

[17] E. M. Pérez, N. Martín, Chem. Soc. Rev. **2015**, 44, 6425–6433.

[18] B. W. Jennings, B. M. Farrell, J. F. Malone, Acc. Chem. Res. **2001**, 34, 885–894.

[19] H. Wu, Y. Chen, L. Zhang, O. Anamimoghadam, D. Shen, Z. Liu, K. Cai, C. Pezzato, C. L. Stern, Y. Liu, J. F. Stoddart, J. Am. Chem. Soc. **2018**, 141, 1280–1289.

[20] W. Meng, B. Breiner, K. Rissanen, J. D. Thoburn, J. K. Clegg, J. R. Nitschke, Angew. Chem. Int. Ed. **2011**, 50, 3479–3483.

[21] N. Kishi, Z. Li, K. Yoza, M. Akita, M. Yoshizawa, J. Am. Chem. Soc. **2011**, 133, 11438–11441.

[22] K. Suzuki, K. Takao, S. Sato, M. Fujita, J. Am. Chem. Soc. **2010**, 132, 2544–2545.

[23] K. Yazaki, M. Akita, S. Prusty, D. Chand, T. Kikuchi, H. Sato, M. Yoshizawa, Nat. Commun. **2017**, 8, 15914.

[24] F. J. Rizzuto, D. M. Wood, T. K. Ronson, J. R. Nitschke, J. Am. Chem. Soc. **2017**, 139, 11008–11011.

[25] B. Chen, J. J. Holstein, S. Horiuchi, W. G. Hiller, G. H. Clever, J. Am. Chem. Soc. **2019**, 22, 8907-8913.

[26] A. Jasat, J. C. Sherman, Chem. Rev. **1999**, 99, 931–968.

[27] J. Gabard, A. Collet, J. Chem. Soc., Chem. Commun. **1981**, 0, 1137–1139.

[28] J. Canceill, L. Lacombe, A. Collet, J. Am. Chem. Soc. **1986**, 108, 4230–4232.

[29] J. Canceill, M. Cesario, A. Collet, J. Guilhem, L. Lacombe, B. Lozach, C. Pascard, Angew. Chem. Int. Ed. **1989**, 28, 1246–1248.

[30] L. Garel, J. Dutasta, A. Collet, Angew. Chem. Int. Ed. **1993**, 32, 1169–1171.

[31] K. Bartik, M. Luhmer, J.-P. Dutasta, A. Collet, J. Reisse, J. Am. Chem. Soc. **1998**, 120, 784–791.

[32] G. Haberhauer, Á. Pintér, S. Woitschetzki, Nat. Commun. **2013**, 4, 2945.

[33] G. Haberhauer, S. Woitschetzki, H. Bandmann, Nat. Commun. **2014**, 5, 3542.

[34] S. Löffler, J. Lübben, L. Krause, D. Stalke, B. Dittrich, G. H. Clever, J. Am. Chem. Soc. **2015**, 137, 1060–1063.

[35] S. Löffler, A. Wuttke, B. Zhang, J. J. Holstein, R. A. Mata, G. H. Clever, Chem. Commun. **2017**, 53, 11933–11936.

[36] R. Pollice, M. Bot, I. J. Kobylianskii, I. Shenderovich, P. Chen, J. Am. Chem. Soc. **2017**, 139, 13126–13140.

[37] B. D. Hibbert, P. Thordarson, Chem. Commun. **2016**, 52, 12792–12805.

[38] C. Sgarlata, J. S. Mugridge, M. D. Pluth, B. E. Tiedemann, V. Zito, G. Arena, K. N. Raymond, J. Am. Chem. Soc. **2010**, 132, 1005–1009.

[39] B. W. Turnbull, A. H. Daranas, J. Am. Chem. Soc. **2003**, 125, 14859–14866.

[40] J. Tellinghuisen, Anal. Biochem. **2008**, 373, 395–397.

[41] T. L. Andrew, T. ager, J. Org. Chem. **2011**, 76, 2976–2993.

[42] A. Burkhardt, T. Pakendorf, B. Reime, J. Meyer, P. Fischer, N. Stübe, S. Panneerselvam, O. Lorbeer, K. Stachnik, M. Warmer, P. Rödig, D. Göries, A. Meents, *Eur. Phys. J. Plus.* **2016**, *131*.

[43] W. Kabsch, *Acta Crystallogr*. *Sect. D* **2010**, *66*, 125-132.

[44] G. M. Sheldrick, *Acta Crystallogr*. *Sect. A* **2015**, *71*, 3-8.

[45] G. M. Sheldrick, *Acta Crystallogr*. *Sect. C* **2015**, *71*, 3-8.

[46] C. B. Hubschle, G. M. Sheldrick, B. Dittrich, *J Appl Crystallogr*. **2011**, *44*, 1281-1284.

[47] D. Kratzert, J. J. Holstein, I. Krossing, J Appl Crystallogr **2015**, 48, 933–938.

[48] D. Kratzert, I. Krossing, J Appl Crystallogr **2018**, 51, 928–934.

[49] A. Thorn, B. Dittrich, G. M. Sheldrick, *Acta Crystallogr. Sect. A* **2012**, *68*, 448-451.

[50] C. Bannwarth, S. Ehlert, S. Grimme, J Chem Theory Comput **2019**, 15, 1652–1671.

5.Conclusion and Outlook

Investigations into metal-mediated coordination cages have been presented in this dissertation.

In chapter 2, a novel approach against entropic effect was developed. Combining the concepts of coordination chemistry, dynamic-covalent chemistry and shape complementary, a series of heteroleptic coordination cages based on cobalt-salphen complexes were successfully synthesized. The most complicated structure is composed of four different organic ligands leading to only one specific structure ($[Co_2\mathbf{ABCD}]^{2+}$ cage), instead of statistical mixtures. All the structures were fully characterized by NMR, HR-MS and X-ray analysis.

In the future, the introduction of functional units to the system would be desirable to obtain a multifunctional system. In the work of this thesis, various functionalities were installed into the cobalt-salphen based coordination cages (chapter 3). A chiral cage $[Co_2\mathbf{A}_2\mathbf{F}_2\mathbf{G}_2]^{2+}$ equipped with phenothiazine units was synthesized, which has potential to be used for asymmetric catalysis or as chiral molecular sensor. In addition, we have proposed the synthesis of generating novel rotaxane structures using the concept of geometric complementarity of bismonodentate banana-shaped ligand and binuclear salphen based macrocycle, which is expected to provide a new aspect for design of molecular machinery.

In chapter 4, the effect of enthalpy related London dispersion interactions has been investigated in a self-assembled host-guest system. Three Pd(II) coordination cages functionalized with methyl, *n*-butyl and phenyl groups as dispersion energy donor, respectively, were synthesized and characterized by NMR, HR-MS and partly by X-ray analysis. Both NMR titrations and ITC experiments confirmed that cage $[Pd_2\mathbf{L}^{\mathbf{Me}}_4]^{4+}$ has the highest binding affinities with all three anionic guests tested (ClO_4^-, IO_4^-, ReO_4^-) due to relatively small interior steric hindrance. According to ITC results, London dispersion effects are supposed to play a more important role in case of cage $[Pd_2\mathbf{L}^{\mathbf{Bu}}_4]^{4+}$ in comparison with cage $[Pd_2\mathbf{L}^{\mathbf{Ph}}_4]^{4+}$. On the other side, higher binding constants of IO_4^- and ReO_4^-compared to ClO_4^-might also related to dispersion effects, since they either have higher polarizability (IO_4^-) or consist of heavier element (ReO_4^-). However, other factors like charge distribution should also be considered.

Next, structural information of the host-guests complexes in gas phase would be collected using ion mobility mass spectrum. In addition, theoretical studies in collaboration with the group of Prof. Mata, are expected to provide a better understanding about the system.

6. Abbreviations and Symbols

Å	Ångström
°C	celcius
BF_4^-	tetrafluoroborate anion
Bu	butyl group
Co	cobalt
ClO_4^-	Perchlorate anion
$CHCl_3$	chloroform
CD_3CN	deuterated Acetonitrile
COSY	correlated spectroscopy
DMSO	dimethylsulfoxid
DCM	dichloromethane
DED	dispersion energy donor
eq.	equivalent
ESI	electrospray ionization
EtOAc	ethyl acetate
GPC	Gel permeation chromatography
h	hour
HR-MS	high resolution mass spectrometry
Hz	hertz
ITC	isothermal titration calorimetry
IO_4^-	periodate anion
J	coupling constant
L	ligand
M	metal ion
Me	methyl group
m/z	mass-to-charge ratio
MeOH	methanol
MHz	megahertz
mM	mmol L^{-1}
NBS	*N*-Bromosuccinimide
NEt_3	triethylamine

NMR	nuclear magnetic resonance
PF_6^-	Hexafluorophosphate anion
Pd	palladium
Pt	platinum
ppm	parts per million
Ph	phenyl group
rt	room temperature
ReO_4^-	perrhenate anion
TBA	*tetra*-*n*-butylammonium

7. List of Figures

8. List of Tables

9. Acknowledgements

First of all, I would like to thank my supervisor Prof. Dr. Guido Clever for offering me the opportunity to finish my Ph.D. project in his group, also thanks very much for leading me into the amazing field of supramolecular chemistry. Thanks for his patient instruction and for providing the well-equipped working conditions. I admire him not only for he is a great scientist but also a great person. It has been an honor to work in Clever group.

I would like to thank Prof. Dr. Sebastian Henke for being on my PhD examination board.

I would like to thank Prof. Dr. Ricardo Mata for the nice collaboration and recommendation.

I would like to thank DFG and SPP1807 for offering financial support for the Ph.D. project.

Thanks all the members of the chemistry department. I would like to thank Dr. Gabriele Trötscher-Kaus, Birgit Thormann, Kristian Surich and Alexandra Klauke for the well-organized working environment. Thank Prof. Dr. Wolf Hiller and André Platzek for NMR support, thank Laura Schneider, Dr. David Engelhard and Christiane Heitbrink for ESI-Mass measurement; thank Dr. Julian Holstein, Dr. Witold Bloch, Dr. Rujin Li, Dr. Bin Chen, Irene Regeni, Philip Punt, Dr. Haeri Lee for picking crystals and X-ray data collections; thank Dr. Julian Holstein, Dr. Haeri Lee for crystal structure measurements and refinements.

Special thanks to all the group members of Clever group; thank Dr. Subhadeep Saha, Irene Regeni, Dr. Sonja Pullen, Dr. Jacopo Tessarolo for their proofreading of my thesis; thank all the members, who used to or currently working in the G lab and office C1-05-726. These four years will be the most unforgettable time in my life, we are not only colleagues but also friends. It is an amazing experience to work with people from different countries and cultures, I have learned much more than just chemistry here.

Last but not least, millions of thanks to my family, especially my parents. Thanks for their selfless love and unending support. From Urumchi to Beijing, and later to Marburg and Dortmund, I have crossed the whole Eurasia, I could fly because you raise me up.